Carboranes and their Incorporation into Siloxane Polymers.

A computational study

Isaac Sugden
6/11/2013

Declaration

I, Isaac Sugden, confirm that the work presented in this thesis is my own. Where information has been derived from other sources, I confirm that this has been indicated in the thesis,

London, September 2013

<u>Abstract</u>

This is a report detailing the computational investigation of copolymers containing carborane and siloxane monomers, to aid in the design an industrially relevant material for use in high neutron radiative environments.

This includes determining the optimal carborane/siloxane ratio in the designed material with regards to macroscale physical properties; with experimentally determined values for pure siloxane phases reproduced, using classical methods. The investigation shows that increasing carborane content increases bulk modulus and decreases the thermal expansion coefficient, levelling off beyond 50% carborane content. It also includes the effect of including specific side groups to polymer strands in order to affect properties; for instance, it is seen that phenyl groups increase the flexibility of the polymer strands. Alongside this, the report includes the simulation of property "aging"; using classical crosslinking methods to model the effect of high energy ions travelling through the material following neutron capture events, and *ab initio* simulation of damage to the monomer. Unsurprisingly, crosslinking sees a reduction in flexibility, leading to an increase in bulk modulus and a decrease in the thermal expansion coefficient, whilst the changes in vibrational spectra as a result of neutron capture events are predicted: due to changes in bond strength and orbital structure, modes involved with cage elements move to a higher frequency, and B-H modes move to lower.

Finally for the designed material, context is given by examining the current state of the art: solid boron carbide, and its remarkable resistance to radiation of several different forms, with experimental theories and mechanisms discussed.

Carborane clusters are further examined in other technological areas: thermal rearrangements of single carboranes and metallo-carboranes, with the 40 to 145 kJ/mol (dependent on mechanism) difference between theoretical and experimental activation energies rationalised, and investigations of icosahedral boron cluster anions in lithium battery electrolytes, where a $\approx$17% improvement in lithium mobility is theorised.

Contents

List of Figures

List of Tables

Note: Where my own scripts are referenced, these are collected on my personal website[1]: www.IsaacSugden.moonfruit.com/scripts/

Acknowledgements

I would like to acknowledge the tutelage and direction of my supervisor, Dr. Robert Bell, whose support has made me want to be a successful scientist, and has put me on the path to achieving that goal. I would also like to acknowledge Dr. David Plant for the creation of the project, and for being a reassuring contact for scientific discussion, along with Dr Furio Cora. My peer group has provided an astonishing amount of both ideas and comfort throughout my PhD, notably, and in no particular order: William Travis, Elisabeth Krizek, Jahangir Malik, Alex O'Malley, Alan Lobo, Nicolas Constantinou, Nuru Noor, and Dr Jamieson Christie. Finally, and forever, my wife (!)Chloe.

1 <u>Introduction</u>

1.1.1 <u>Objectives</u>

This thesis is a computational investigation into boron clusters in a variety of environments, with the ultimate aim to design new materials with industrial relevance. The main thrust of the project is to study the effect on bulk physical properties of introducing carborane entities into siloxane polymer backbones. This will help to resolve the optimal siloxane/carborane monomer ratio when creating carborane-siloxane copolymers, with respect to favourable physical properties, and boron density, within the industrial context.

The intended industrial context is for the material to be used sacrificially in high neutron radiative environments, taking advantage of the high neutron adsorption cross section of ^{10}B. This will reduce the danger of radiation to humans working in these environments by between 5-20 times depending on neutron velocity, and protect equipment.

The project will include:

1. The derivation of a forcefield for carborane/ siloxane copolymers.

2. The construction of polymer phases containing a user-specified percentage of carborane monomer, reproducing experimental observables such as density.

3. The derivation of physical properties as a function of carborane monomer % in the sample, using molecular dynamics.

4. An observation of the change in physical properties when a small percentage of monomer substitution is performed, for instance, phenyl-methyl-siloxane for dimethyl-siloxane, or *para-* for *meta-*carborane, using the same methods.

5. Some study of expected changes in physical properties given its industrial setting, for instance: the change in DFT predicted IR spectra for carboranes with boron positions removed by neutron capture events, or the change in molecular dynamics derived physical properties for polymers experiencing cross-linking as a result of high energy lithium ions travelling through the material following neutron capture events.

The project will also contain the study of boron clusters in general, although within the context of the main investigation. These will include:

- The study of the thermal rearrangement mechanism in carboranes, given the potential high working/synthesis temperature of the material in industry, and that when these polymers were synthesised experimentally: "... The integrity of the *m*-carborane cage and the segmental dynamics were found to be significantly reduced at temperatures

above 580˚ C, in line with the known cage rearrangement temperature for icosahedral carboranes"[2]

- The study of solid boron carbide under irradiation, which, when embedded in resin represents the current state-of-the-art material for neutron capturing in high neutron radiative environments

- A study on the possibility of using $B_{12}H_{12}^{2-}$ in place of BF_4^- in lithium battery electrolytes, in order to increase power density.

1.2 Neutron capture properties of boron

The ^{10}B isotope has the highest neutron absorption cross section of any light element; meaning that it is many times more likely to capture neutrons from a neutron flux than comparable elements[3]:

Table 1. Showing relative neutron adsorption cross sections of common elements and Boron	
Element	Coefficient (barns)
^{10}B	3838
^{1}H	0.333
^{12}C	0.0035
^{16}O	0.00019

Upon capturing a neutron, a ^{10}B nucleus will undergo a nuclear reaction[4], decomposing into short range particles: a lithium ion and alpha particle, and a percentage of long range radiation: gamma rays (the percentages quoted below are for thermal neutrons):

Scheme 1

$$94\%: {}^{10}B + n \rightarrow {}^{7}Li\ (0.84\ \text{MeV}) + {}^{4}He(1.47\ \text{MeV}) + \gamma\ (0.84\ \text{MeV})$$

$$6\%: {}^{10}B + n \rightarrow {}^{7}Li\ (1.02\ \text{MeV}) + {}^{4}He(1.78\ \text{MeV})$$
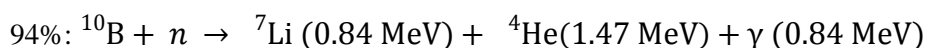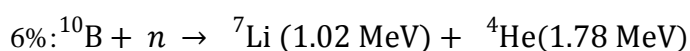
The property described above is under investigation in tumour therapy; the kinetic energies of Li and He produced by this reaction lead to a path length of 14 μm[5], which is approximately 1 or 2 human cells. This makes molecular species with a high boron density ideal for cancer therapy; using Boronophenylalanine (BPA), which is a blood brain barrier permeable amino acid analogue containing one boron atom, and a source of neutrons focused on the tumour, brain tumours have been treated experimentally[6]. The bulkiness and high boron content of carborane molecules make them ideal for this treatment: higher molecular weight molecules persist in the brain tissue longer than smaller molecules[7], and the forefront of this field involves using large, carborane unit containing molecules for tumour therapy[8].

However, the neutron absorbing property of ^{10}B nuclei, offers a more conventional use as a sacrificial material in high neutron radiative environments. This could include: protecting a spaceship against neutron and proton radiation from solar flares[9], at the emission end of a neutron diffractometer device to collect undetected neutrons[10], and to aid storage and handling of neutron emitting materials such as uranium, for the weapons and energy industries.

Introduction

A high ^{10}B density neutron absorbing material would be of use to several industries then. The current industry standards are:(i) boron carbide particles embedded into resins[10], which have ≈15 %wt boron, and are thick and expensive as a result, and (ii) boron fibre, which is laid down by CVD in layers, and prone to orientation problems[11], as well as being expensive to manufacture. Both materials have low gas permeability, meaning that neutron capture events lead to helium gas bubbles, and therefore inter-granular cracking

Improving this field would require a cheap, easy to manufacture, high ^{10}B density material. Other desirable properties would include stability to fluctuating temperature, chemical and pressure environments (due to the expected range of environments it is likely to experience), gas permeability, and an amorphous structure (in order to accommodate helium gas bubbles produced by the nuclear reactions that occur as part of the material's design).

1.3   Carboranes

With the preceding section's aims in mind, carboranes were investigated. Carboranes, and boron clusters in general, are interesting polyhedral molecular species, with exceptional stability considering their low packing density:
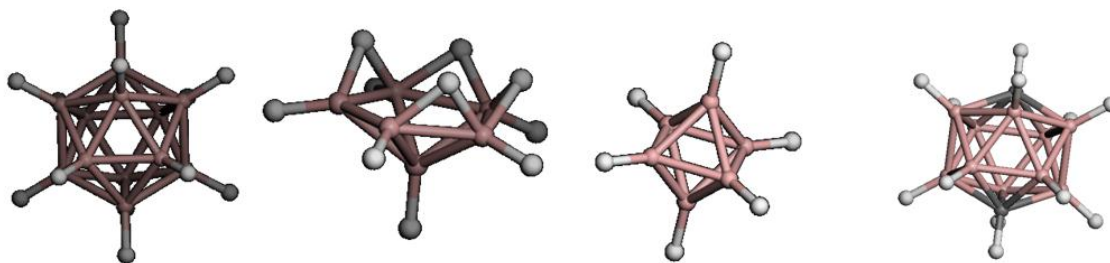
Figure 1. From left: $B_{12}H_{12}^{2-}$, nido-B_6H_{10}, closo-$B_6H_6^{2-}$, *para*-$C_2B_{10}H_{12}$ (carborane). White spheres represent hydrogen, grey carbon, and pink boron.

This stability is afforded by a complex bonding structure; the vertices of polyhedral shapes are occupied by boron atoms that are sp hybridised[12], with one sp orbital pointing out of the cage, making an exohedral bond to a radial atom, and the other sp orbital directed into the cage making one very low energy orbital contributed to by every vertex atom. This leaves 2 p orbitals for each vertex atom, perpendicular to the radial bonds, which combine to make several delocalised orbitals extending around the surface of the molecule:

Orbital diagram of $B_{12}H_{12}^{2-}$
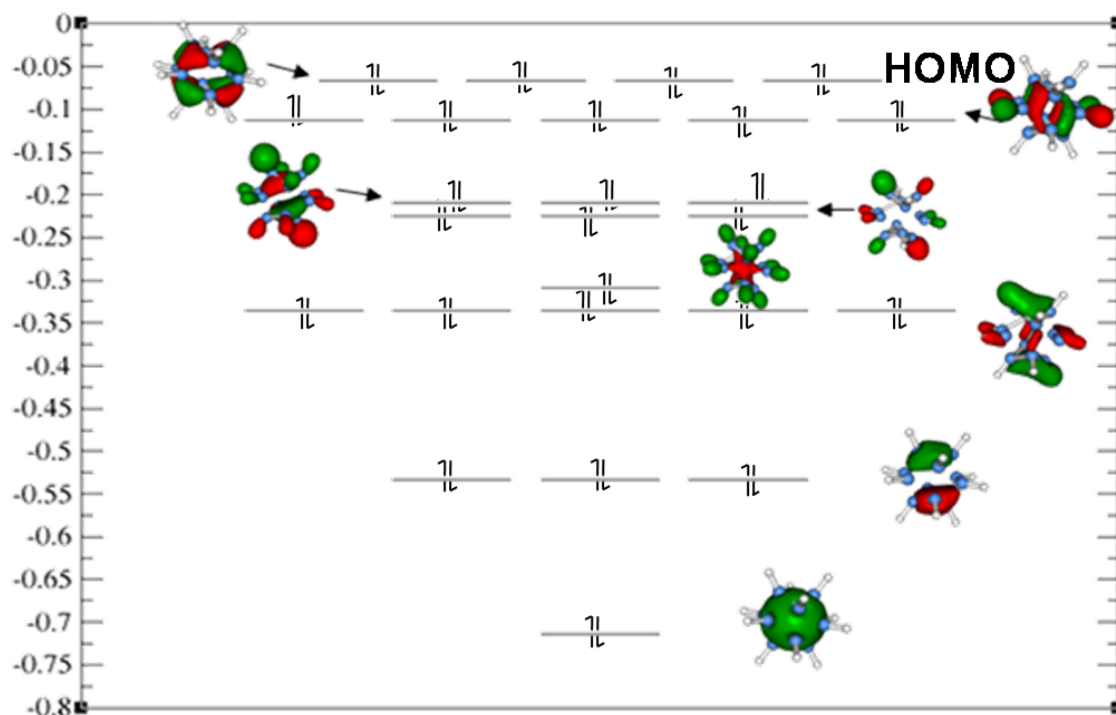
Figure 2. Hartree-Fock predicted orbital diagram of $B_{12}H_{12}^{2-}$, produced using the Gaussian program. Boron 1s orbitals excluded. Energies are given in hartrees. Degenerate bands have one molecular orbital diagram pictured that represents the band

The manner in which the orbitals are constructed is reminiscent of diborane, B_2H_6, in which an electron deficiency is overcome by the creation of 3 centre 2 electron bonds, where the s orbital on a "bridging" hydrogen combines with two boron sp^3 orbitals:
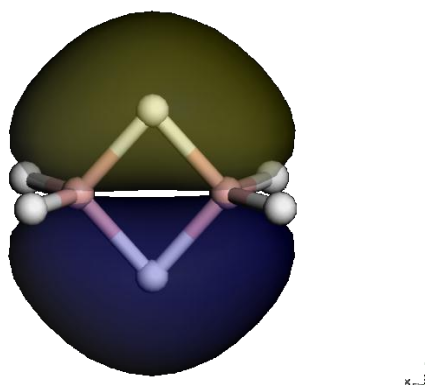
Figure 3. The diborane molecule, B_2H_6, displaying the B_{1u} orbital as calculated by $DMOL^3$

As suggested, this is a way in which boron containing molecules make up for electron deficiency. Boron can also be seen as a bridge between (i) non-metallic 2- centre, 2- electron covalent bonds, and (ii) many centre, 1 electron metallic bonding, in view of the fact that boron exists on the boundary of metals and non-metals in the periodic table.

Given the orbital diagram described in Figure 2 (core electrons ignored), two more electrons are required to complete the orbital set. Boron has the atomic configuration $1s^2 2s^2 2p^1$, and as such contributes 3 valence electrons to molecular bonding. Hydrogen contributes 1 s electron, for a total of 48 electrons in $B_{12}H_{12}$. As observed, there are 25 molecular orbitals, requiring 50 electrons, so $B_{12}H_{12}$ will exist as a double anion. Another way to overcome this deficit is by substituting 2 boron atoms for higher valence atoms, most commonly carbon (atomic configuration $1s^2 2s^2 2sp^2$). In this way, the charge neutral carborane, $C_2B_{10}H_{12}$, series is derived as seen in Figure 4:
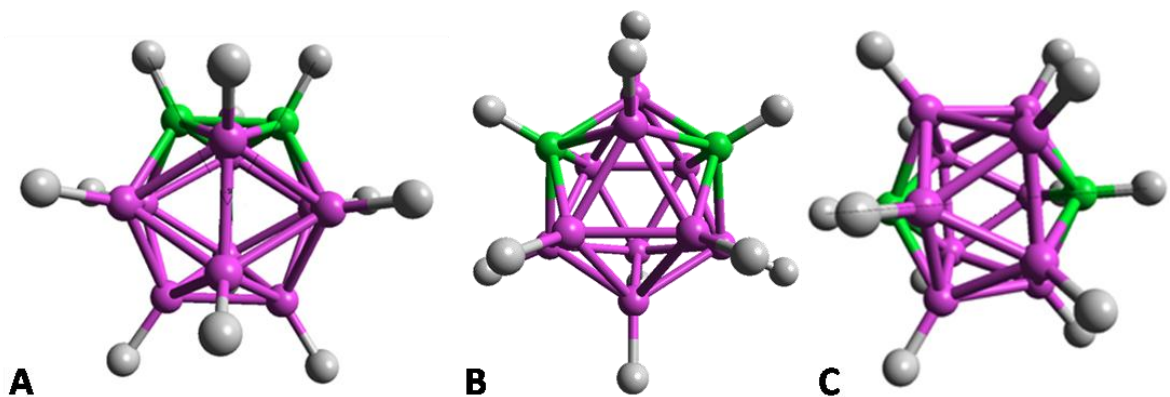
Figure 4. The carborane series. A: *ortho-*, B: *meta-*, C: *para-* carborane

The boron clusters identified in Figure 1 include a *nido*-carborane, B_6H_{10}, which is a pentagonal pyramidal complex, with one boron vertex missing. For the completion of this orbital set, 4 electrons are required, provided by four bridging hydrogens in this example. *Arachno-* complexes, which have two missing vertices, require six electrons to complete the orbital set. This system of electron counting is referred to as Wade's rules[13], and is simply implemented by applying the formulae: *closo-*polyhedral complexes require 4n+2 electrons, *nido* require 4n+4, and *arachno* require 4n+6 electrons; where n is the number of vertices in the polyhedra.

Medical applications of boron were mentioned in the introduction of this section, within the context of brain tumour therapy. Carboranes can expand this field dramatically, since the high chemical stability and hydrophobicity of the molecules give them a low toxicity, essentially equal to that of salt[14,15] (LD50 of o-carborane[16] is 9g/kg, and for caesium

chloride[17] and sodium chloride[18] it is 10 and 3g/kg respectively). Studies in man have seen the molecules excreted in urine promptly. In order to cross the blood-brain barrier, organic groups are bonded via the carbon linkage to facilitate their diffusion. This is an example of the functionality of carboranes suggested in the objectives: it has been known for some time[19] that the lithiation of the C-H bonds in carboranes, and subsequent acidification with carbon dioxide and work up, yields a carbon to carbon bond, from which much functionality can be derived:

$$HC\text{---}CH + 2n\text{-}C_4H_9Li \longrightarrow LiC\text{---}CLi + 2C_4H_{10}$$

$$\underset{B_{10}H_{10}}{\diagdown O\diagup}$$

$$LiC\text{---}CLi + 2CO_2 \xrightarrow{HCl}$$

$$\underset{B_{10}H_{10}}{\diagdown O\diagup}$$

$$HOOCC\text{---}CCOOH + 2LiCl$$

$$\underset{B_{10}H_{10}}{\diagdown O\diagup}$$

II
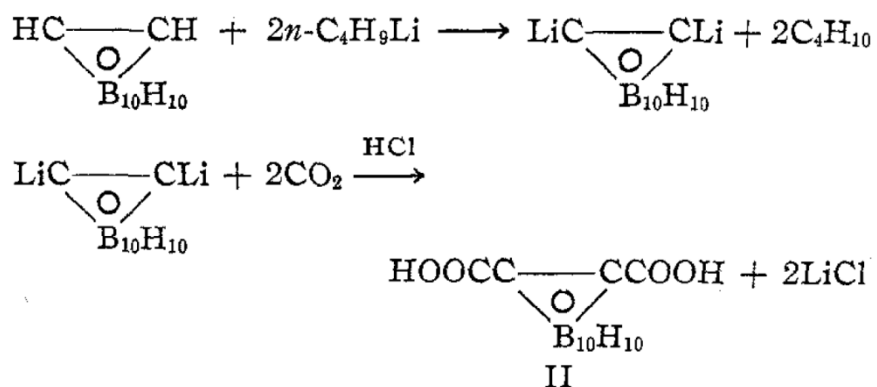
Figure 5. Carbon-carbon bond creation in carboranes[19]. Image taken from experimental paper.

1.4   Siloxane polymers

The material under investigation in this thesis will be a copolymer of siloxane monomers and carborane containing monomer units; it is therefore useful to discuss the nature of siloxane polymers here.

"Silicones", or, as they are more commonly referred to in the materials industry, siloxanes, were first characterised by Kipping in 1904[20], although Ladenburg's discovery[21] in 1871, of an oil that decomposed only at a "very high temperature" preceded this. The original naming format is an analogy of the imagined organic equivalent: ketones, because it was first thought that the empirical formula RR'SiO, described molecules with a silicon to oxygen double bond, similar to the carbon to oxygen double bond in ketones. As is now clear, these large molecules contain exclusively silicon to oxygen single bonds, forming long chains (or rings), with the orbital set of silicon atoms being completed by each silicon atom making single bonds to two capping R groups. The more recent term, siloxane[22], is a catenation of **si**licon, **ox**ygen and alk**ane**, describing the three main components of the materials.

Siloxane polymers were originally described as "sticky messes of no particular use" by Kipping[23], but his techniques allowed the use of siloxanes commercially for the first time in the second world war, through the use of silicone grease in aeroplane engines[23]. Over the following decades many more applications arose, ranging from damping fluids[24], hydraulic media[25], heat transfer media[26], fire retardants[27], and liquid dielectrics[28]. These applications make use of the high shear modulus, high hydrophobicity, temperature stability, heat release capacity, insulator and electric susceptibility properties of siloxane polymers respectively.

The commercial synthesis of siloxane polymers typically uses the Rochow[29] method, which creates silane(diol) monomers from methanol, sand and hydrochloric acid, as outlined by the reactions below.

$$SiO_2 + 2C \rightarrow Si + 2CO$$

$$CH_3OH + HCl \rightarrow CH_3Cl + H_2O$$

$$Si + CH_3Cl \rightarrow SiCl_2(CH_3)_2 (> 50\%) + \textit{side products}$$

Scheme 2
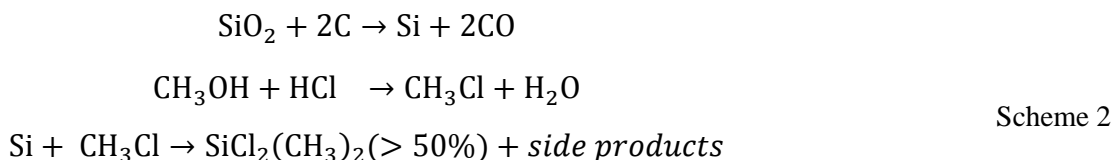
A copper catalyst is used in the final reaction. Polymerisation of the dichloro-dimethyl-silane described is then performed using hydrolysis processes[30]:

$$SiCl_2(CH_3)_2 + excess(H_2O) \xrightarrow{-HCl} SiOH_2(CH_3)_2 \xrightarrow{-H_2O} HO(Si(CH_3)_2O)_nH$$

Scheme 3
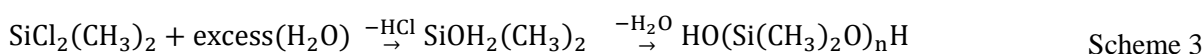
Where n = 20-50. Strand length is increased using a base catalysed process[31]:

$$HO(Si(CH_3)_2O)_nH + HO(Si(CH_3)_2O)_nH \xrightarrow{KOH} HO(Si(CH_3)_2O)_{2n}H + H_2O$$

Scheme 4
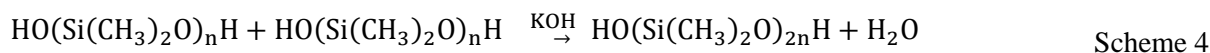
The production of elastomers from siloxane polymer phases requires crosslinking: the chemical bonding of independent polymer strands. This can be performed through a few methods; radical catalysed[31], for instance by hydrogen peroxide, and condensation catalysed, by introducing ethanol groups to the end groups of linear strands, which, when exposed to moisture, bond with nearby Si-OH groups releasing ethanol. The condensation catalysed method can be improved by the use of crosslinking agents, such as boric acid[32], creating ester linkages, or by addition e.g. of catalytic metal groups which create bonds between vinyl group endblocked strands, or of short polymer strands like poly(vinylmethoxysiloxane), plus a catalyst like tin(II) 2-ethylhexanoate, to create longer crosslinks[33], referred to as condensation curing.

Introducing reactive side groups, such as vinyl groups, can also be a route to crosslinking, as at high temperature, inter strand reactions occur[34].

1.4.1 The study of siloxane polymers experimentally

The range of characterisation techniques used for siloxane polymers is rich and varied, and worth discussing within this section, in order that the computationally derived physical properties have some analogy with equivalent experimental techniques. For instance: positron annihilation lifetime spectroscopy (PALS) techniques have been used to study siloxane polymer phases with varying chain length alkyl groups[35]. This is a technique that studies the free volume available in a material by irradiating with positrons, which combine with an electron more quickly in small voids, where their path length is constrained, than in larger voids. Void volume in a material can then be estimated based on positron lifetime. As will be seen, this thesis estimates free volume in computationally derived polymer phases using the random placement of points, and checks for overlap with the VDW radii of atoms, before building up an analogous picture of void volume distribution.

Other methods used to characterise siloxane polymers include:

- studying volume changes under varying pressure[36], mechanical shear strain[37], and temperature[38],
- calculation of gas permeability through thermal gravimetric analysis[39] (TGA),
- calculating viscosity using surface viscometer techniques[40];
- estimation of water sorption through swelling[41], and near Infra-red spectroscopy[42],
- the study of changes in bonding nature using Infra red spectroscopy[43],

- estimation of glass transition (T_g) using calorimetry and dynamical-torsional analysis[44], where changes in physical properties with temperature occur at different rates above and below T_g.

1.4.2 Carborane-siloxane copolymers

The two carbon atoms in a carborane molecule allow for bonding with a single sp bond, and, given the desirable properties outlined in section 1.1.1, there has been some investigation into the possibility of substituting carborane molecules for dimethyl siloxane units in poly-dimethylsiloxane (siloxane). Carbon atoms in carboranes could then make single bonds to silicon atoms and become part of a polymer strand, which, when viewed on the macro scale, represents a material with many useful properties:

1. Ductile, malleable (Poisson's ratio of 0.5[45]) material with good adhesion properties,
2. Stable over a range of theoretically useful temperatures (-55˚ to >300˚C)[46],
3. Chemically inert, and non-toxic,
4. Viscoelastic.

The angle between C-radial atom bonds is 113˚ in *meta*-carborane, which most closely mimics the ≈117˚ tetrahedral bond angle experimentally observed in the Si-O-Si section being substituted, so *meta*-carborane was chosen in order to cause the least disruption to the local structure. *Ortho* and *para* carborane have equivalent angles of 59.6˚ and 180˚ respectively, (see Figure 4). A central research drive of this project therefore is to ascertain how much boron (in the form of carborane units) can be incorporated into a siloxane polymer, without significantly affecting the useful properties outlined above. Siloxane polymers offer an impressive flexibility, with a shear elastic modulus (G) of ≈250kPa[47], which is a result of one of the lowest glass transition temperatures of any polymer system: T_g ≈ - 125˚C[47], compared to ≈ -73˚ for polyisobutylene. The shear modulus is independent of temperature, making the material particularly useful in variable temperature environments.

Attempts have been made to incorporate carboranes into siloxane polymers in the past, although computational studies are lacking. In these cases the carborane units have improved the polymer, by acting as a radiation sink when exposed to gamma radiation[16] and high temperature[17]. Carborane units also improve the flammability[48] characteristics of siloxane polymer systems, performing well in oxidative environments at 300˚C. However, the glass transition temperature is increased, and thermal expansion coefficient decreased, as will be seen, due to crystalline regions appearing, possibly as a result of electrostatic interactions between polar *meta*-carborane units and chain oxygens[34].

Introduction

Typical synthetic routes to poly(siloxane-carborane) polymers include:

- FeCl$_3$ catalysed route, reacting bis-(di-methyl-methoxy-silyl)-*meta*-carborane with di-chloro-di-methylsilane at 180˚, which sees some cross-linking, and random joining of monomer units[49].

- A method seeking to avoid crosslinking and side reactions using an alternative cationic catalyst: antimony pentachloride (SbCl$_5$) at room temperature, producing equivalent polymers, although crosslinking again occurs at higher temperature[34].

- The more hazardous and air-sensitive poly-condensation technique of bis(hydroxyl-dimethylsilyl)-*meta*-carborane reacting with bis-(ureido)-silane, which leads to exactly alternating linear polymers[50].

- The more green chemistry oriented (ammonia gas evolved, high temperature avoided, HCl not evolved) condensation of hexamethyl-cyclotrisilazene and bis(hydroxyl-dimethyl-silyl)-*meta*-carborane[51].

- Another method seeks to create a polymer directly from the carborane unit, by reacting dilithiocarborane with dichlorosiloxane[52]. However, the polymers produced are of too low a molecular weight to be of significant use.

This report will assume polymer phases are created by the FeCl$_3$ route, with a random distribution of monomer units, and hydroxyl terminating groups. Branching was not simulated: "No evidence of branching was observed (which might occur during polymerisation), suggesting the polymer was essentially linear"[53], and a Gaussian distribution of polymers was simulated, for the "long" phases (see section 6) in an analogy to Figure 6:
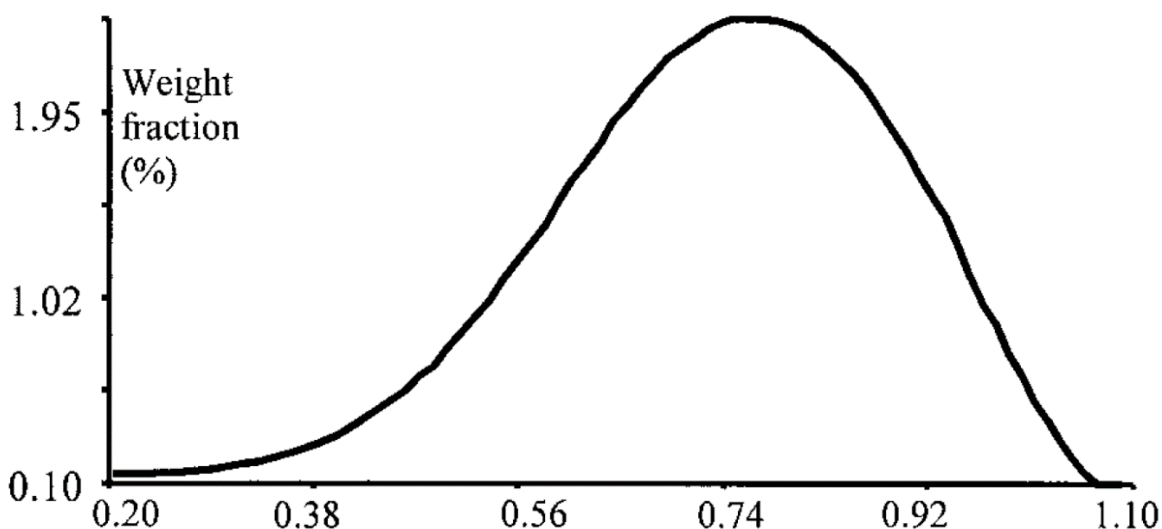
Figure 6. GPC spectrum of unmodified poly-(m-carborane-siloxane) [53].

A few of the experimental properties for the polymer phases discussed in this section are given in Table 2, as well as for a material containing a percentage of phenyl and/or vinyl groups in place of methyl groups on siloxane units.

Table 2. Experimental physical properties of siloxane and carborane substituted siloxane polymers[53]

Property	PDMS	Carborane rubber	Phenyl modified rubber	Phenyl-vinyl modified rubber
Linear toluene swell (% of thickness) per unit density	70	dissolves	40	19
Coefficient of Thermal expansion (x $10^{-4}K^{-1}$)	3.19	1.28	2.59	2.64
% B from Atomic Emission spectroscopy	0	28.8	29.5	26.4
Glass transition (˚C)	-115	-39	-35	-35
Melting point (˚C)	-45	60	-	-
Enthalpy of melting (j/g)	22.7	9	-	-

It is clear from initial experimental studies then, that introducing carborane units to siloxane polymers has the effect of lowering the thermal expansion coefficient and increasing glass transition temperature, whilst incorporating some phenylmethylsiloxane content offsets the change in thermal expansion coefficient, whilst maintaining the glass transition temperature.

Introduction

This thesis will include an investigation into the rate, the extent, and the cause of changes in physical properties such as these, as a function of monomer content. Classical molecular dynamics and static calculations will be employed to determine these factors.

1.5 Thermal rearrangement of carboranes

As mentioned earlier in this report, the three possible isomers of $C_2B_{10}H_{12}$ have an order of energy stability where carbon atom separation improves stability; *meta*- $C_2B_{10}H_{12}$ is more stable than *ortho*-$C_2B_{10}H_{12}$ and *para*- more stable than *meta*-. This is borne out through experiment in that *ortho* carborane will irreversibly rearrange to *meta* carborane at raised temperatures, and *meta* will rearrange in a dynamic equilibrium to *para*:

$$ortho - C_2B_{10}H_{12} \overset{(i)}{\rightarrow} meta - C_2B_{10}H_{12} \overset{(ii)}{\rightleftharpoons} para - C_2B_{10}H_{12} \qquad \text{Scheme 5}$$
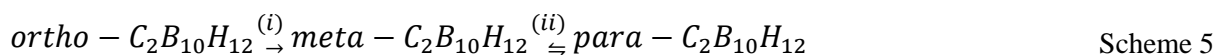
In Scheme 5, (i) is 675K, and (ii) is 925-975K.

This process is important for a number of reasons, beyond academic interest in the internal workings of these structures:

- Applications are emerging for carboranes at elevated temperatures, most relevantly for this thesis in incorporation into siloxane polymers. Knowledge of how molecular rearrangement might affect macroscale properties, for example in entanglement of polymer chains, is essential, and control of this process if possible, desirable. Experimental studies have reported the upper working temperature of polymers to be at rearrangement temperature, with rearrangements blamed for polymer failure[2].

- Carborane complexing of metals appears to lower the rearrangement barrier, to ambient conditions. This will undoubtedly affect the properties of these complexes, which is important to catalytic[54] and biological[55,56] applications.

- There is evidence to suggest that it is not simply the carbon atoms in carboranes[57,58], or indeed only the carbons of the boron clusters that exhibit rearrangements. Solid superacid applications of $[CB_{11}H_{11}]^-$ may see access to catalytic sites affected by rearrangements[59], for example.

Probably as a result of the breadth of areas affected by these processes, there have been several theoretical[57] and experimental[58] investigations into them. However, no firm conclusion has been reached regarding the mechanism, although much useful information has been derived. For instance, isotope labelling of boron positions in the carborane systems showed a complete scrambling of positions. This suggests that there may be more than one mechanism, and/or it may involve more than one boron vertex.

Some of the proposed mechanisms are: Triangle Face Rotation (TFR)[60], where a triangular face involving one carbon vertex rotates 120˚, thereby moving carbon atoms relative to each other; Diamond-Square-Diamond (DSD)[61], where the central bond in a diamond of atoms is broken, and the orthogonal bond made, via a square intermediate (this

mechanism would require several concerted DSD steps to properly remake the icosahedron); via a cubeoctahedron intermediate[62], where all vertices become penta-coordinated in the intermediate and remake the icosahedron; or via a nido-intermediate with one face opening[63].

Suggestions for the mechanism have been proposed since the 1980's, however, the problem of orbital symmetry, proposed by Wales in 1993[64] has been largely ignored by more recent papers. Put simply, many of the proposed mechanisms require the breaking of orbital symmetry: the operations require the p orbitals of boron atoms to move through areas with which they are out of phase. This particularly refers to the delocalised orbitals spread around the surface of the molecule, a band of four orbitals which in $B_{12}H_{12}^{2-}$ are degenerate and are the HOMO (see Figure 2). In carborane systems, the energy levels are split, but the problem of out of phase orbital overlap remains.

Further to the thermal rearrangement discussed above, a reductive-oxidative[65] rearrangement is available, to rearrange *meta-* carborane back to *ortho-* carborane, via a *nido-* carborane^{2-} intermediate. This process will not be considered here, but is pertinent when discussing frontier orbital progression through the thermal rearrangement process.

Therefore, predicting Transition States (TS) and Intermediates (INT) through conventional potential energy surface sampling methods appears redundant, as the orbital symmetry will be decided instantaneously, based on the lowest possible energy. For this reason, *ab initio MD* calculations will be performed, with the wavefunction retained over the course of the calculation.

1.6   Icosahedral boron solids

Boron carbide is a solid based on B_{12} icosahedra connected in hexagonal sheets. These layers connected via linear chains along the trigonal [001] direction, with one chain per icosahedron. In the general form, the icosahedra are B_{12} units and the chains are C-B-C units, making three tetrahedral bonds to icosahedra at either end, as seen in Figure 7.
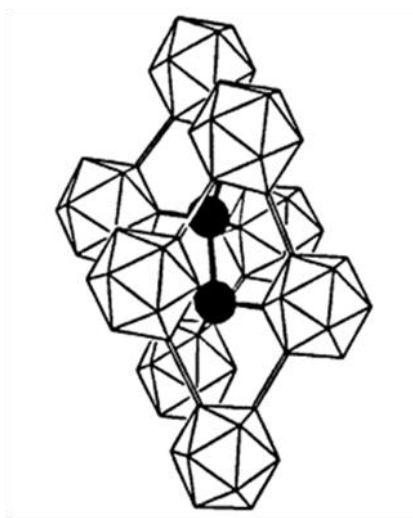
Figure 7. General icosahedral solid structure[66]

This system does not conform to Wade's rules[67], in that each chain-icosahedron unit has an unpaired electron. As a result the true structure of boron carbide is disordered, with the extent of disorder not fully characterised; carbon composition can vary in the range 9-20 atom %[68,69], whilst X-ray experiments do not distinguish between carbon and boron atoms[70], and neutron diffraction is ineffective when analysing boron solids, due to neutron capture events with ^{10}B nuclei, although enrichment with ^{11}B has allowed for some characterisation[70]. Theoretically the lowest energy structure[71] of stoichiometric (C_3B_{12}) boron carbide would contain solely CB_{11} cages, and C-B-C chains. This represents the most carbon rich end of the range, whilst the boron-rich end has a high proportion of B_{12} icosahedra and B-[vacancy]-B chains. However, it is accepted that the composition of any boron carbide system will include some C_2B_{10}, CB_{11}, and B_{12} cages, and some C-B-C, C-B-B, B-B-B, and 2 or 4 atom chains[72]. It is therefore regarded as a "frustrated" system, without an ideal structure[73].

Boron carbide is one example of a family of solids based on layers of boron icosahedra with a double tetrahedral X-X or X-B-X chain of hetero atoms. Other examples include boron phosphide[74], arsenide[75], and oxide[76], as well as β-boron. Boron carbide is the most prevalent example of this family, with the most experimental data available, due to its uses in varying fields; for example, as a component in control rods in nuclear reactors[77] and body and vehicle armour[78], taking advantage of the high neutron absorption cross-section of

[10]B and the extreme hardness of boron carbide respectively. Considering the amount of data available, it was decided to make boron carbide the focus of this study. However, all of the solids exhibit the same exceptional resistance to radiation: previous studies in which "icosahedral" boron solids are exposed to radiation have involved the bombardment of $B_{12}P_2$ with 400 keV electrons[14], and β-boron bombarded with 160keV N^+ ions[66,79]. This is detailed in Figure 8
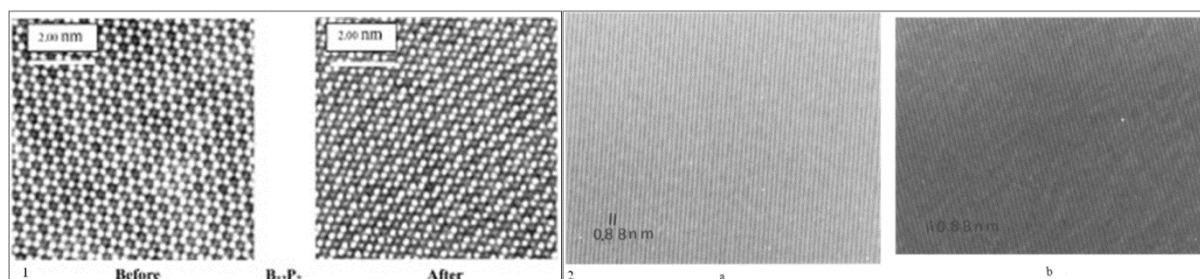
Figure 8. Left: Very high-resolution transmission electron microscopy[66] shows no damage to $B_{12}P_2$ after an intense bombardment (10^{18} electrons/cm²/s) by 400 keV electrons to a net dose of about 10^{23} electrons/cm². Right: Beta boron before (a) and after (b) bombardment with 160 keV N^+ ions, showing no loss of crystallinity (lattice fringe images)[79]

In both cases the radiative impact energies are five orders of magnitude greater than common bond dissociation energies, but the crystal structure appears to remain unaltered in both cases. When boron carbide is irradiated with thermal neutrons, lithium and helium ions are produced by neutron capture events of [10]B, which cause bubbles to form in the structure without affecting nano-crystallinity[80,81], although micropores are observed. Amorphisation is possible, using H^+ ion radiation, which alters the structure chemically[82], but 1MeV electron impacts do not affect the crystal structure[83]; 2MeV impacts are required to induce amorphisation through electron impact.

This resistance of the material to structural damage has been attributed to two possible mechanisms. One theory is that crystallinity is retained by a "self healing" method, whereby impacted atoms are displaced as positive ions, leaving behind electrons composing the cage bonding orbitals. Over the timeframe of observation, it is proposed that Coulombic attractions drive the displaced atom back to its atom site[66]. An alternative mechanism is one in which the displaced atom is incorporated into a nearby chain, whilst the cage is reformed by extracting an adjacent chain atom[84]. In this way twelve atom cages are retained, whilst chain disorder is increased; an effect that would not readily be observed using crystallographic characterisation methods, given the accepted disorder in boron carbide chains[84].

Introduction

In this thesis, we examine the proposed mechanisms using classical and *ab initio* computation. Impact events are simulated using molecular dynamics, by increasing the velocity of a targeted bulk atom in a random direction, and the damage sustained by the bulk solid, after the defect stabilises during the classical MD simulations, is analysed using *ab initio* techniques.

Computational investigations into the boron carbide surface are absent from the literature, despite emerging nanotechnology applications of boron carbide particles and wires[85], used as abrasive shields[86], and fibres in ceramic body armour[87] respectively, making use of its ultra hard properties. Boron carbide thin films[88] have also been investigated as potential photovoltaic devices. Considering this, and the possibility of the icosahedral solid's resistance to radiation to be a surface phenomenon, it was decided to also investigate the boron carbide surface.

1.7 Lithium battery electrolytes

A further quality of boron cluster derivatives is their non-coordinating nature as anions; the completed icosahedral orbital set is very stable, meaning that changes to the electronic structure has a high energy cost. Also, the HOMO is spread across the molecule, making the negative charge large and diffuse, leading to low coordination with cations. This characteristic has been exploited in the industrial areas of ionic liquids[89] and superacids[59], and a logical extension would be for use in lithium batteries.

The efficacy of lithium batteries is in part determined by the rate of diffusion of lithium ions between electrodes, which is limited by the formation of ion pairs, or any coordination with counter anions within the electrolyte. The current industry standard is to use $[BF_4]^-$ or $[PF_6]^-$ anions, for their non-coordinating nature[90]; accordingly, this project will also include an investigation into the viability of $[B_{12}H_{12}]^{2-}$ as anionic replacements, using classical MD.

2 Theoretical methods

Recent advances in computer science, including the installation of supercomputers like those of HECToR and Legion, which have hundreds of cores available for parallelisation with OPENMP and the message passing interface (MPI) methods, have allowed for increasingly complex calculations to be performed within a reasonable time. Calculations within computational chemistry essentially require evaluating the energy of a system based upon its atomic coordinates. From this calculation, many other properties can be derived. The energy of a system can be calculated in two broad ways: classical methods and quantum mechanical or *ab initio* methods. Classical investigations ignore electronic effects, and calculate energy using empirically (or *ab initio*) derived mathematical potentials, which approximate the interactions of atomic nuclei and electrons. *Ab initio* methods treat electronic interactions explicitly, typically calculating approximate solutions to the Schrödinger equation and are based on quantum mechanics

2.1 Molecular mechanics methods

Molecular mechanics methods sum the many interactions between particles in a system via a set of equations that describe the energy of a system as a function of the particle's positions. The parameters of the equations are either taken from existing forcefields (in this project, uff[91] or pcff[92] were used), or created as part of the project to fit to experimental observables. Therefore the total energy of the system (E_{total}) is given by:

$$E_{total} = E_{bond} + E_{angle} + E_{torsion} + E_{charge} + E_{vdw}$$

Equation 2.1

Where the energy due to bond, angle, torsion, electrostatic and Van der Waals interactions are given by E_{bond}, E_{angle}, $E_{torsion}$, E_{charge}, E_{vdw} respectively.

The bonded potential (E_{bond}) represents the energy required to distort bonded atoms from equilibrium position. This report makes use of harmonic and Morse potentials, which were fitted to vibrational spectra (IR and Raman spectra) of the material in question, and also takes quartic potentials from the pcff forcefield, which have been fitted in the same manner:

$$\text{Harmonic: } E_{bond} = K\,(r_{ab} - r_0)^2$$

Equation 2.2

$$\text{Morse: } E_{bond} = D_e(1 - e^{-a(r_{ab}-r_0)})^2$$

Equation 2.3

$$\text{Quartic: } E_{bond} = K_1(r_{ab} - r_0)^2 + K_2(r_{ab} - r_0)^3 + K_3(r_{ab} - r_0)^4$$

Equation 2.4

Where K is the bond stretch constant, r_{ab} is the distance between atoms a and b, and r_0 is the equilibrium bond distance. D_e is the experimental bond dissociation energy, and a controls the width of the potential, so relates to the vibrational spectra.

The angle potential (E_{angle}) is a harmonic function that represents the energy required to deform three atoms a, b, and c, (where a and c are both bonded to b), from an equilibrium angle:

$$E_{angle} = K(\theta_{abc} - \theta_0)^2$$

Equation 2.5

Where K is the angle stretching constant, θ_{abc} is the bond angle, and θ_0 is the equilibrium angle.

The torsion potential ($E_{torsion}$) represents the energy required to rotate four atoms through a dihedral angle, viewed down the bond between the central two atoms, as seen in Figure 9.
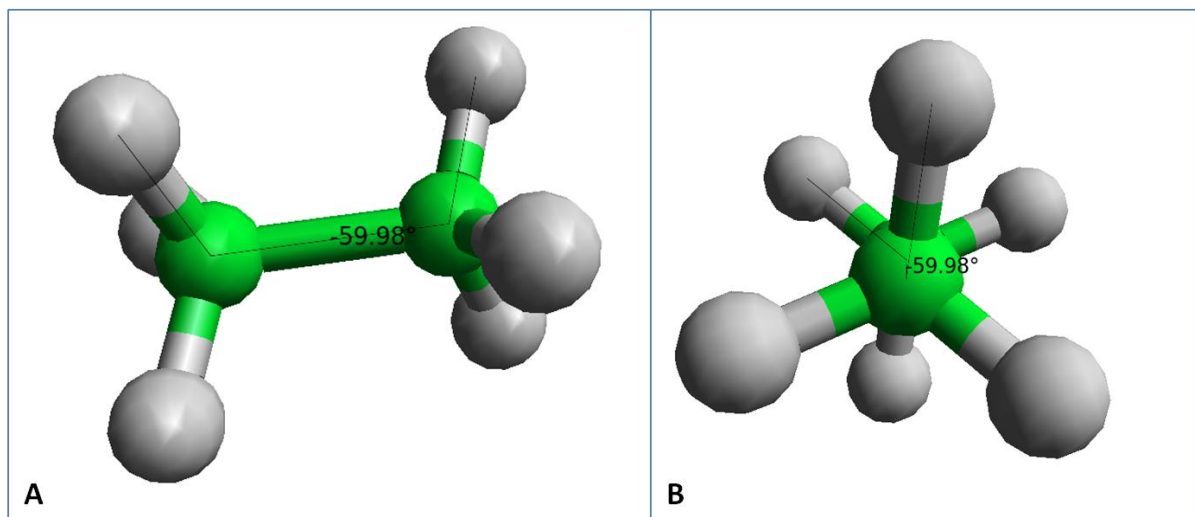
Figure 9. A: image highlighting the four atoms involved in a torsion term, B: sighting down the bond between the central two atoms, to show how torsion angles are derived

It is given in this work by the triple cosine potential:

$$E_{torsion} = K_1(1 + cos(\varphi)) + K_2(1 - cos(2\varphi)) + K_3(1 + cos(3\varphi))$$

Equation 2.6

The long range non-bonded interactions between unbonded atoms are treated by a Lennard-Jones potential:

$$E_{vdw} = 4\varepsilon((\sigma/r_{ab})^{12} - (\sigma/r_{ab})^6)$$

Equation 2.7

The terms in this potential represent the long range "dispersion" interaction between non-bonded atoms, and the short range "exchange-repulsion" interaction. The dispersion term

is always attractive, and arises from the fact that at a particular moment in time, a dipole is seen on a neutral, closed shell atom; an electron has to be somewhere at that moment, and unless it is exactly on the nucleus, there must be a small dipole moment from nucleus to electron (this effect is smeared out by studying the atom for even a very short time, as the electron will move throughout its orbital, creating an isotropic sphere (for an s orbital) of electron density). However, the *instantaneous* effect of the dipole is correlated on a nearby atom. Therefore this effect is often referred to as induced dipole interaction, and is approximated by $-(\sigma/r_{ab})^6$.

The exchange repulsion term arises from the increase in energy associated with redistributing electrons that would otherwise be occupying the same region of space. The exchange part refers to the attractive integral, which is representative of the anti-symmetry requirement that some electron motion can extend over both molecules/atoms. This is small compared with the repulsion term, which represents the increase in energy from two electrons occupying the same region of space. Overall then, the exchange-repulsion term is repulsive (increase in energy), and for a spherical atom is proportional to charge overlap, and is approximated to the form $(\sigma/r_{ab})^{12}$.

The electrostatic interactions are represented by partial charges on atoms; that is, ignoring occupation of orbitals etc., and assigning a value derived from *ab initio* calculations that represent each atom's share of electron density, subtracted from the positive charge at the nucleus. Electrostatic interactions (E_{charge}) can then be calculated using the Coulomb equation:

$$E_{charge} = \frac{q^a * q^b}{4\pi\varepsilon r_{ab}}$$

Equation 2.8

Where q^a is the charge on atom *a*, and ε is the dielectric constant. Of course, in a periodic system of charged atoms, the contribution to total energy by electrostatic interactions takes a long distance to converge; while the interaction decreases with *r*, the number of interactions increases in periodic space, therefore, introducing a cutoff radius will often result in an unrealistic sudden jump in energy as atoms transgress the cutoff radius. This situation is addressed using the Ewald sum, which works by converting the Coulomb sum into two series that do converge rapidly, one in real space and the other in reciprocal space.

So to split the series *1/r*:

$$\frac{1}{r} = \frac{f(r)}{r} - \frac{1 - f(r)}{r}$$

<div align="right">Equation 2.9</div>

Where $f(r) = erfc(\alpha r)$, where α is the Ewald splitting parameter, and *erfc* is the error function that ensures all the real space interactions converge to 0 within the simulation cell, which results in the ewald formula:

$$U = U(r) + U(k) + U(self) + U(dipolar)$$

<div align="right">Equation 2.10</div>

Where *U(r)* is the real space contribution, *U(k)* is the reciprocal space contribution, *U(self)* is the particles interaction with itself, and *U(dipolar)* is the dipolar correction term. The expressions are detailed in the following equations:

$$U(r) = \frac{1}{2} \sum_i^N \sum_j^N \sum_{n \epsilon Z^3}^{\dagger} q_i q_j \frac{erfc(\alpha|r + nL|)}{|r + nL|}$$

<div align="right">Equation 2.11</div>

$$U(k) = \frac{1}{2L^3} \sum_{k \in K^3, k \neq 0} \frac{4\pi}{k^2} \exp(\frac{-k^2}{4\alpha^2}) \sum_i^N \sum_j^N q_i q_j \exp(-i\boldsymbol{k} \cdot r_{ij})$$

<div align="right">Equation 2.12</div>

$$U(self) = -\frac{\alpha}{\sqrt{\pi}} \sum_i^N q_i^2$$

<div align="right">Equation 2.13</div>

$$U(dipolar) = \frac{2\pi}{(1 + 2\epsilon')L^3} (\sum_i^N q_i r_i)^2$$

<div align="right">Equation 2.14</div>

Where *L*=simulation cell length, and k is the reciprocal lattice vector with n_x, n_y, n_z=0...., n_{max} in $K^3 = (2\pi n/L : n\epsilon Z^3)$.

2.2   Electronic structure methods

The term *ab initio* literally translates as "from the beginning" and in this sense, refers to the calculation of observable properties through the knowledge of the interactions between nuclei and electrons. It will almost always include the approximate solving of the time-independent Schrödinger equation:

<div align="right">Equation 2.15</div>

$$\hat{H} \phi = E \phi$$

Where ϕ is the wavefunction that describes the positions of all electrons and nuclei in the system, *E* is the energy of the system, and $\hat{H}$ is the Hamiltonian operator:

$$\hat{H} = \sum_{n=1}^N T_n + V$$

<div align="right">Equation 2.16</div>

Where *V* is the potential energy, and *T* the kinetic energy operator:

$$T_n = -\frac{p.p}{2m_n} \qquad \text{Equation 2.17}$$

Where m_n is the mass of particle n, and p is the momentum operator:

$$p = -i\hbar\nabla \qquad \text{Equation 2.18}$$

Where ∇ is the gradient operator. This leads to:

$$\hat{H} = -\sum_n \frac{\hbar^2}{2m_n}\nabla_n^2 + V \qquad \text{Equation 2.19}$$

All electronic structure methods require some approximations in order to describe the wavefunction. For instance, an important consideration is the Born-Oppenheimer approximation, which states that given the considerably higher mass of nuclei when compared to electrons, it is possible to equate the velocity of the nuclei to zero when considering electron positions and energies. This effectively removes the kinetic energy operator for nuclei from the Hamiltonian, as well as nuclei interaction.

A second approximation is that the Hamiltonian is solved independent of time, and the Schrodinger equation is considered time independent.

Finally: relativity, the assertion that as particles approach the speed of light, their mass increases, according to Einstein's famous equation, is ignored, which may affect the core electrons of heavy atoms.

2.2.1   Hartree-Fock methods

The Schrödinger equation is known as an eigenvalue equation, as an operator (the Hamiltonian) acts on a function (the wavefunction), to produce an eigenvalue (the energy), and reproduce the function ("eigen" in German means "the same", and refers to the reproduction of the wavefunction). It is important then, to have a description of the positions of nuclei and electrons in the system, which constitutes the wavefunction. Hartree-Fock methods involve direct solving of the Schrödinger equation, with electron positions described exactly. The potential energy operator calculates the potential energy as a function of spatial configuration. This is described, more relevantly for this report, by the Fock operator:

$$F(1)\Phi_i(1) = \varepsilon_i\Phi_i(1) \qquad \text{Equation 2.20}$$

Where ε_i is the energy of electron i, and $\Phi_i(1)$ is the function describing electron i in orbital 1. Or, more completely:

$$F(1)\Phi i(1) = -\left(\frac{1}{2}\nabla_i^2\right)\phi_i(1) - \sum_A \left({Z_A}/{r_{1A}}\right)\phi_i(1)$$
$$+ \sum_{j\neq i} J_j(1)\phi_i(1) + \sum_{j\neq i} K_j(1)\phi_i(1)$$

Equation 2.21

The first term is a simplified form of the familiar kinetic energy term, whilst the second term is the coulombic term for the interaction between the electron and nucleus A. The Coulomb operator (J_u), and exchange operator (K_u), are two electron terms because the Coulomb operator expresses the Coulombic repulsions between an electron in orbital $\Phi_i(1)$, with electrons in every other, $\Phi_j(2)$:

$$J_j(1)\phi_i(1) = \left\{\int \phi_j * (2)\left(\frac{1}{r_{12}}\right)\phi_j(2)d\tau\right\}\phi_i(1)$$

Equation 2.22

And the exchange operator takes into account the modification in the energy due to the effects of spin correlation between like-spin electrons:

$$K_j(1)\phi_i(1) = \left\{\int \phi_j * (2)\left(\frac{1}{r_{12}}\right)\phi_i(2)d\tau\right\}\phi_j(1)$$

Equation 2.23

The exchange operator is a non-local term, as the wavefunction being operated on, Φ_i, needs to be known across all space, as it is included in the integral ($\int d\tau$). The Coulombic operator is a local term, as the only orbital included in the integral across space, is whatever the studied electron is interacting with, Φ_j.

Calculating the exact positions of electrons is expensive in terms of computer time, and for most systems, Density functional theory (DFT) is more appropriate. DFT is a computational technique wherein the absolute position of each electron is ignored, and all of the electron-position dependent parts of the Hamiltonian operator are described by a probability density of where the electrons reside.

2.2.2 Density Functional Theory (DFT)

As noted above, DFT methods involve evaluating the energy of a system based on the probability, or electron density, $\rho(r)$. It also involves evaluating the Kohn-Sham effective potential, $V_{eff}(r)$[93], which is given by:

$$V_{eff}(r) = v(r) + \int \frac{e(r`)}{(r-r`)}dr + V_{xc}(r)$$

Equation 2.24

Where $v(r)$ is the term for nuclear field, $\int (e(r`)/(r - r`) \, dr`$ is the coulombic term, and $V_{xc}(r)$ is the exchange correlation potential, which is at the heart of DFT calculations. It is obtained from the operation of the exchange only energy functional, $E_{xc}[\rho]$. A functional is a function of function, since $E_{xc}[\rho]$ is dependent on electron density, ρ, which itself is dependent on distance from the nucleus, r. From the calculus of functionals:

$$V_{xc}(r) = \frac{\partial E_{xc}[\rho]}{\partial \rho(r)}$$

Equation 2.25

So the exchange correlation potential at distance r is equal to the derivative of exchange only energy functional at density ρ, by the density at point r. The example Kohn used to evaluate the exchange only energy functional is of a fictitious system called Jellium, often referred to as the homogenous electron gas. This was chosen as it would be a system where ρ varies extremely slowly (or none at all) with position. In this situation $E_{xc}[\rho]$ is given as:

$$E_{xc}[\rho] = \int \rho(r)\varepsilon_{xc}(\rho)dr$$

Equation 2.26

Where ε_{xc} is exchange correlation energy per electron. This can be separated into exchange and correlation components, ε_x and ε_c. The ε_c is difficult to evaluate but has been done; the ε_x can be written as:

$$\varepsilon_x(\rho) = -0.75\left(\frac{3}{\pi}\right)^{1/3}(\rho(r))^{1/3}$$

Equation 2.27

The exchange only potential can also be separated in this situation, and is given as:

$$V_x = -\left[\left(\frac{3}{\pi}\right)(\rho(r))\right]^{1/3}$$

Equation 2.28

This is an example of Local Density Approximation (LDA), where the E_{xc} functional is dependent only on the density where the functional is evaluated: the exchange-correlation energy at point r, is considered to be equivalent to the energy of a homogenous electronic gas with density equal to that at point r. A more accurate version of DFT is the Generalised Gradient Approximation (GGA), which is dependent on the gradient of the density where the functional is evaluated, and is described, for instance, by the Perdew-Burke-Ernzerhof (PBE) functional[94].

For real calculations, the energy is evaluated iteratively, analogously to the Hartree-Fock self consistent field approach, using the following equation:

$$E_{XC}^{GGA} = \int d^3r e_{XC}^{GGA}(n_\uparrow(r), n_\downarrow(r), |\nabla n_\uparrow(r)|, |n_\downarrow(r)|)\nabla$$

Equation 2.29

Where $n_\uparrow$ and $n_\downarrow$ are the spin up and spin down densities at r and ∇ is the local gradient of the density at point r for the two states.

Initially some guess at density is made, yielding a Kohn-Sham potential. The Kohn-Sham equations (Equation 2.24 and Equation 2.26) are then solved iteratively until the fields are described self-consistently, by varying the coefficients of atomic orbitals that construct molecular orbitals, evaluate density and calculate energy. This is necessary as $V_{eff}(r)$ depends on the density through the exchange-correlation potential $V_{xc}(r)$, itself dependent on $V_{eff}(r)$.

2.2.3 Basis Sets

Basis sets describe the molecular orbitals in quantum mechanical calculations as atomic functions. These were originally described by Slater type orbitals[95]:

$$R(r) = Nr^{n-1}e^{-\zeta r}$$

<div align="right">Equation 2.30</div>

Where the radial part is described by: N, a normalising constant, n, describing the principal quantum number, r, the distance of the electron from the atomic nucleus and ζ, a constant describing the effective charge of the nucleus. This is typically approximated by a set of rules called Slater's rules.

Slater type orbitals are most often approximated in Gaussian form[96];

$$\Theta_{ijk}(r_1 - r_c) = (x_1 - x_c)^i(y_1 - y_c)^j(z_1 - z_c)^k e^{-\alpha|r_1 - r_c|^2}$$

<div align="right">Equation 2.31</div>

This is a way of representing probability density, of electrons at distance r_1 from the nucleus at r_c. The indices i, j and k are non negative integers and α is a positive exponent. When i, j and k are 0, then the orbital is representative of an s orbital; when one of i, j or k is 1 then this represents a p orbital and so on. By representing the basis set in this manner, calculations avoid the 'two-electron integral problem', which makes Slater type orbitals computationally unfeasible[97]. However, it is an approximation; only at certain distances does it map the density well. For instance, there is no cusp at the nucleus, so accuracy must be improved by using contracted Gaussians.

A contracted Gaussian is a linear combination of primitive Gaussians that better approximates the exponential function of a real electron density. The primitive Gaussians that compose it have their weightings varied by multiplying their contribution by a contraction constant, which are frozen once the best approximation is reached. Calculations can then use

these frozen coefficients, making large savings in computer time, with little loss of accuracy, providing the coefficients are good.

A common notation for Gaussian basis sets is X-YZG, where X is the amount of functions used to describe the core electrons, and Y and Z are the amount of contracted and diffuse functions used to describe the valence electrons respectively.

A further increase in accuracy is afforded by the addition of polarization functions. This method works by adding an element of higher angular momentum number to the basis set, representing the perturbation of an electron cloud by an atom's environment. For example, in isolation, hydrogen has a spherical electron cloud; in a H_2 molecule, its electron cloud is directed towards the other hydrogen atom. To properly represent this, an element of p character must be added to an s orbital. In the old notation polarization functions for heavy atoms are indicated by adding an asterisk (*) to the Basis Set notation, two asterisks indicate polarizations on light atoms also, whilst in the newer notation polarisation orbitals are explicitly stated in brackets after the basis set: i.e. (d,p).

2.2.4 Gaussian Plane Wave (GPW) methods

For simple molecular systems, describing electron density with the above method is appropriate; however, for more complex periodic systems, there is a significant increase in the amount of computer power required to describe the density. For periodic systems then, plane waves[98] represent an improvement; the orbital wavefunction is described by a series of plane waves, with frequency the width of a unit cell (for later ease of mathematical operations):

$$\varphi(r) = \sum_G \alpha_G e^{(i(k+g)r)}$$

Equation 2.32

The Fast Fourier Transform (FFT) technique simplifies algebraic manipulations of equations in this form, whilst Basis Set Superposition Error (BSSE) is also avoided; this is where, at short ranges, overlapping atomic functions allow atoms to "borrow" functions, unrealistically decreasing energy. GPW's are also atom position independent, but require pseudo-potentials to describe the high variance of wavefunctions close to the nucleus, or else the number of plane waves required becomes unmanageable.

2.3 Energy minimisation

The processes described in sections 2.1, 2.2.1, and 2.2.2 are different methods for evaluating the energy of a system described by the Cartesian coordinates of its N particles. The static potential energy surface of a system accordingly, is a function of its 3N coordinates, or, when described by a Z-matrix, a function of its 3N-6 coordinates.

A description of coordinates, where displacement of any coordinate will result in an increase in potential energy (i.e. the second derivative of the position of the particles with respect to energy is zero) is defined as a minimum. For a many-atom system, there may be several minima, of which the lowest energy case is referred to as the global energy minimum, and other cases as local minima, corresponding to metastable states in real–life chemical species.

In many of the studies in this report, locating the minima of a chemical species, starting from a non-optimal state is necessary, so free energy minimisation, or "geometry optimisation" techniques are employed.

The technique used in this report is the Newton-Raphson method, which calculates the matrix of the second derivative of the energy with respect to the internal coordinates, referred to as the Hessian matrix. A unit vector (S_k) is then followed for each particle k, defined by Equation 2.33:

$$S_k = \frac{-g_k}{|g_k|}$$ Equation 2.33

Where g_k is the first derivative of the energy with respect to particle coordinates. The Hessian matrix is then recalculated at this new step until a minima is found.

2.4 Transition state searching

A parallel process to energy minimisation techniques is transition state searching; a transition state is defined as the lowest energy point on the potential energy surface connecting two minima. Another definition of a transition state is as a saddle point: a stationary point with one negative frequency along the vector that connects minima.

The main technique for finding transition states used in this report is the *Synchronous Transit-Guided Quasi-Newton* (STQN) method, which generates an initial guess for the transition state as the highest energy point along the shortest vector connecting two minima. The transition state is then found by searching for a minimum along a vector perpendicular to the first generated vector.

2.5 Molecular Dynamics

Molecular dynamics allows the nuclei in the system to progress according to Newtonian laws of motion:

1. A particle will move in the direction of its momentum unless a force acts upon it.
2. Force is given as a change of momentum.
3. Every action has an equal and opposite reaction.

By giving each nucleus a momentum, decided randomly within the constraints offered by the system temperature and the Boltzmann distribution, the nuclei are able to progress over the potential energy landscape. Forces are derived by atom interaction, offered by any of the schemes discussed above.

To generalise, a system of N particles of mass m, with force F, is progressed with time, t, for a particle i:

$$M_i r''(t) = F_i(r_i..r_N) \qquad \text{Equation 2.34}$$

Progression in time involves calculating forces on the particle at time t, given coordinates and vectors, and recalculating coordinates and vectors at time $t + h$, where h is a suitable timestep. Difficulties arise with this method, since the motion and progression of many particles are coupled together, with a continuous potential.

This is overcome by using a simple time progression algorithm: the Verlet algorithm, which works by including the forward and backwards steps into the progression. To accomplish this, a Taylor expansion is used; describing position (r), velocity (r'), acceleration (r'') etc., although conventionally only the third term is used:

$$r_i(t + h) = r_i(t) + hr'_i(t) + \frac{h^2}{2}r''_i(t) + \ ...$$

$$\text{Equation 2.35}$$

$$r_i(t - h) = r_i(t) - hr'_i(t) + \frac{h^2}{2}r''_i(t) - \ ...$$

$$\text{Equation 2.36}$$

Combining these two equations produces a final progression for r, t and h, giving the following:

$$r(t + h) = 2r(t) - r(t - h) + h^2 a(t) \qquad \text{Equation 2.37}$$

Where a represents acceleration (second derivative).

The information that can be derived from molecular dynamics calculations will include the trajectory of cells and atoms. For example, trajectories can indicate melting points and mobilities, which would be useful in real world applications, whilst cell volume changes in response to changes in environment can be indicative of bulk physical properties, such as thermal expansion coefficient and bulk modulus.

2.5.1 Barostat and thermostat

The temperature and pressure fluctuations in molecular dynamics calculations are pertinent to real world problems, and are controlled by the internal thermo- and barostat. This report makes use of the Berendsen examples.

In the thermostat mentioned, the system is coupled to an external "heat-bath" in order to maintain a stable temperature. Since the temperature of the system and the kinetic energy of its components are linked, the thermostat controls temperature by scaling the velocities of the components:

$$\chi(t) = \sqrt{\left[1 + \frac{\Delta t}{\tau_T}\left(\frac{\sigma}{E_{kin}(t)} - 1\right)\right]}$$

Equation 2.38

Where:

$$\sigma = \frac{f}{2}k_B T_{ext}$$

Equation 2.39

T_{ext} is the specified target temperature, k_B is the Boltzmann constant, f the number of degrees of freedom, E_{kin} the kinetic energy of the system and τ_T is a specified time constant for temperature fluctuations.

In the isotropic NPT regime, the barostat controls the pressure thusly:

$$\frac{dP(t)}{dt} = \frac{P_{ext} - P(t)}{\tau_P}$$

Equation 2.40

Where P_{ext} is the instantaneous pressure and τ_P is the barostat relaxation time constant. The cell size is allowed to fluctuate to maintain a constant pressure, with cell size scaled by η, and cell vectors and coordinates scaled by $\eta^{1/3}$:

$$\eta(t) = 1 - \frac{\beta \Delta t}{\tau_P}(P_{ext} - P(t))$$

Equation 2.41

Where β is the isothermal compressibility of the system (of liquid water in the DL_POLY_4 implementation of this regime).

2.6   Monte Carlo methods

Monte Carlo method are so named, as the process involved is to sample a space that does not have an easily defined closed form expression, using many random points, analogous to playing casino games enough times to understand the probability of winning them. Within the chemical context, the Monte Carlo method can be understood by randomly inserting a molecule with a random orientation into a unit cell, and checking for overlapping of the target molecule's Van der Waals radius with that of the host structure. With sufficient numbers of target insertions ($\approx 10^6$), the ratio of overlapping : non-overlapping molecules will give an indication of free volume available to solvent molecules in porous structures etc.

2.7   *Ab initio* MD

The implementation of molecular dynamics based on electronic structure methods is performed in the CP2K code using the Born-Oppenheimer MD technique[99]. The central tenet of this technique is that nuclear and electron motion can be separated, given the three orders of magnitude difference in velocity, reducing the nuclear motion to a single potential energy surface. Therefore potential energies and forces for atoms are evaluated instantaneously at each timestep, by solving the *time independent* Schrödinger equation.

3 Methodology

A broad range of system sizes, timescales and computational levels are used in this thesis; investigating boron clusters in different environments. The methods used to study each system will be covered in more detail within each section, but generally:

3.1 Classical studies

Geometry optimisations, least squares fitting etc. were performed using the GULP code[100], using default parameters unless otherwise stated. Molecular dynamics calculations were performed using DL_POLY, typically DL_POLY_4[101] (as this offers an improved parallelisation of the calculation over several nodes) , with 1 femtosecond timestep, NPT ensemble and 1.5 ps thermostat and barostat control. Input files were created using either my own scripts, or the freeware program ATEN.

3.2 Electronic structure methods

Geometry optimisations and single point calculations were performed using Gaussian03[102], whilst vibrational spectra calculations, molecular dynamics, and potential energy surface calculations were performed using the CP2K code[103]. [DMOL^3][104] has also been employed. In all cases DFT calculations typically used the PBE[94] exchange-correlation functional and the 6-31G* basis set. Input files were created using my own scripts

In all cases, the High Performance Computing cluster Legion was typically used, making use of Dell C6100 nodes, with six processors per node, for parallel jobs. For serial jobs, the Faraday cluster was used.

4   Siloxane-carborane polymers

There are two main ways of representing polymer strands in simulation: by having the polymer repeat infinitely through the walls of a periodic box[105], or by treating the strands explicitly[106]. Attempts have been made to confine the polymer strands in a solvent box, thereby discretely isolating polymer-solvent effects and reducing the complexity of analysis of the system[107]. However, it is clear that treating the strands explicitly by generating finite strands is necessary to best predict physical properties.

Creation of computational models of polymer phases is a complicated process given the amorphous nature of the systems, and there remain few freely available programs for the task, nor indeed an agreed method. The possibility of Monte Carlo insertion of strands into a largely empty box, and reducing volume over time has been suggested as a possible route to polymer phases[108], although the entanglement of polymer strands may not be representative of real systems, and long MD runs may be necessary to equilibrate the system, given the size of the molecules involved. The amorphous cell builder, as part of the Materials Studio suite of programs[109], adds monomer units sequentially, allowing rotation of the principal polymer torsion to give the best interaction. A random element is added by accepting or rejecting interactions given a specified system temperature and the Boltzmann distribution. However, for rigid, bulky systems or systems with many rings, low density starting positions are again necessary, as well as long MD runs. This investigation will make use of both methods.

The aims of the following investigation were to create a series of polymer phases computationally, and to test them, using simulation methods, for physical properties of relevance to the industrial context outlined in the introduction. This required the derivation of a forcefield for carboranes, to combine with siloxane polymer terms taken from the pcff forcefield[110]. Three methods of generating polymer phases will be discussed, with carborane monomer content varied in steps of 10%, in order to analyse the effect of carborane content on bulk physical properties of the designed material.

The physical properties referred to include: density, thermal expansion coefficient, bulk modulus, glass transition temperature and shear modulus, derived either from static second derivative calculations, or by analysing the atomic trajectories and changes in cell volume obtained from molecular dynamics calculations under varying conditions. These will be compared with experimentally determined values to show the validity of the techniques, and be used to indicate an optimal carborane/siloxane ratio for a given material function.

Experimentally, *meta-* carborane was chosen over *ortho* or *para*, based on the similarity of the Si-O-Si bond angle in siloxane, and the Si-[cage]-Si angle in the carborane monomer, derived experimentally; 117 and 113° respectively as seen in Figure 10. The corresponding angle in *ortho* and *para* carborane is 59.6 and 180° respectively, as seen in Figure 11.
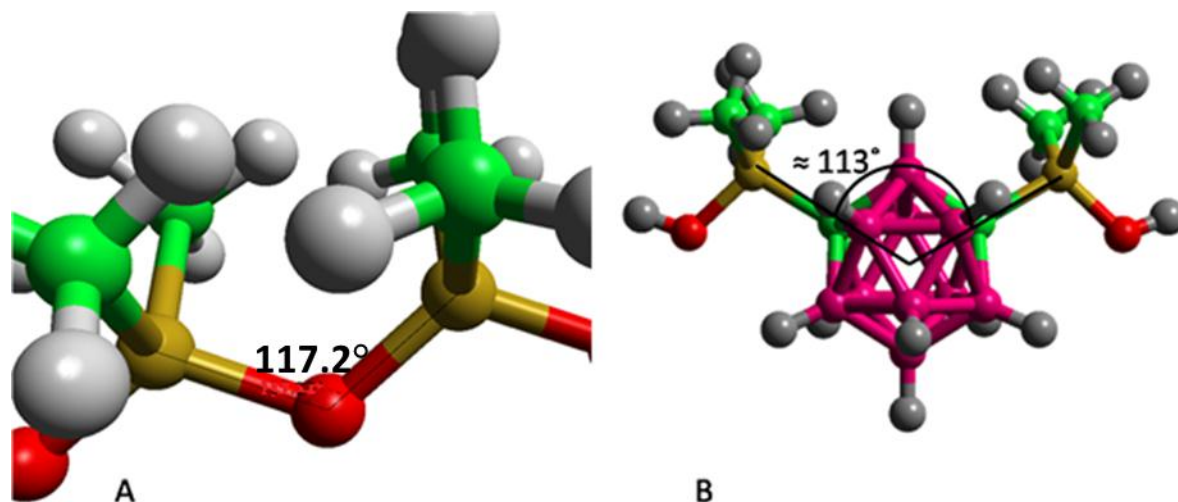
Figure 10. A: Si-O-Si bond in siloxane polymers, B: Si-[cage]-Si bond in carborane monomers
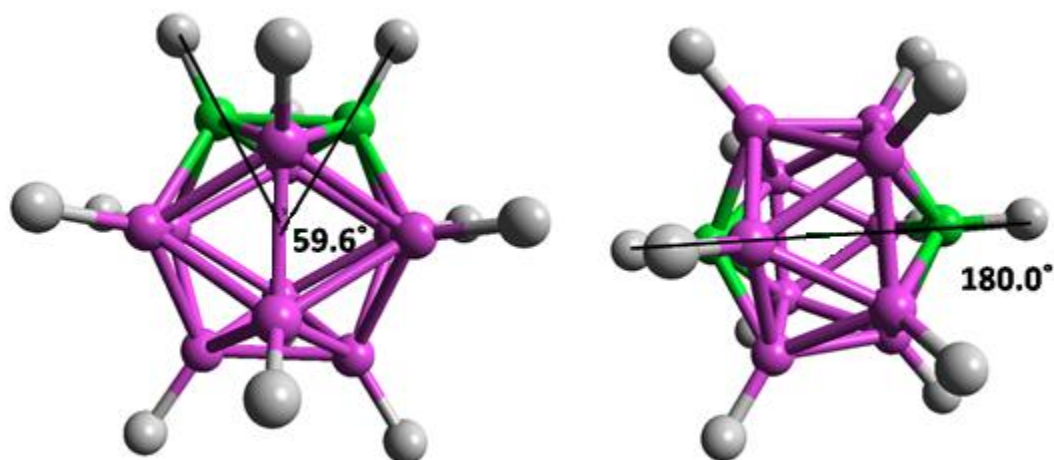
Figure 11. *Ortho-* (left) and *para-* (right) carborane molecules, with the angle subtended by extending the C-H bond vectors indicated

Given the preceding considerations, the two monomers dealt with in the bulk of this report are shown in Figure 12, where A is dimethyl-silane-diol, referred to hereafter as siloxane monomer, and B is bis(hydroxyl-dimethyl-silyl)*meta*-carborane, referred to hereafter as carborane monomer.
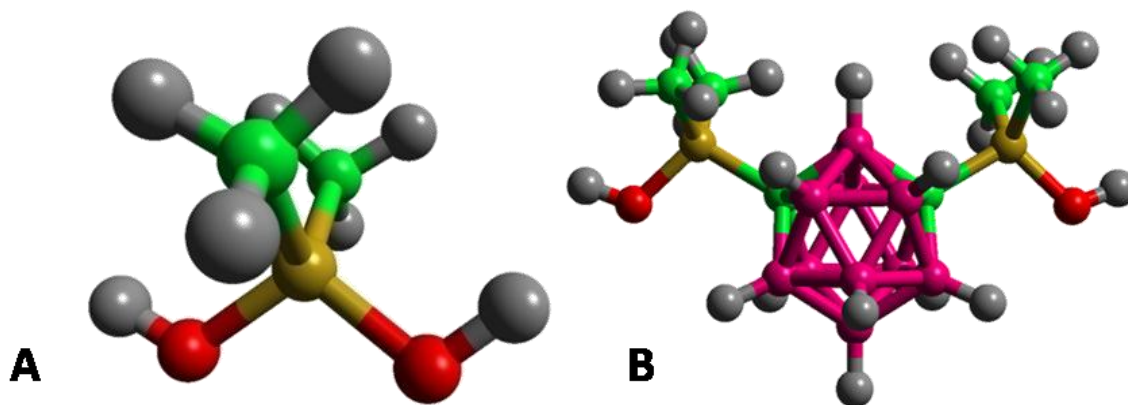
Figure 12. A: siloxane monomer, B: carborane monomer

The forcefield terms required for the description of siloxane-carborane copolymers, which are absent from the pcff forcefield and will require fitting are: B-H, B-B, B-C, and C-Si bonding terms, and non-bonding terms for the new atom types B_{cage}, C_{cage} and H_{cage}. As will be seen, the changes in energy occurring from rotating around the C_{cage}-Si bond (i.e. a B-C-Si-X torsion, where X is C_{methyl} or O), are governed solely by electrostatic interactions between oxygen atoms and the highly positively charged boron atoms sandwiched between carbon atoms.

For this reason, the B-C-Si-X was not fitted, whilst angles and torsions between cage atoms are controlled solely by the bonding terms within the cage, so were likewise not fitted. For example, for a group of atoms B1-B2-B3, where B1 is bonded to B2, and B3 is bonded to B2, a forcefield term describing the deviation of the B1-B2-B3 angle will be described by the B1-B3 bonding term.

4.1 Forcefield derivation

4.1.1 B-B and B-C bond stretching terms; boron carbide

The intra-cage bonding terms and non-bonded terms in carborane complexes were derived from fitting to the crystal structure, bulk modulus and vibrational spectra of natural boron carbide.

Given the broad compositional range of boron carbide samples, discussed in Chapter 1.6, it was decided to represent the structure using an idealised CB_{11} cage, C-B-C chain symmetrical system. The cage carbon atom was placed at the chain bonding "equatorial" site for computational simplicity, implying C1 symmetry.

Bonding within and between cages (intra- and inter-icosahedral bonds), between chains and cages (chain-icosahedral bonds), and chain bonds, was represented by Morse potentials. For convenience, a harmonic angle term was also required for the chain bend, as were non-bonding terms, using Lennard-Jones potentials. Charges were derived at the Mulliken method in *ab initio* calculations on the boron carbide system. These were performed using the CP2K code[103], and produced the charges described in the following figure and table:

Figure 13. Motif of C_3B_{12} with atomtypes labelled

Table 3. Charges and atomtypes in boron carbide motif, labelled in Figure 13	
Atomtype	Charge (qe)
C1	-0.896
B3	0.700
C3	-0.680
C4	-0.576
B1	0.197
B2	0.078
B4	0.078
B5	0.078

The presence of so many atomtypes is necessary to differentiate between inter and intra icosahedral bonds; a B2-B2 interaction is inter icosahedral for example, while B2-B* (where B* represents B1, B3, B4 or B5) is intra. However, B2 B4 and B5 atoms are considered equivalent in a chemical sense. As Figure 13 shows, the negative charge is localised at the tetrahedral bonding sites, consistent with the higher electronegativity of carbon atoms, and the more covalent nature of the bonds they are involved in (in distinction from the delocalised bonding of the cages).

Fitting was performed on this structure, on a 6x6x3 supercell, with initial parameters chosen from the OPLS forcefield[111], and a fitting process was conducted using the least squares fitting algorithm in the GULP program. Fitting was performed to the experimental bulk modulus, 240 GPa[112], as well as the vibrational spectra[113] of natural boron carbide. The fitting procedure produced the forcefield in Table 4:

Table 4. Boron carbide forcefield			
Bonded terms (Morse, coulomb subtracted)			
parameters	D (eV)	a(Å^{-1})	r$_0$ (Å)
B-B$_{intra}$	1.500	1.780	1.758
B-C$_{intra}$	1.845	1.795	1.757
B-B$_{inter}$	0.810	1.530	1.715
B$_{cage}$-C$_{tetra}$	1.440	1.880	1.605
C$_{cage}$-C$_{tetra}$	1.440	1.880	1.605

C_{tetra}-B_{chain}	1.445	1.865	1.4332
Angle term (harmonic)			
parameters	K_θ		θ (degrees)
C-B-C_{chain}	10.0		180.0
Non bonded terms (Lennard Jones, combination rules apply)			
parameters	σ (Å)		ε (eV)
C	4.01		0.0052
B	4.0495		0.00815

The constant volume optimisation of the experimental structure with this forcefield has a maximum absolute internal derivative of <0.001, suggesting a strong correlation to crystal structure. The minimum-energy structure, when optimised in GULP at constant pressure, has the cell parameters a=5.880Å, c=12.074Å. Experimentally the lattice constants vary with carbon content and method of preparation. Towards the higher end of carbon content (roughly for $x \geq 2$, where approximate stoichiometry is $B_{15-x}C_x$) lattice parameters lie in the ranges a=5.591-5.653Å and c=12.059-12.163Å[70,114,115]. Our c parameter lies within the reported range, although the a parameter is slightly larger. However it should be borne in mind that ours is an idealised structure with maximum C content and overall composition C_3B_{12}. In reality high carbon content is believed to correlate to a high number of boron chain vacancies and other defects. The larger simulated cell volume is thus not inconsistent with the assumptions made in our structural model.

The bulk modulus for this system was 240.8 GPa, as calculated by GULP, and the vibrational spectra is compared to experiment in Figure 14.

The forcefield also sees a reasonable fit to vibrational spectra[113]. Experimentally[113], the peak at $\approx$1600 cm^{-1} is attributed to the chain stretch term, 1100 cm^{-1} is attributed to the inter-icosahedral B-B vibrations, and the peak at 800-900 cm^{-1} to intra–icosahedral B-B vibrations, corresponding to the assignments in this investigation. It is acknowledged that peaks below $\approx$500cm^{-1}, indicative of whole lattice vibrations, are not well modelled; however, classic simulations typically do not model this area of the spectrum well, and there are no negative frequencies.
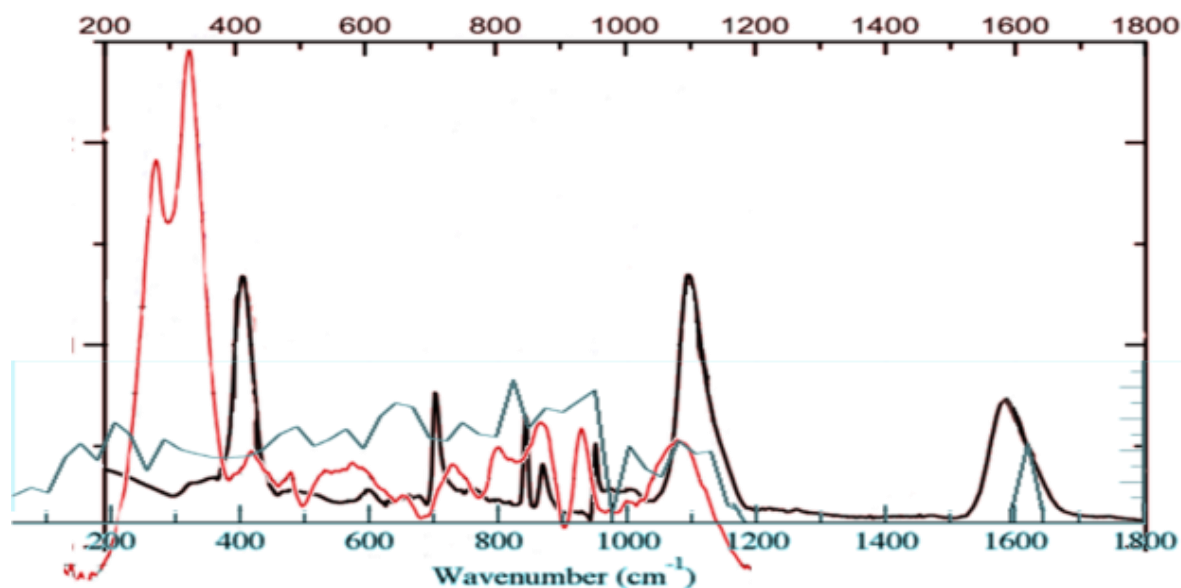
Figure 14. The experimental[113] and theoretical vibrational spectra of boron carbide. Black line is Infra red, Red is Raman spectra, and blue is theoretical.

The experimental bulk modulus of boron carbide is variously quoted as 236-247 GPa[112], and the bulk modulus given by GULP for this forcefield is 240 GPa. The modulus was also calculated using molecular dynamics; an MD run was performed at ambient temperature, on a 60750 atom system, with cell parameters a = 91.64, b = 91.63, c = 79.00Å (i.e. a 15 x 15 x 6 supercell), at a high pressure (60 MPa), as seen in Figure 15. Bulk modulus was then derived using Equation 4.1:

$$K = -V\left(\frac{dP}{dV}\right)$$

Equation 4.1

Where K, V, P is bulk modulus, volume and pressure respectively. This leads to a modulus of 247GPa, which is indicated in Figure 15, within the range of experimental values and very close to the value derived by the Reuss method.
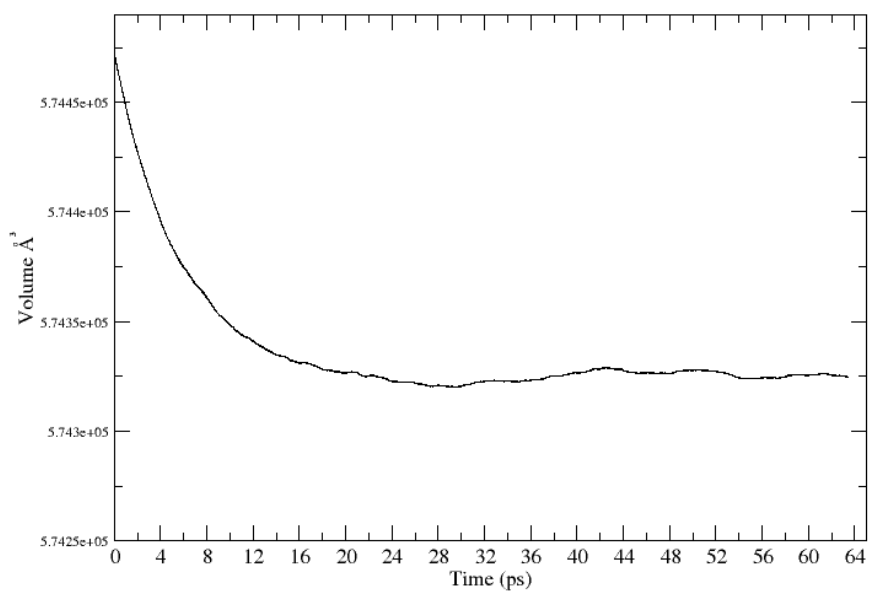
Figure 15. Volume change in equilibrated boron carbide with 600 atm pressure applied.

4.1.2 C-Si bond stretching term; *ab initio* fit

For the carbon to silicon bond required in siloxane polymer investigations, *ab initio* fitting was performed, shown in Figure 16. The carborane monomer (see Figure 12B) was optimised using Gaussian03, then one C-Si bond was manually altered about the optimal C-Si bond length, along the C-Si bond vector, with all other bonds and angles kept constant. This produced a graph of DFT energy against C-Si bond length, which was fitted manually, using a Morse potential with a correction applied for the energy of the rest of the structure, as seen in Figure 16.
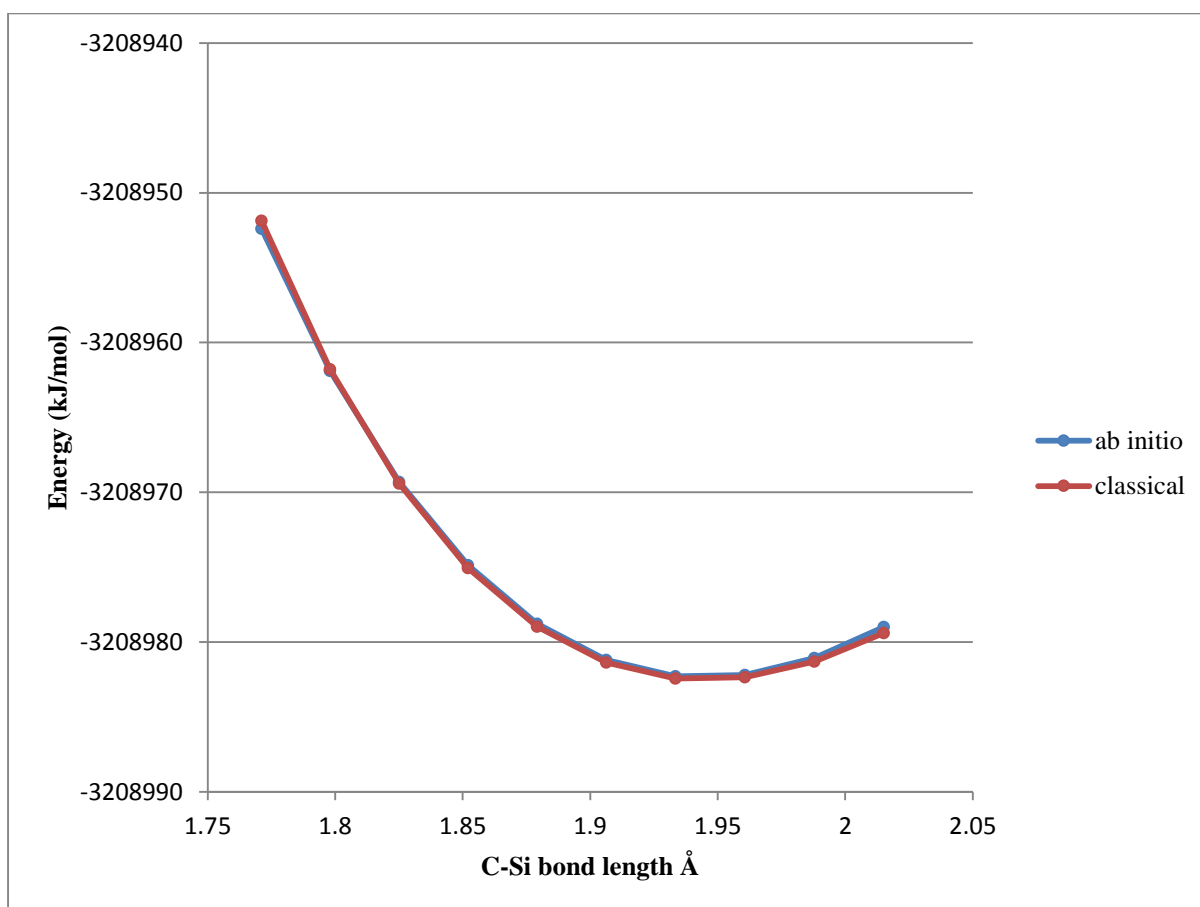
Figure 16. Ab initio and classical energies derived from deformations of monomer bond length, with classical values energy base shifted by 3208982.5 kJ/mol representing the binding energy of the rest of the structure. $R^2 = 0.9999$, values D= 159.20kJ/mol, a=1.88Å, r_0=1.945Å

4.1.3   B-H bond stretching term; sodium dodecahydro-*closo*-dodecaborate

Boron to hydrogen bonding terms were derived by fitting to physical properties of $Na_2B_{12}H_{12}$ (sodium dodecahydro-*closo*-dodecaborate), an example of a solid containing icosahedral boron clusters with B-H bonds. The crystal structure ($P2_{1/n}$ space group, and a 3 x 3 x 3 supercell) is shown in Figure 17.
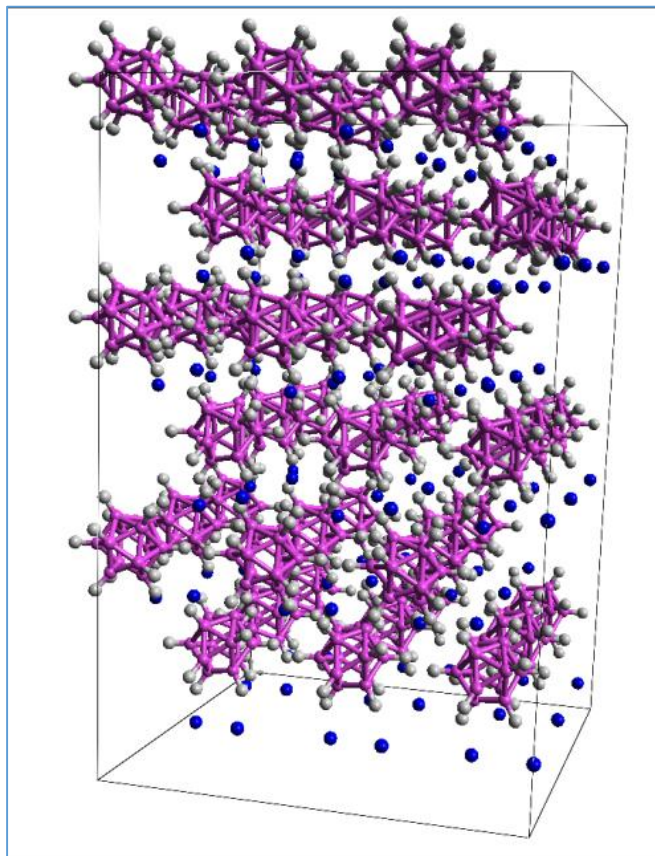
Figure 17. 3 x 3 x3 supercell of $Na_2B_{12}H_{12}$

As an initial guess, a B-H breathing term was derived by fitting a quadratic potential to deviations in *ab initio* energy (static calculations using the PBEPBE/6-31G* level of theory) when boron to hydrogen bonds are all simultaneously varied in the range -0.1 to +0.1Å in a single $B_{12}H_{12}^{2-}$ molecule, as shown in Figure 18.
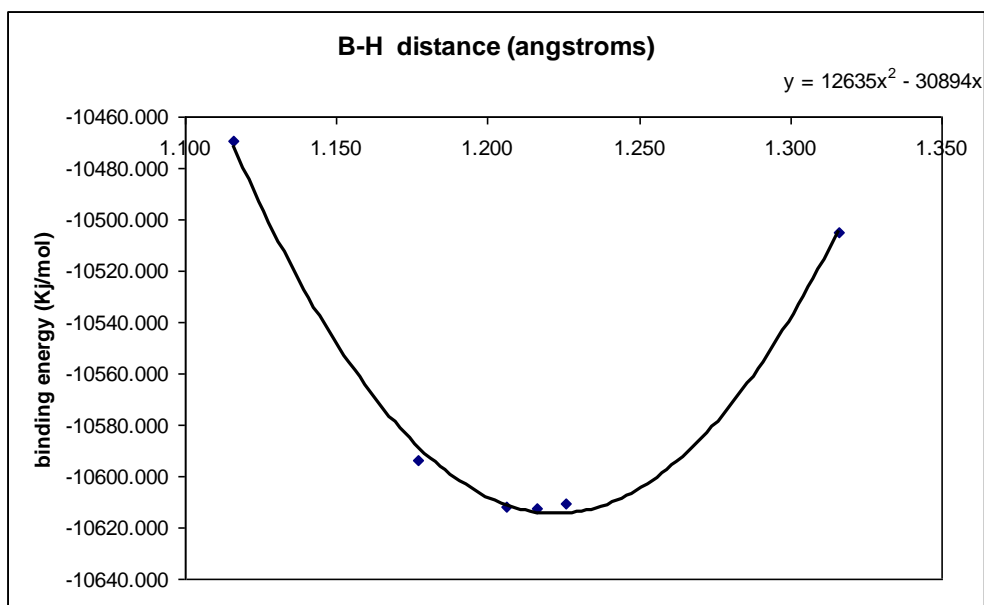
Figure 18. Binding energies of gas phase $B_{12}H_{12}^{2-}$, with optimal B-H distances varied simultaneously along the relevant B-H bond vector. $R^2 \approx 0.997$

Following this, potentials were fitted to the experimentally determined crystal structure[116] (maximum absolute internal derivative <0.1), and vibrational spectra of $Na_2B_{12}H_{12}$[117], as shown in Figure 19.
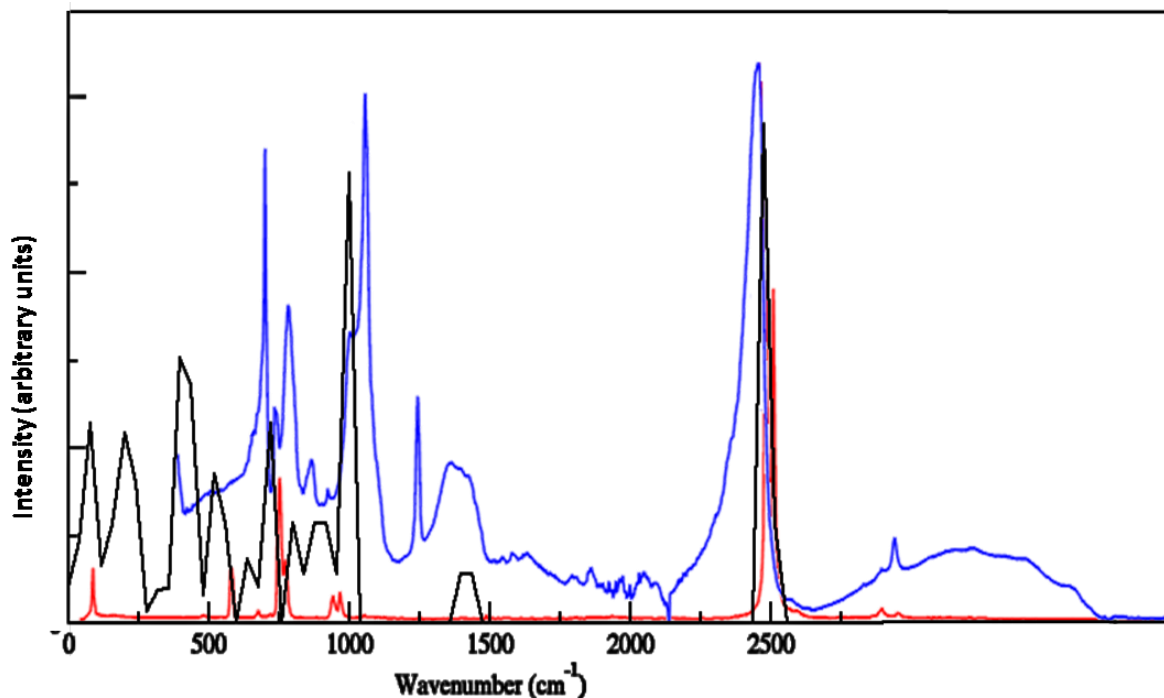
Figure 19. Vibrational spectra for $Na_2B_{12}H_{12}$ overlaid on each other. Black: theoretical, Red : experimental Raman, Blue: experimental infrared spectra[117]

Partial charges were taken from the Mulliken values obtained from Gaussian03 PBEPBE/6-31G (d,p) calculations on the gas phase $B_{12}H_{12}^{2-}$ cluster, whilst missing Na non–bonding parameters were taken from the UFF forcefield, which were also fitted to the structure, once the B-H peak had been isolated and fitted to. This gave rise to the complete forcefield given in Table 5:

Table 5. Forcefield used to describe sodium dodecahydro-*closo*-dodecaborate			
Bond terms (coulomb subtracted)			
Morse			
	D (kJ/mol)	a (Å)	r0 (Å)
B-B	159.2012	1.9	1.787
Harmonic			
	k (kJ/mol)		r0 (Å)
B-H	2020.872		1.18
Non-Bonding (Lennard-Jones, combination rules apply) and partial charges			
Species	Lennard-Jones σ (Å)	Lennard-Jones ε (kJ/mol)	Charge (q)
Na	5.00	0.0024	1.0
B	3.45	0.7530	0.06
H_{cage}	2.50	0.1255	-0.226

4.1.4 Full forcefield

Finally, all siloxane potentials, including: Si-O, Si-C, C-H, O-H bonds, H-C-H, H-C-Si, C-Si-O, O-Si-O, Si-O-Si, Si-O-H, C-Si-C angles and Si-O-Si-O, Si-O-Si-C, H-C-Si-O, H-C-Si-C, C-Si-O-H and O-Si-O-H torsions were taken from the pcff force field[92]. This led to a complete forcefield for siloxane-carborane copolymers being described, given in Table 6.

Table 6. Forcefield used to describe siloxane-carborane copolymers in this report			
	Bonding terms (coulomb subtracted)		
	Morse		
	D (kJ/mol)	a (Å)	r0 (Å)
C-B	144.725	1.9	1.705
B-B	159.20	1.9	1.787
C_{cage}-Si	204.53	1.88	1.945
	Harmonic		
	k (kJ/mol)	r0 (Å)	
B-H	2020.872	1.18	
	Quartic		
	k1 (kJ/mol)	r0 (Å)	k2 (kJ/mol)	k3 (kJ/mol)
C_{methyl}-Si	1313.82	1.9073	-2983.64	5958.57
Si-O	2561.64	1.636	-6493.68	11275.16
C-H	2886.96	1.101	-8684.603	14135.23
O-H	4521.76	0.9494	16466.55	35688.62
	Angle Terms		
	Harmonic		
	k1 (kJ/mol)	Theta0 (°)	k2 (kJ/mol)	k3 (kJ/mol)
H-C-H	276.144	108.711	0	0
H-C-Si	253.12	111.54	194.88	0
C-Si-O	192.65	114.91	394.12	418.09
O-Si-O	192.65	114.91	394.12	418.09
Si-O-Si	75.93	157.03	245.49	142.26
Si-O-H	198.96	122.88	248.72	161.22
C-Si-C	192.65	114.91	394.12	418.09
	Torsional Terms		
	Cosine 3		
	k1 (kJ/mol)	k2 (kJ/mol)	k3 (kJ/mol)	
Si-O-Si-O	0.0000	0.0000	-0.5439	
Si-O-Si-C	0.0000	0.0000	-0.5439	
H-C-Si-O	-5.6538	0.0000	-0.2427	

	Cosine 3			
	k1 (kJ/mol)	k2 (kJ/mol)	k3 (kJ/mol)	
H-C-Si-C	-5.6538	0.0000	-0.2427	
C-Si-O-H	-2.8204	1.5318	-0.4217	
O-Si-O-H	-2.8204	1.5318	-0.4217	
Non-Bonding (Lennard-Jones, combination rules apply) and partial charges				
Species	Lennard-Jones σ		Lennard-Jones ε	Charge (q)
Si	4.0		0.418	$1.35 \leftrightarrow 1.28$
B	3.45		0.753	$-0.1 \leftrightarrow 0.08$
C_{cage}	3.5		0.276	-0.74
C_{methyl}	3.5		0.276	-0.81
O	2.96		0.878640	$-0.86 \leftrightarrow -0.72$
H_{cage}	2.5		0.126	0.1
H_{methyl}	2.5		0.126	0.2
$H_{alcohol}$	2.5		0.126	0.29

In order to maintain charge neutrality, the charge can vary on the silicon and oxygen atoms according to where they are on the strand, given that hydroxyl oxygens have a different charge to bridging oxygens. Also, boron charge is dependent on proximity to the carbon atoms in the cage, as revealed by *ab initio* (PBEPBE/6-31G (d,p)) investigations. These charge variations are outlined in Figure 20.
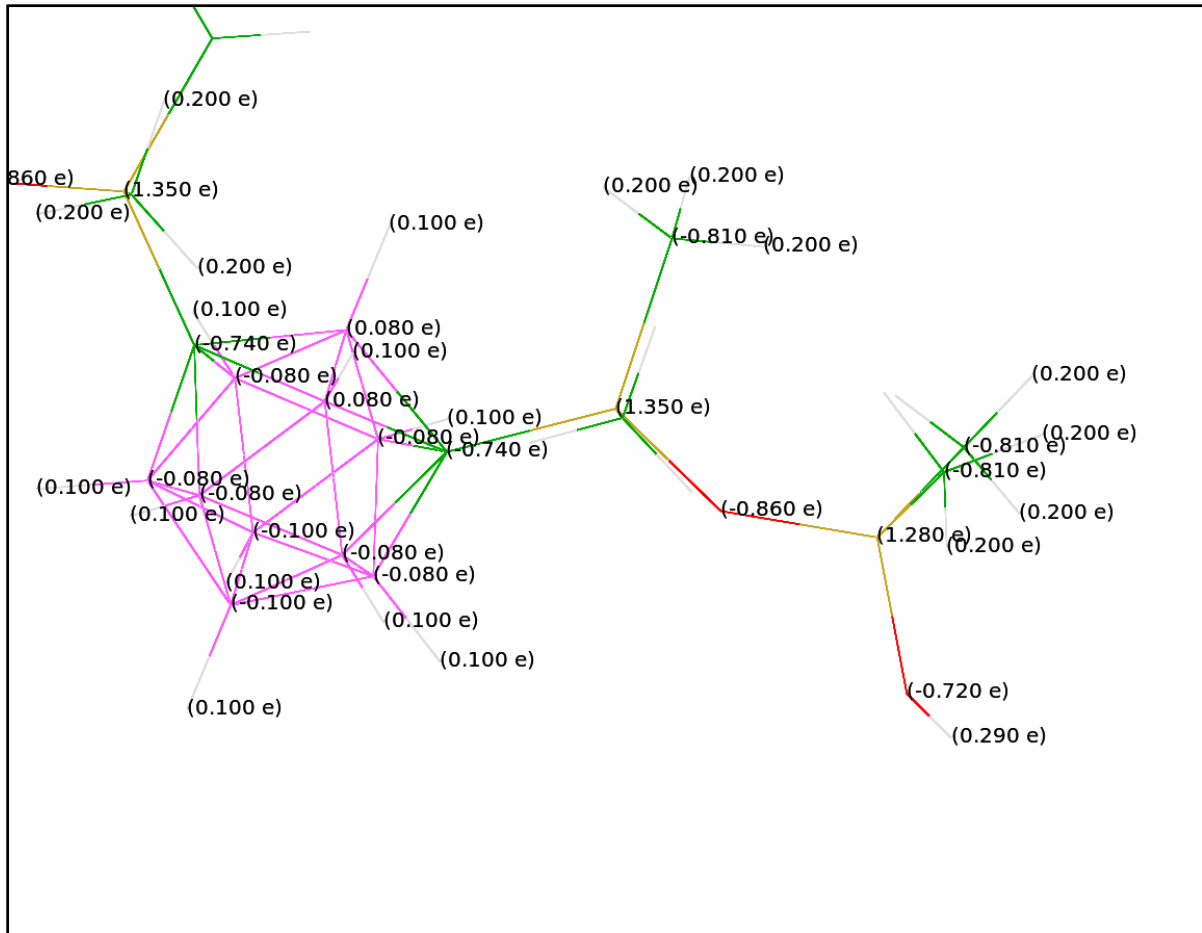
Figure 20. Showing charges in copolymer strands

Therefore, for a polymer strand of A carborane monomers (-Si(CH$_3$)$_2$-CB$_{10}$H$_{10}$C-Si(CH$_3$)$_2$O-) and B siloxane monomers (-Si(CH$_3$)$_2$O-), the charge is maintained in the manner shown in Figure 21.
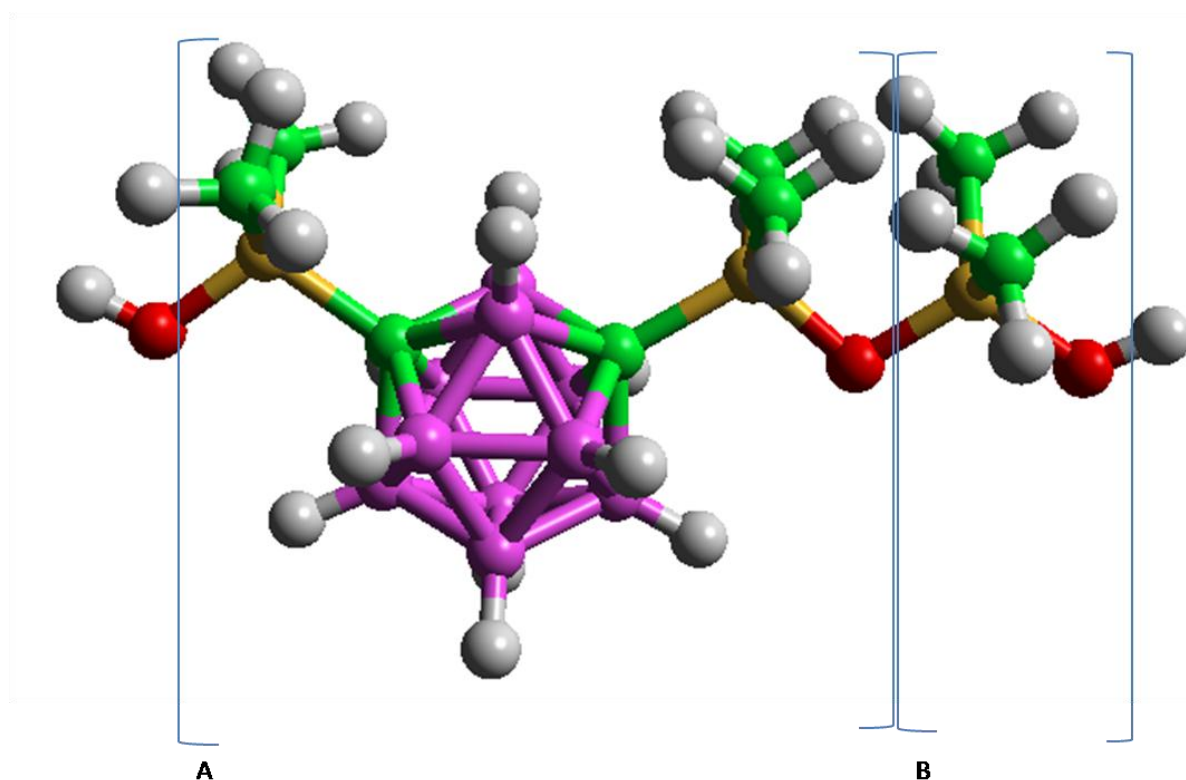
Figure 21. Showing the repeating unit of carborane monomer A, and siloxane monomer B. white spheres denote hygrogen atoms, green carbon, red oxygen, yellow silicon, and boron pink.

For the purposes of the investigation, the repeating units are charge neutral, the confirmation of which is shown in Scheme 6:

$A = 4 * C_{methyl}(-0.81) + 12 * H_{methyl}(0.2) + 2 * Si_{cage}(1.35) + 2 * C_{cage}(-0.74) + O_{cage}(-0.86) + 2 * B_1(0.08) + 2 * B_3(-0.1) + 6 * B_3(-0.08) + 10 * H_{cage}(0.10) = 0.0$

<div align="right">Scheme 6</div>

$B = = Si_{cage}(1.28) + 2 * C_{methyl}(-0.81) + 6 * H_{methyl}(0.2) + O_{siloxane}(-0.86) = 0.0$

The charges on boron atoms are an approximation of the charges for the carborane monomer from *ab initio* (PBEPBE/6-31G*) calculations, whilst the values for siloxane monomer are taken from the pcff forcefield. Meanwhile, outside of the repeating units, there are two hydroxyl hydrogens and one hydroxyl oxygen. The hydroxyl oxygen atom is given a charge of -0.72, which when considering the change in charge for one "strand" oxygen in a repeating unit, gives charge neutrality across the polymer strand.

4.2   The effect of varying *m*-carborane content in siloxane polymer backbone

Having derived a forcefield for the description of carborane-siloxane copolymers and identified the monomers and makeup of the strands desired, it was necessary to create polymer phases based on this composition. This was accomplished in three ways, identified in the following sections: (i) Short strand polymer phases, composed of 10 strands of 10 monomers, (ii) medium strand polymer phases, composed of 10 strands of 56 monomers, and (iii) long-strand polymer phases, composed of 25 strands of a Gaussian distribution centred on 40 monomers. These represent increasingly accurate models of polymer phases, with increasing levels of complexity in their calculation.

4.2.1   "Short"-strand polymer phases

As an initial investigation, polymer phases were created using the amorphous cell builder as part of the Materials Studio program. This was performed with 10 polymers of 10 monomer strands, built into a cell close to experimental density. The monomer content was varied by introducing one carborane monomer for one siloxane monomer per strand, to obtain a series of polymer phases, where carborane content varies in steps of 10%. The forcefield used was pcff with harmonic approximations of the Morse potentials derived in Table 6 (B-B k= 610 kJ/mol, r_0=1.787, C-B k=580 kJ/mol, r_0=1.705, χtest =1 correct to 8 decimal places over 0.2Å range around bond minimum), a necessary approximation for the use of the Materials Studio software.

Having produced the initial phases, molecular dynamics runs were performed using the forcefield derived in section 4.1, until cell volumes were stable (no deviation of cell volume >0.1% over a 20 ps NPT MD run, with barostat control = 1.0 ps. 1 femtosecond timestep, NPT ensemble and 1.5 ps thermostat and barostat control.) at ambient (298K, 1 atm) conditions, a process taking between 0.5 and 1 ns depending on cell size. This process produced the densities observed in Figure 22.
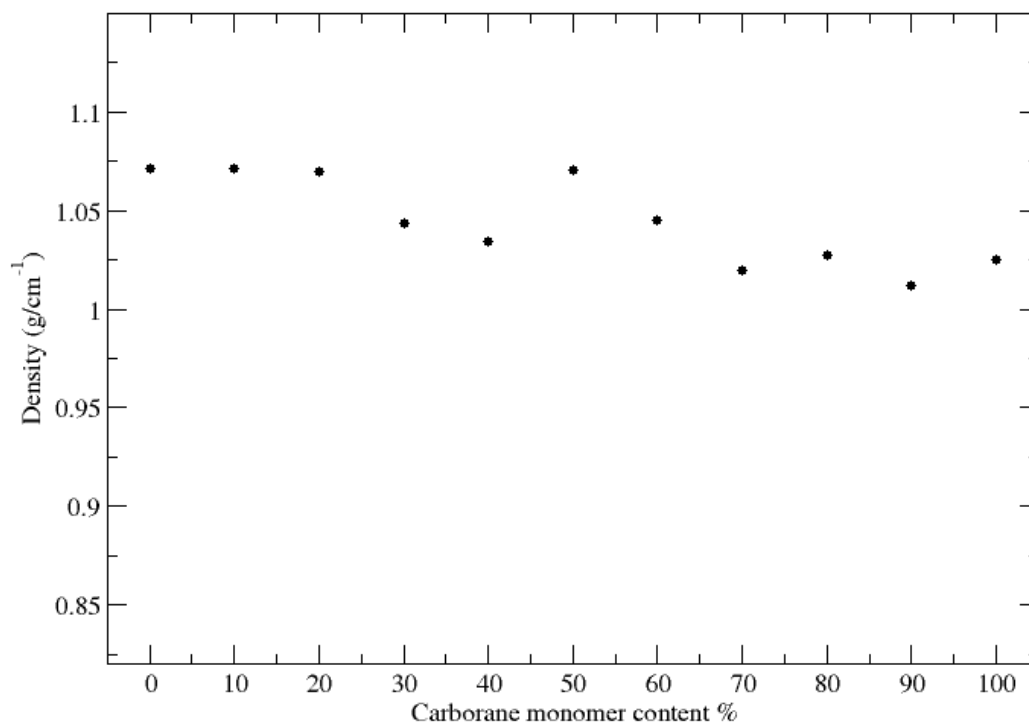
Figure 22. Densities obtained for "short" polymer strands with varying carborane substitution

The modelled 0% carborane, or "pure siloxane" amorphous density is 1.0711 g/cm^3; this is equal to the experimental[36] crystalline density of siloxane: 1.07 g/cm^3, suggesting that the polymer phases created had strands that were too short, leading to the construction of dense phases, which would not represent a good model of amorphous polymeric behaviour. Nevertheless, phases were retained, as the properties calculated could be instructive.

The "crystallinity" of the phases was analysed using radial distribution functions (RDF). The Si-O RDF shows essentially that the long-range structure is amorphous: beyond approximately 7 Å the plot tends to 1, meaning the likelihood of finding an atom at that distance is random, as seen in Figure 23.
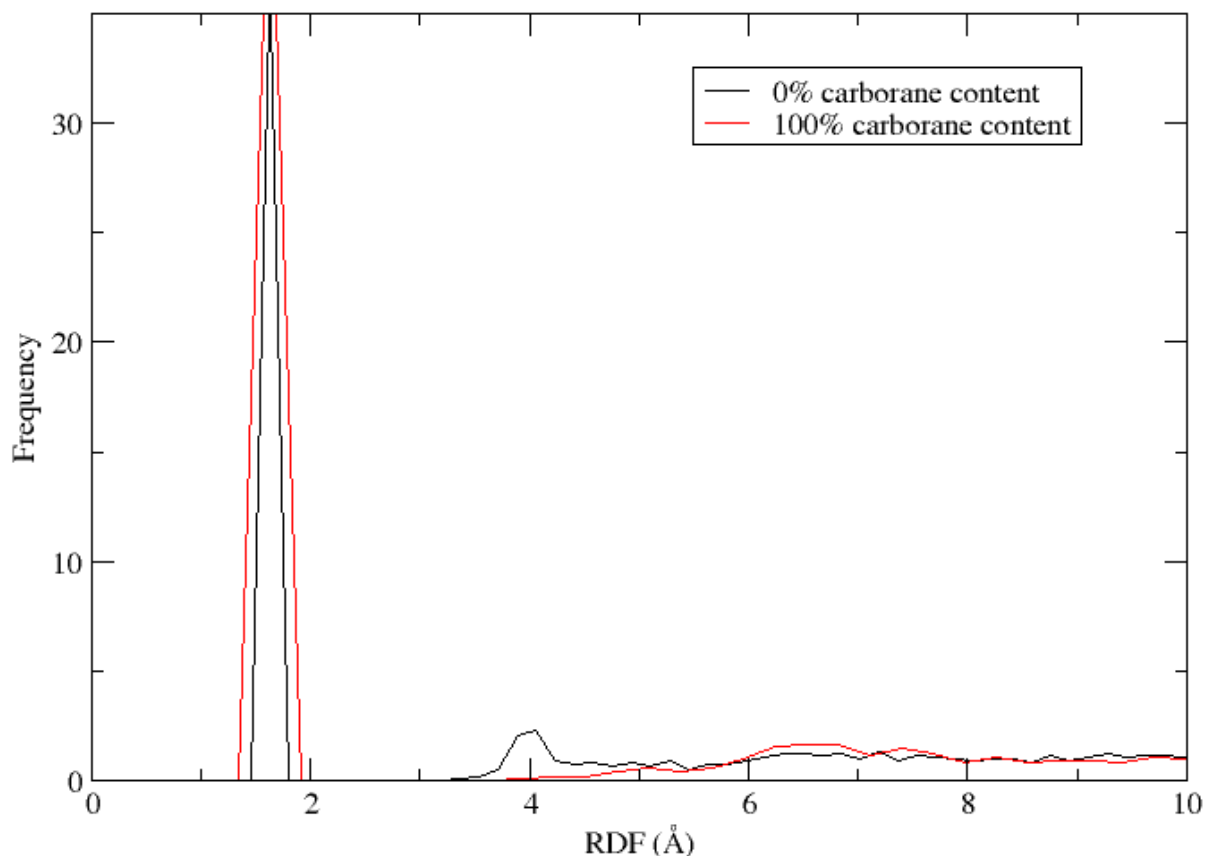
Figure 23. Si-O RDF data for 0 and 100% carborane content short polymer phases

As noted, the RDF data shows amorphous nature beyond 7Å. However, the peak in the 0% carborane content graph at 4Å is indicative of the oxygen atom one monomer unit away from the selected silicon atom, as it is not observed in the 100% carborane content case. There is a small broad peak in the 100% carborane content phase at 6.5Å, which is perhaps indicative of an "inter-strand" distance.

In all though, crystallinity is clearly not observed in either case, so it is maybe more useful to refer to the phases as attaining crystalline density due to the length of strands, rather than attaining true crystalline structure.

4.2.2 "Medium"-strand polymer phases

Owing to the fact that the previous investigation had strands that appeared to be too short, leading to phases with a level of ordering/alignment in strands that produced densities unrepresentative of experiment, the process was repeated with 10 strands of 56 monomer lengths for each phase. A percentage of carborane/siloxane substitutions were performed dependent on phase. It was also desirable to move away from the commercial Materials Studio program, in order to avoid having to use approximations of forcefield terms, and allow more control of cell construction. The strands were built linearly using a simple python script, and were then randomly inserted into a large empty box, in one Monte Carlo step, using the program Aten[108]. Molecular dynamics (298K, 1 femtosecond timestep, NPT ensemble and 1.5 ps thermostat and barostat control) stabilisation of cell volume was necessarily a longer process (1-2ns MD runs), and produced the densities observed in Figure 24.
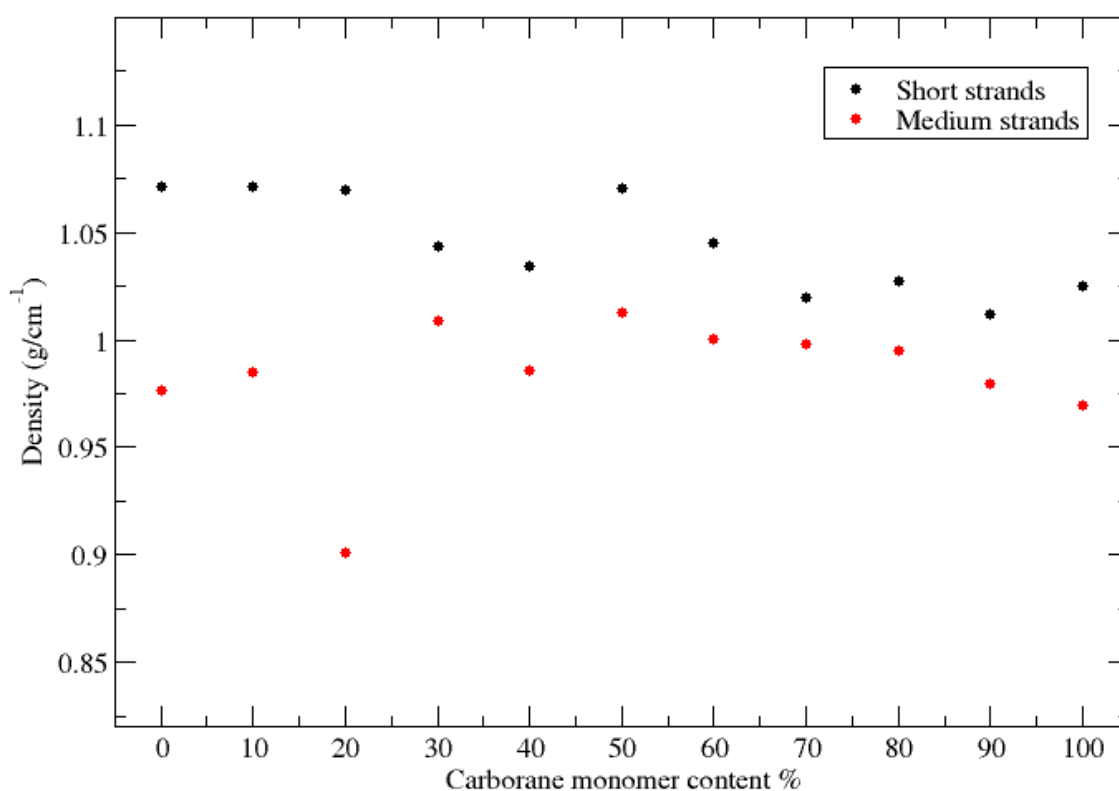
Figure 24. Densities of short and medium strands, obtained by NPT MD runs to stabilise cell volumes.

The amorphous polymeric density[36] of pure siloxane, 0.97 g/cm^3, has been replicated, with carborane content appearing to increase density, an effect that levels off above 50% content for the medium strand length polymer phases, and in fact there is a decrease in density for higher carborane content phases. The example of 20% carborane substitution is

anomalous, and is due to a large pocket of free volume, that is stable over $\approx$ 20ps, in that cell volume is unchanged. The pocket is shown in Figure 25.
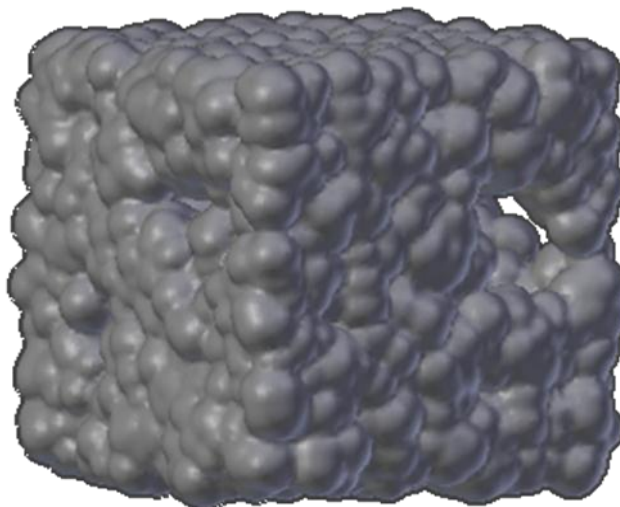
Figure 25. Visualization of solvent occupiable surface in 20% carborane polymer system

Physical properties calculated for this phase must therefore be treated with some caution. Experimentally[36,118] the 50% copolymer density is 1.074g/cm^3, which is here simulated as 1.02 g/cm^3, suggesting the medium-strand phases slightly under predict experimental density as a whole.

4.2.3 "Long"-strand polymer phases

It was decided to extend the calculations of varying carborane content in siloxane polymer phases, and to streamline the process for creating them. Inspiration was taken from the ZEBEDDE program, written by Lewis[119] *et. al*. This is a piece of software aimed at predicting organic templates for zeolite synthesis that works by inserting a small organic "seed" into the pore of a theoretical zeolite, and builds organic linkers from terminal hydrogens. Small deviations of organic template position through translation, torsion angle rotation etc. is allowed, in order to obtain an organic cation with the best interaction with the zeolite structure. In this way, optimal cation templates can be predicted, for zeolite synthesis.

The methodology was replicated, with the static zeolite removed, and polymers were built using a monomer as the seed, and more monomers built along the vector of each successive terminal –OH bond, outlined in Figure 26.

The initial idea for this experiment was to adapt the existing ZEBEDDE code to effect these changes, and incorporate the new monomers. However, there was some difficulty in increasing atomic configuration to six, and incorporating new forcefield terms. Therefore the code was rewritten in python, from scratch. As calculations became more computationally intense, the shedskin[120] program was used to convert back to C++ machine code, and some speed-up of certain loops was also implemented. However, all the phases generated by this method employ essentially the same methodology. The ERMINTRUDE code is available via my website[1].
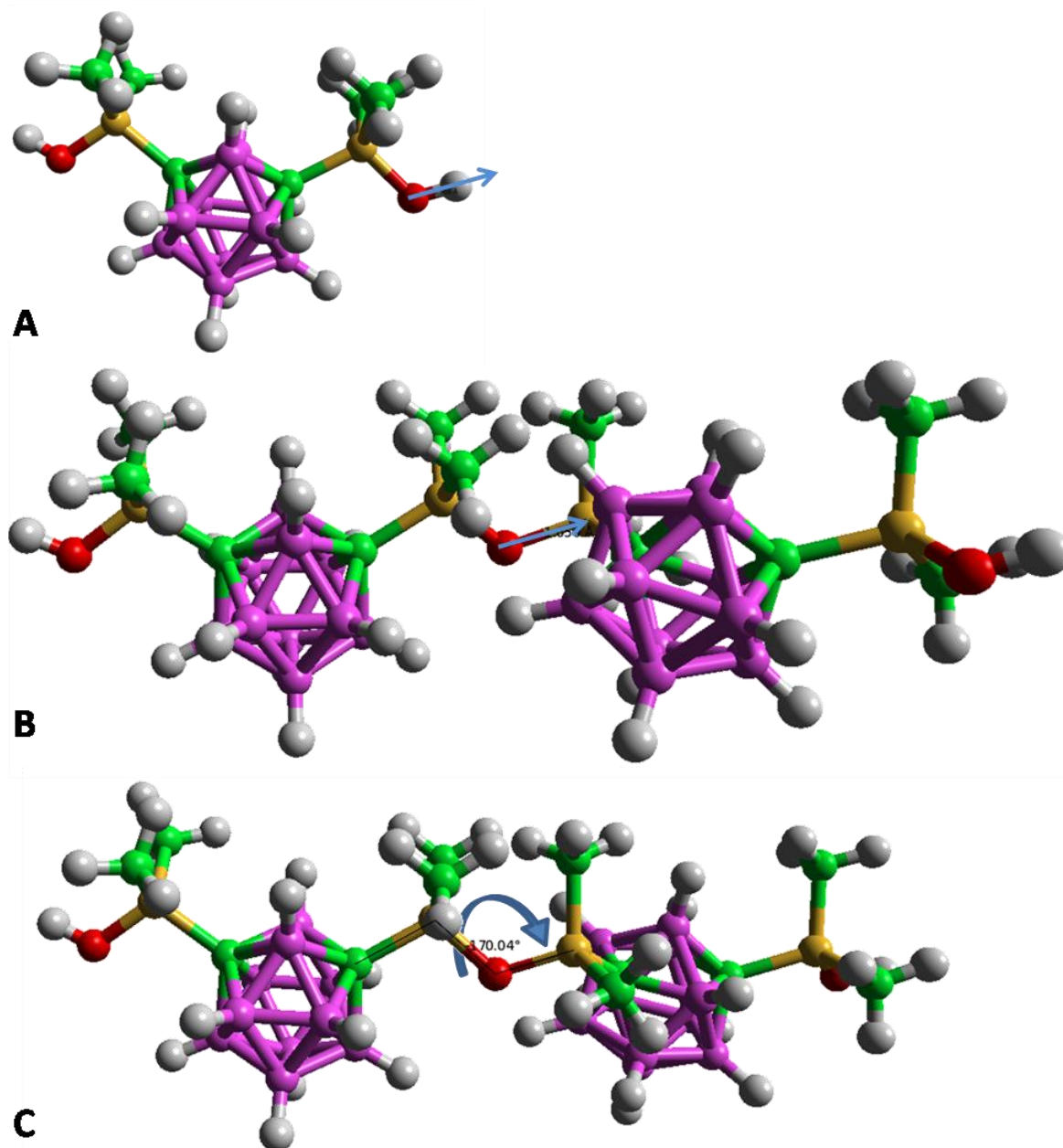
Figure 26. An illustration of the action of the ERMINTRUDE program. A: a point is taken along the terminal O-H vector at the O-Si bond length. B: the silicon atom of a new monomer is placed at that point, with the terminal hydrogen, and new monomer's first hydroxyl group deleted (i.e. H_2O eliminated overall). C: the newly created monomer is rotated around the new O-Si bond to find a stable conformation.

A water molecule is deleted with each addition, an approximation of experimental conditions, and each new monomer addition is allowed to rotate around the newly generated Si-O bond, in order to assume a stable conformation. Once the desired strand length is achieved, a new seed is generated, treating the already generated polymer structure as a rigid solid structure to build around. This is summarised in Figure 27.
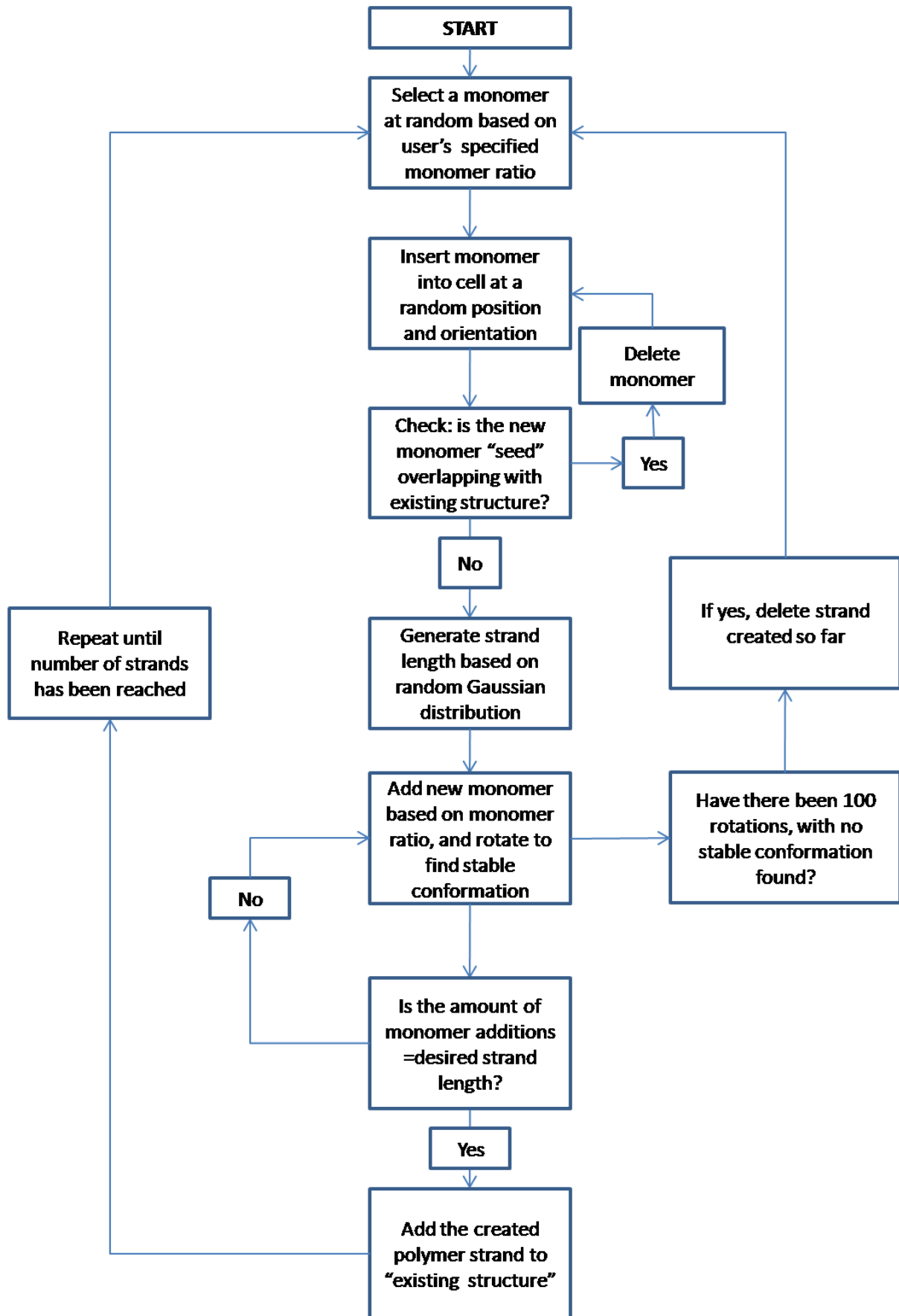
Figure 27. Flow chart summarising the process involved in the Ermintrude code

Finally, it is worth noting that crystallisation is avoided by allowing strand length to vary according to a Gaussian distribution, by assigning a random strand length at the start of each strand's build, as seen in Figure 28:
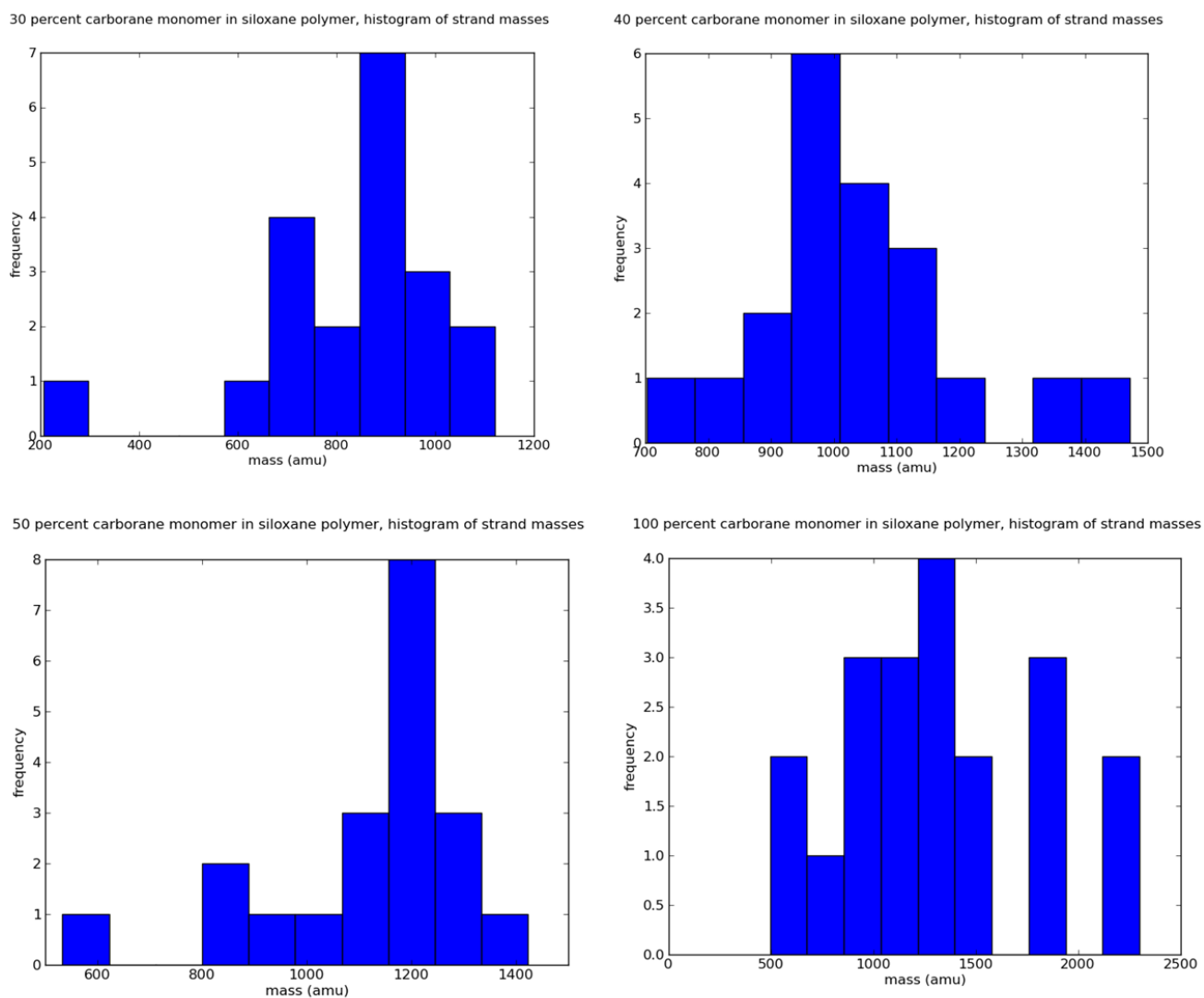
Figure 28. Distribution of strand mass (related to strand length, and easier to calculate) for a few representative systems produced by ERMINTRUDE

This is achieved by performing monomer additions according to Equation 4.2, where X is a random number generated by python's rand() function, between 45-55:

$$No.\,of\ strands = 40 \pm \left(80 \times e^{\frac{(X-7)^2}{128}} \right)$$
Equation 4.2

The initial densities produced by this code are shown in Figure 29, for a variety of cell sizes, for 100% carborane content:
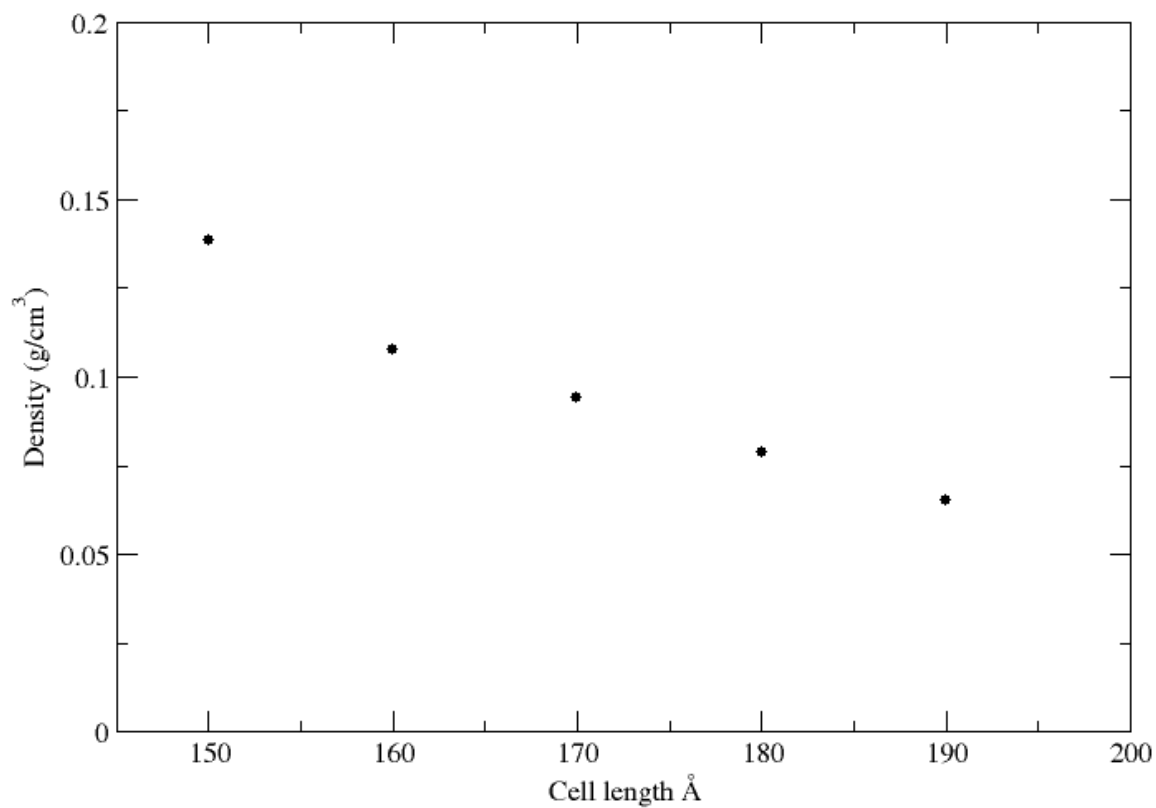
Figure 29. Density against cell length for 100% carborane polymer systems produced by ERMINTRUDE, before equilibration. Strand length is a gaussian distribution around 45 monomers

So, for 100% carborane, a cell size of 140 x 140 x 140 Å gives a density of ≈0.16 g/cm^3, an eighth of experimental density. This is completed over a two and a half days on one core, as seen in Figure 30.
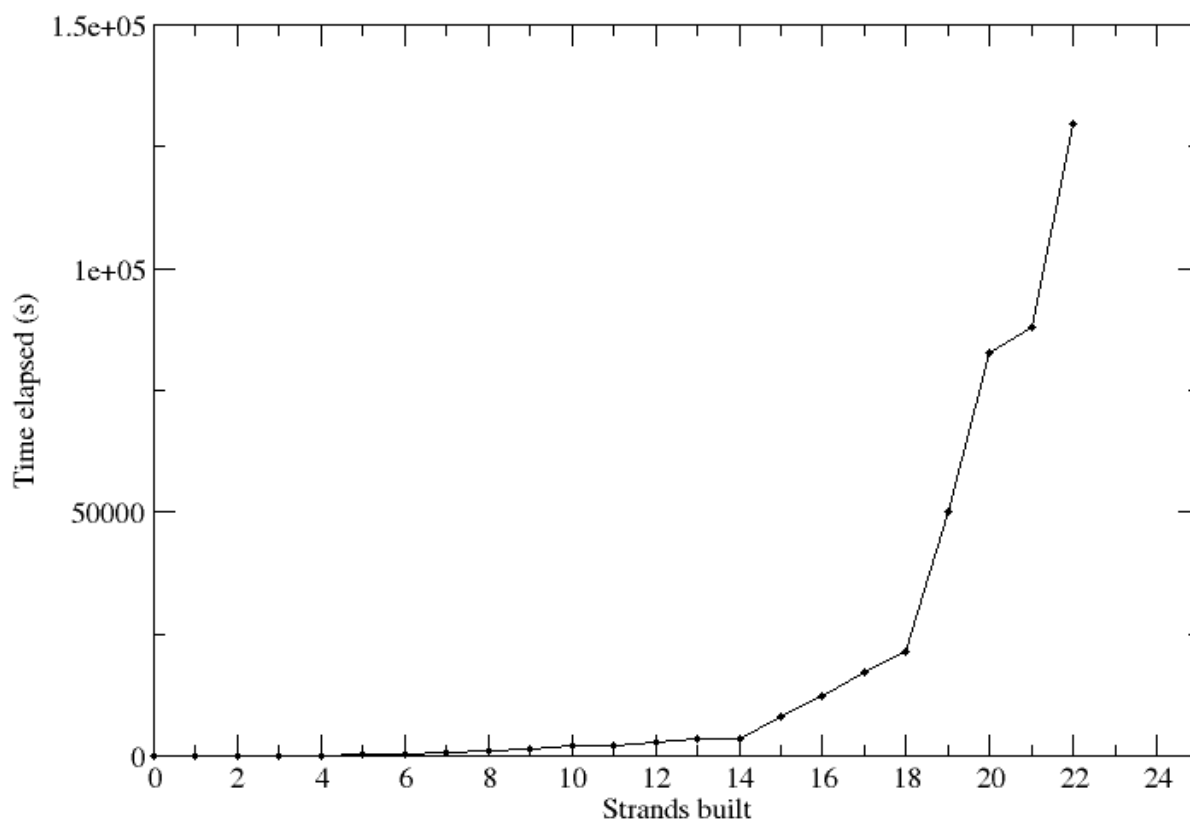
Figure 30. Machine time elapsed for ERMINTRUDE polymer phase builder, for each strand of 25, in 100% carborane content example

So, having produced polymer phases of roughly an eighth of experimental density, constant pressure MD (1 femtosecond timestep, and 1.5 ps thermostat and barostat control) was performed at ambient conditions (298K, 1atm) until cell volumes stabilised, for phases of 20 strands of a Gaussian distribution centred at 36 monomers as seen in Figure 31.
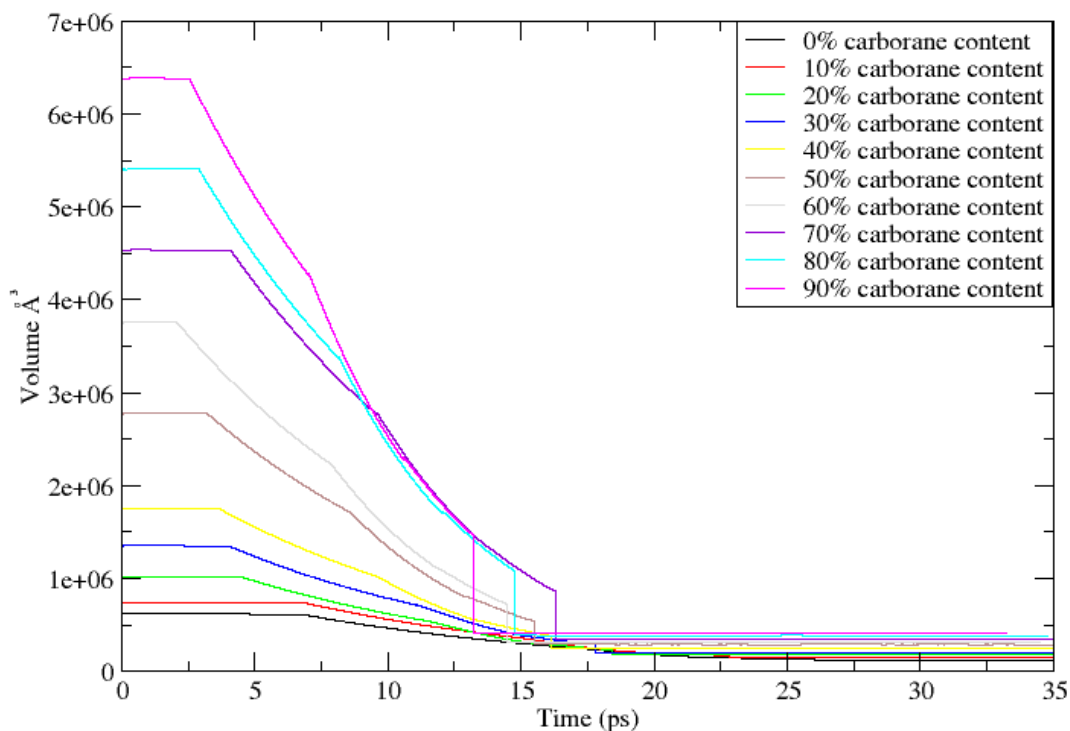
Figure 31. Stabilisation of long-strand polymer phase's cell volumes, during NPT MD runs, with varying conditions, namely 10K 1atm, 50K 2katm, 298K 1atm.

This process typically took between 0.5 and 4ns. The densities produced by this method are shown in Figure 32. This shows that 0% carborane, or pure siloxane, density is slightly above experiment (1.005 as opposed to 0.97 g/cm^3), whilst carborane percentage appears to increase density, levelling off above 50% at $\approx$1.07 g/cm^3. Experimentally[36] the 50% copolymer is 1.074g/cm^3, suggesting good agreement. The 100% carborane content example is anomalously low as a result of a large pocket of free volume existing in the phase.
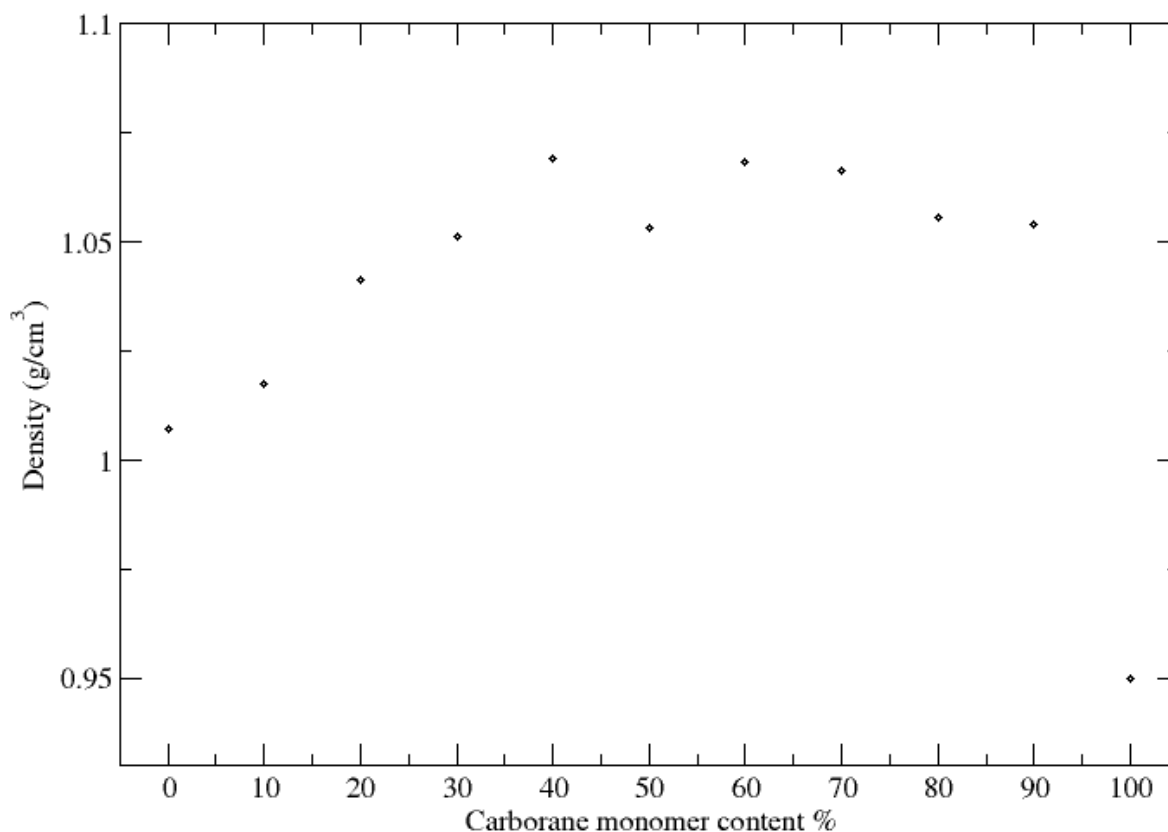
Figure 32. Density as a function of carborane substitution for longer strands, obtained by the NPT stabilisation at ambient conditions of ERMINTRUDE produced polymer phases, 20 strands of a Gaussian distribution around40 monomers.

In total then, three methods have been investigated for producing polymer phases composed of varying carborane/siloxane ratio copolymer strands, with different degrees of success.

Initially, the amorphous cell builder was employed, producing polymer phases that included strands that we believe were too short, leading to unrealistic ordering of strands, and reproducing experimental crystalline density for pure siloxane polymer, with increasing carborane content appearing to reduce density linearly. The "medium" phases, composed of 10 strands of 56 monomers, built as linear strands and inserted into an empty box, were able to reproduce the experimental polymeric density of pure siloxane, with carborane content increasing density, an effect that levels off above 50% carborane content.

Finally, the long-strand polymer phases were produced using a method that best approximates experiment, by building polymer strands by monomer, avoiding overlap with the rest of the modelled polymer, with 20 or 25 strands of lengths that replicate a Gaussian distribution centred on 40 monomers, again with the intention of mimicking experiment. This simulation slightly overestimates pure siloxane density, but reproduces the 50:50

carborane:siloxane density, with carborane content appearing to increase density, again levelling off after 50% carborane content.

Therefore the method most likely to reproduce experimental density, and give the best indication of bulk physical properties, is the final one, although the possibility of creating a free volume pocket that is stable over typical simulation times is unavoidable for the medium and long-strand strand methods, and must be checked before the calculation of physical properties.

An indication of the variation in density among phases generated by the three methods is shown in Figure 33.
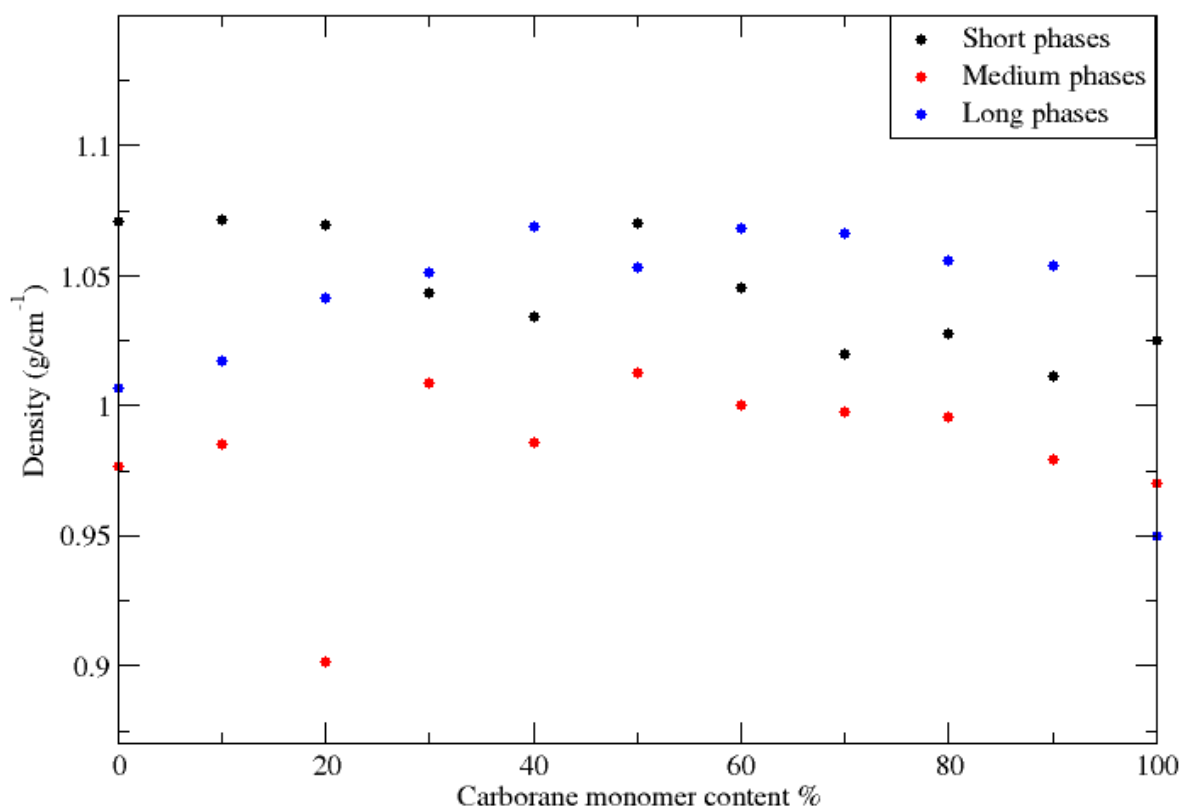
Figure 33. Density against carborane content for the three methods of generating polymer phases.

As is clear, the long-strand phases follow the same trend as the medium-strand phases (carborane content increasing density, levelling off after 50%), but with a higher overall density, that reproduces experimental density for 50% carborane content. In total then, experiment sees a sharper rise in density than is seen in either simulation, so physical properties will be calculated for medium and long strand phases where possible, and the results considered as a whole.

4.2.3.1 GULP derived bulk modulus

Bulk modulus was first calculated using the GULP program, for the short-strand polymer phases. In this method, the elastic constant tensor is calculated for the material based on static deformation of atom positions, and is averaged across the material. Three definitions are output, Reuss and Voight definitions are given in Equation 4.3 and Equation 4.4 respectively, and the Hill definition is the average of the other two:

$$K_{reuss} = \frac{1}{9}(C_{11} + C_{22} + C_{33} + 2(C_{12} + C_{13} + C_{23}))$$

Equation 4.3

$$K_{Voight} = (S_{11} + S_{22} + S_{33} + 2(S_{12} + S_{13} + S_{23}))^{-1}$$

Equation 4.4

This is a fairly intense calculation given the polymer phase size, and the anisotropic, random nature of the polymer phase. Nevertheless, bulk moduli have been derived by this method, for short-strand polymer phases, up to 90% content and are given in Figure 34.
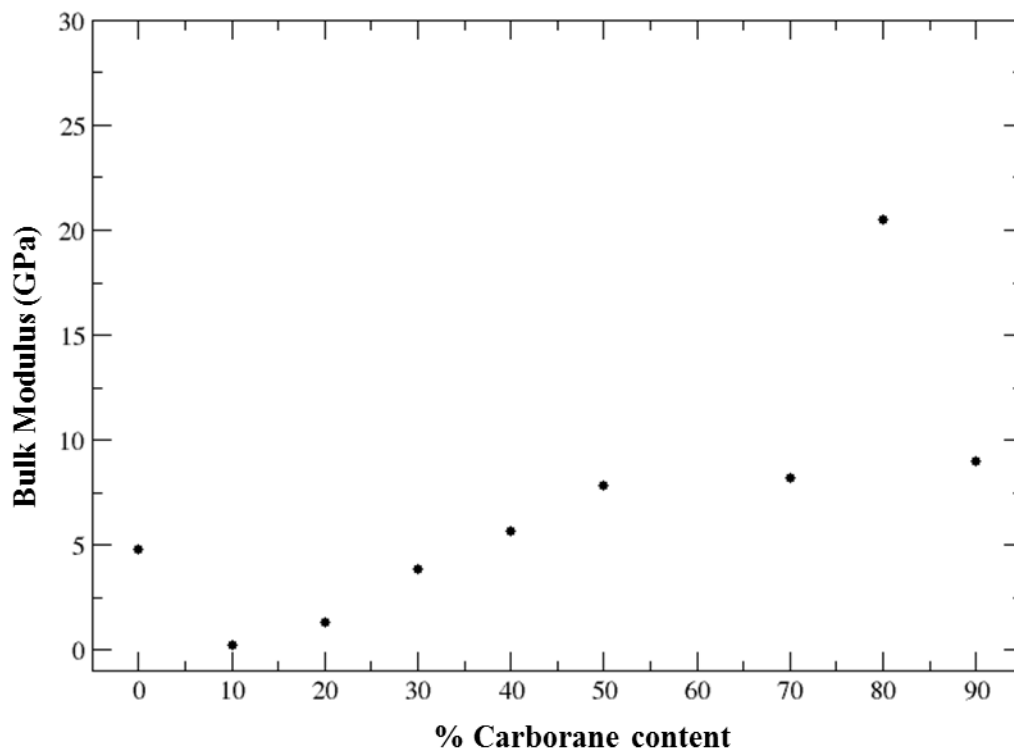
Figure 34. Gulp derived Reuss bulk modulus for short-strand polymer phases, as a function of carborane content

The bulk modulus for 0% carborane content (pure siloxane) is experimentally in the range 0.91-23.73 GPa (explained in detail in section 4.2.3.2) whilst the theoretical value (which will be discussed in section 4.2.3.2) is 10.1 GPa. Consequently the value is within experimental range, suggesting that the forcefield and method are sound. It is also clear that

with increasing carborane content, bulk modulus increases, an effect that levels off above 50 percent carborane substitution, with the 80 percent case anomalous. The 0% case could also be considered anomalous, since there is an initial dip in the bulk modulus value, before an almost linear rise.

Since it has already been acknowledged that the density produced by the "short" pure siloxane is equal to the crystalline experimental value, it is therefore proposed that the unrepresentative ordering of strands in the polymer phase has had an effect on the material's response to isotropic pressure.

For this reason, the results of the medium and long strand polymer phases will be considered more relevant to real–world values, but as an initial result, it is clear that the forcefield can reproduce experimentally meaningful bulk moduli, and that carborane content increases this property. In the designed material then, this is representative of a stiffening of the material in its response to isotropic pressure, as a result of introducing carborane units. However, these properties are likely to be a function of strand lengths, which are unequal in the theoretical and experimental cases, so a slight difference is expected. For example, the bulk modulus is likely to be lower with shorter strand lengths.

4.2.3.2 MD derived bulk modulus

Due to the large number of atoms, the memory available on supercomputers became an issue for the GULP bulk modulus calculations on the 100% carborane content of the short-strand polymer phases, as well as the medium and long strand polymer phases, as second derivative information for each of the degrees of freedom for each of the atoms is stored in the RAM.

As a result, Molecular dynamics runs at high pressure were completed (1fs timestep, Berendsen NPT ensemble using 1 ps control used, in 10 ps runs. Systems were equilibrated at 298K/1atm for 5ps, then had pressure changed), to calculate cell volume changes as a function of pressure, and derive bulk modulus explicitly, using Equation 4.5:

$$K = -V\frac{dP}{dV}$$

Equation 4.5

Where K is bulk modulus, V is Volume, and P is pressure. Therefore, the bulk modulus is given in pressure units.

Initial calculations were performed at 0.01, 0.1, 1.0, 2.0, 5.0, 10.0 katm pressure. Figure 35 shows the response of polymer phases to varying pressure (0.1, 1.0, 2.0 katm simulations shown). As will be seen, results between $0.01 - 2.0$ katm are of most use, as at very high pressures, there is a levelling off of volume change, and a linear fit of pressure against volume change has low R^2 values. This is expected from experiment, as if a material's response to pressure was truly linear at all pressures, there would be a pressure sufficient to leave 0% volume, which is obviously impossible. A levelling off of volume versus pressure is expected then, and only the initial values up to 2.0katm will be considered for bulk moduli calculation, where $R^2 > 0.995$ for a fit to a linear plot.
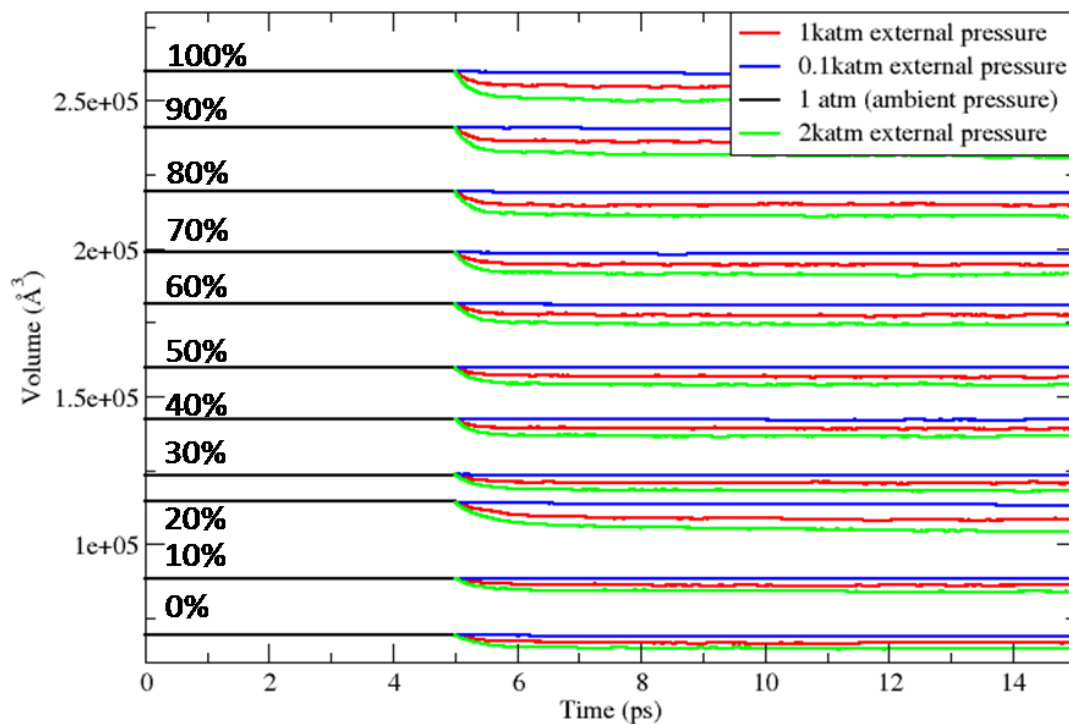
Figure 35. Evolution of long-strand polymer phases' cell volume with time under varying applied pressure. Degree of carborane content indicated on graph's left hand side. All phases at ambient conditions (1atm, 298K) until 5ps, with high pressure (100 atm, 1000atm, and 2000atm) cell volume response overlaid on the same graph

The change in cell volume after volume had stabilised (volume change over 2ps < 0.1%), is given in Figure 36 (incomplete 20% carborane substitution phase excluded), alongside the experimentally[121] derived changes in volume:
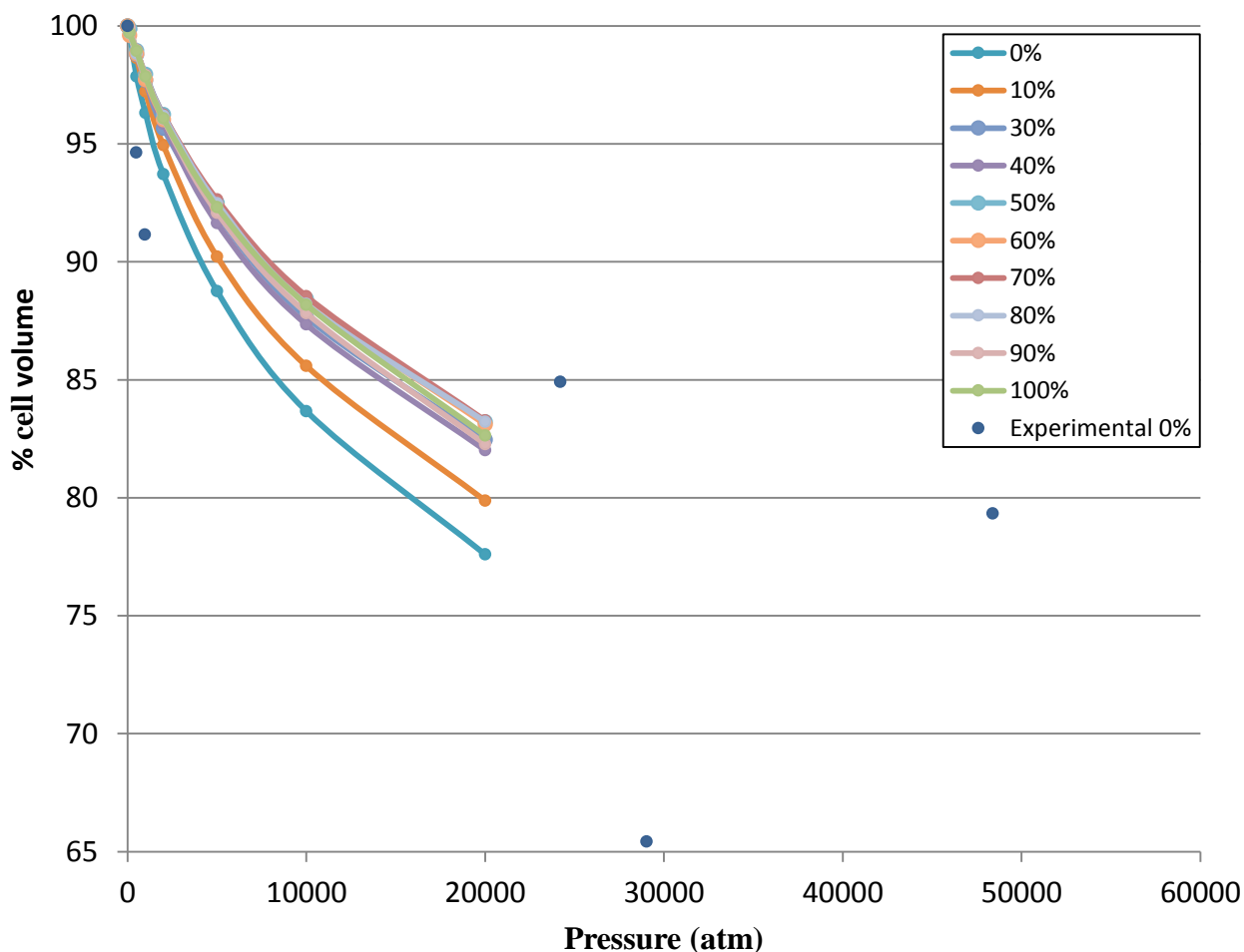
Figure 36. Medium-strand polymer phase equilibrated cell volume, taken as a percentage of ambient cell volume against applied pressure.

Looking at the experimental data; it is clear that there is a lot of variability in the results, so attempts to fit the results to a linear graph to obtain dP/dV for input into Equation 4.5 are obviously redundant (R^2=0.551). However, it is pleasing that the theoretical results appear to fall within the range of the experimental results, which suggests that the theoretical model is a good one. Calculating bulk moduli for each individual point, gives bulk moduli in the range 0.91-23.73 GPa, and an average of 10.1 GPa. This will be used as the value to compare theoretical results to, although the large error in the value is acknowledged.

The second trend to gather from this graph is that increasing carborane content appears to reduce the change in cell volume as a result of high pressure. This will be analysed in more detail below.

As previously stated, bulk moduli were calculated by taking the results at or below 2katm, using Equation 4.5, the results of which are given in Figure 37:
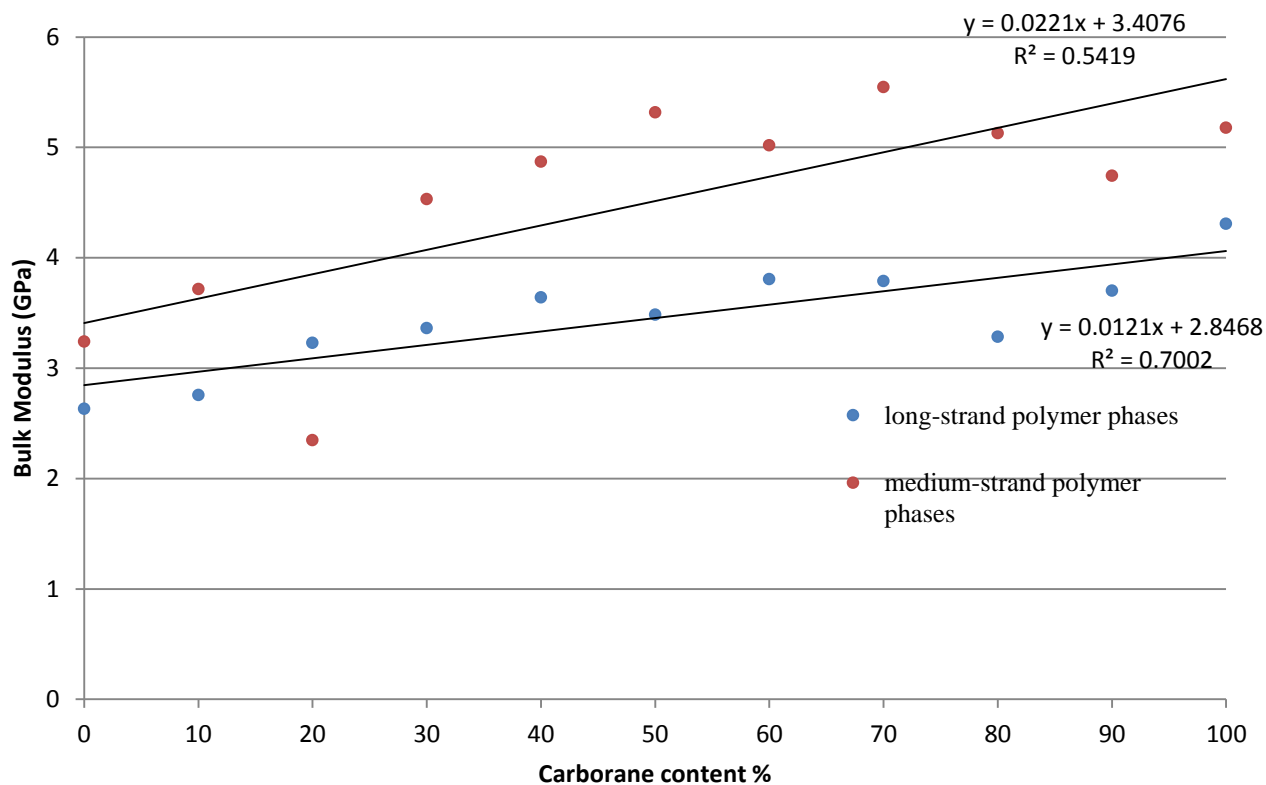
Figure 37. MD calculated bulk modulus for medium and long strand phases.

As can be seen in Figure 37, the bulk modulus increases with increasing carborane content, as suggested by the raw data in Figure 36. It is also observable that the 0% carborane content, or pure siloxane, example is within the experimental range of values (0.91-23.73 GPa). To compare between medium and long strand schemes, the rise in bulk modulus with increasing carborane content occurs with the same rate, but the values for the medium-strand phases are about 1GPa higher overall when compared to the long-strand polymer phases.

The angle distributions and radial distribution functions of the atoms in the polymer phases are of interest, as the phase goes through pressure cycling. These are seen in the following Figures, for the pure siloxane medium-strand polymer phase.

A Si-C-H angle distribution in 0% carborane phase
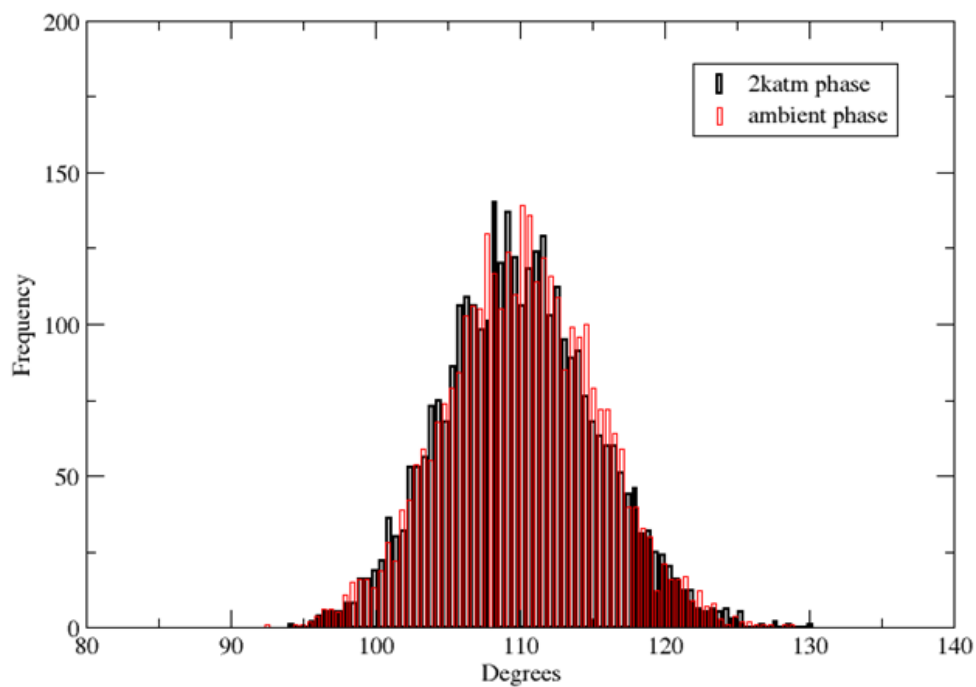
B H-C-H angle distribution in 0% carborane phase
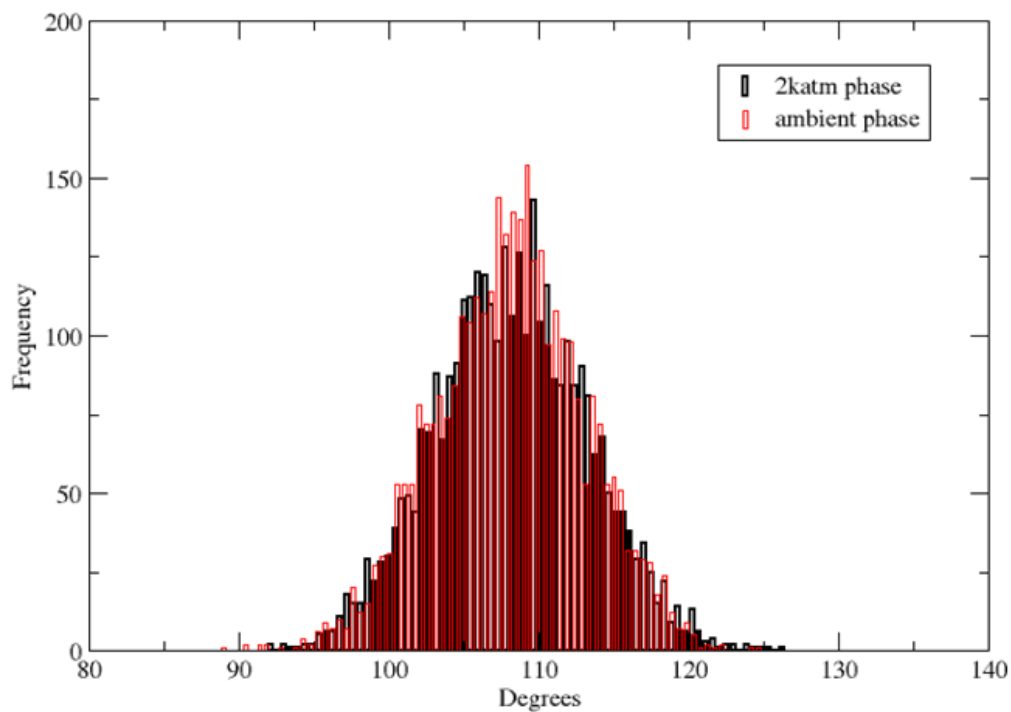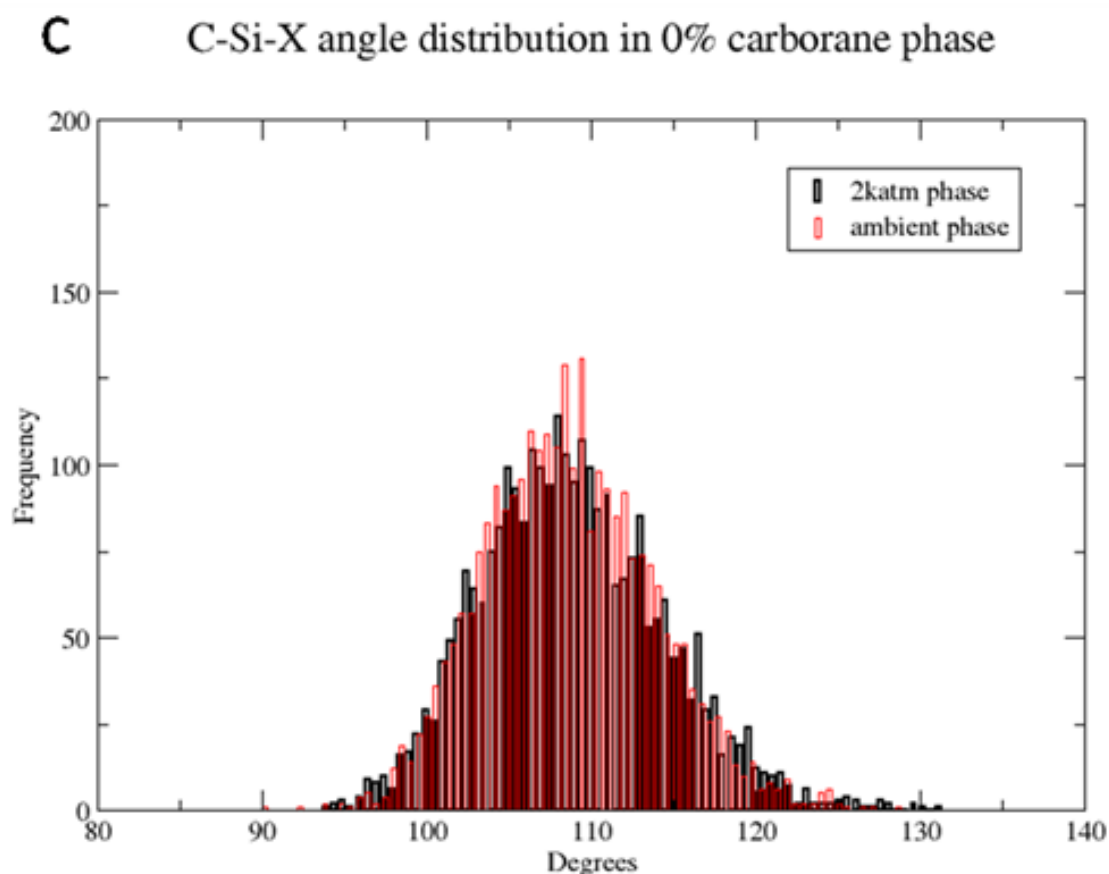
Figure 38. Histograms of key angle terms in pure siloxane (0% carborane content) phase.

reveals that, as pressure increases, the peak and breadth of the histograms of Si-C-H, H-C-H, and C-Si-X angles, show little change. The X in this case refers to any atom (a factor in the production of the RDF plots using the referenced script), which in this case either means oxygen, or the carbon atom in the other bonded to methyl group of the central silicon atom. Clearly these interactions are the most rigid, which is reflective of the short, stable bond lengths between atoms involved in a methyl group. High pressure induced deformations in the structure will not be accounted for by these structural elements.

For comparison, in Figure 39, there is a much larger observable change in O-Si-O and Si-O-Si angles, suggesting that the volume change is accommodated largely by these deformations: high pressure shifts the peak of the O-Si-O angle to a lower angle by ≈ 3°, whilst the Si-O-Si is shifted to a lower angle by ≈ 10°. There is also evidence of a broadening of the two distributions, suggestive of a wider range of acceptable conformations for these structural elements. This is representative of the longer bond lengths and wider angles in silicon-oxygen chains in siloxane polymers.

A O-Si-O angle distribution in 0% carborane phase

B Si-O-Si angle distribution in 0% carborane phase
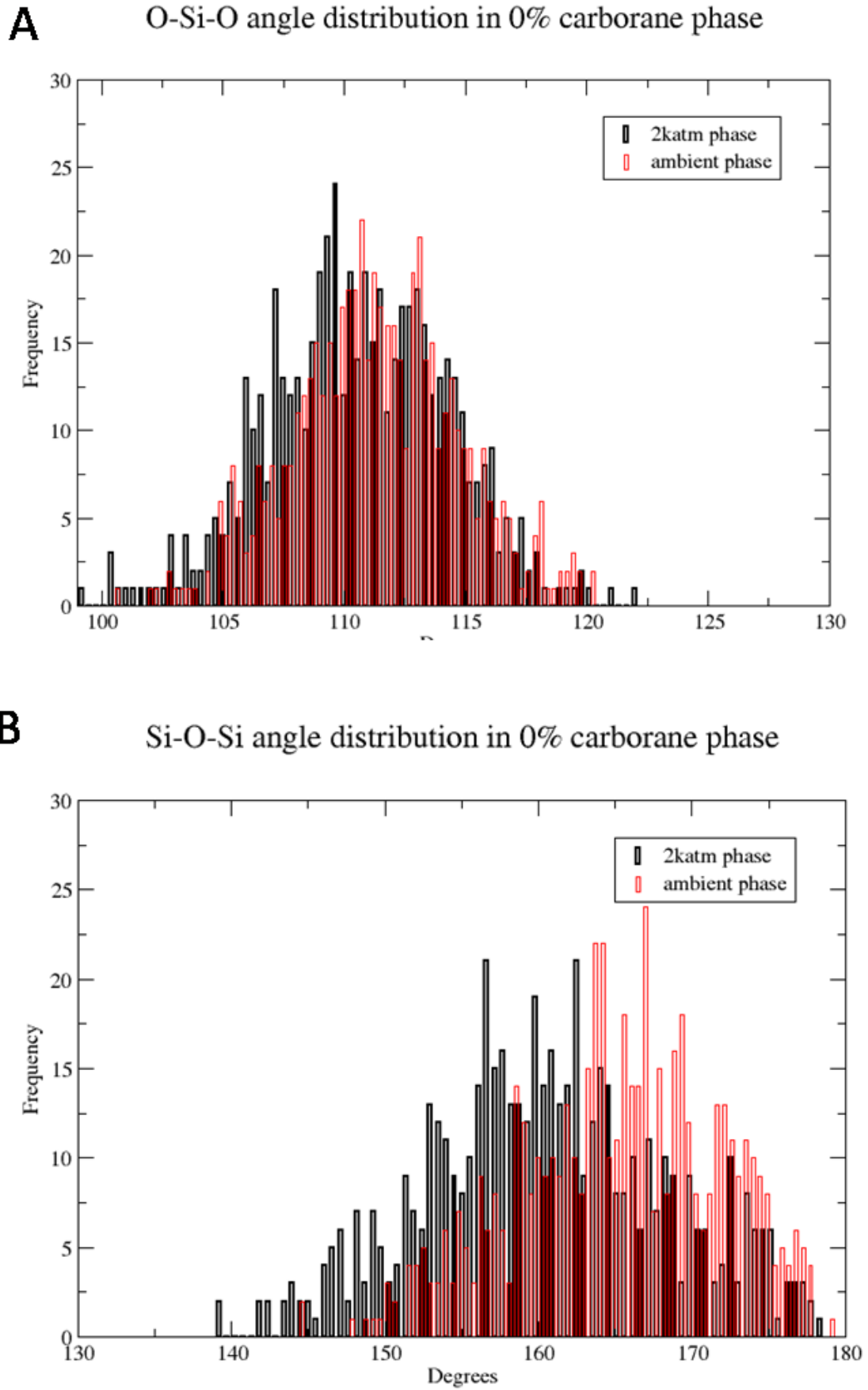
Figure 39. O-Si-O, and Si-O-Si angle histogram changes at high pressure.

The Si-O-Si angle of siloxane polymers is remarkable[122], in that there is an accepted broad range of angles, from 110-180˚, which is the source of many of their interesting properties, due to the flexibility of the strands. It is unsurprising then, that there appears to be a shift in peak for this distribution upon applying high pressure.

The RDF plots for polymer phases contain less data, due to the amorphous nature of the systems, meaning the likelihood of an atom being in a position at an intermediate distance is effectively 1. This "intermediate distance" varies between atomic characterisations, but is typically 5-7Å. However, a shortening of second coordination sphere distances (i.e. 3-4 Å) is evident in some cases, as seen in the following figures.
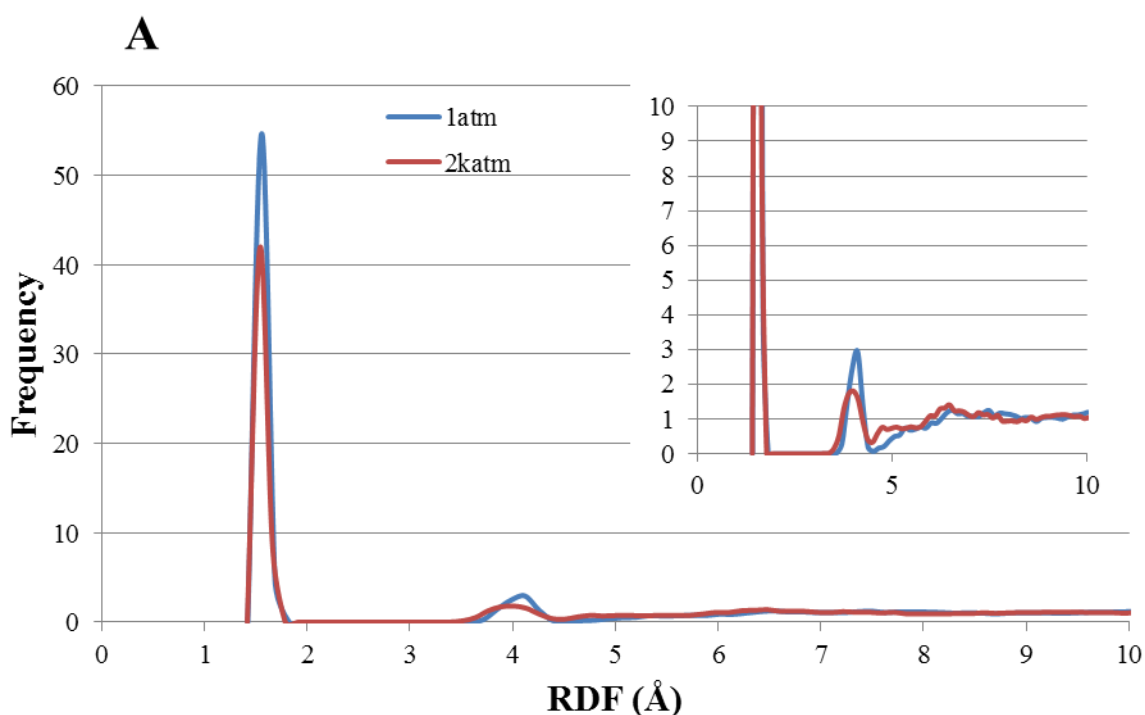
Figure 40. RDF data for key interactions in 0% carborane content phase. A: Si -O RDFs for pure siloxane at varying pressure, B: C-H RDFs for pure siloxane at varying pressure, C: Si-C RDFs for pure siloxane at varying pressure. Inset shows zoomed in spectra.
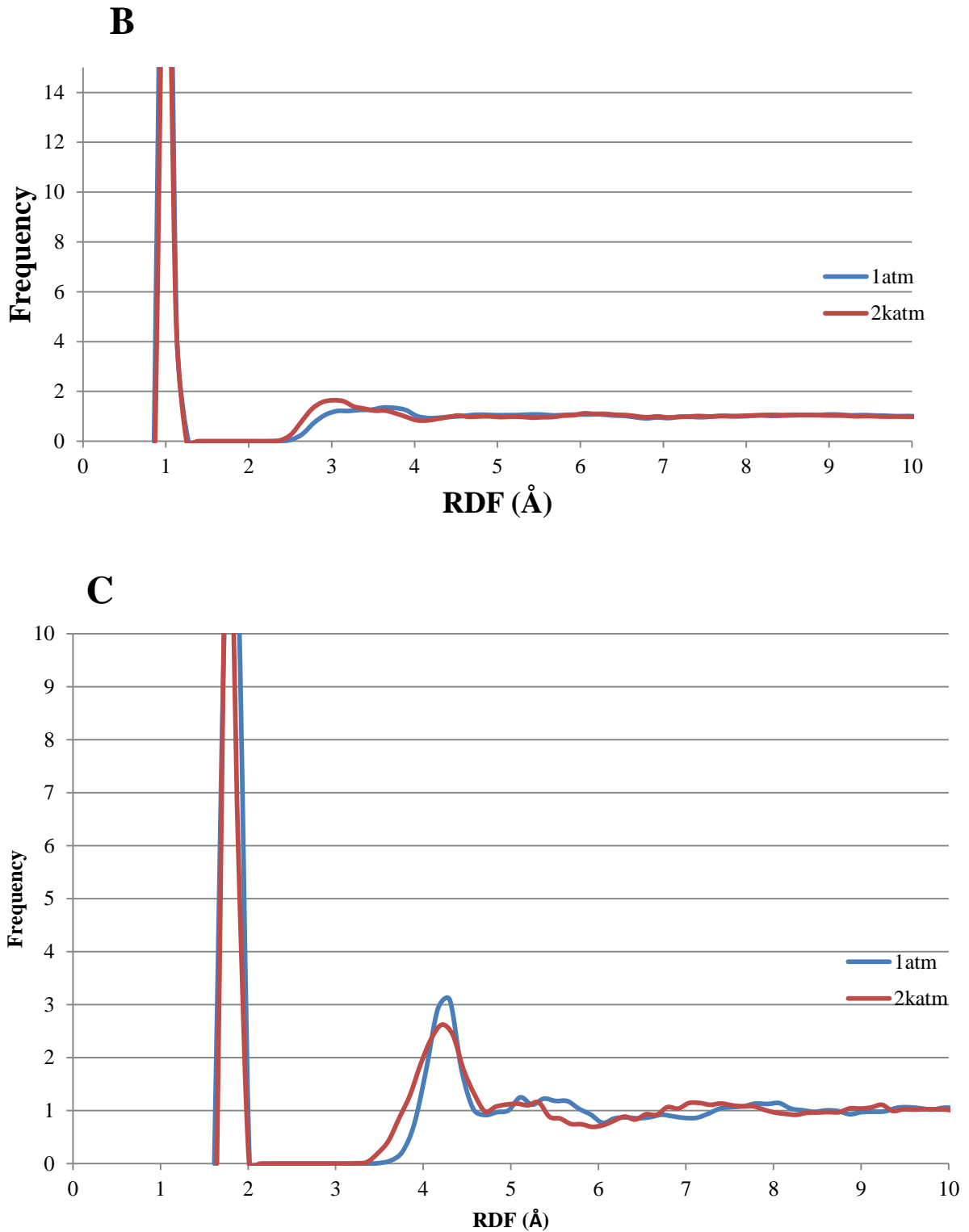
Figure 40. RDF data for key interactions in 0% carborane content phase.A: Si -O RDFs for pure siloxane at varying pressure, B: C-H RDFs for pure siloxane at varying pressure, C: Si-C RDFs for pure siloxane at varying pressure

As can be seen in Figure 40, at 2katm, bonded distances typically have a narrower range, and shift to slightly shorter distances, which is predictable in a more constrained system. Meanwhile, there is a more qualitative change in second order distances, referring to interactions with atoms on neighbouring silicon atoms of the same strand, i.e. **Si**-O-Si-**O**, or **Si**-O-Si-**C**. This therefore correlates to the reduction in Si-O-Si bond angle. In the case of 100% carborane content, the **Si**-O-Si-**O** interaction at ≈ 4Å is absent, as seen in Figure 41B.
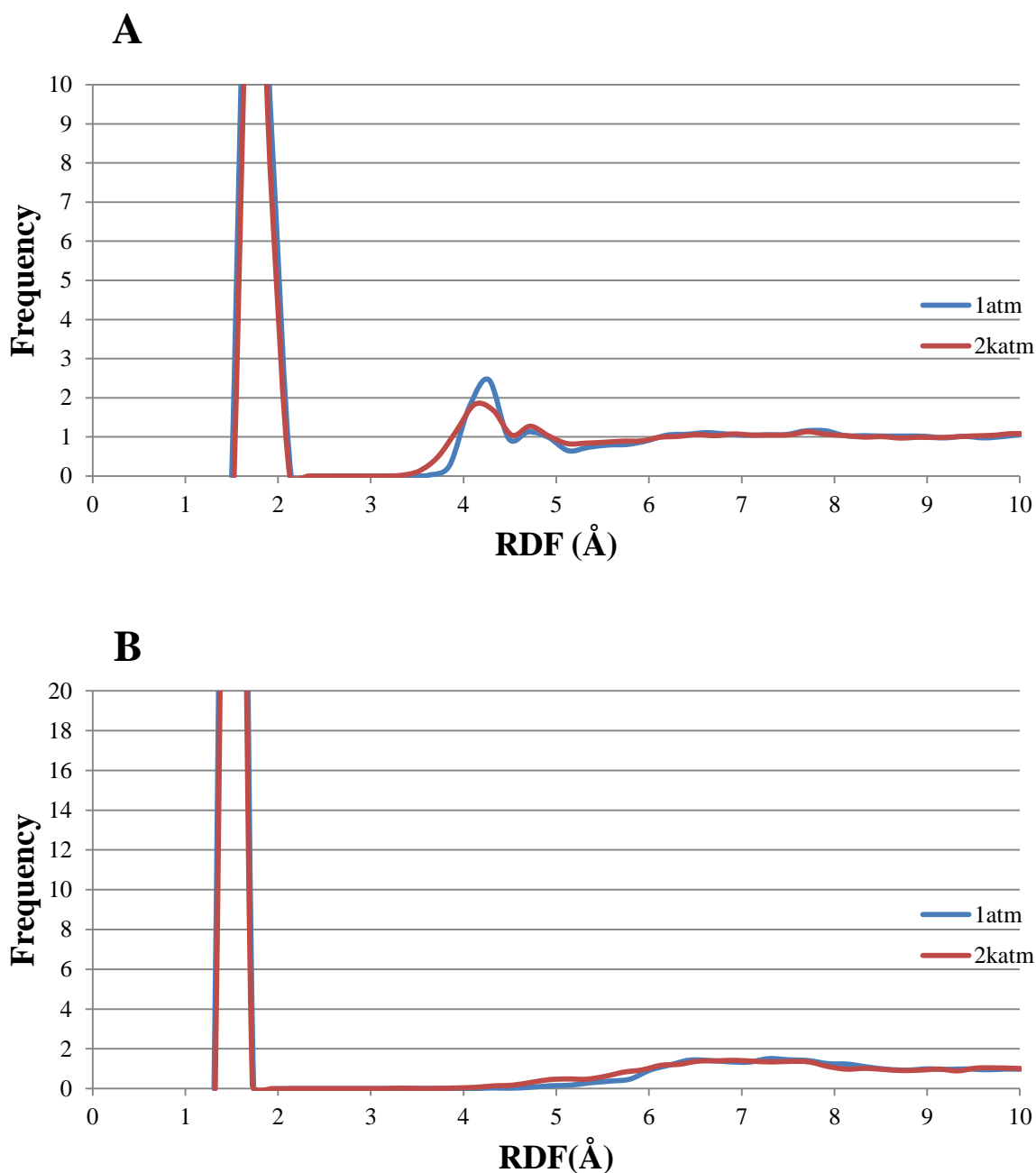
Figure 41. RDF data for key interactions in 100% carborane content phase.A: Si-C RDF; 100% carborane content, B: Si-O RDF; 100% carborane content

The torsions in polymer strands are analysed in Figure 42; at ambient pressure the O-Si-O-Si torsion has a large peak at 180˚, whilst at high pressure the distribution is perhaps more evenly spread, and for the X-Si-O-Si (where X refers to carbon or hydroxyl oxygen) the change from ambient to high pressure sees a slight reduction in ≈120˚, and a slight increase in ≈0-30˚ angles. This may be an indication of the way in which high pressure is accommodated; strands assume a more random orientation, to make a better use of available space, allowing a volume change without a corresponding change in energy. This is available due to the large, flexible bond angle of Si-O-Si about which there is fairly free rotation[123]. This will in turn, contribute to the low bulk modulus observed for siloxane polymers. However, there is not a large enough quantitative change to be make a definite conclusion.

A O-Si-O-Si angle distribution in 0% carborane phase
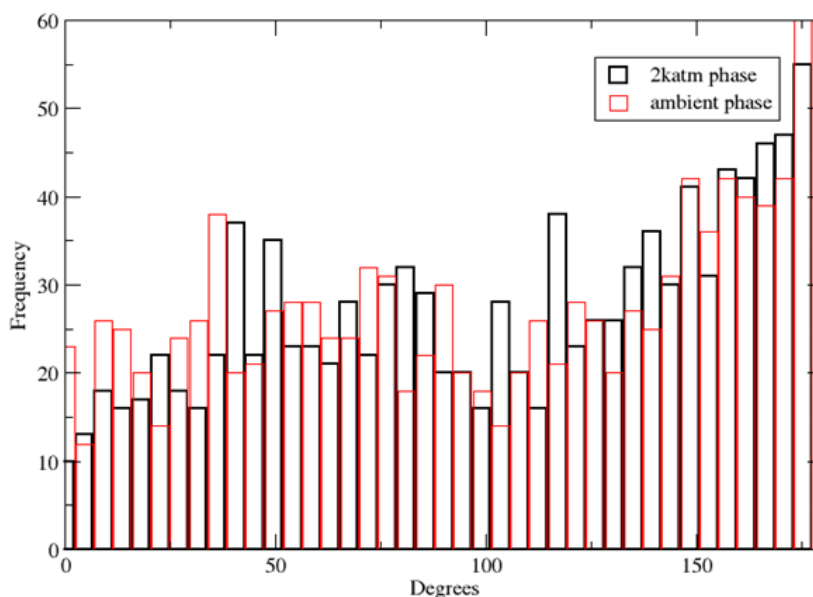
B X-Si-O-Si angle distribution in 0% carborane phase
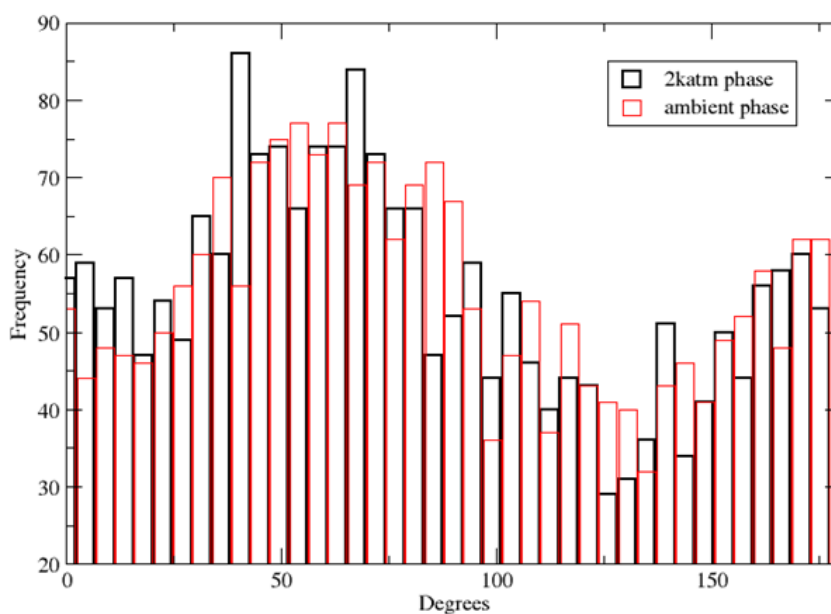
Figure 42. A: O-Si-O-Si, and B: X-Si-O-Si dihedral histograms for 0% carborane phase

Figure 43 shows the corresponding results for 100% carborane substituted polymer, where the ordering of Si-O-Si-O torsions can no longer occur. The equivalent Si-O-Si-X (where X refers to cage carbon) torsion again shows a qualitative change under high pressure, in which the graphs are more flat: peaks are decreased, and troughs are increased.
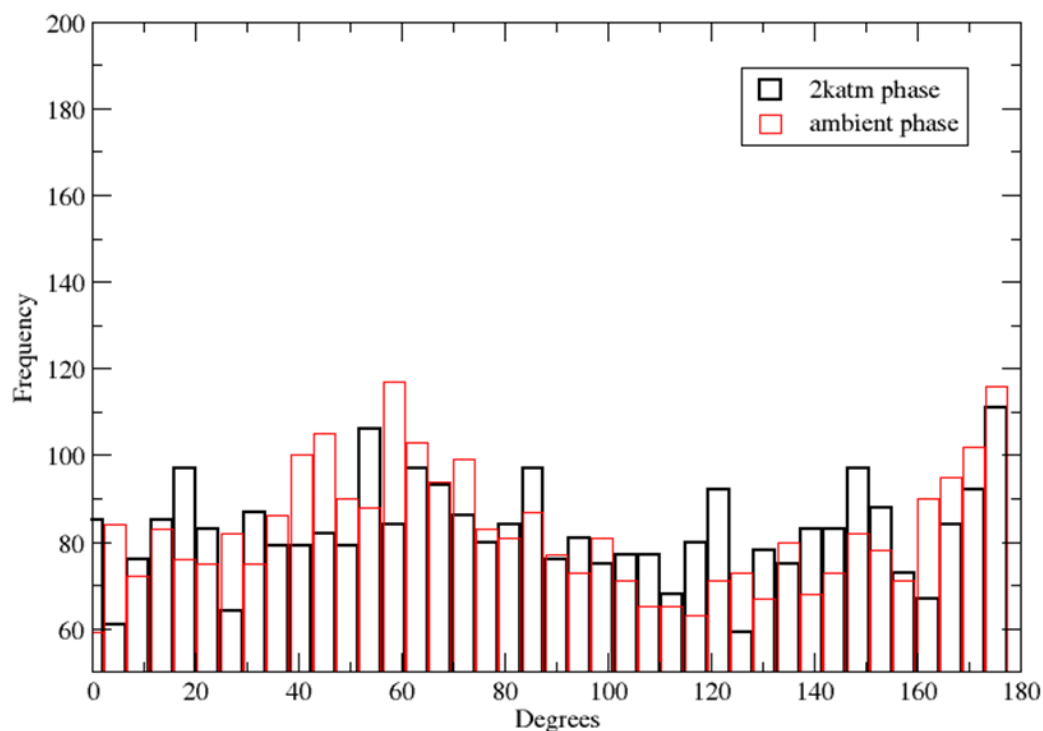
Figure 43. X-Si-O-Si dihedral angle change at high pressure for 100% carborane content at medium-strand phase

As discussed, with the introduction of more bulky carborane cage units, and the removal of the labile O-Si-O-Si torsions, the ordering of strands is perhaps less available, which could lead to a higher bulk modulus.

The angular distribution data is also of interest for the 100% carborane example, where the O-Si-O angle had been one of the key accommodators of volume change in the 0% carborane content example:

A

B
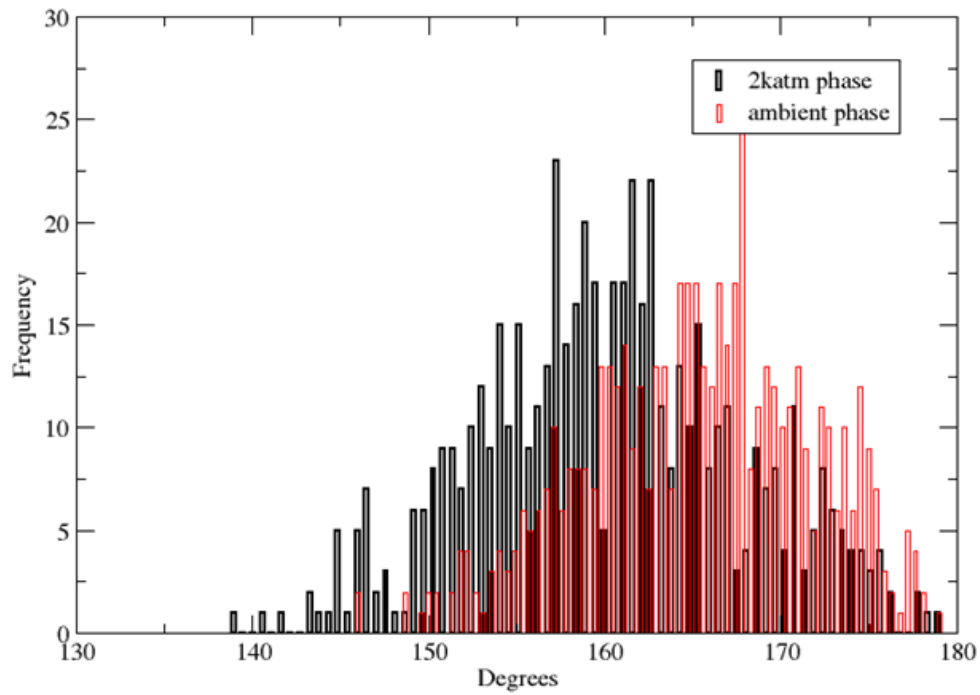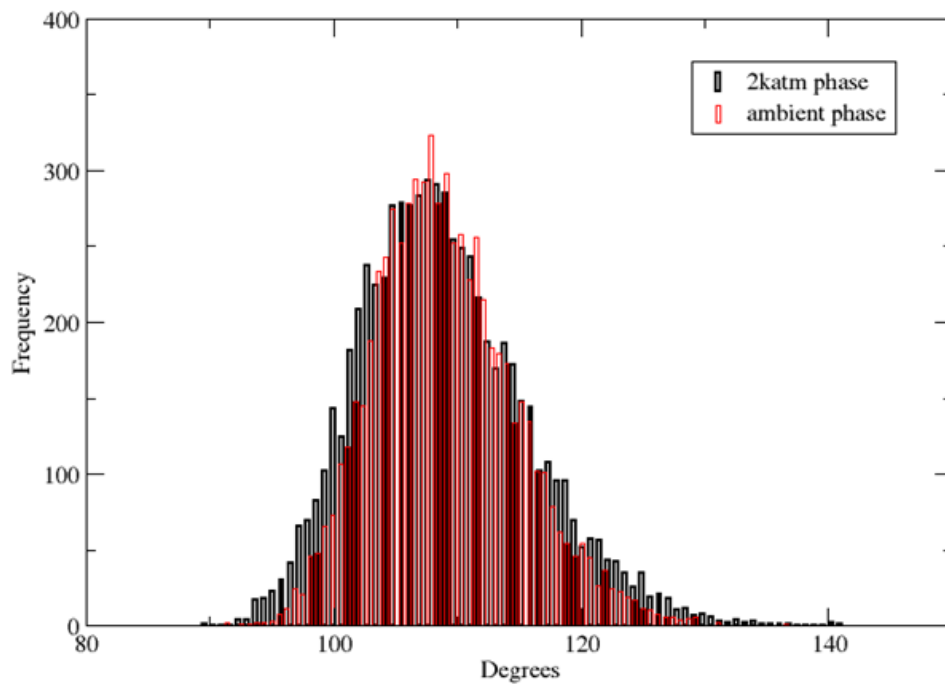
Figure 44. Angle distributions in 100% carborane content phases

Figure 44 shows there is a slight broadening in the range of C-Si-X angles, under high pressure, suggesting that this could be a way in which volume change is accommodated, alongside the expected downward shift in Si-O-Si angles. However, the absence of flexible Si-O-Si angles, and O-Si-O-Si torsions, is suggested as the root cause of the higher resistance to volume decrease, and consequently a higher bulk modulus in the high carborane content phases.

The response on returning to ambient pressure is also of interest, to see how reversible the process is. The results of performing 10 ps runs (1 femtosecond timestep, NPT ensemble and 1.5 ps thermostat and barostat control) on medium-strand polymers are shown in Figure 45, showing an almost complete return to ambient cell volume.
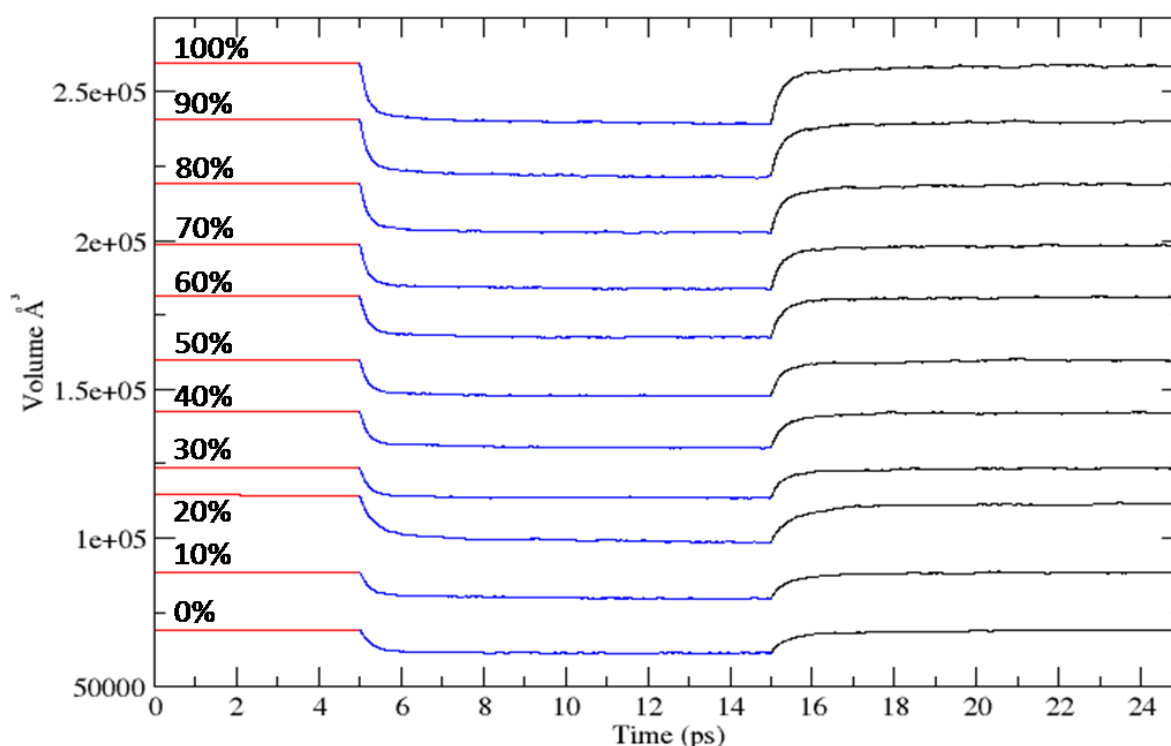
Figure 45. Effect on cell volume of varying pressure in medium-strand polymer phases. Degree of carborane content indicated on left hand side of graph .0-5 ps: 1atm, 5-15ps: 5katm, 15-25ps: 1atm.

The % change in cell volume following the pressure cycle is given in Table 7. Clearly, this is a reversible process, except in the case of 20% carborane substituted polymer phase, which had unrealistic vacant pockets in the phase. Therefore, pressure cycling may be a route to eliminating pockets in phases containing excessive free volume.

Table 7. Polymer cell volumes after high pressure MD is returned to ambient pressure	
% carborane substitution	Cell volume as % of original cell volume, after pressure cycling (±0.5)
0	99.8
10	99. 9
20	97.5
30	100.0
40	99.8
50	100.0
60	99.8
70	99.9
80	99.8
90	99.7
100	99.6

4.2.3.3   Thermal expansion coefficient as a function of *m*-carborane content

A further use of molecular dynamics calculations to predict macroscale properties is in thermal expansion coefficient (T_c) calculations. The molecular dynamics bulk modulus calculation process was repeated (1 femtosecond timestep, NPT ensemble and 1.5 ps thermostat and barostat control), except pressure is kept at 1atm and temperature is varied, with volume calculated at ambient (1atm) pressure, with varying (298, 348 and 398K) temperature, after 20 ps. The results are shown in Figure 46, and it is clear that a linear fit is applicable at each composition.
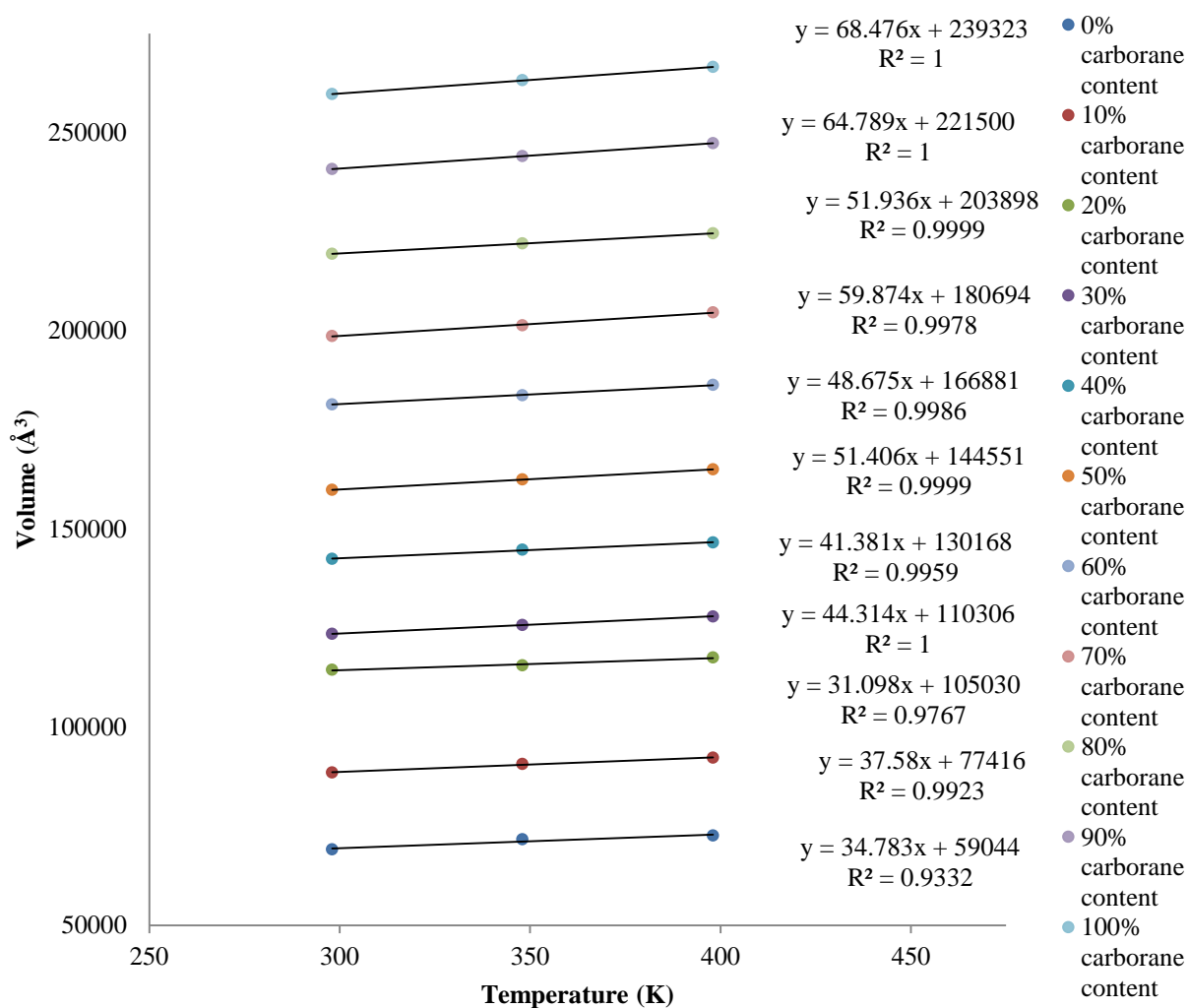
Figure 46. Thermal expansion coefficient derivation for medium-strand polymer phases: Volume vs temperature. Legend indicates carborane substitution.

Taking the gradient of the graphs in Figure 46 allows the calculation of thermal expansion coefficient, using Equation 4.6.

$$T_c = \frac{1}{V}\frac{dV}{dT}$$

Equation 4.6
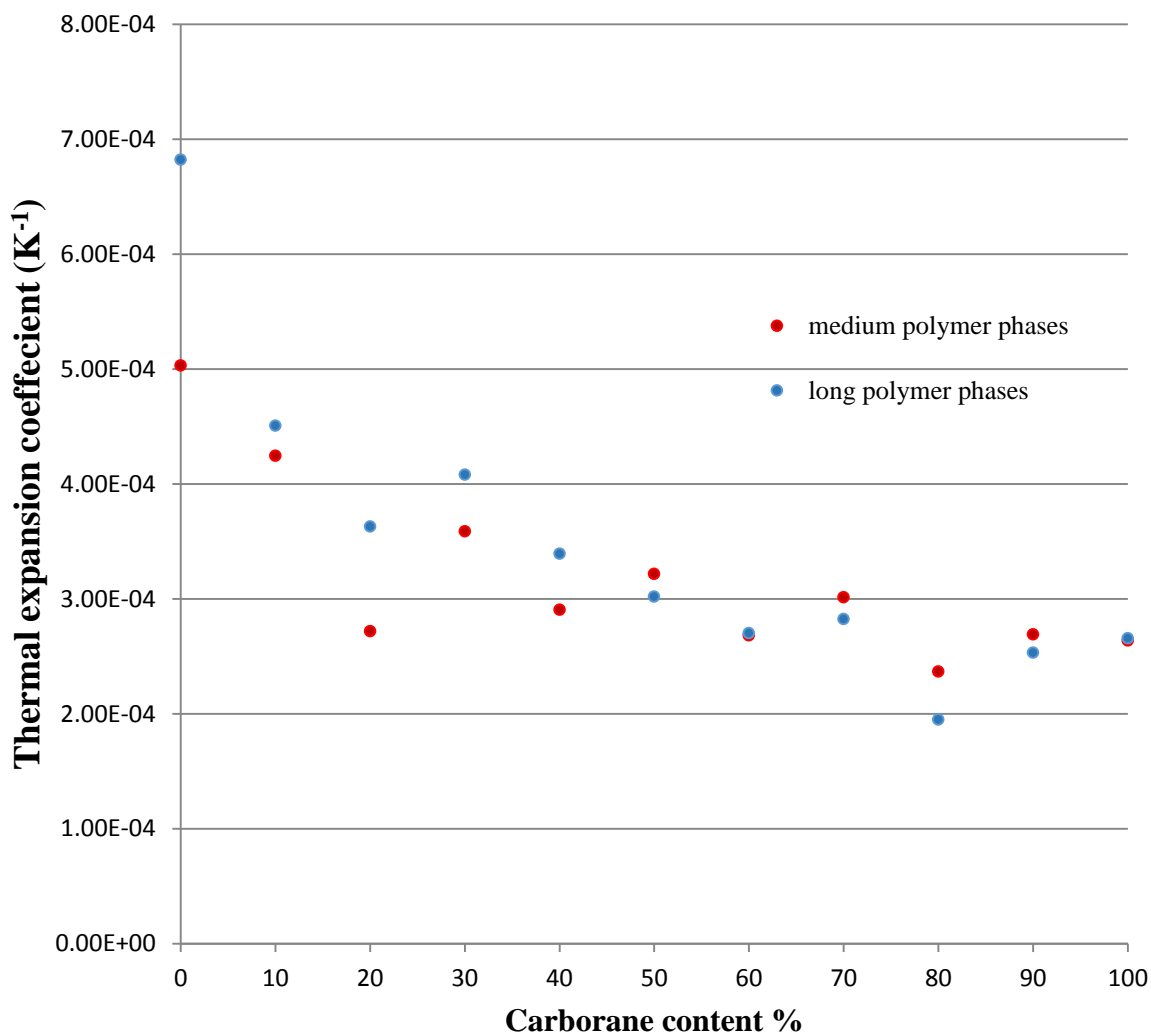
Figure 47. Calculated thermal expansion coefficients, for medium and long strands polymer phases, with varying carborane content, at 1 atm pressure, 300-400K. Fitting to a logarithmic function R2<0.6, so not included

The T_c for pure siloxane in this calculation is 5.03 x 10^{-4} K^{-1}, whilst experimentally[53]; the value is 3.19 x 10^{-4} K^{-1}, or 9.07 x 10^{-4} K^{-1} at low pressure[36]. Our value falls within the between these values, and the simulation was repeated at 0 atm, as this may be relevant to the low pressure experiment, producing a value for T_c of 8.23 x 10^{-4} K^{-1}, which is in good agreement. Meanwhile, for ≈ 50% carborane content, experimentally the ambient pressure T_c

is 1.28 x 10^{-4} K^{-1}, whilst theoretically is 2.84 x 10^{-4} K^{-1}, suggesting that the ambient pressure calculations slightly over-predict experiment, whilst reproducing the trend of roughly halving T_c by introducing 50% carborane monomers.

The full set of results for low pressure thermal expansion is given in Figure 48.
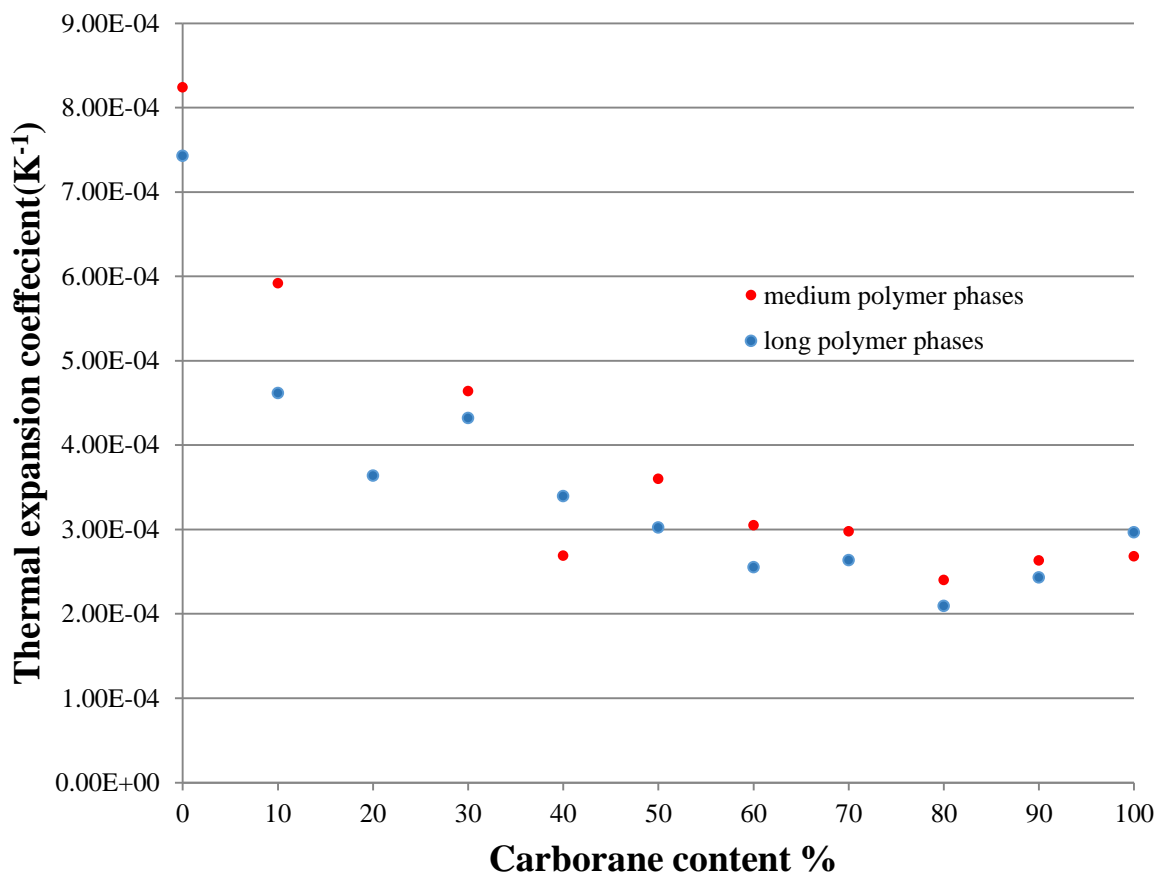
Figure 48. Calculated 0 atm pressure thermal expansion coefficients, with varying carborane content. Anomalous 20% medium strand value omitted.

The combined data show that the experimental values are fairly well reproduced, for 0% carborane, and that there is less of an effect of pressure on T_c for high (<50% carborane content) polymer phases. The reduced T_c with increased carborane content could be as a result of carborane units acting as "heat sinks": the extra potential energy supplied by heat is stored in the vibrational modes of carboranes[2,124]. Thus, the phase volume and inter-strand distances of high carborane content phases are less affected by temperature, leading to a reduction in temperature dependent physical properties, such as expansion[2].

Finally, the response to cooling of polymer phases is an indication of glass transition temperature (T_g), which controls a lot of material properties. At temperatures above T_g, contraction will be swift; whilst below, contraction of cell volume will be sluggish, as there is

insufficient kinetic energy to overcome barriers and arrive at thermodynamically preferable states. This was investigated by cooling the output structures from 298K simulations to a series of lower temperatures, producing the graphs shown in Figure 49.
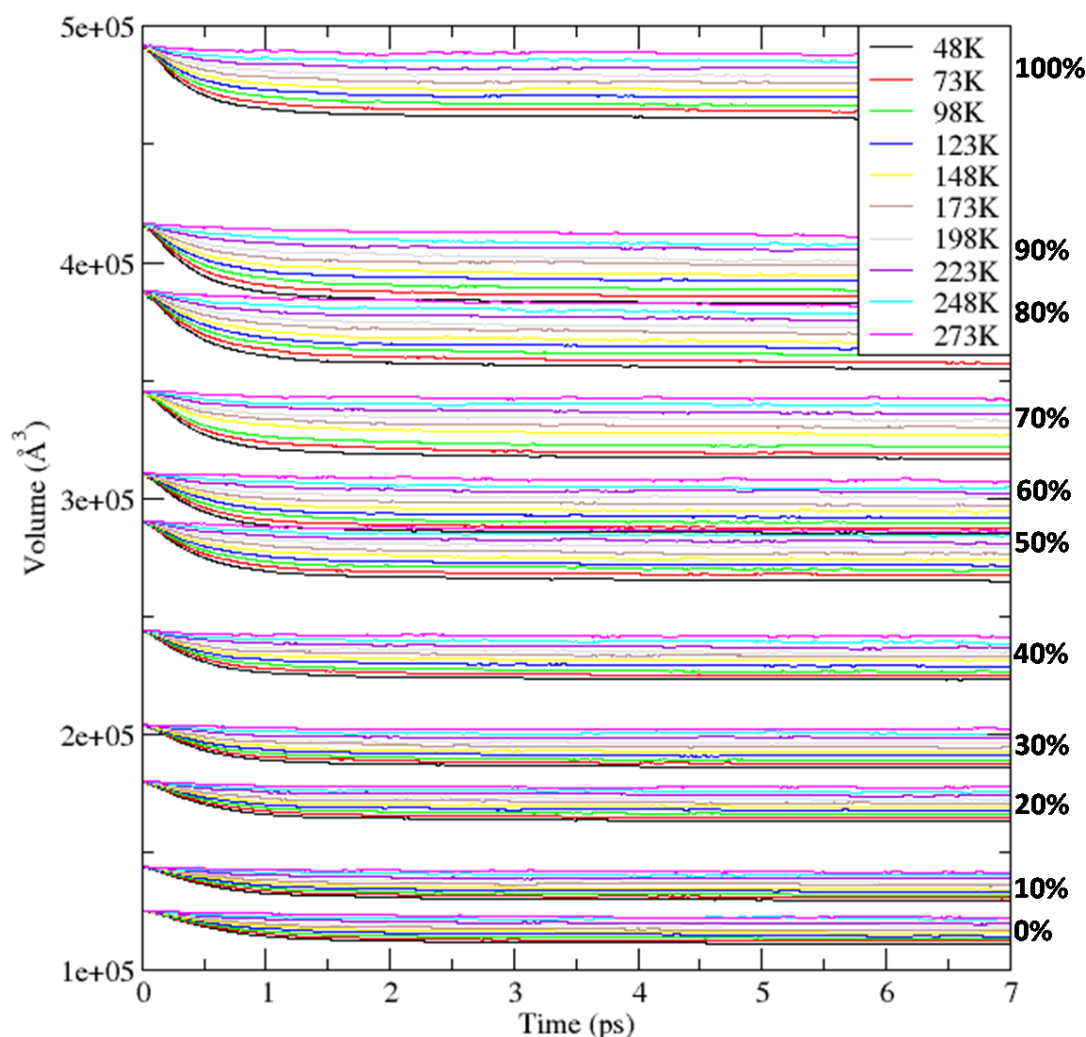
Figure 49. Medium-strand polymer phase volume against time for a range of temperatures (in steps of 25K). Carborane content indicated on right hand side of graph

As can be seen in Figure 49, as temperature is lowered, the rate at which phase volume stabilises changes. However, trying to find the "time taken for cell volume to stabilise" at different temperatures was non-trivial; the choice of cutoff, Z, in -Z≤M ≤ Z, is arbitrary, and can lead to a large range in results, taking M from Equation 4.7. (i.e. finding where the cell volume has stabilised, and volume vs time is flat. Y=volume and X=time).

$$y = Mx + C$$

Equation 4.7

It was consequently decided to investigate the glass transition temperature using free volume sampling, by taking snapshots of the cooled output structures, which will be detailed in the following section.

4.2.3.4   Free Volume in polymer phases; glass transition temperature

One method of extracting the glass transition temperature (T_g) from a polymer is through free volume sampling; free volume will increase linearly with increasing temperature, but there will be a difference in rate above and below T_g; above T_g the strands will be much more mobile and be more responsive to increases in temperature.

Free volume was sampled using a python script[1], which estimated free volume by inserting a point randomly into the polymer system and checking if there is overlap with any atom's VDW radii. Free volume %, is the amount of non overlapping points divided by the total points * 100. The accuracy of the free volume estimate is therefore dependent on the amount of points used, which is summed up in Figure 50.
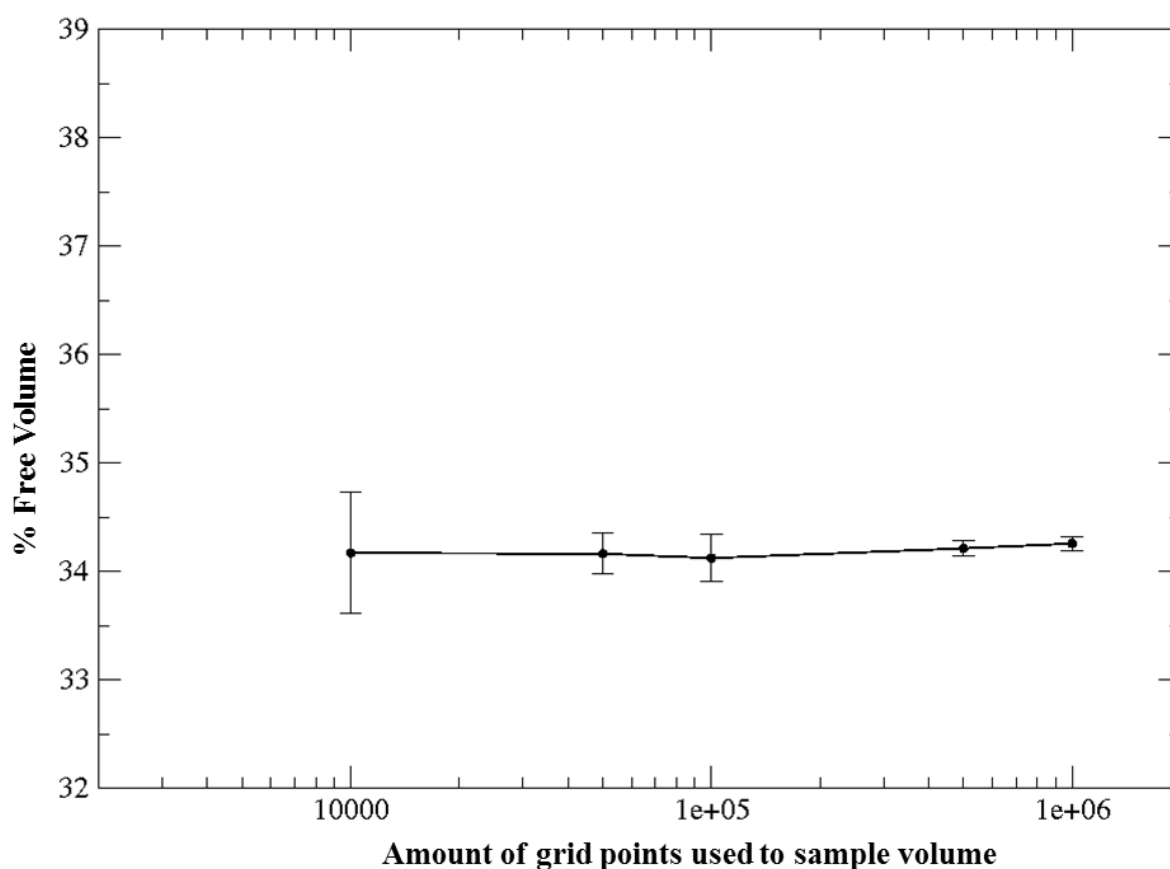
Figure 50. Free volume estimated on 100% carborane content, ambient (298K, 1atm) conditions system, against number of sample points. Data points are mean of 10 results, error bars are 1 standard deviation in the 10 results

Given these results, 1 million dots were judged sufficient for sampling polymer systems with approximately the volume/density of the standard system (100% carborane content at ambient conditions).

The program took ~6 hours to run on 1 core, which is a little unwieldy, and it was judged that using the "random" module in python, and coding in python itself, were the reasons for such a long run time. As a result, the program was rewritten, so that points were inserted along a grid of user specified fineness, and was converted to C++. These changes allowed a significant speed-up, as seen in Figure 51.
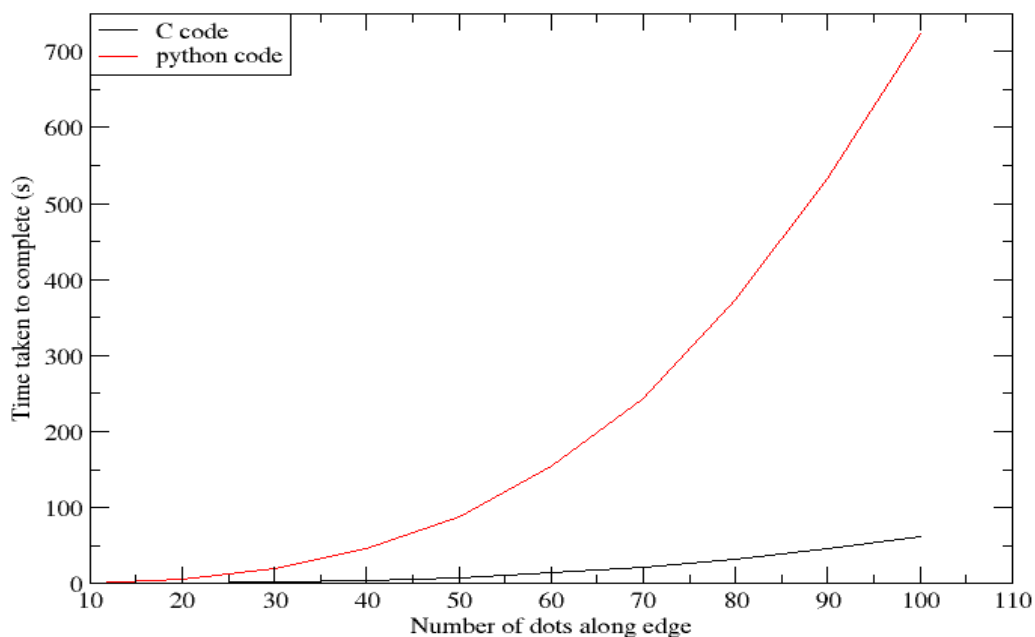
Figure 51. Machine time against grid fineness, for the python and C++ free volume programs, using grid points rather than random points.

So for a dots/edge of 100, this equates to a million points, which takes ~1 min. The results generated by the python and C++ codes are the same, since the grids are equivalent, and the optimisation of free volume % estimation is given in Figure 52:
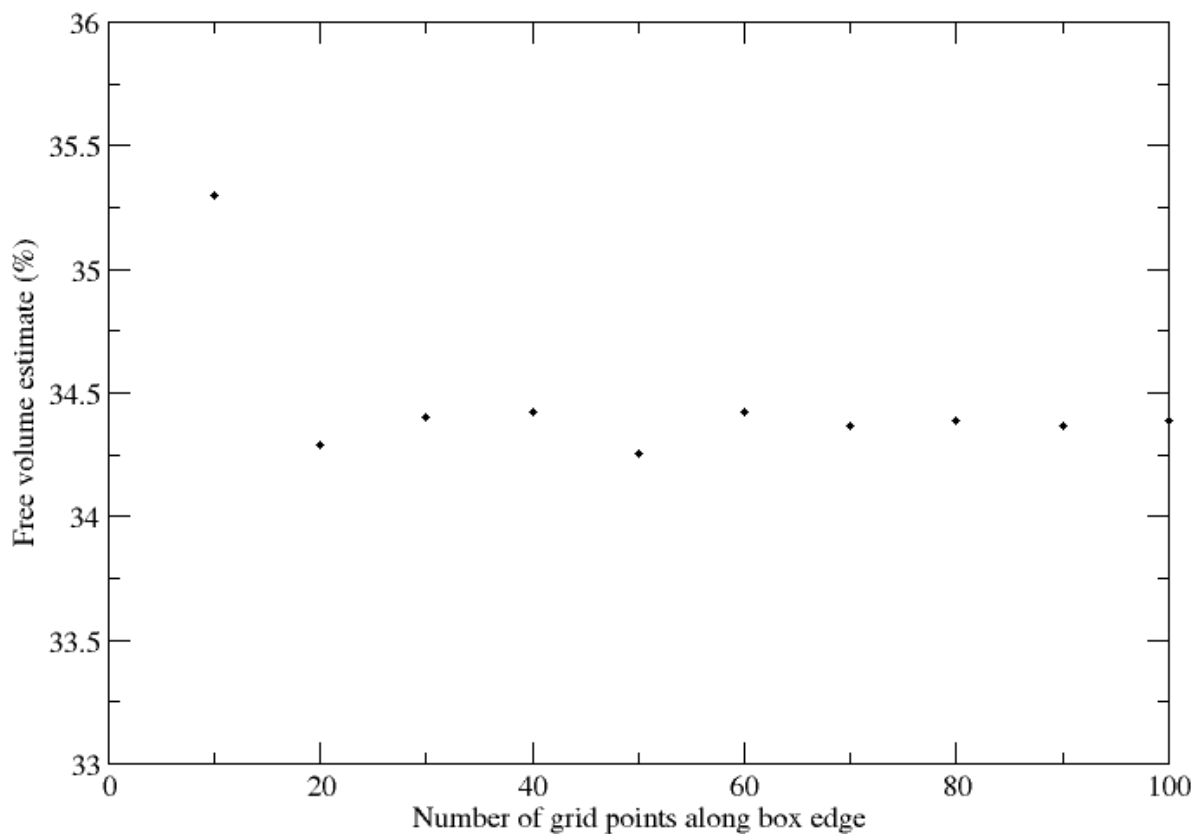
Figure 52. Free volume % estimation using different levels of grid fineness, for 100% carborane content at ambient conditions polymer example, showing the optimisation of the grid

A visualisation of the technique is given in Figure 53. For comparison, the same system was run on Materials Studio[109], which also uses a grid method, completing in ~40s, and giving a free volume of 34.8%, which is equal to the value found in this technique.
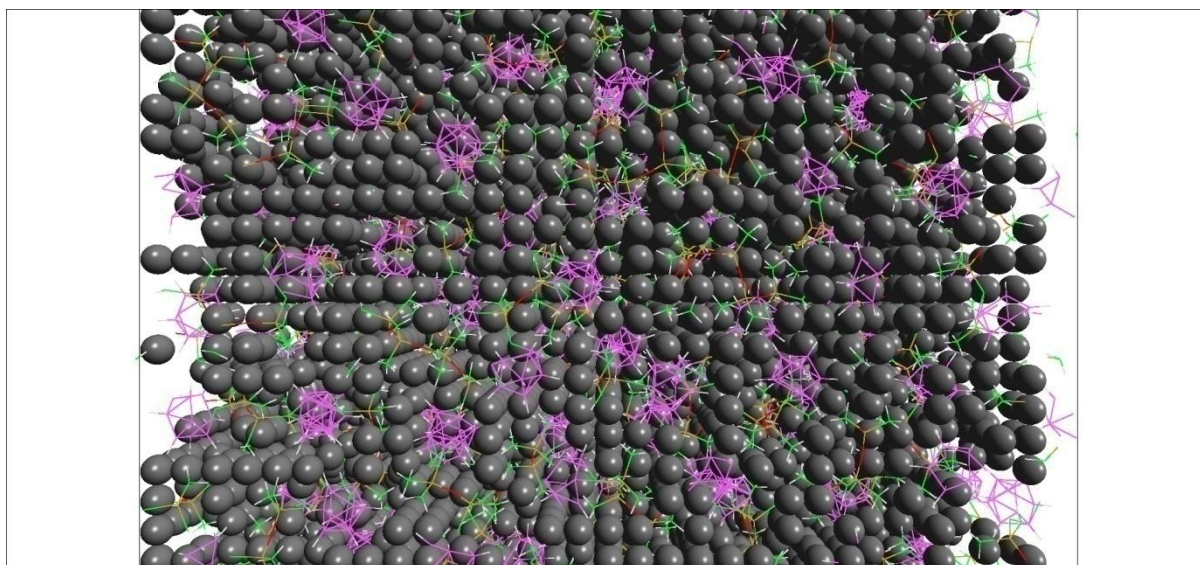
Figure 53. Free volume estimation visualisation; non-overlapping grid points depicted with grey spheres

Another advantage of this technique is that it allows a quick estimate of void volume and distribution. A second loop looks at non overlapping points and checks that their surrounding points do not overlap with the polymer, and repeats for those points, until all atoms are selected for a void, enclosed on all sides by polymer atoms. Void volume is then the sum of all the points' volumes, treating them as cubes with edges equalling the distance between points. A picture of void volume distribution is then built up, which can be related directly to the PALS experimental results discussed in Section 1.4.1.

The results for free volume % calculation in long-strand polymers discussed in this section are given in Figure 54.
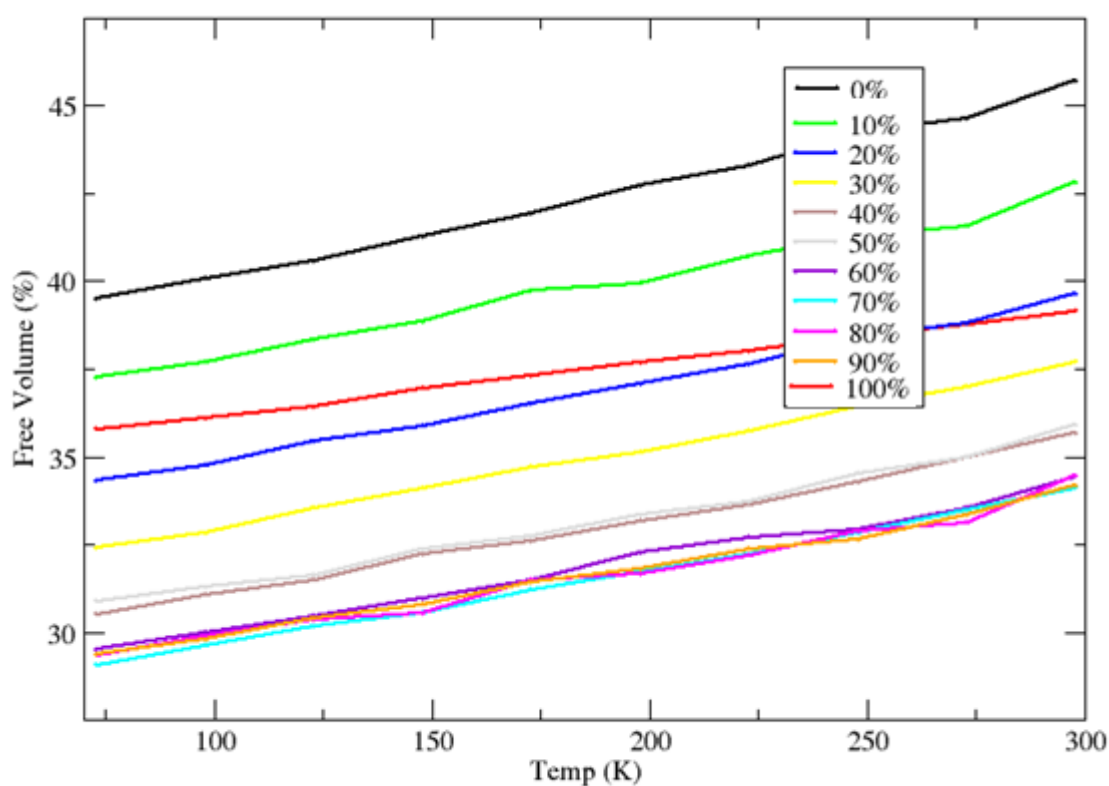
Figure 54. Free volume against temperature for long-strand polymer phases, with plots representing different carborane content as shown in the legend.

As can be seen, with increasing temperature, free volume % increases as expected. However, this effect occurs at a slower rate with increasing carborane content, the 100% carborane content example is anomalous, in that it is ≈ 5% higher overall than the trend would suggest; increasing carborane content does not appear to affect free volume above 60% carborane content, except for the 100% case. This is as a result of the uncharacteristically low density for this phase, with one large gap accounting for a large

amount of free volume. Nevertheless, the rate of change is lower for this example, as expected. This is of course directly related to the thermal expansion coefficients discussed in Section 4.2.3.3, which decrease with increasing carborane content.

The amount of volume accessible to a solvent molecule can also be simulated, by adding a radius term to the grid points, where points count as overlapping with an atom if the distance is less than the specified radius and the VDW radius of the atom. The effect of varying this radius is shown in Figure 55:
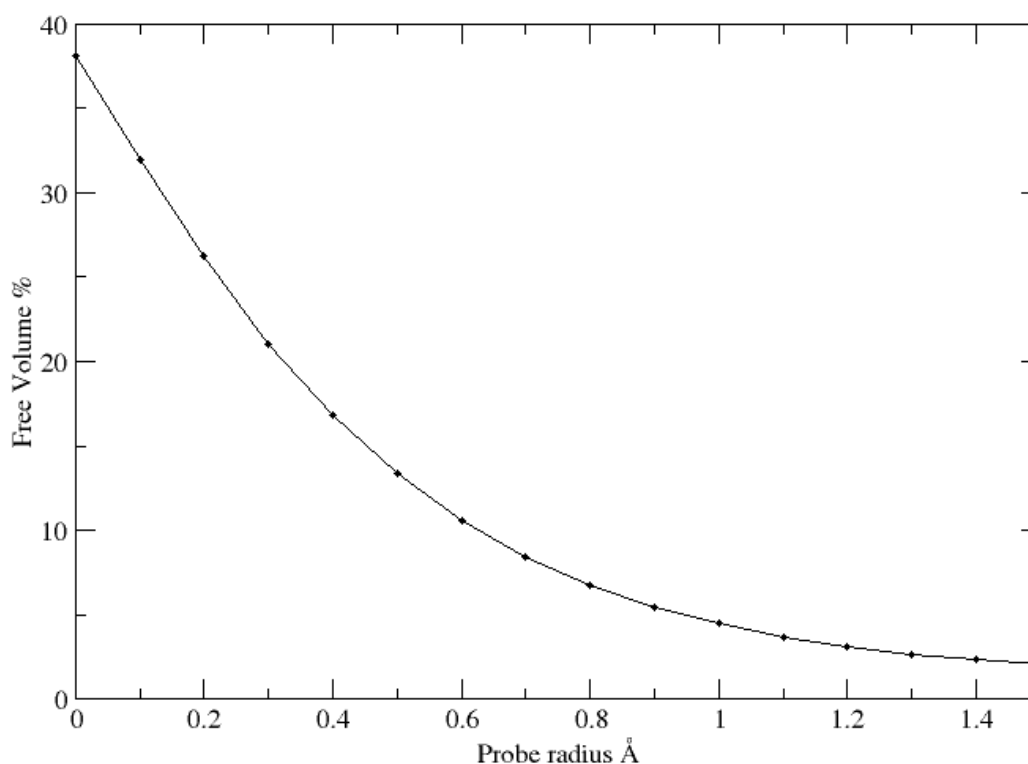
Figure 55. Probing free volume % available in example phase with solvents of varying radii, where grid density is 50 points per edge

This shows that with increasing solvent probe radius, the occupiable volume decreases sharply, as expected. For reference, the radius of a water molecule is $\approx$1.4Å[125], N_2 is $\approx$1.85Å, He is $\approx$1.3Å[126] etc. The latter is of particular interest within the context of this report, in that He is released following a neutron capture event in ^{10}B. Therefore, this gives an indication as to the likelihood of a space being available for Helium atoms produced by neutron capture events within a polymer phase. This returns to the definition of the material's desired properties in the introduction: it must be permeable to gases, particularly Helium, in order to avoid bubbles and cracking, once placed in industrial context.

Comparing the pure siloxane and 100% carborane data is instructive, and gives an idea of glass transition temperature (T_g), as shown in Figure 56.
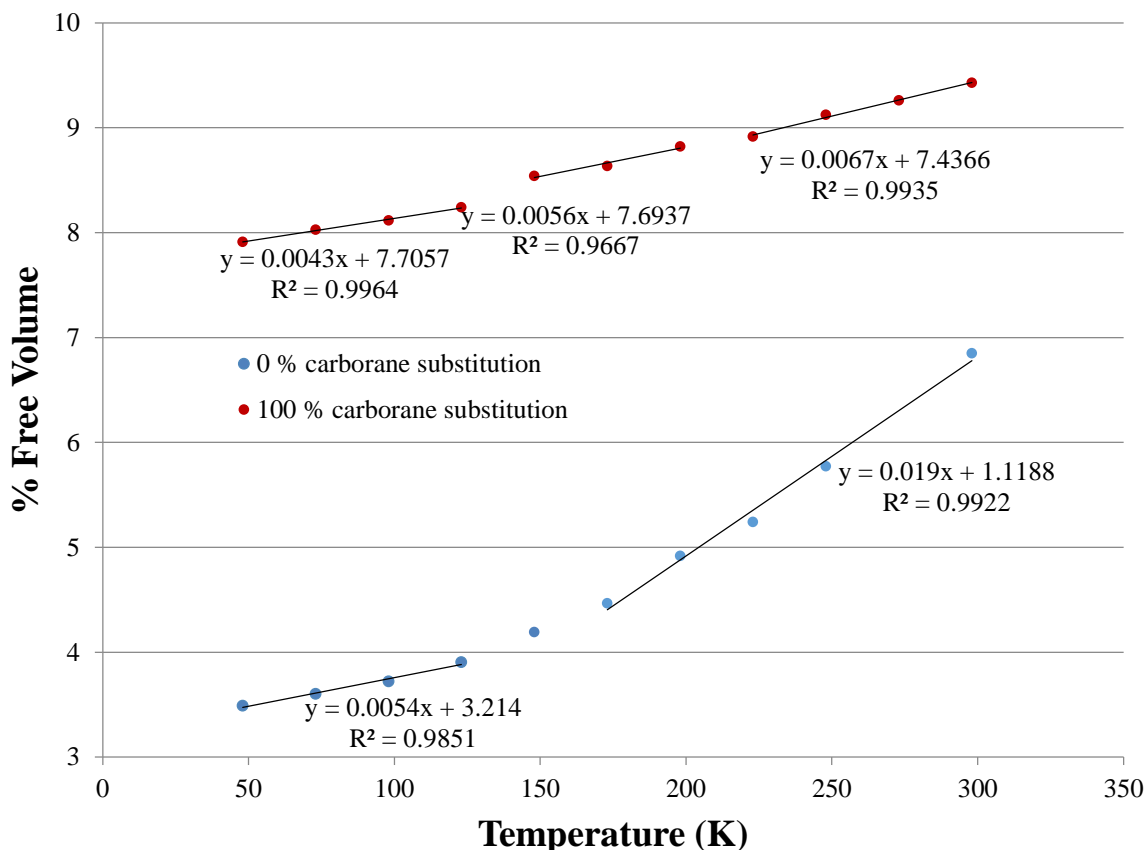
Figure 56. Free volume of pure samples as a function of temperature, using a water probe.

The experimental T_g is given as 148K, and at 150±12.5 K in the simulation results, for the 0% carborane content, or pure siloxane, phase there is a change in rate of free volume against temperature. This is indicative of a change from glassy to molten behaviour, and is also an indication of the lowest temperature at which the material can perform its function: i.e. it is required to be deformable within an industrial context, in order to accommodate helium gas bubbles for example. The 100% carborane example has a less obvious change in rate, which was expected from experiment[2], and from the lower overall thermal expansion coefficient calculated in section 4.2.3.3. There appear to be three behaviours, with gradually increasing rate with increasing temperature. While this could mean that there are two controls of glassy/molten behaviour, it is much more likely that the glassy transition temperature is found in the range 173-223K, and more data points are required to get a more certain result, which became computationally prohibitive. Nonetheless, an increase in glass transition temperature with carborane content as predicted by experiment is observed[53].

Of further interest are the histograms of void volume distribution, shown in Figure 57.
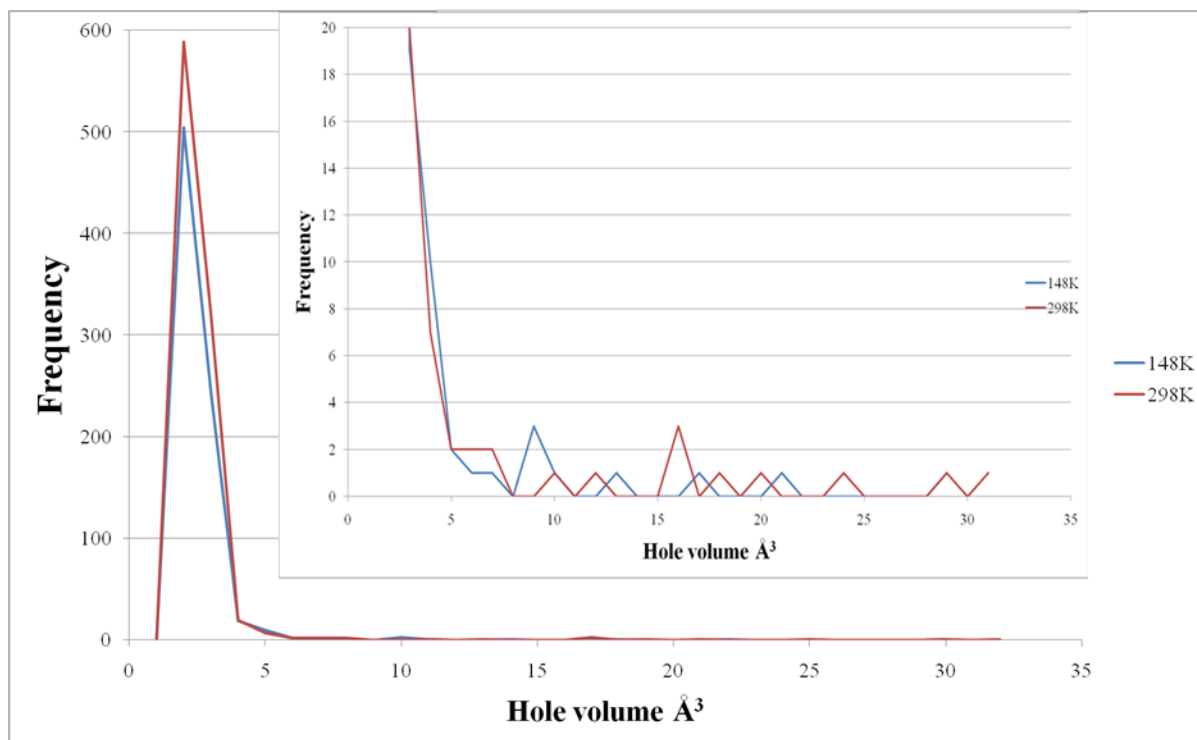
Figure 57. Change in void volume distribution at different temperatures for medium-strand 0% carborane content phase

This shows that fairly large (>8Å) pockets of free volume exist at low temperature, although predictably less than in the 298K case, suggesting that helium atoms can be accommodated into the structure even at low temperature, without cracking in the material, referring to the gas permeable quality desired in Section 1.1.1. This quality is also observed in the 50% carborane case, as seen in Figure 58.
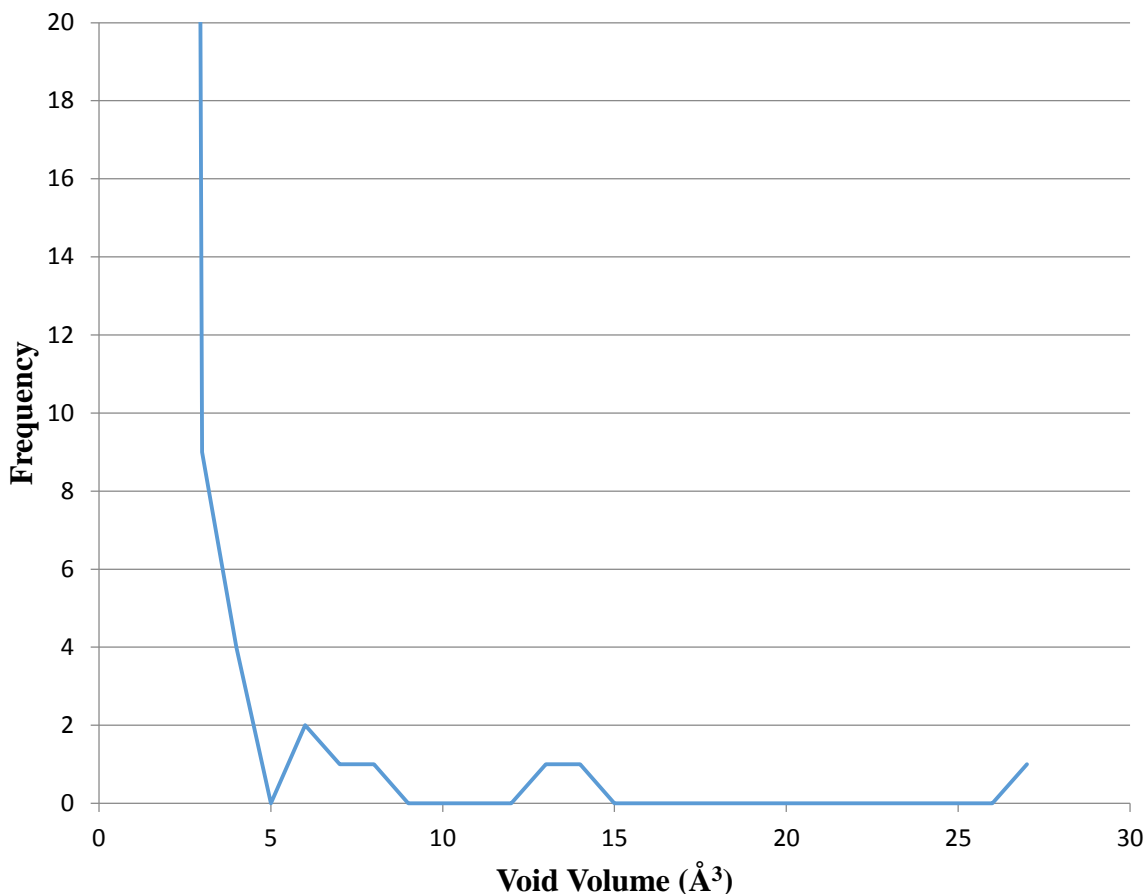
Figure 58. Void volume distribution of 50% carborane content phase at 148K. Peak at 2.1 Å has a frequency of 429.

Finally, taking the void volume distributions at 5ps later in the ambient conditions simulation and comparing the overlap of points with the original, 57.77% of points are present in both snapshots, suggesting that the pore distribution is fairly short-lived, that helium atoms can move through the polymer phase, and that the material is gas permeable. A plot of changes in void volume against time may be a useful avenue for further work. The pore distributions for the ambient conditions simulation at different times are shown in Figure 59.
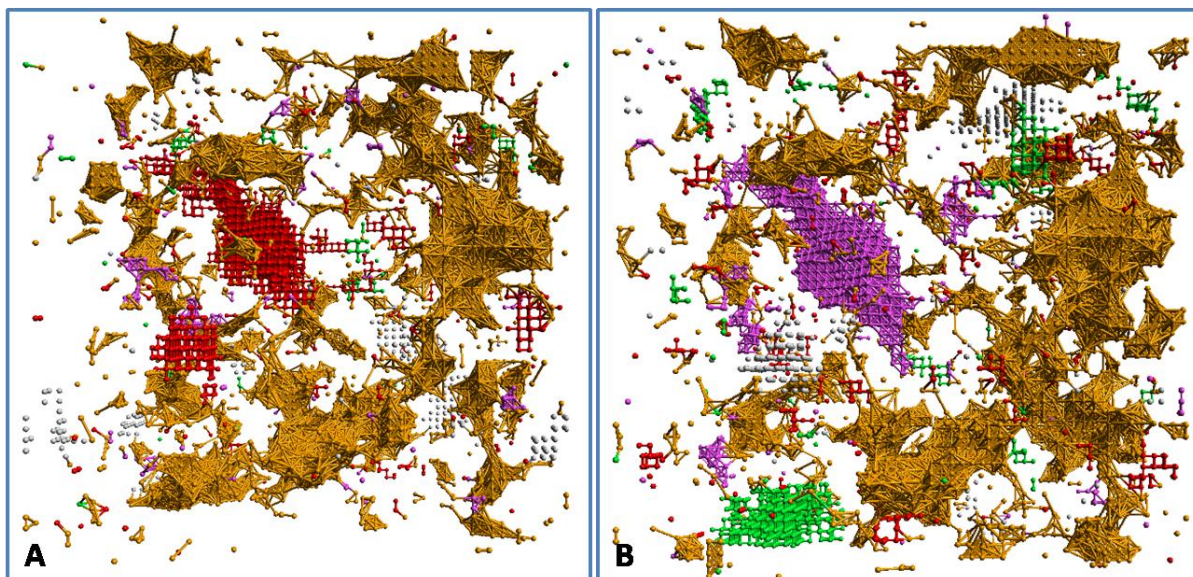
Figure 59. Pore distribution in ambient (1atm, 298K) MD simulation for 50% carborane content polymer phase, viewed along the +Z cell direction, at A: 20ps and B: 25ps in the simulation. Connected grid points are given the same colour, in order to differentiate between distinct pores.

4.2.3.5   Shear Modulus as a function of *m*-carborane content; manipulation of cell parameters

Another important property that can be extracted from stable polymer phases is shear modulus (G). This is a measure of how the material responds to a force parallel to one of its surfaces, whilst simultaneously experiencing a force in the other direction along the opposite surface. It is also defined as the ratio of shear stress to shear strain[127], where shear stress is the force applied (F) divided by the area parallel to the applied force (A), and shear strain is the deformation in the material due to the force (Δx), divided by the length of the surface perpendicular to the force (l). This is given in Equation 4.8 and Figure 60:

$$G = \frac{Fl}{\Delta xA}$$

Equation 4.8
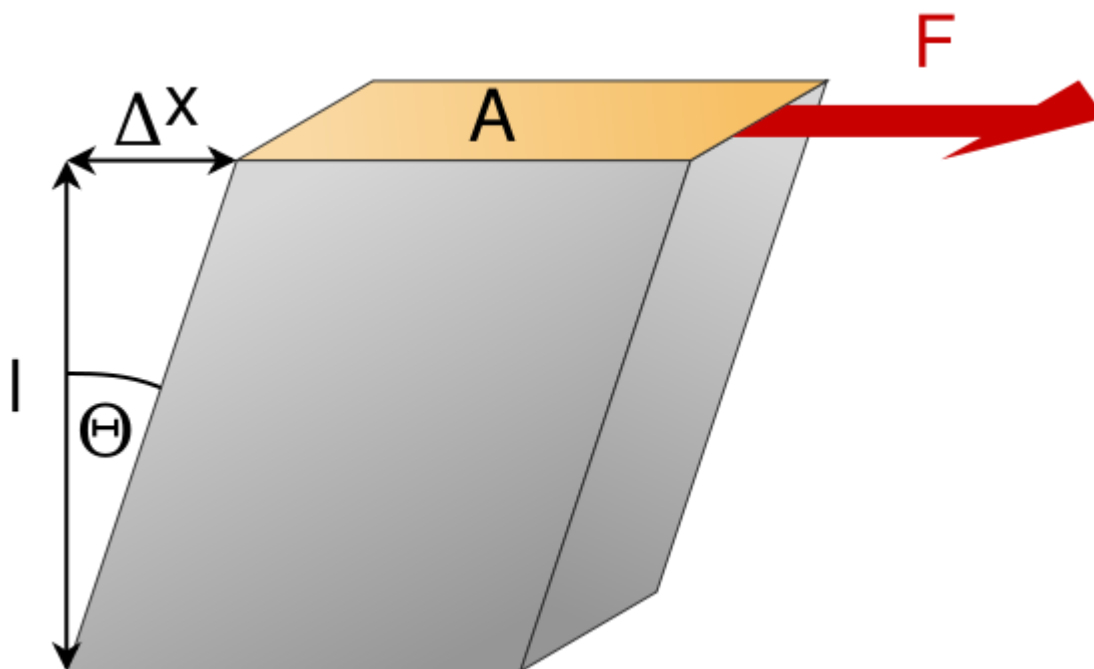
Figure 60. Depiction of shear modulus calculation. Image taken from Wikipedia[128]

This was calculated using a python program[1], by applying the deformation (in cell parameters, with atoms shifted correspondingly) and studying the change in energy. The deformation supplies l, Δx and A, whilst the force can be inferred by the change in energy; the energy required to deform the system will be the same as the change in energy between stable and deformed phases, through the conservation of energy law[129]. Force is therefore change in energy/Δx, giving force in J/m, or N. Varying theta between 90-95˚ gave the force vs deformation graph in Figure 61:
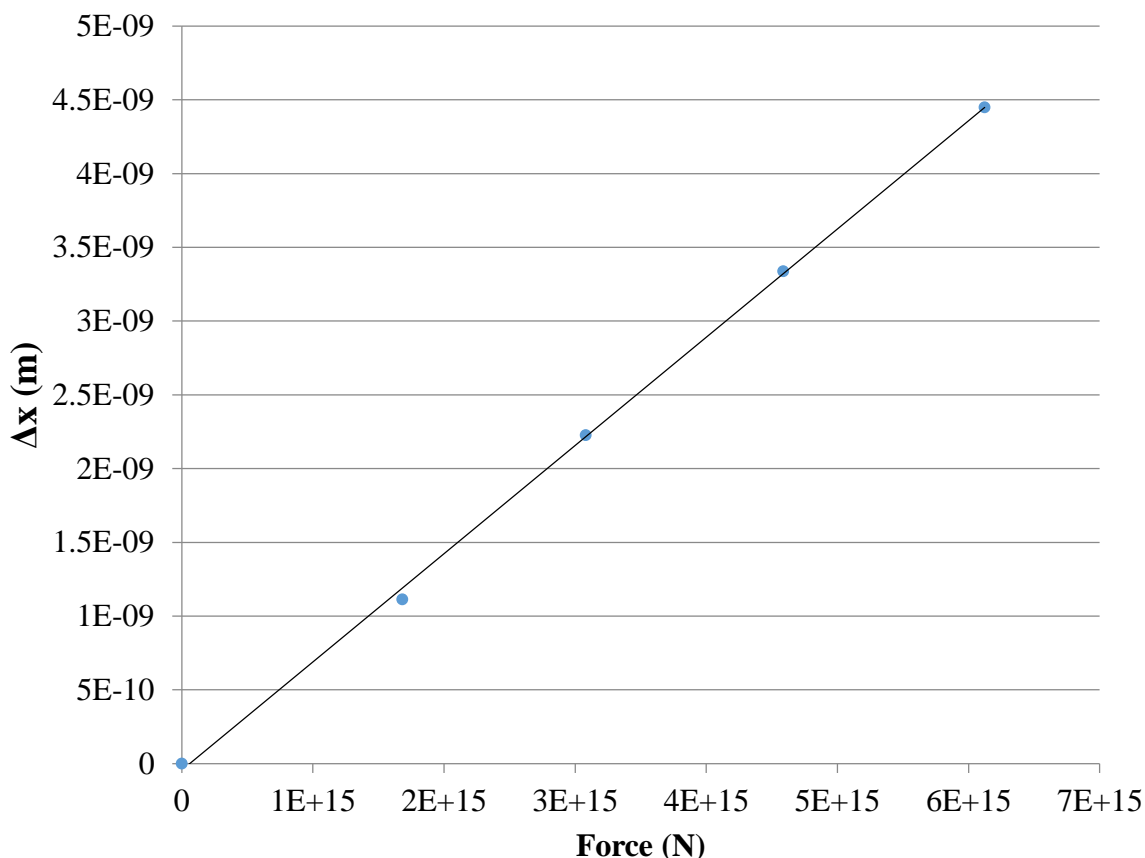
Figure 61. Force against deformation (Δx) in 100% carborane content medium-strand polymer phase. Linear fit, $y=7.1*10^{-25}x + 0$, $R^2=0.999$

Applying Equation 4.8 gave a shear modulus of 2.6×10^{-2} GPa for 0% carborane phase. The experimental value is again subject to some error, and is variously quoted as 2.03 and 2.32×10^{-4} GPa[36]. The instantaneous value we have then is 2 orders of magnitude higher than experiment. However, the evolution with time is not simulated, which will have an effect on the calculation: strained systems will relax with time, reducing the change in energy and therefore force, leading to a lower calculated shear modulus. For instance, taking the final energies from a 20 ps NPT MD run for unmodified 0% phase and the same phase shifted by 1 degree, gives a 40.8 kJ/mol change in energy and a shear modulus of 3.20×10^{-6} GPa, which is now an underestimate. With sufficient relaxation time, it is conceivable that the change in energy will equal 0, since these are amorphous systems. The relaxation time cannot be chosen arbitrarily then, and it is probably more useful to make comparisons between instantaneously calculated moduli, with allowances for lack of relaxation, for the range of *meta* carborane phases, producing the values shown in Figure 62.
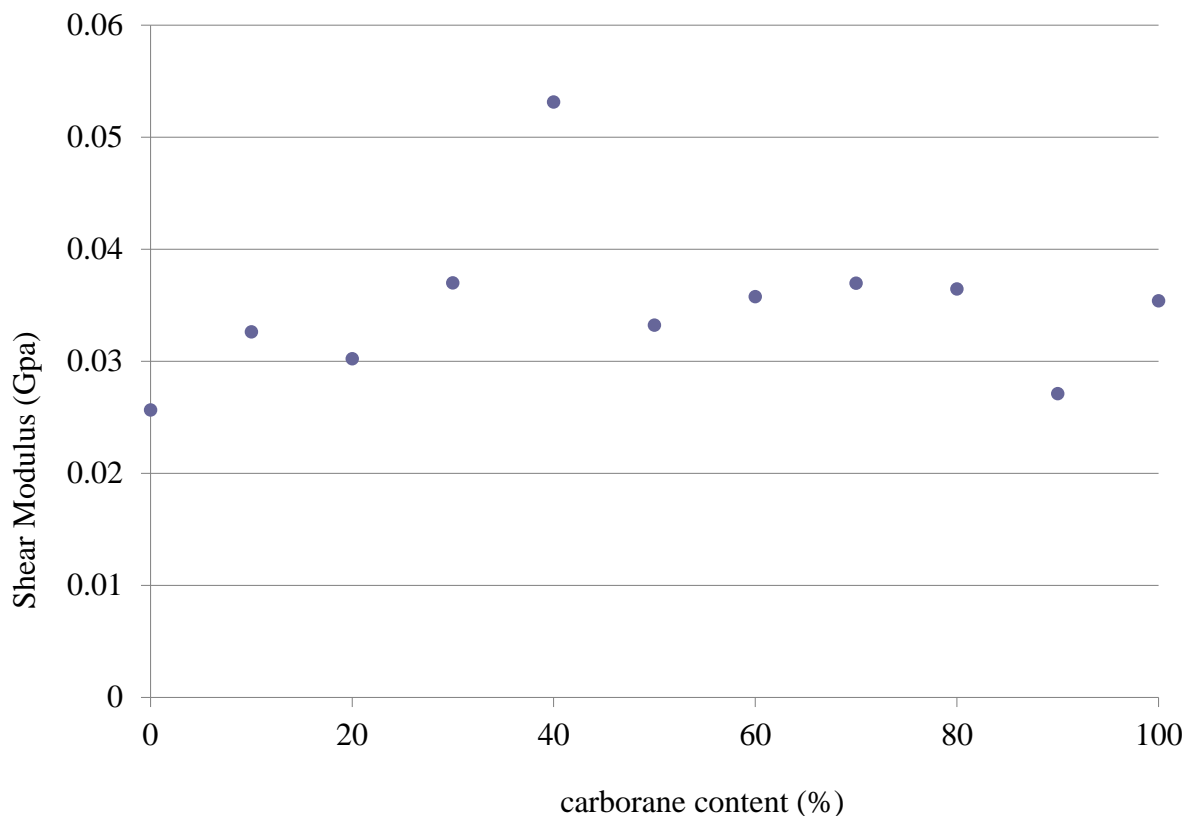
Figure 62. Shear modulus as a function of carborane content for medium-strand polymer phases

It is observed that shear modulus does not appear to be correlated to carborane content, with all values in a fairly flat range from 0.025-0.04 GPa, with 90 and 40% carborane content examples anomalous. This suggests that the response to shear strain is largely governed by factors other than Si-O-Si-O torsions, such as inter-strand Van der Waals interactions, although a slight increase with increasing carborane content is perhaps discernable. It is clear that there will be quite a few factors that could control shear modulus, and a statistical distribution would be more useful to get a clearer picture. However, at this point in the investigation, it was decided to investigate shear modulus using other methods, explored in the following section.

4.2.3.6 Shear Modulus as a function of *m*-carborane content; shear wave propagation

The shear modulus for a material can also be derived from the velocity of a shear wave; a wave where the motion of atoms is perpendicular to the direction of the wave. This is possible to investigate, using the external field "oshr" in the DLPOLY code[130]. This applies a deformation to atoms as given in Equation 4.9:

$$F_x = A * cos\left(2 * \pi * n * \frac{z}{L_z}\right)$$ Equation 4.9

Therefore, with an atom's increasing z position, the force applied to its x position follows a cosine graph, leading to the construction of a shear wave propagating along the Z direction, with displacements along the X direction, summarised in Figure 63.
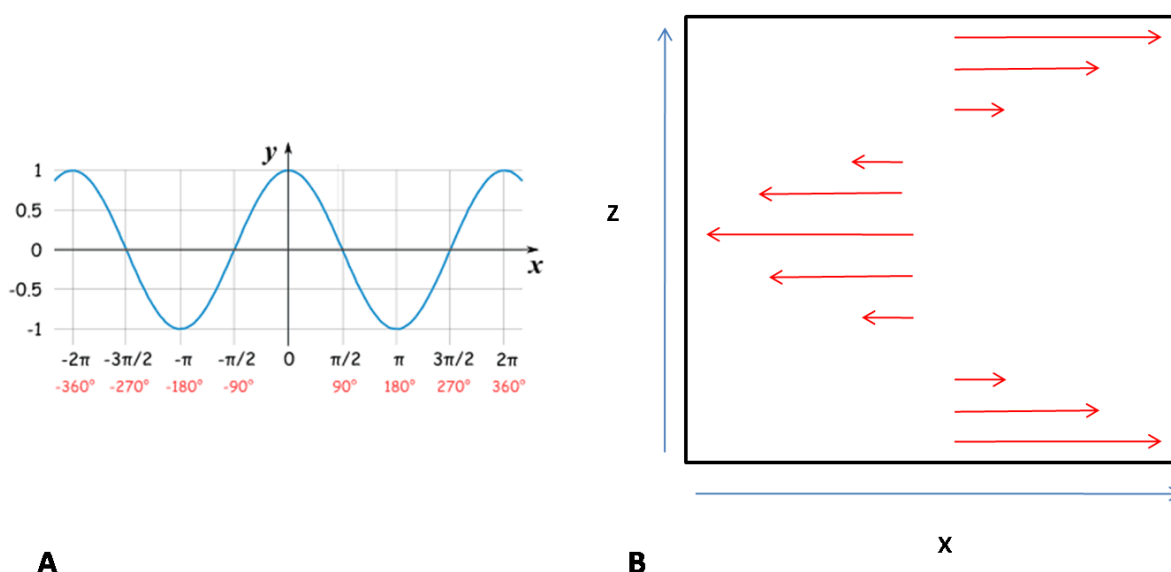
Figure 63. A: cosine graph, B: transformations due to oshr field, from equation 4.10, where n=1.0, and A is arbitrary. Red lines indicate changes in force along X for atoms of position Z. Increasing n increases frequency of oscillations

A and n from Equation 4.9are inputted by the user, and it is possible to analyse the x positions of varying z positions over the course of a NVT run (i.e. maintaining cell volume), to derive the parameters of the shear wave. This is related to shear modulus via Equation 4.10:

$$v_s = \sqrt{\frac{G}{\rho}}$$ Equation 4.10

Where v_s is the velocity of the shear wave, G is shear modulus, and ρ is density.   The shear modulus can therefore be calculated by analysing the propagation of the shear wave with constant volume.

However, in our experiments only two outcomes were observed: (1) with a high (1.0) amplitude, the system appears to tear; strands untangle from each other due to the force, and begin to slide over each other, interacting only through inter-strand non-bonded interactions of parallel strands; when strands are tangled it provides a greater surface area for inter-strand bonding. This is illustrated in Figure 64.
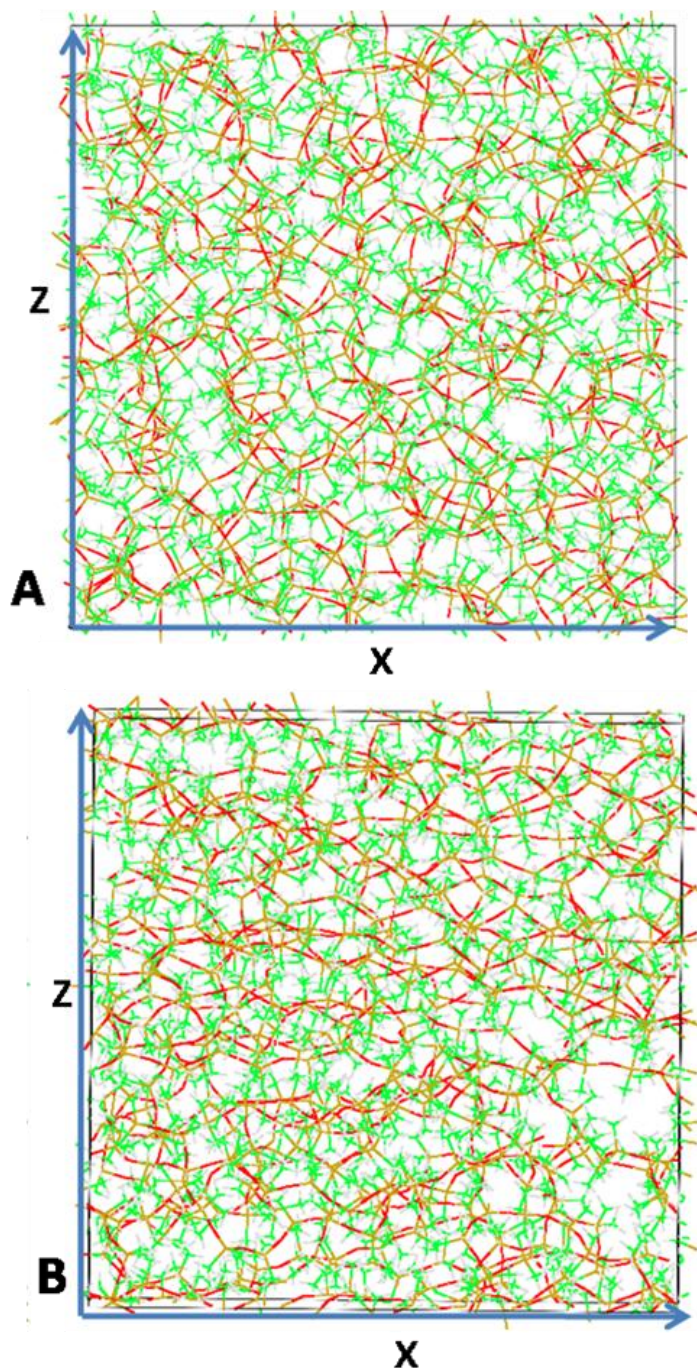
Figure 64. A: random orientation of strands in starting phase. B: strands aligned along x direction following application of a shear field. Snapshots from MD simulations carried out at 1atm and 298K.

The shear wave does not dissipate over 250 ps, nor is the motion of particles recognisable as a shear wave, as depicted in Figure 65.
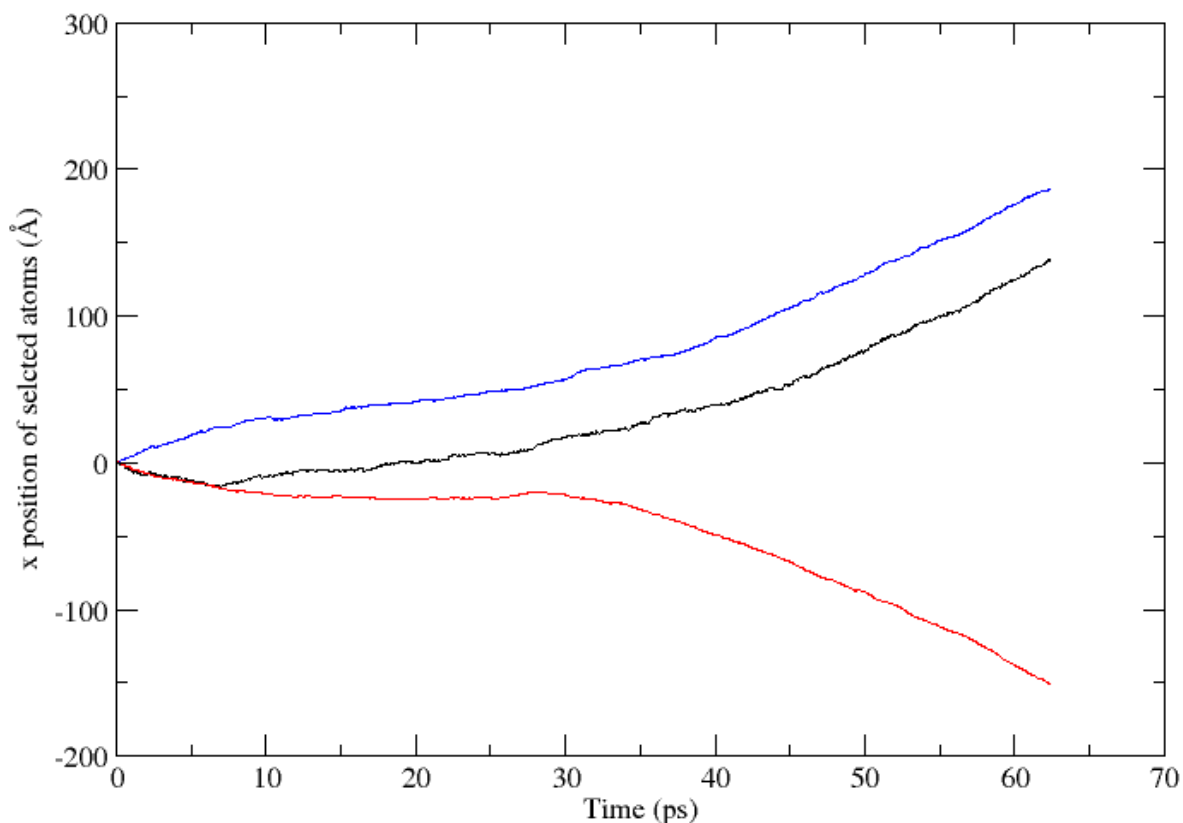
Figure 65. Change in x positions of atoms with distinct z positions (where $z \approx 0$ (black), 0.5 (red) and 1.0 (blue) cell lengths), against time, for the 0% carborane content medium-strand polymer phase with shear potential applied

Given computational restraints, the strands are necessarily shorter than experiment (experimentally[53] it is observed that strands have an molecular weight of 154,000 g/mol average, roughly 2500 monomers), and strand length will have an effect on tensile strength, however this result could still be indicative of tensile strength. For example, the same shear wave applied on the longer strands has the same "tearing" effect, as observed in Figure 66, albeit at a longer timescale.
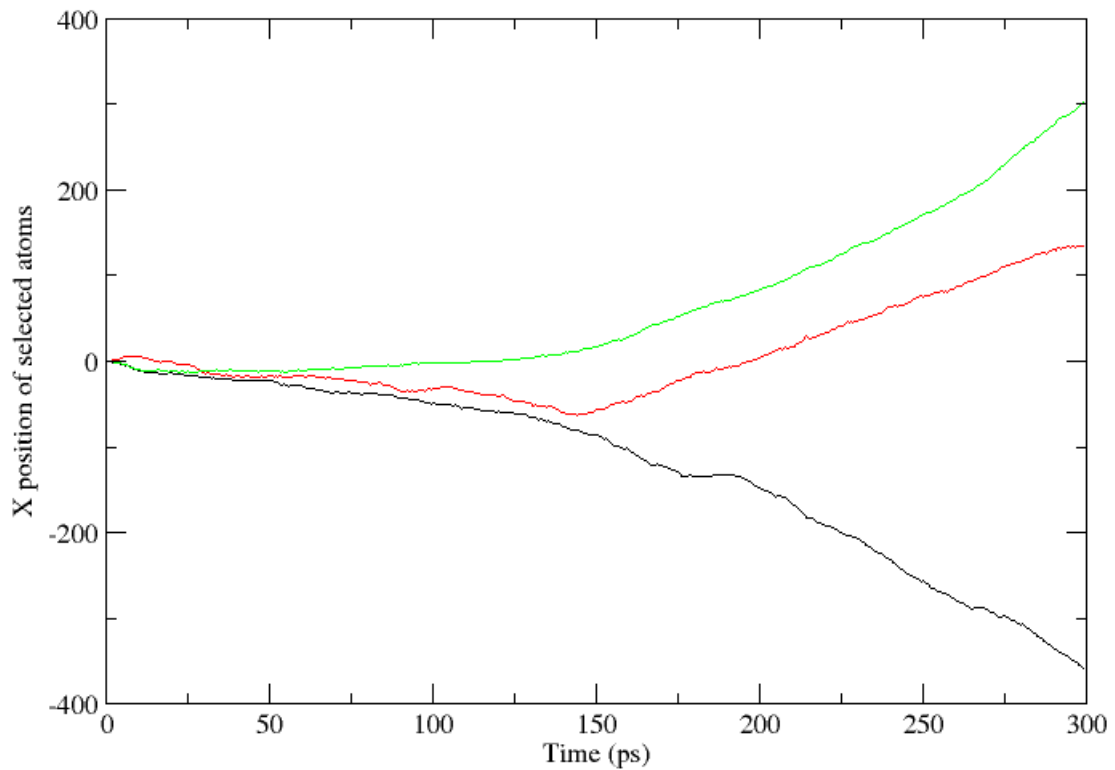
Figure 66. Change in x positions of atoms with distinct z positions (maximum (black), minimum (red) and mean (green) z positions) against time.0% carborane content long-strand polymer phase with 0.3Å shear potential applied.

The other possible outcome (2), is that it is possible to infer a "shape memory" property of the material[131]. Using a smaller amplitude shear wave (where the A value = 0.1 cell lengths) has the effect shown in Figure 67.
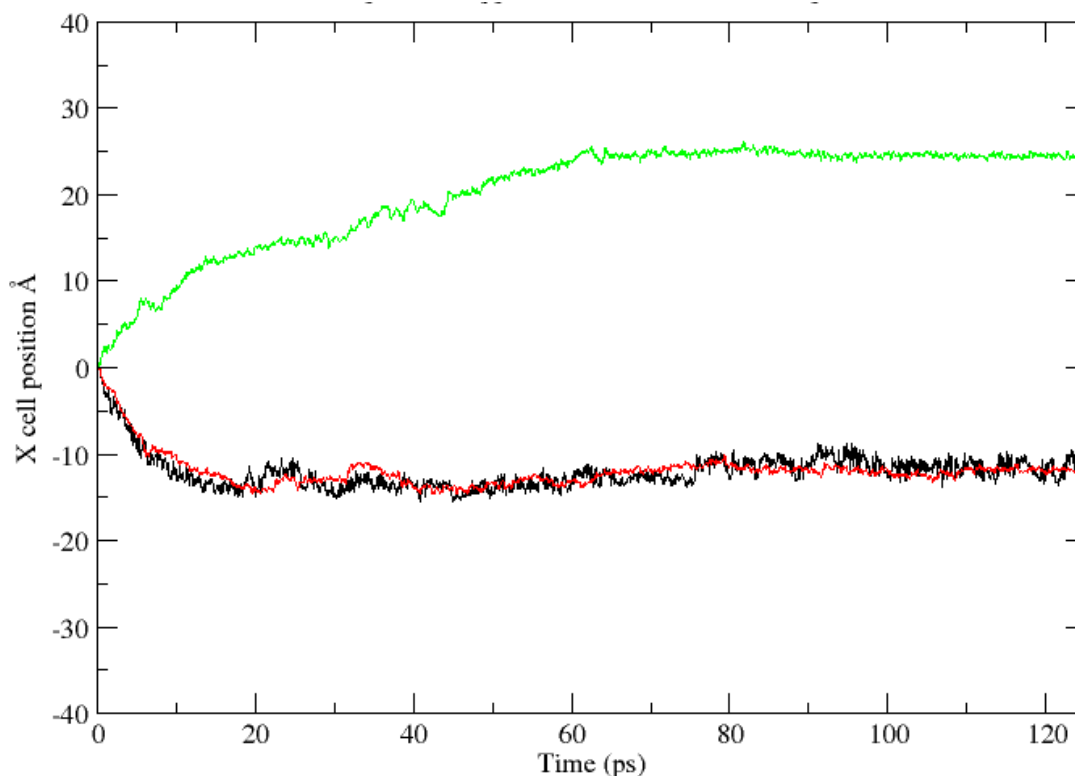
Figure 67. X positions of selected atoms (z positions are maximum (black), minimum (red) and mean (green)) for 0% carborane substitution medium-strand polymer phase, depicting the effect of shear potential (A=0.1) applied along Z at t=0.

Again, the motion is not representative of a shear wave: for the first 60ps the atoms move through the first phase of a shear wave but then return to a "random" motion, showing a dissipation of the shear wave. The difference in noise for the three plots is due to selection of atom to study: an atom is chosen that is closest to z = 0, 0.5 or 1.0 cell lengths, and lighter atoms will see more noise than heavier atoms.

This behaviour is observed for the full range of polymer phases (0-100% carborane content, both medium and long strand cases), so it was decided to abandon the derivation of shear modulus through this technique. However, the effect of shear potentials on polymer phases will be analysed in more detail in Section 4.6.2, which deals with cross linking, where the polymer phase acts more like a solid, and the propagation of a shear wave is more likely.

121

4.3 The effect of varying *para*-carborane content

The *meta* carborane isomer is chosen as the Si-[cage]-Si angle in bis-dimethylsiloxy-*meta*-carborane most closely mirrors that of the Si-O-Si bond in siloxane, so is likely to have the least effect on the physical properties of the polymer, and allow easiest synthesis. However, the *meta* carborane units within the chains are fairly polar[49], meaning a higher chance of ordering due to electrostatic interactions, and a consequent increase in glass transition temperature, T_g, observed experimentally[53], and simulated in section 4.2.3.4. Many other physical properties could also be affected. Attempts to inhibit the crystallisation of chains include: replacing a small percentage of the *meta*-carborane units with the less polar *para* isomer[132]; replacing a small percentage of the dimethyl siloxane units with phenyl-methyl-siloxane; introducing cross-linking between chains, and branching chains. The polarity discussed for *meta*- and *para*- carboranes is shown in Figure 68.
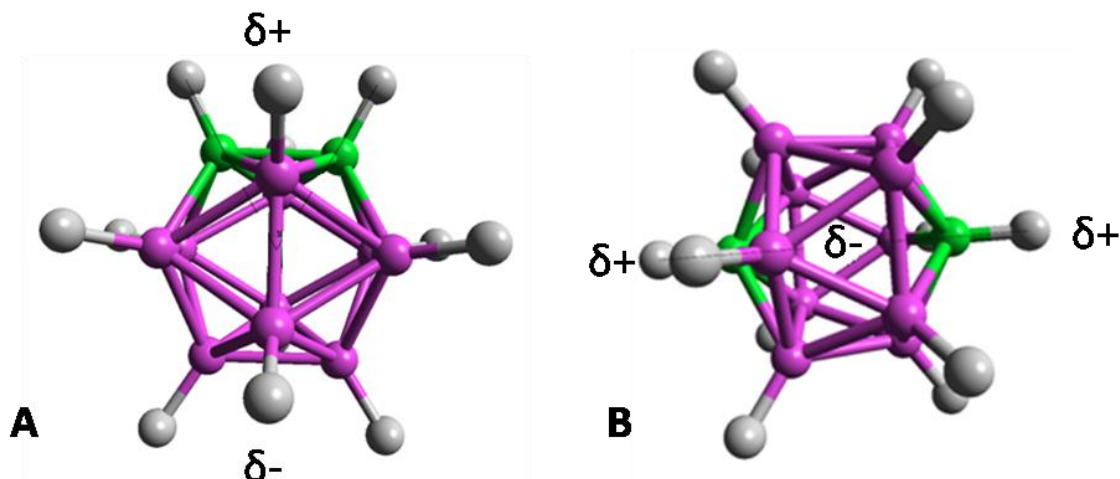
Figure 68. Model of electrostatic field as calculated by PBEPBE/6-31G (d,p) calculations on A: *meta* and B: *para* carborane. The calculated net dipole for these molecules at this level of theory is isotropically 0.0 for *meta* and 2.6302 in the z axis (through the carbon atoms) in *para*.

The first investigation involves changing the *meta*/*para* ratio in line with an experimental paper[48], to see how reproducible the physical properties are with this method. Carborane percentage is fixed at 50%, while the *meta*/*para* ratio is set at 7, 15, 30, and 50 percent in the different polymer phases.

The polymer phases were created in the same way as for the "long" phases, with a ratio of 50:50 siloxane to carborane building. A % chance of a carborane build being *meta* or *para* is then introduced, with the forcefield unchanged except for the charges on carborane atoms, which were taken from the PBEPBE/6-31G* optimised structure of the monomer. Boron

atoms are equivalent and have a 0.04 charge, whilst carbon atoms have a charge of -0.42, this is a change from boron = -0.08 to 0.08 and carbon = -0.74 as in the *meta* example.

. The densities for this method are seen in Figure 69, producing the thermal expansion coefficients and bulk moduli seen in Figure 70 and Figure 71. Therefore, it appears that with increasing *para*-carborane content, density decreases as a result of the lower coordination between strands, which is not unexpected.
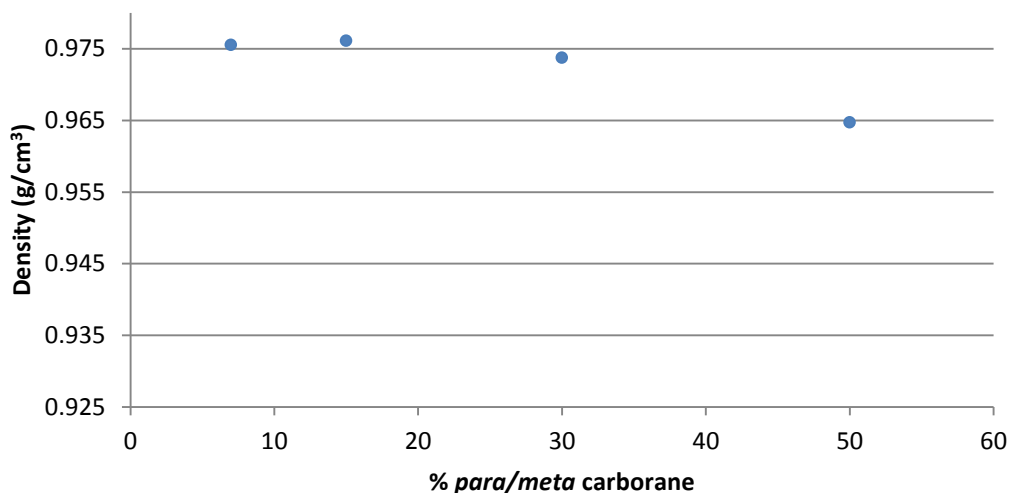
Figure 69. Density of polymer phases as a function of *para* carborane content. 50% carborane monomer content overall
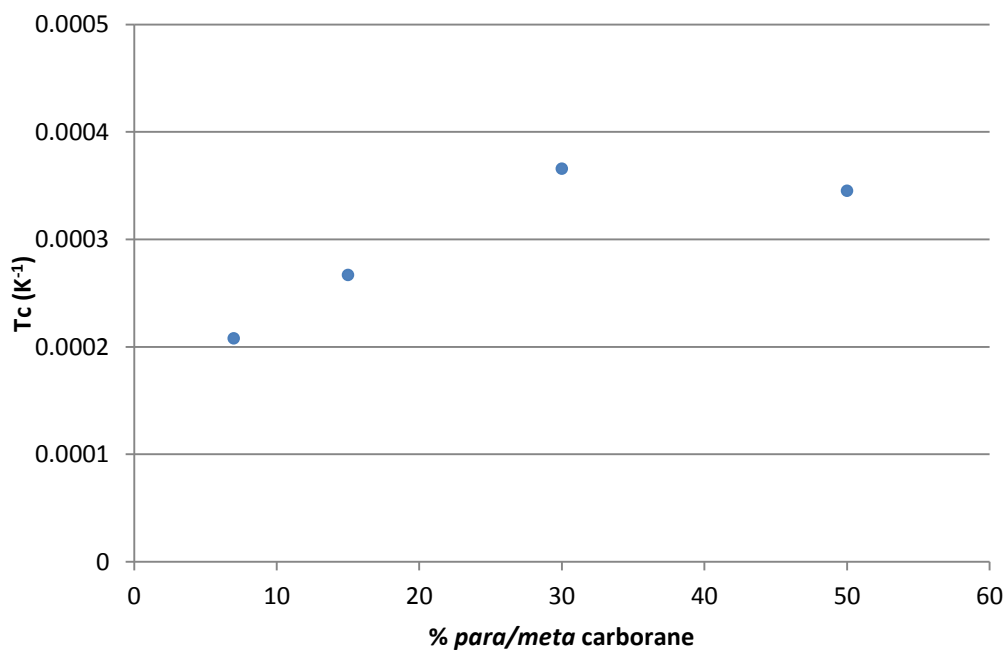
Figure 70. Thermal expansion coefficient as a function of *para* carborane content
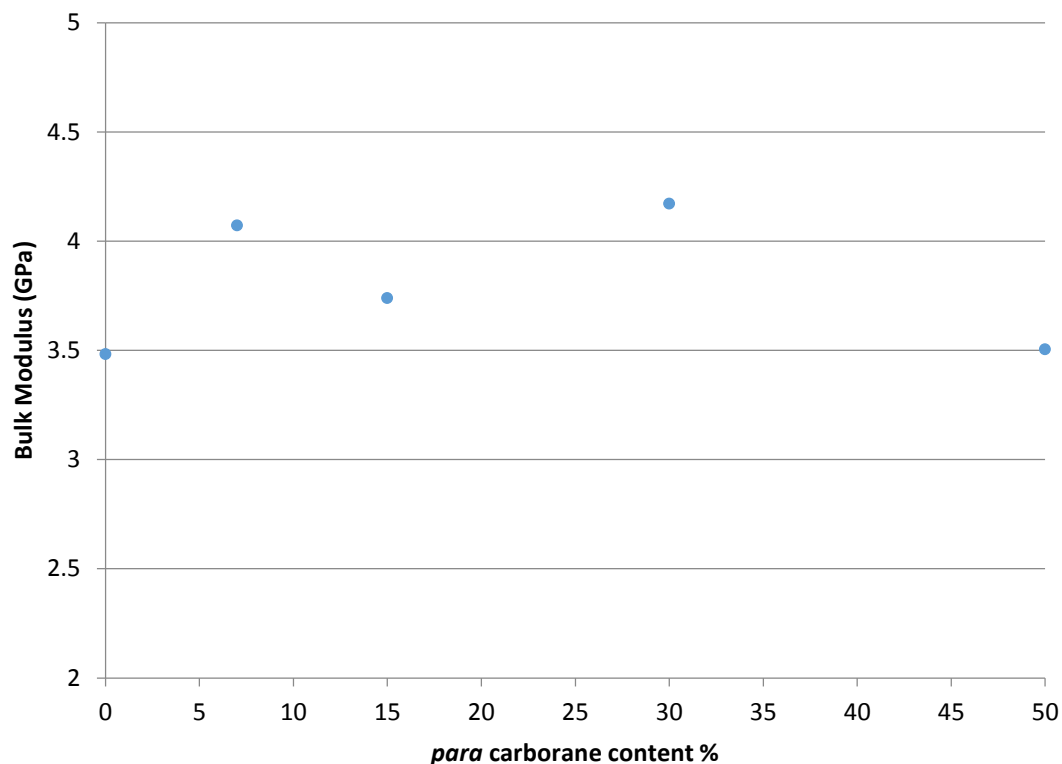
Figure 71. Bulk modulus as a function of *para* content. 0% value taken from equivalent "long strand" experiment.

With increasing *para*-carborane content, thermal expansion coefficient increases, whilst bulk modulus shows some scatter, and a trend is difficult to discern.

As a result of less coordination between strands, an increase in temperature will lead to higher inter-chain mobility, and a greater effect on volume change, and in turn, a higher thermal expansion coefficient.

In the case of the bulk modulus calculations, the lack of correlation between bulk modulus and *para*-carborane content suggests that the flexibility, in terms of torsion and angles, of O-Si-O-Si units in polymer strands is the main control over a phase's response to changing pressure. The number of O-Si-O-Si units in polymer strands in this investigation is determined by the amount of siloxane monomers in the initial set-up: 50% for each phase.

4.4   The effect of varying phenyl-methyl-siloxane monomer content

A common method for reducing inter-strand interaction, and therefore creating a more malleable, plastic material in siloxane polymers is to introduce a small percentage of phenyl-methyl-siloxane monomers in place of dimethyl siloxane monomers[49]. This has the effect of holding strands apart due to the bulky non-polar moieties bonded to the silicon atoms of the linear strands, possibly leading to a lower glass transition temperature, lower thermal expansion coefficient etc.

This effect is studied within the context of this work by creating polymer phases (20 strands of a Gaussian distribution around 40 monomers length) using the ERMINTRUDE code developed in section 4.2.3, at a 50:50 siloxane : carborane ratio, but with a percentage of phenyl-methyl siloxane monomer additions instead of siloxane monomer additions, in an analogous way to that discussed in section 4.3. The phenyl-methyl siloxane monomer is shown in Figure 72.
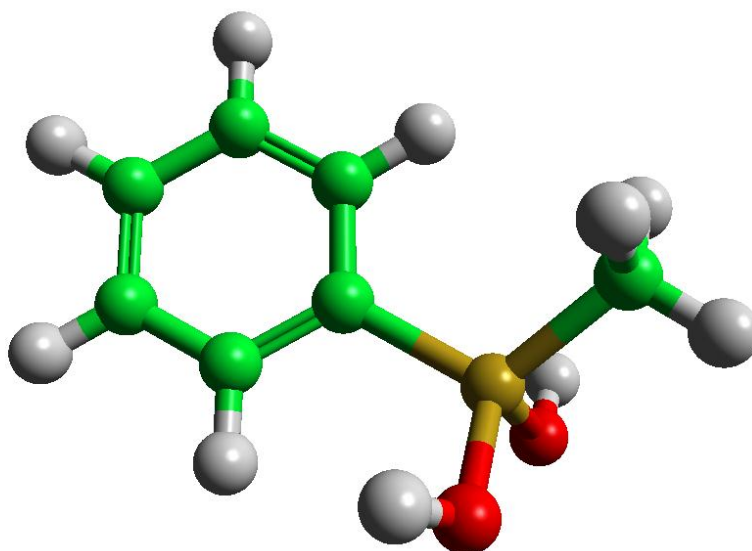
Figure 72. Phenyl-methyl siloxane monomer.

The densities of polymer phases created using the technique detailed above are shown in Figure 73, cell volumes stabilising in 1-4 ns:
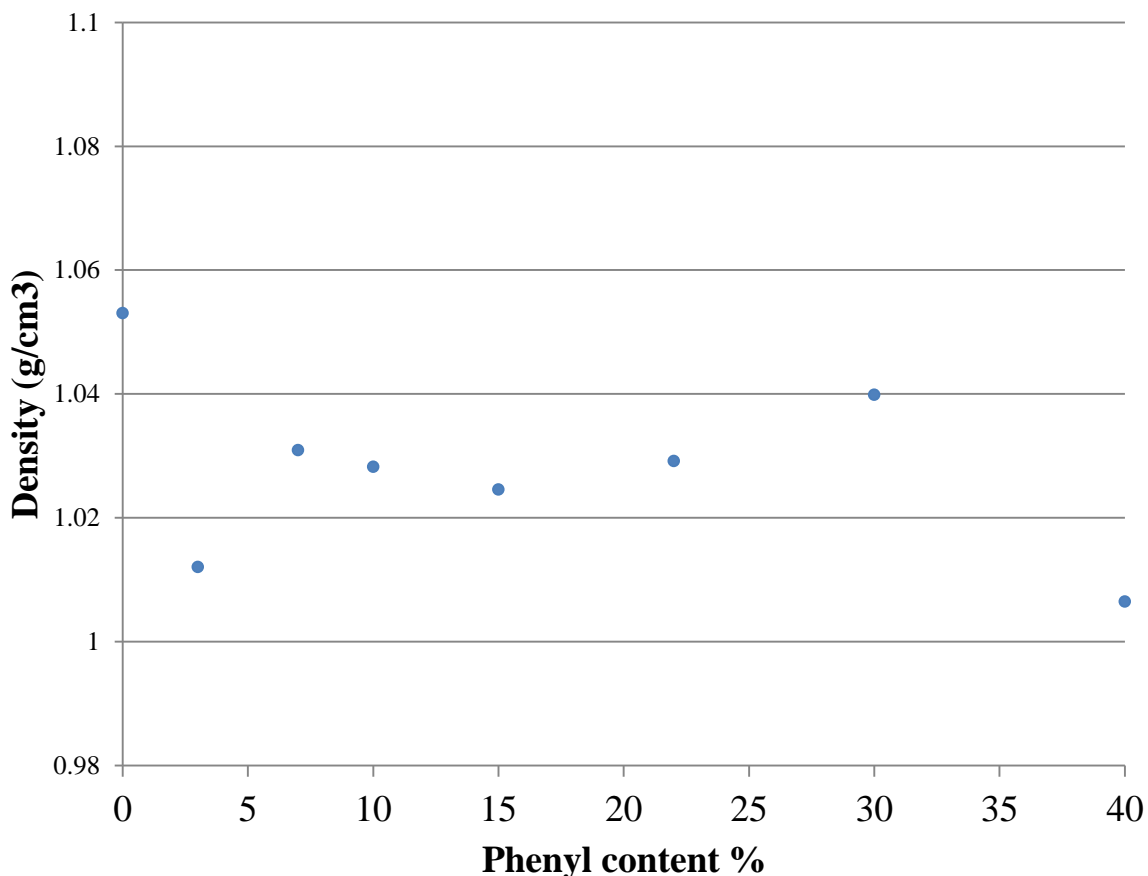
Figure 73. Densities of ERMINTRUDE produced phases of varying phenyl siloxane monomer content. *Meta* carborane content fixed at 50%

The 3 and 40% compositions have lower density than expected, due to a pocket of unoccupied volume in the polymer phase, but a trend of decreasing density with increasing phenyl monomer content is discernable. This is expected, as phenyl units will have the effect of holding strands apart, reducing density and inter strand interaction.

The effect of phenyl content on thermal expansion coefficient and bulk modulus, in line with previous studies (i.e. measuring changes in stable cell volume as a result of increasing temperature and pressure respectively) is seen in Figure 74 and Figure 75. However, the VdW cutoff was reduced from 12 to 8 Å in order to improve parallelisation (by increasing the amount of link cells and therefore nodes available[130]) leading to a slight reduction in thermal expansion coefficient overall.
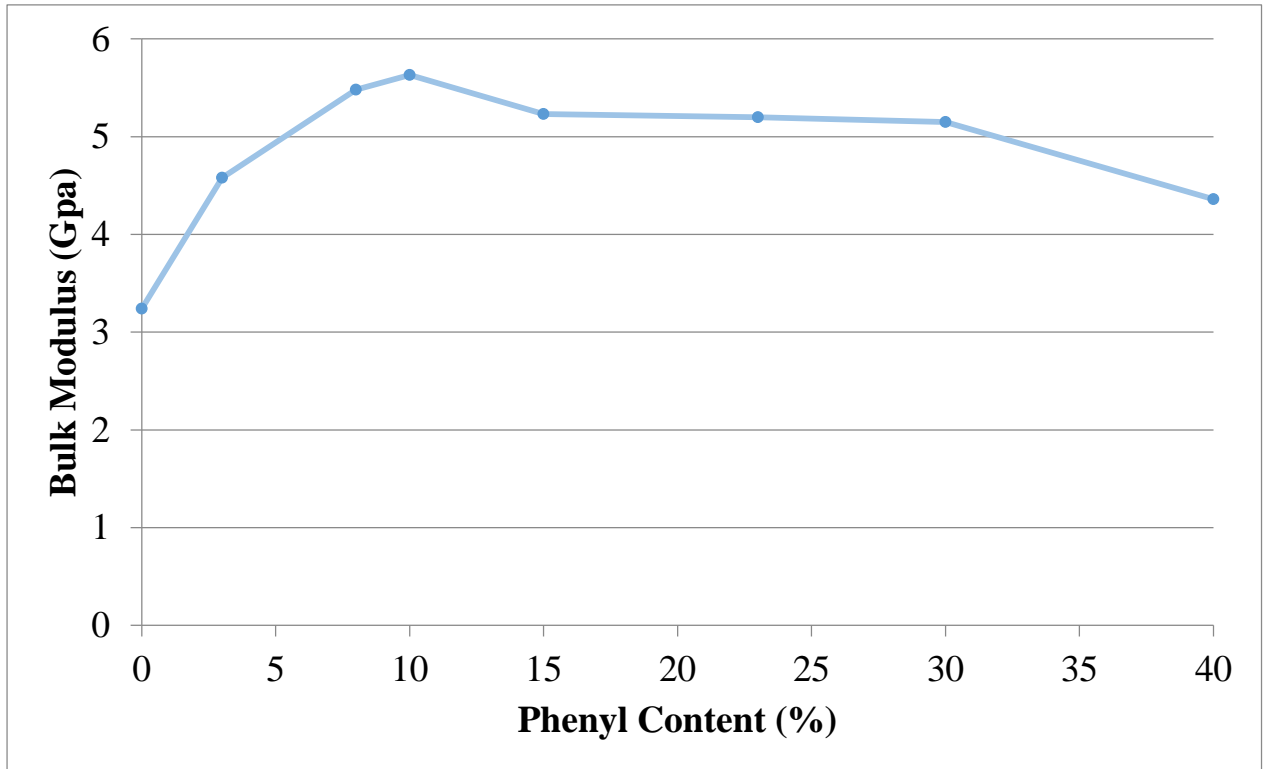
Figure 74. Bulk modulus as a function of phenyl-monomer composition in 50% carborane : siloxane copolymer phases
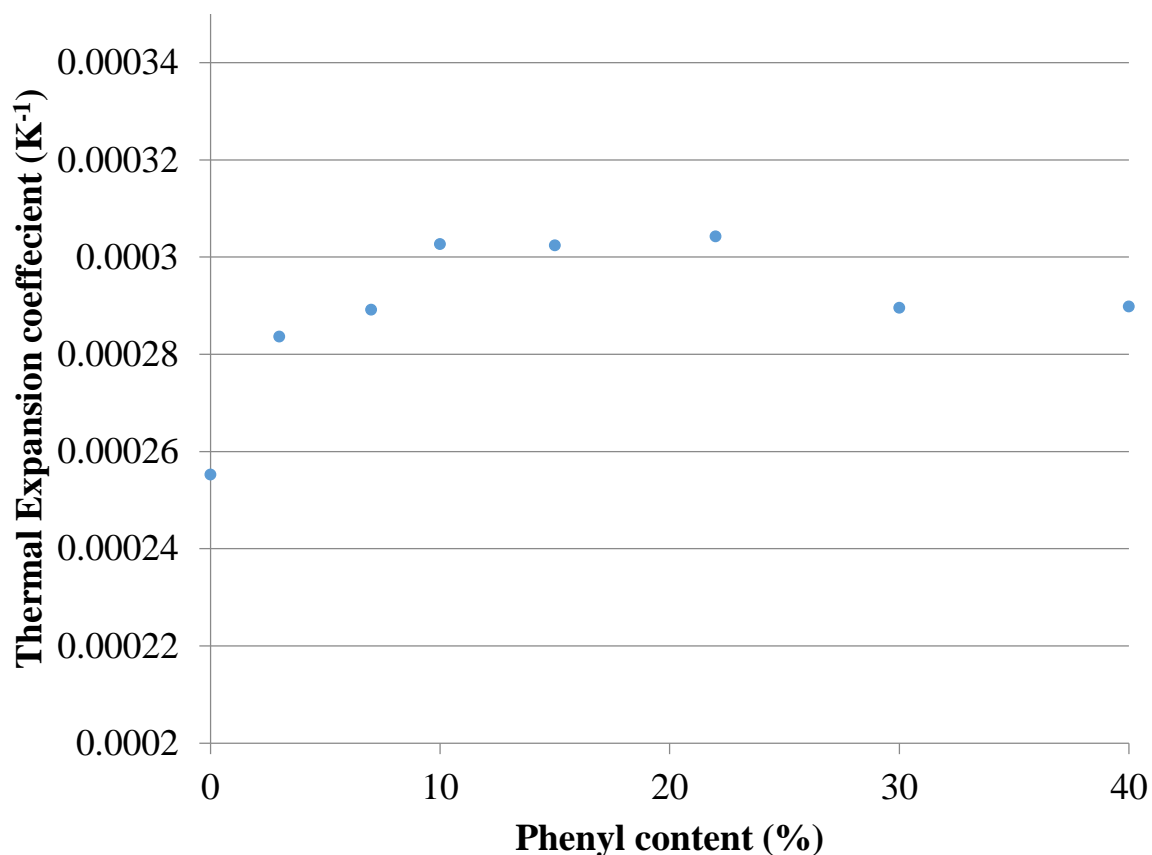
Figure 75. Thermal expansion coefficient as a function of phenyl monomer composition in 50% carborane content polymer phases

As can be seen, with increasing phenyl monomer content, bulk modulus increases, as the ability of the strands in the material to order themselves, and therefore accommodate a reduction in cell volume is impeded, due to the steric role of phenyl groups. However, this effect is slight, and levels off and reverses above 15% phenyl content, as seen in Figure 75.

The RDF of carbon to carbon is shown in the following figure, in order to isolate peaks due to phenyl carbons.
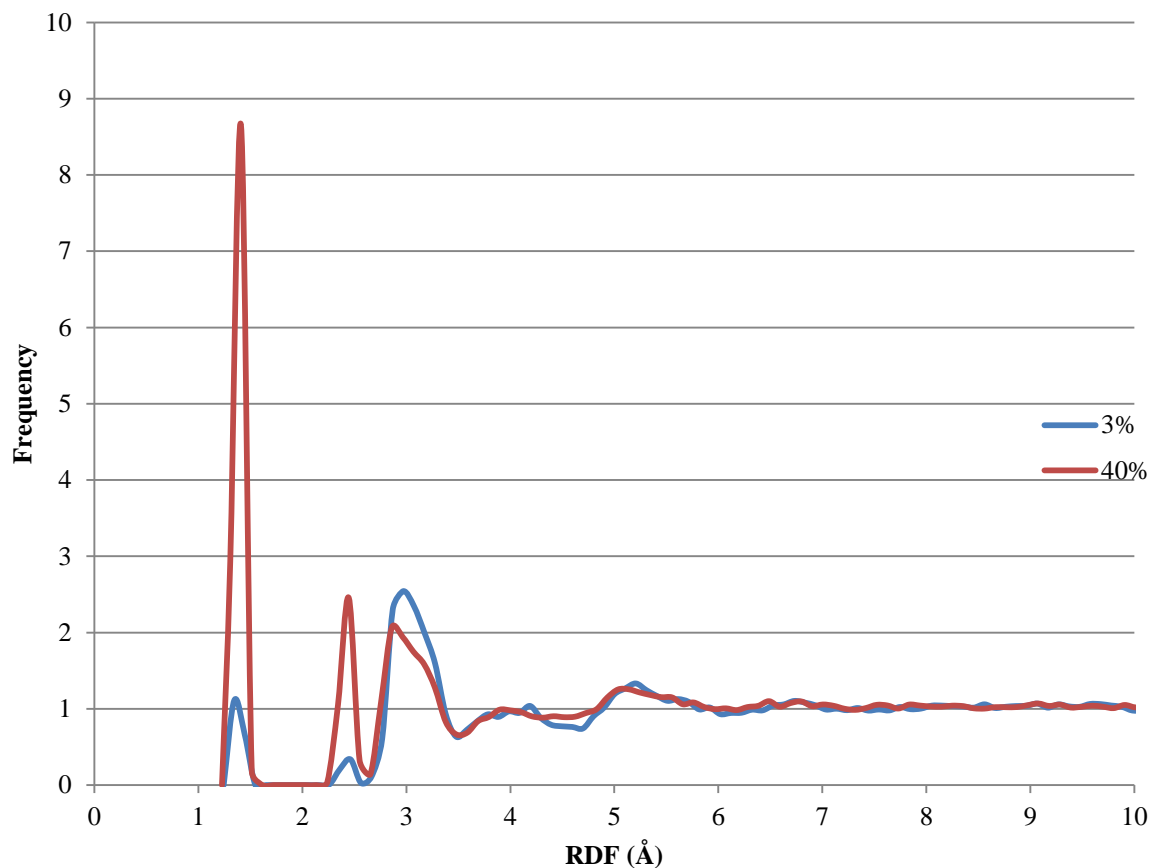
Figure 76. Ambient C-C RDF data for polymer phases composed of varying phenyl monomer content

It is clear from Figure 76, that the peaks at 1.2 and 2.5 Å are due to phenyl content, and can be interpreted as bonded and near neighbour carbons in phenyl groups, whilst the peak due to **C**-C-C-**C** is lost in the broad peak at 3Å, which is also composed of carbons bonded to the same silicon i.e. **C**-Si-**C**. The effect of high pressure is seen in Figure 77:

C-C RDF data; 15% phenyl composition
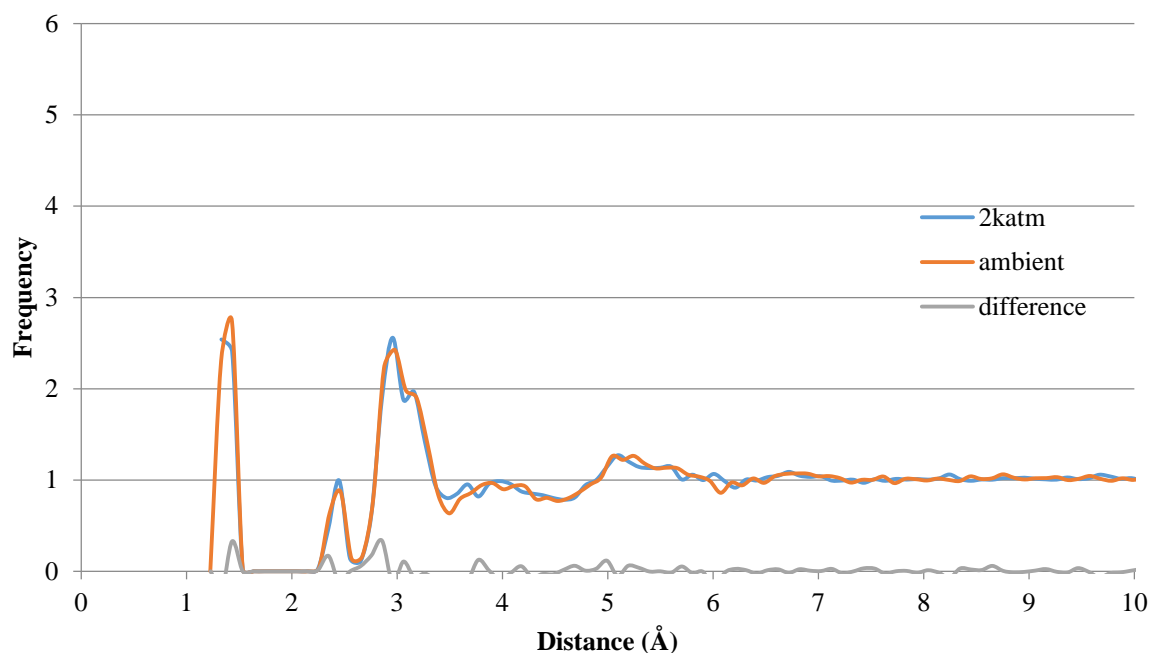
Figure 77. C-C RDF data at ambient and high pressure for 15% phenyl monomer phase

There is very little change upon applying high pressure (no shift in frequency above 0.3), suggesting that there is no scope for accommodating a reduction in phase volume by compressing the phenyl units. It is also useful to analyse the change in C-C-C angle distribution, as seen in Figure 78; the peak of the angle distribution is perhaps broadened by pressure, suggesting that the aromatic carbon ring is slightly distorted.
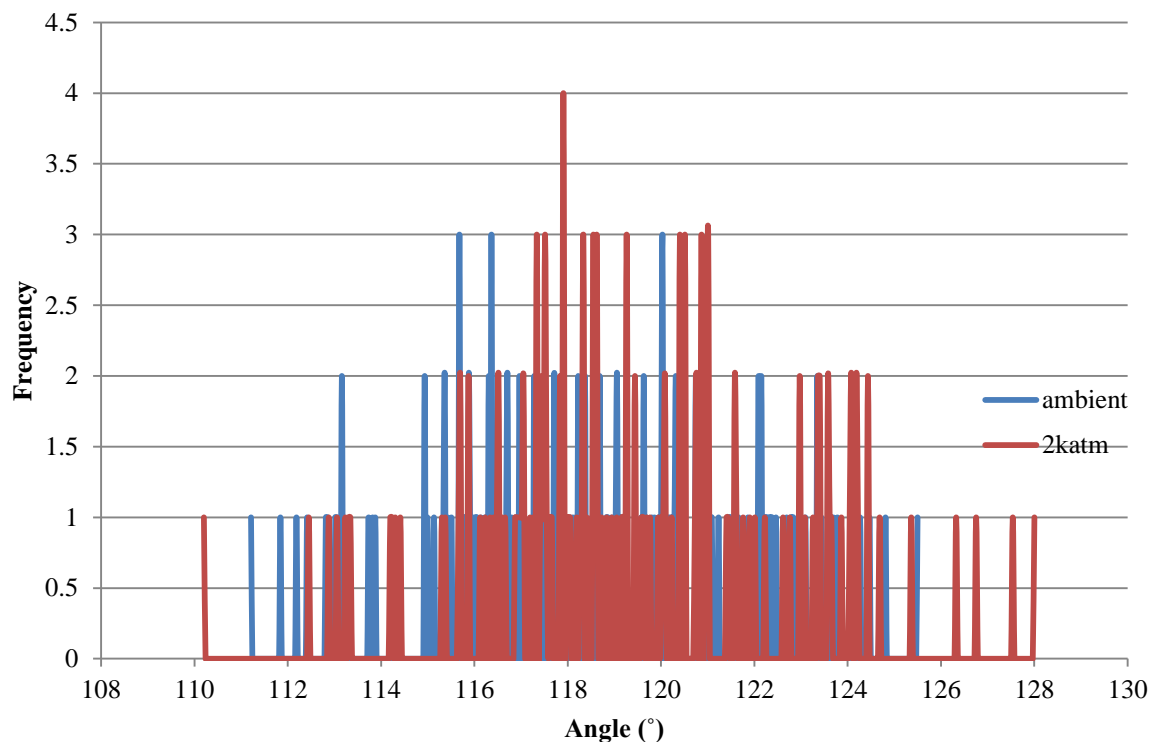
Figure 78. C-C-C angle distribution in 40% phenyl monomer content phase, at varying pressure

Regardless, with 10-15% phenyl monomer content in carborane-siloxane polymer phases, the material is more resistant to pressure than the equivalent methyl substituted copolymer, a potentially useful property given its industrial context. The increase in thermal expansion coefficient with phenyl content reproduces what is observed experimentally: strands are held apart by rigid side groups, so react to increases in temperature by becoming more mobile than their dimethyl equivalents. A second advantage of introducing phenyl groups discussed is that they show "enhanced elastomeric characteristics due to the disruption of crystallinity found in the unmodified poly(*m*-carborane-siloxane) rubber" [53]. This is a more difficult concept to show computationally, as alluded to in section 4.2.1., but the thermal expansion coefficient is increased.

4.5   The effect of varying ethyl-methyl-siloxane monomer content

Given the potential of crosslinking for affecting the physical properties of a polymer material, it was decided to investigate the effect of incorporating ethene moieties into the polymer system, by adding a percentage of ethene-methyl-siloxane to the monomer mix, in place of dimethyl siloxane. The more reactive nature of the ethene moiety means that cross linking is more easily instigated, through a heat[133] or light[134] catalysed process, although typically a crosslinking agent such as tetrapropylorthosilicate and a catalyst[53] is used. However, the reaction of ethene groups to create organic linkers between strands during gelation is a possible mechanism, and the first part of this investigation will be a study into how close ethene groups are to each other in polymer phases with varying ethene content. This investigation will also include a look at how raw ethene content affects physical properties of the bulk material, before crosslinking is considered.

The phases were produced in the same way as the previous study, with 20 strands of a Gaussian distribution centred at 40 monomers, with NPT MD used to stabilise cell volumes at ambient (1atm, 298K) conditions, with a small cutoff to improve parallelisation and produce the phases quicker (8Å). The densities produced using this system are given in Figure 79:
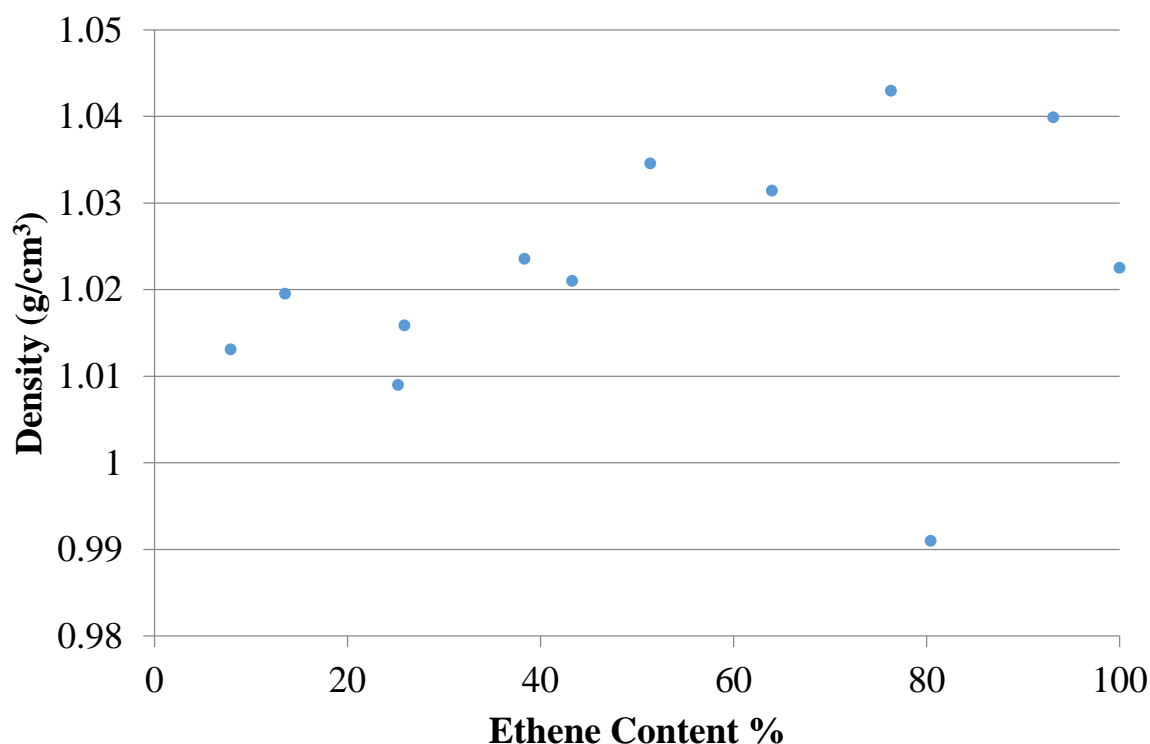
Figure 79. Density as a function of ethene monomer content in polymer phases. Carborane content fixed at 50%.

It would appear that with increasing ethene content there is increased density. However, the density is lower overall, than the 50% "long" phase: 1.053 g/cm^3, analogous to 0% ethene in Figure 79. This is possibly as a result of the reduction in cutoff to improve parallelisation, leading to stabilisation of cell volume at a lower density than would be expected. Comparison with 0% ethene content therefore will not be made. The increase in density with ethene content is possibly as a result of increased electrostatic interactions with more ethene groups, as the corresponding methyl groups have carbon atoms shielded by their hydrogens, whilst ethene carbons are more exposed.

The effect of ethene content on thermal expansion coefficient is seen in Figure 80.
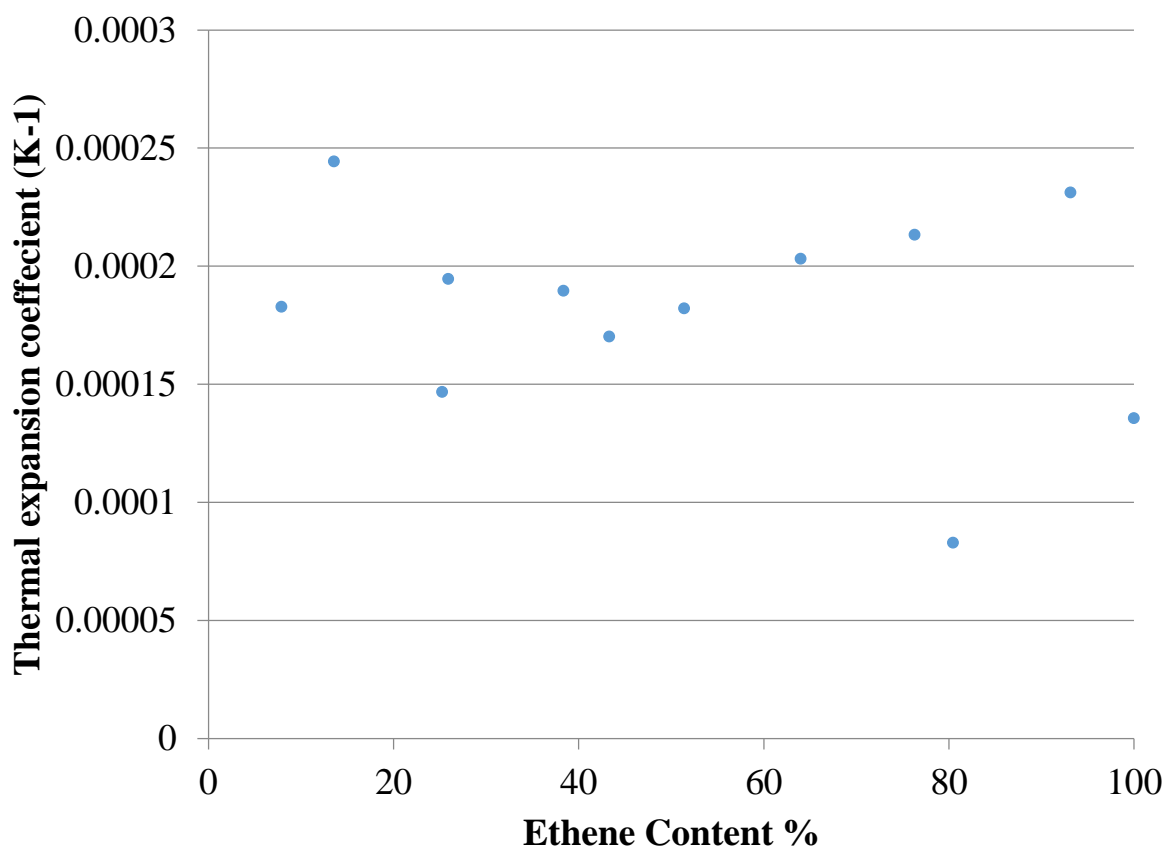
Figure 80. Thermal expansion coefficient as a function of ethene monomer content

Ignoring the anomalous result at ≈82% ethene content (due to a pocket of free volume to expand into), the thermal expansion coefficient appears to reduce from 3 to 50% ethane content, and then increases from 50% to 100%, perhaps indicative of a peak inter-strand interaction at 50% ethene content, which will reduce the thermal expansion coefficient. However, a large scatter in results is apparent. The effect on bulk modulus is given in Figure 81.
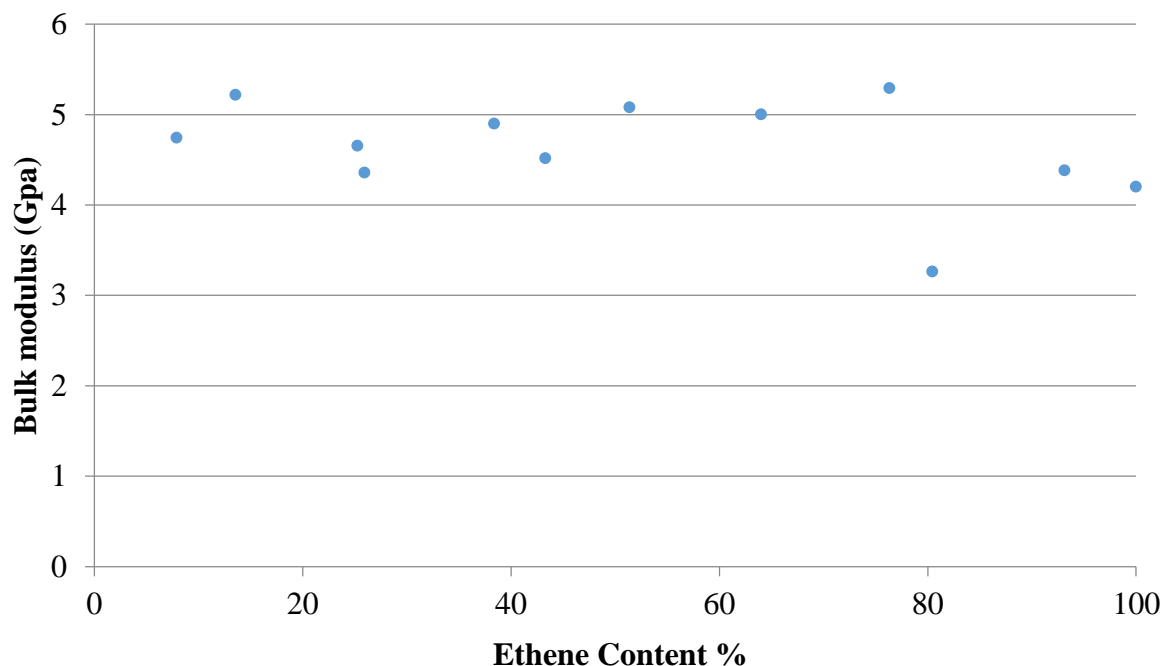
Figure 81. Bulk modulus as a function of ethene content

In this case, increasing ethene content does not appear to affect bulk modulus, with all results within a narrow range above 4.2 GPa and below 5.2 GPa, with the 82% case anomalous due to a pocket of free volume to expand into.

It is known experimentally[53] that the material's properties are altered by the vinyl groups causing crosslinking: "..the phenyl-vinyl modified poly(m-carborane-siloxane) rubber showed the lowest degree of swell, indicative of the greater cross-link density of this material. This is due to the additional cross-links introduced by the vinyl groups during gelation/fabrication" typically catalysed by the crosslinking agent dichlorobenylperoxide. This will have a greater effect on the flexibility of the material than simply having bulkier side groups for obvious reasons. The effect of crosslinking will be analysed in more detail in section 4.6.

The method by which crosslinking in gelation occurs is suggested[135,136] to be via the binding of a vinyl and methyl group through a free radical catalysed process, with some redistribution of hydrogen atoms, shown in the scheme below.

1:$(OR_2)Si\text{-}CH\text{=}CH_2 + RO^{\cdot} \rightarrow (OR_2)Si\text{-}CH^{\cdot}\text{-}CH_2\text{-}RO$

2:$(OR_2)Si\text{-}CH^{\cdot}\text{-}CH_2\text{-}RO + _3HC\text{-}Si(OR_2) \rightarrow (OR_2)Si\text{-}CH_2\text{-}CH_2RO + _2HC^{\cdot}Si(OR_2)$

3:$(OR_2)Si\text{-}CH\text{=}CH_2 + _2HC^{\cdot}Si(OR_2) \rightarrow (OR_2)Si\text{-}CH^{\cdot}\text{-}CH_2\text{-}_2HC\text{-}Si(OR_2)$

4:$(OR_2)Si\text{-}CH^{\cdot}\text{-}CH_2\text{-}_2HC\text{-}Si(OR_2) + _3HC\text{-}Si(OR_2) \rightarrow$

Scheme 7

134

$(OR_2)Si$-CH_2-CH_2-$CH2$-$Si(OR_2)$ +$_2HC^.Si(OR_2)$

$5:2(OR_2)SiC^.H_2 \rightarrow (OR_2)Si$-$CH_2$-$CH_2$-$Si(OR_2)$
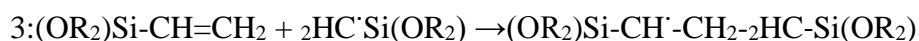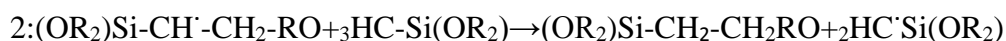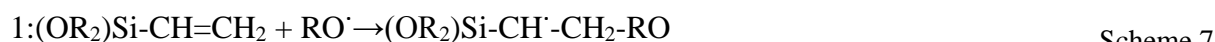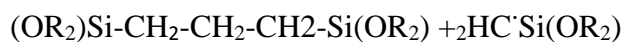
This is depicted in Figure 82 showing the RDF of ethene carbon – ethene carbon, which reveals the low probability of finding two vinyl groups in close proximity at any given moment, even in high ethene content phases.
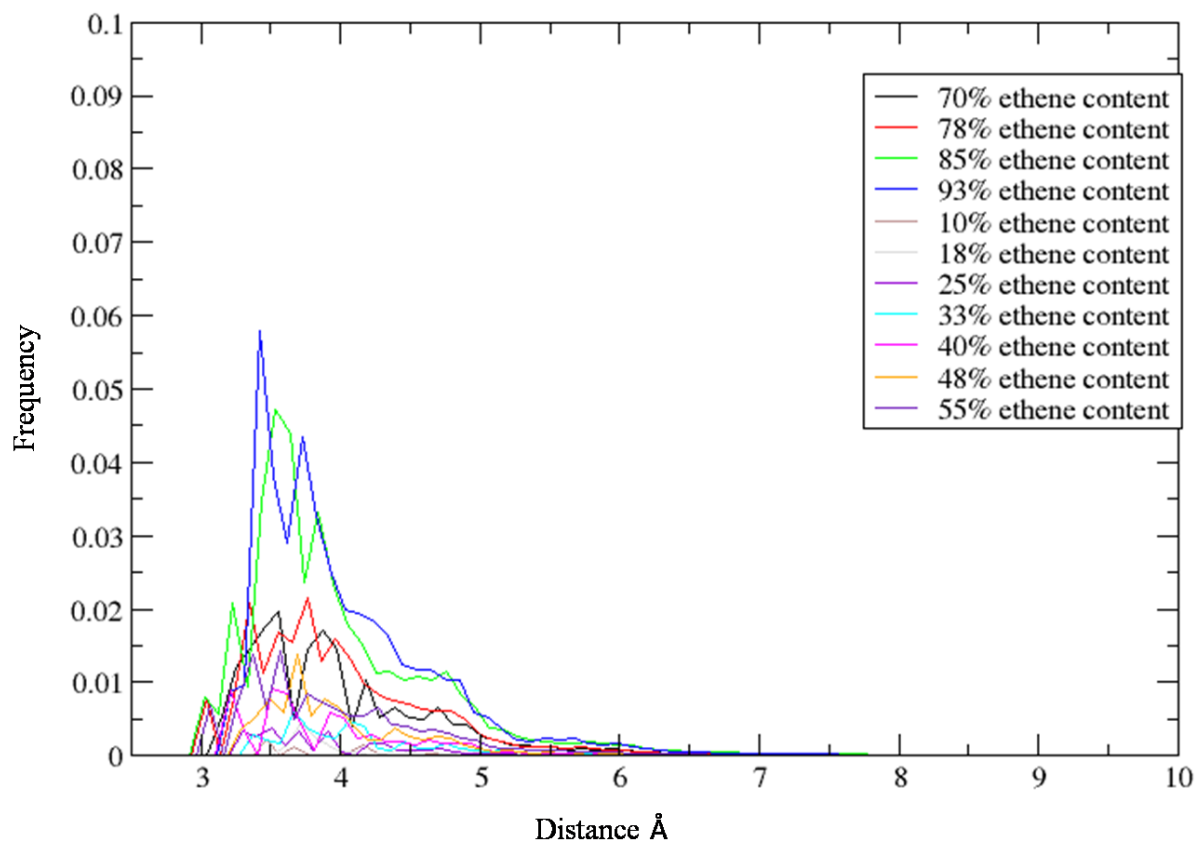
Figure 82. Second peak of ethene carbon-ethene carbon RDF for varying ethene content phases

It is clear then, that crosslinking is unlikely to occur via a radical terminated process of two vinyl groups, and a process whereby a vinyl group reacts with a methyl group on a neighbouring strand is the likely mechanism, when using peroxide and a crosslinking agent. For this reason, only very low concentrations of vinyl groups are required to achieve high crosslink densities, but an alternative mechanism where radicals are light generated and crosslinks are formed by the reaction of vinyl groups, may benefit from control over vinyl-vinyl distance, provided by ethene content and presented here.

4.6   The effect of cross linking

Cross linking is often carried out by polymer scientists in order to alter the physical properties of the material. This can come in the form of a reaction of the material with boric acid, which promotes cross linking by reacting with the terminal hydroxide groups of polymer strands, via condensation bonding[32]. Given the three hydroxyl groups per boric acid molecule, the ends of three strands can then be bonded together. This immobilisation of strands reduces the amount of crystallisation in the material, whilst retaining the deformable, elastic nature of the material due to the intermediate strength of the B-O bond: inter-strand VDW interaction strength < B-O bond strength < Si-O bond strength. The range of interactions can accommodate different changes to volume.

Another method for cross linking is by the bonding of strands via their organic substituents, typically catalysed by heat, chemical treatment[134] or photolysis[137], and also usually governed by the selection of labile side groups in monomers. The exact method of inter strand connection through radiation is poorly understood; one mechanism being a Si-Si bond formed through the removal of respective methyl groups, with an ethane molecule produced as a side product[138], another being the removal of two hydrogen atoms from separate methyl groups[139] as in:

$$Si\text{-}CH_3 + H_3C\text{-}Si \rightarrow Si\text{-}CH_2\text{-}CH_2\text{-}Si + H_2$$
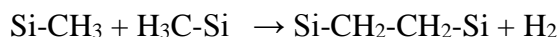
<div align="right">Scheme 7</div>

In any case, this method creates strong contacts between strands. Cross linking will be considered in the next two sections.

4.6.1 Boric acid induced cross linking

Boric acid cross linking was simulated by writing a python code[1] that selected three terminal hydrogens in close proximity (2.5Å) in the polymer phase. These hydrogens were removed from the phase and a boron atom placed at the average of these positions. An example of this code's action is given in Figure 83.
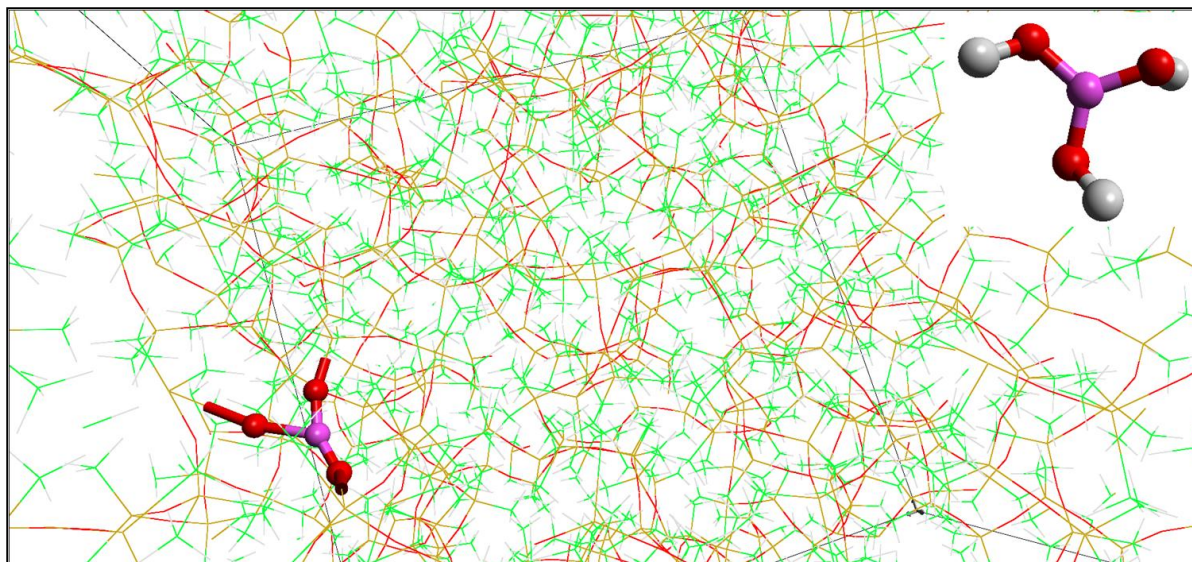
Figure 83. Image of "chemically treated" 0% siloxane phase. Boron and bonded oxygens are highlighted with spheres. The insert is of boric acid as optimised by Gaussian03.

The new terminal oxygens were given a different atom type name, and the non-bonded interaction between boron and this oxygen atom type was then set as the UFF[91] Morse potential, shown in Equation 4.11. Where r is the B-O bond distance in Å, and the units are kJ/mol.

$$E_{B-O\ bond} = 0.24 * \left[\left\{ 1 - e^{9.601*(r-1.45)} \right\}^2 - 1 \right]$$

Equation 4.11

In this way the condensation-reaction-mediated tying together of three polymer strands is simulated in this polymer phase, although the production of three water molecules is ignored.

Cell volume and energy were then equilibrated using NPT molecular dynamics, and physical properties recalculated. Neither thermal expansion coefficient or bulk modulus is changed (5.05 x 10^{-4} K^{-1} and 3.18 GPa respectively) from the unmodified pure siloxane phase. Therefore 1 boric acid molecule per 10 polymer strands does not initially appear to affect the material's response to pressure or temperature.

It would be interesting to extend this "chemical treatment" simulation across all polymer phases, and to add more boric acid molecules; this would give an idea of the effect on physical properties of the ratio of chemical treatment to amount of polymer, as well as potentially determining the difference in effects of boric acid compared to tetraalkoxy silane curing treatment. It is also of interest to examine how likely it is to find three terminal hydrogens in close proximity to each other, which will shed light on the idealised bonding together of three polymer strands by a boric acid molecule (in the 11 phases examined, only three had viable nearby terminal hydrogens).

However, at this point in the investigation, we had conversations with experimentalists planning experiments using these polymers. The most interesting route for theoretical calculations was discussed, and crosslinks between polymer strands, via ethyl and methyl linkage was put forward. Therefore the crosslinking calculations were extended to those discussed in Section 4.6.2.

4.6.2   Radiation-catalysed cross linking

As noted in section 4.6, cross linking of polymers affects physical properties, and is exploited in polymer science in order to produce materials with desirable physical properties. However, given the industrial context, cross linking will also be a factor in the aging of the designed material. This is due to the high energy lithium and helium ions travelling through the material as a result of neutron capture events, as stated previously. Therefore, it is of particular interest in this work to analyse the effect of cross linking.

The creation of cross links in this context is likely to be via the removal of methyl hydrogens by the progress of high energy positive ions moving past strands. This will have the effect of catalysing an organic linkage between strands, as hydrogen deficient carbon atoms make short C-C bonds to quench the high energy low coordination states.

This effect was simulated by writing a python code[1] that selects two methyl hydrogens on neighbouring strands within a user specified radius (typically 2.6 Å). These are removed, and a methylene ($-CH_2-$) unit placed at the average of their positions. This method was chosen as it would be an analogy of experimental conditions whilst it would also avoid making entirely new polymer phases. The phases studied were the "medium" examples. The cell volumes were stabilised at ambient (298K, 1.0 atm) conditions using molecular dynamics (1 femtosecond timestep, NPT ensemble and 1.5 ps thermostat and barostat control) after crosslinks had been created.

Thermal expansion as a function of carborane content is recalculated for the polymer phases with a varying amount of cross linking. This is shown in Figure 84.
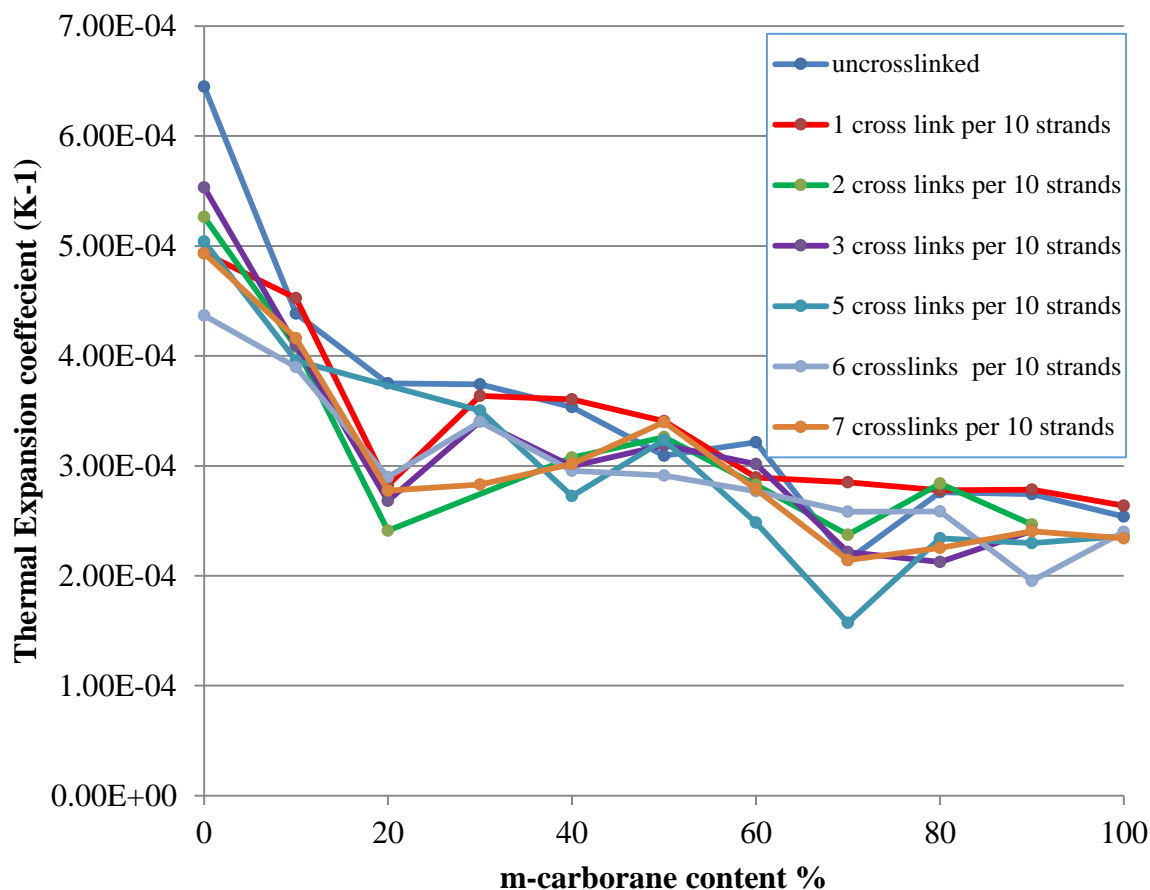
Figure 84. Thermal expansion coefficient as a function of carborane content for cross linked materials

As can be seen, with increasing carborane content, thermal expansion coefficient (Tc) is reduced for reasons discussed in Section 4.2.3.3. With cross linking, Tc is also reduced, although with some variance in the effect. This variance is likely due to the position of cross links; a cross link at the end of two strands will have a different effect than in the middle of said strands.

The effect of crosslinking is very slight, with several points overlapping, for 1 cross link per 10 polymer strands, and large, qualitative changes are observed only for 3 crosslinks per 10 strands, with effect on thermal expansion coefficient increasing with crosslink density after this cutoff. This is an indication of the density of cross linking required to make a noticeable change in physical properties, in terms of flexibility. It would be interesting to compare these results with experiment, as localisation and density of crosslinks is likely to be slightly different to these idealised results.

Bulk modulus as a function of carborane content is also calculated for the cross linked materials, which is seen in Figure 85:
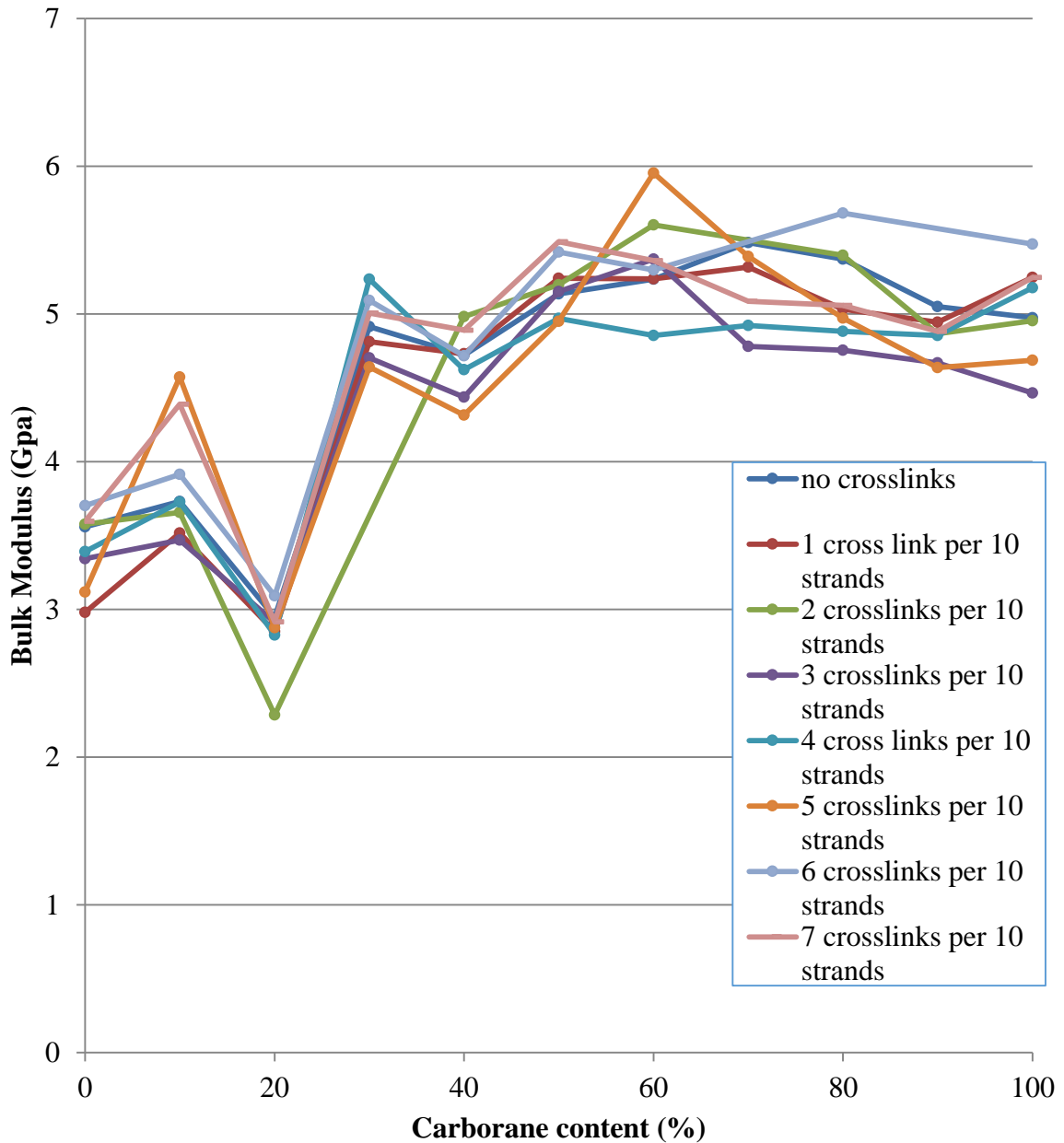
Figure 85. Bulk modulus as a function of carborane content for cross linked materials

As can be seen, the effect on bulk modulus is different to that of T_c. For uncrosslinked materials, increasing carborane content increases bulk modulus, due to there being less possible ordering of Si-O torsions to accommodate a reduction in cell volume, and 1, 2, 3, 4 and 5 crosslinks per 10 polymer strands show little variation in this trend from the uncrosslinked phase, but with a large amount of scatter in the results. However, 6 and 7 crosslinks see a slight shifting to higher bulk modulus, suggesting a stiffer material, and again, is an indication of the density of crosslinks required to cause a change in the material's response to isotropic pressure.

Given the effect of crosslinking on isotropic physical properties, it was decided to repeat the shear modulus experiments cautiously explored in section 4.2.3.6. In these experiments, cell size is not altered, and the interactions within the material are the source of physical property prediction.

With a shear field of 0.25 cell lengths, a shear wave is again not observed for pure siloxane (0% carborane substitution), even at seven crosslinks per 10 strands as seen in Figure 86, where the atomic positions are more representative of a material experiencing tear:
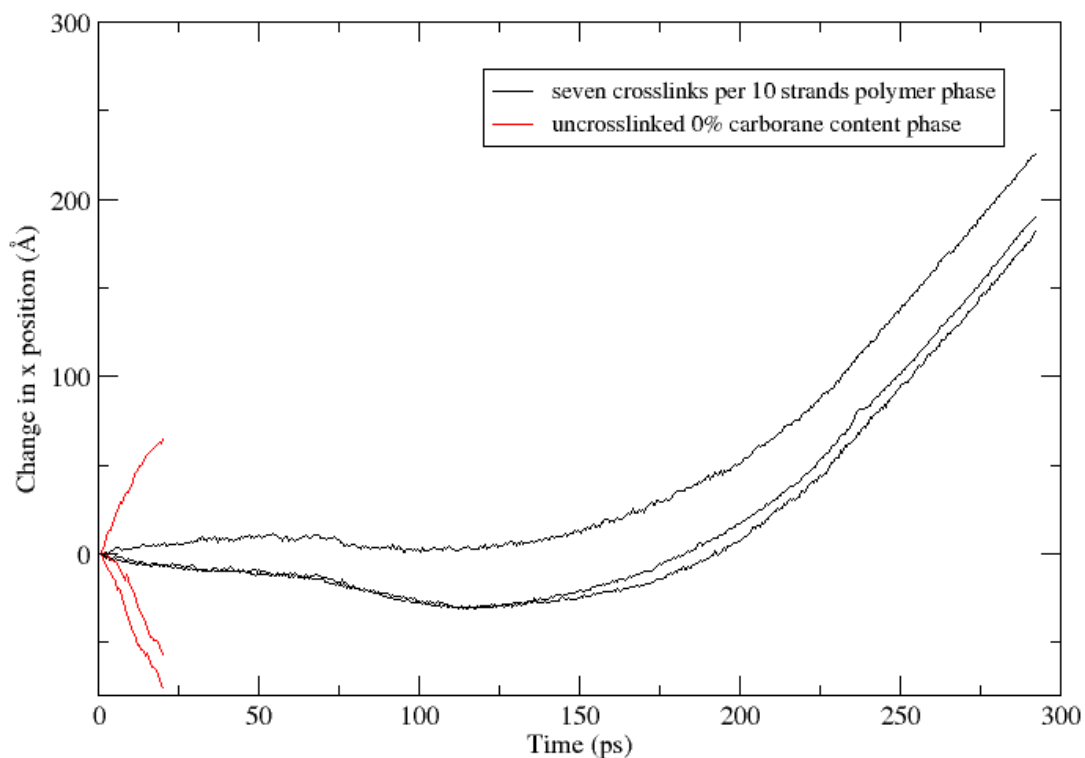
Figure 86. Effect on x position of atoms at z edges of cell, or halfway through cell, when A=0.25 shear wave is applied, for pure siloxane phase, with seven crosslinks per 10 polymer strands

As previously stated, shear modulus can again not be calculated, as a shear wave cannot be clearly determined. What is clear is that crosslinking significantly delays the "tearing" effect, suggesting an increase in tensile strength, when compared with the uncrosslinked example. Tearing in this sense could be represented by a change of more than one cell length in one direction, or ≈30Å in Figure 86. For instance, the uncrosslinked example tears at 30ps, whilst seven crosslinks per 10 strands appears to tear at 120ps. This is an indication of inflexibility in the crosslinked example.

4.7   Modelling radiation damage in copolymers

Given the potential industrial context of these materials, it was decided to study, using electronic structure methods, the effect on vibrational spectra of removing boron vertices. This will allow the changes in vibrational spectra observed theoretically to be a diagnostic tool in studying these materials experimentally; to determine the likely structure of the carborane cages following exposure to radiation that might remove boron vertices.

The assumption in this technique is that the remaining carborane cage remains intact, following the nuclear reaction of one of its vertices. This may not be the case, as the high energy particles could destroy the cage completely, perhaps leading to the formation of boron oxide/ baron carbide systems, as observed when the material is taken to $\approx 600°C^2$. This investigation will consider a range of charge states to give an idea of the likely cage system's state.

The *meta*-carborane monomer has four inequivalent boron positions; B1: bonded to both carbon atoms (2 atoms), B2: bonded to 1 carbon atom and B1 (4atoms), B3: bonded to 1 carbon 2 B2's (2 atoms), and B4: not bonded to carbon atoms (2 atoms), shown in Figure 87:
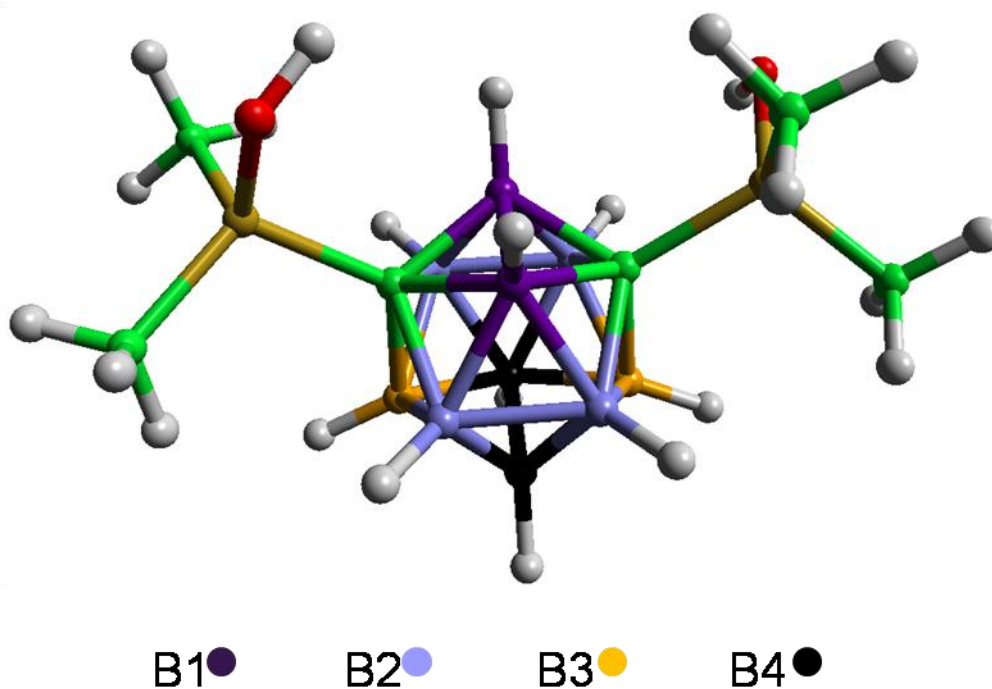
Figure 87. Monomer with boron positions labelled

From the optimised carborane monomer, each of the boron positions, and associated hydrogen atoms were removed in turn, and five further optimisations were performed on the cluster, with the charge +2, +1, 0, -1, -2. This represents the loss of a BH^{2-}, BH^{1-}, BH^0 etc. unit due to neutron capture events.

The geometry optimised energies are given in Table 8:

Table 8. Geometry optimised energies for damaged cage system			
Residual charge	Vertex removed, optimised energy, relative to lowest energy for that charge state (kJ/mol)		
	B1	B2	B3	B4
2	-	0.000	123.4	-
1	708.9	0.000	36.8	57.8
0	0.000	-	-	-
-1	0.000	107.6	123.4	220.5
-2	0.000	128.6	141.8	254.7

In this table, dashes represent calculations that failed as a result of no stationary point found on the potential energy surface. The optimised structure in each case is shown in Figure 88:
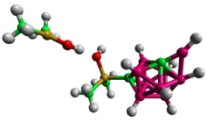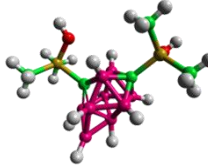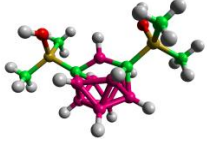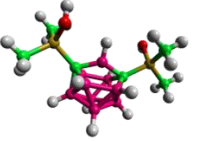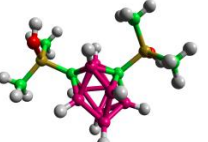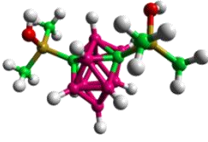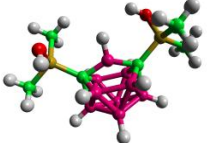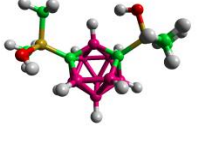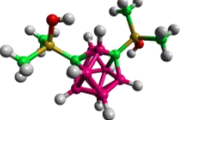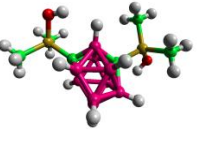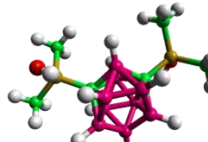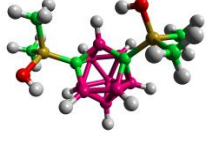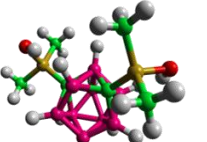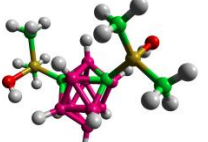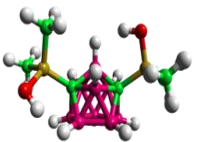
Residual charge	Vertex removed, optimised geometry			
	B1	B2	B3	B4
+2	-			-
+1				
0		-	-	-
-1				
-2				

Figure 88. Geometry optimised structures for damaged cage system

A few trends are immediately clear from the preceding figure and table. Firstly, with a 2+ state remaining on the damaged cluster, the calculation either fails, or produces a highly strained/unnatural stationary point. This suggests that if the removal of a boron vertex is accompanied by a removal of two electrons, there is likely to be a destruction of the cage. This may lead to boron oxide/ boron carbide solids in the material, as in the case when high temperature leads to cage degradation.

The -2 cases see the assumption of a *nido* configuration as anticipated by Wade's rules: that is, a closed boron polyhedron with one missing vertex (nido configuration), will be stable with four extra electrons, in this case provided by two carbon atom substitutions and the two electrons from the residual charge.

In the -1 case, B2 and B3 assume almost the same configuration, with similar energies, in a slightly distorted *nido* configuration. The B1 case is structurally very similar in

the +1 and -1 cases (a BH bridge is formed between carbon atoms), but is the most stable -1 case and least stable +1 case. The average charge on boron atoms is equal in the two states (+0.037), suggesting that the occupation of cage orbitals is maintained regardless of overall charge in the monomer. However, the +1 case sees more polarisation of key atoms (Si= +1.00, cage carbon=-0.65, bridging boron=+0.22, compared to Si= +0.69, cage carbon =-0.38, bridging boron =0.14 in the -1 case) in order to maintain cage orbital occupation, and the increased electrostatic repulsion between nearby carbon atoms is the likely source of the change in stability. The trend is repeated across the other +1 and -1 cases

The neutral cases all failed, or formed an unrealistic configuration, with a BH carbon bridge as in the B1 case.

All things considered then, impact events in the material are likely to leave some excess electron density in the cage, with some form of *nido* configuration, if the cage is not completely destroyed by the particles produced in the aftermath of a neutron capture event.

The frequency changes caused by removal of vertices are of most interest to experimental investigation of radiation damaged polymers. A few of the available modes are illustrated in Figure 89:
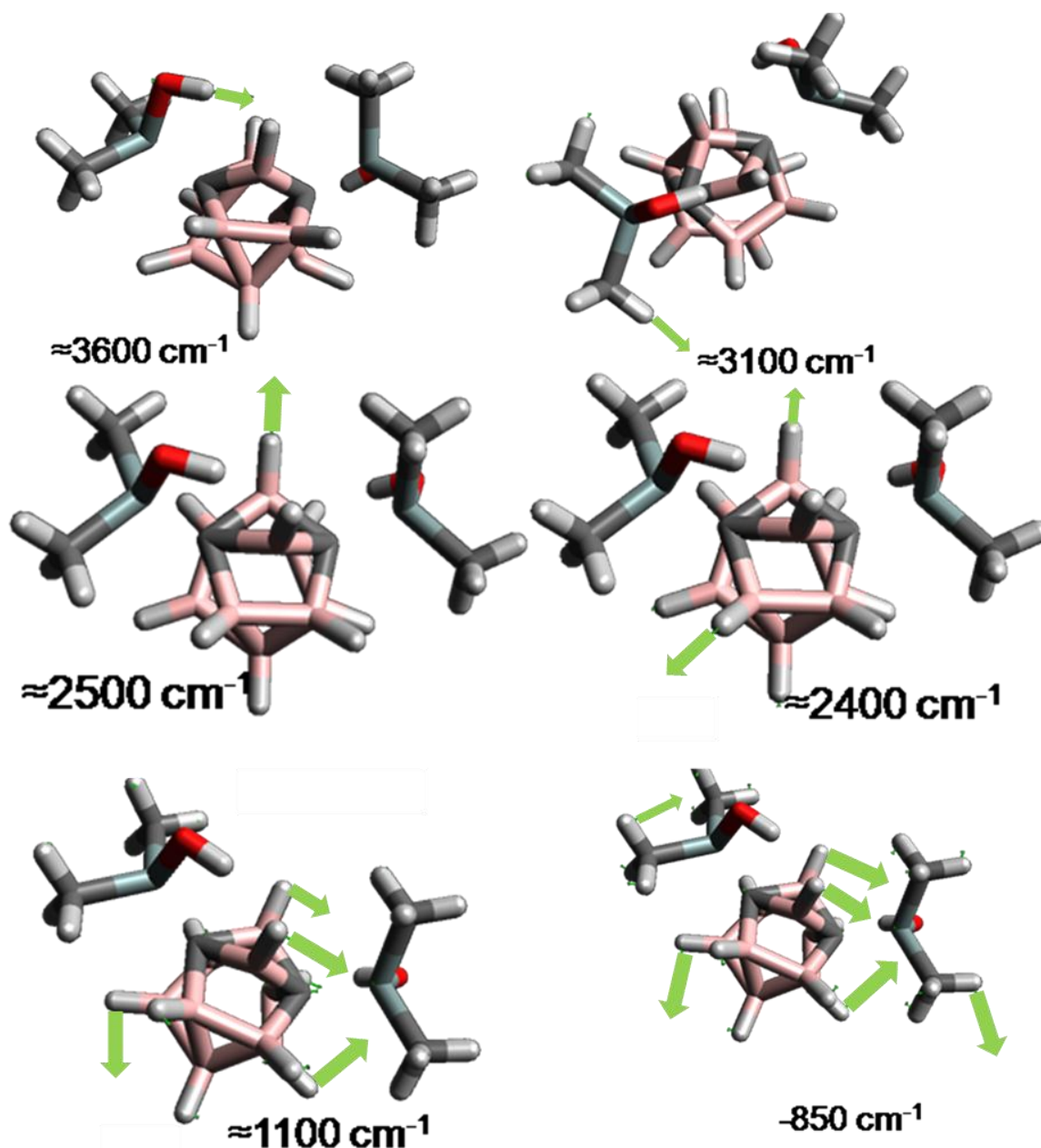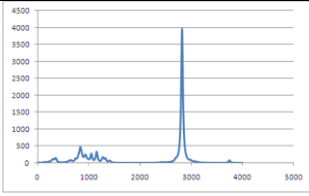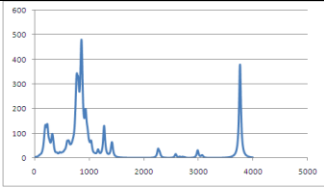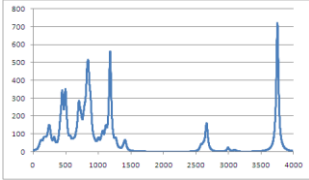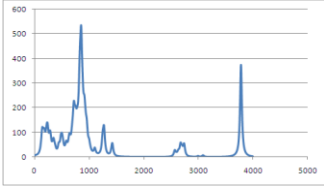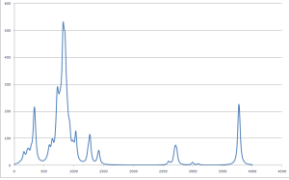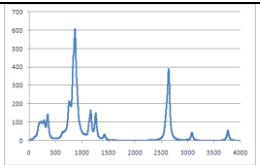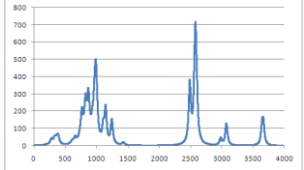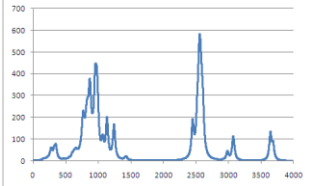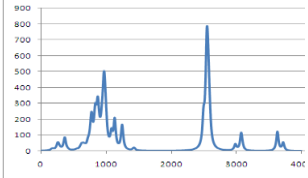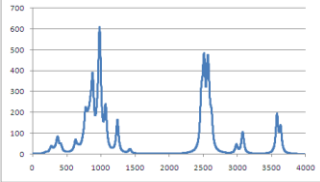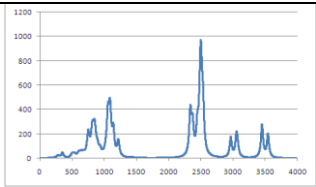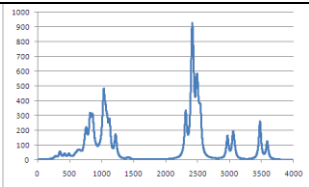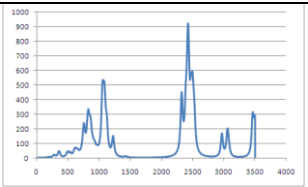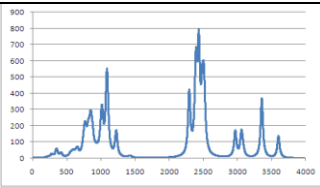
Figure 89. Vibrational modes in stable *meta* carborane monomer. Green arrows represent mode direction at that wavenumber (these have been manually increased in size to exaggerate their effect).

It is clear that the cage elements are most involved in the bands at ≈2500 and ≈1100 cm^{-1}, so it is expected that removing a cage vertex will have most effect on these bands. The vibrational spectra for each system are given in Table 9, the comparison with experiment is given in Figure 90, while the key spectra are collected in Figure 91:

charge	B1	B2	B3	B4
Table 9. Calculated vibrational spectra for damaged cage systems				
+2	-			-
+1	-			
0		-	-	-
-1				
-2				

Figure 90. Anionic damaged monomer's calculated vibrational spectra, with neutral undamaged and experimental infrared[53] (background grey plot) spectra overlaid. The aromatic C-H stretch is obviously redundant as phenyl groups are not simulated in this example, but other assigned peaks are picked.

Siloxane monomer with boron positions removed, -2 charge
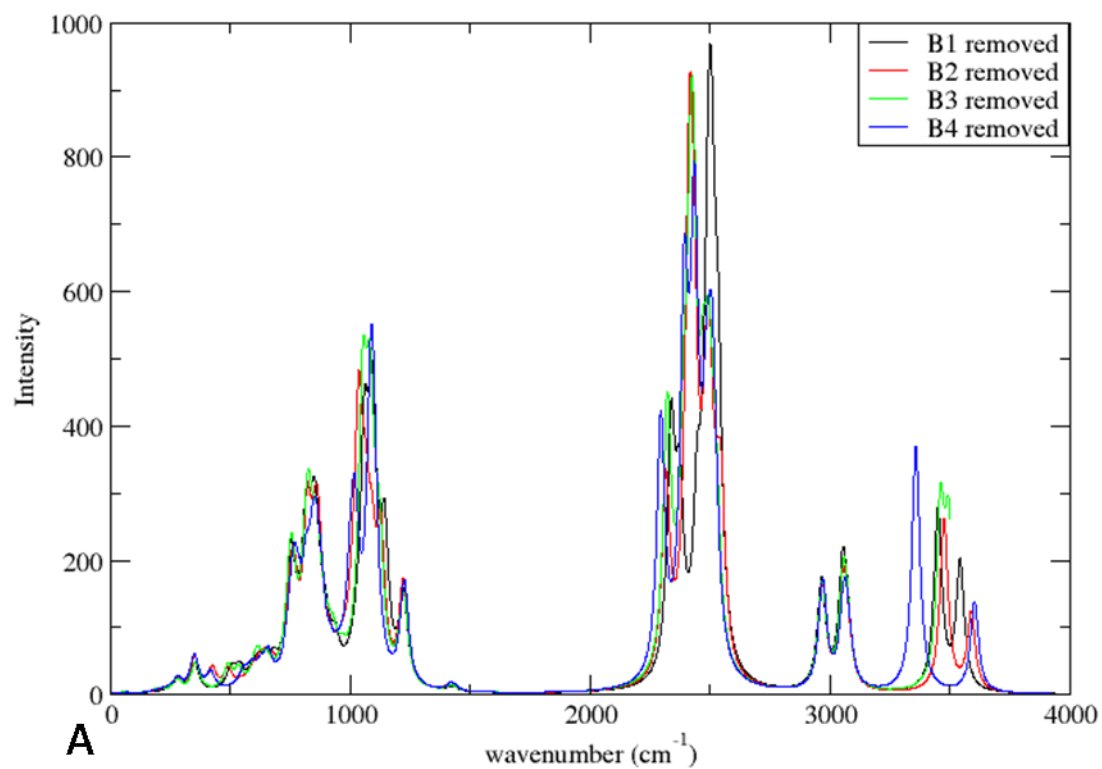
Siloxane monomers with boron positions removed, -1 charge
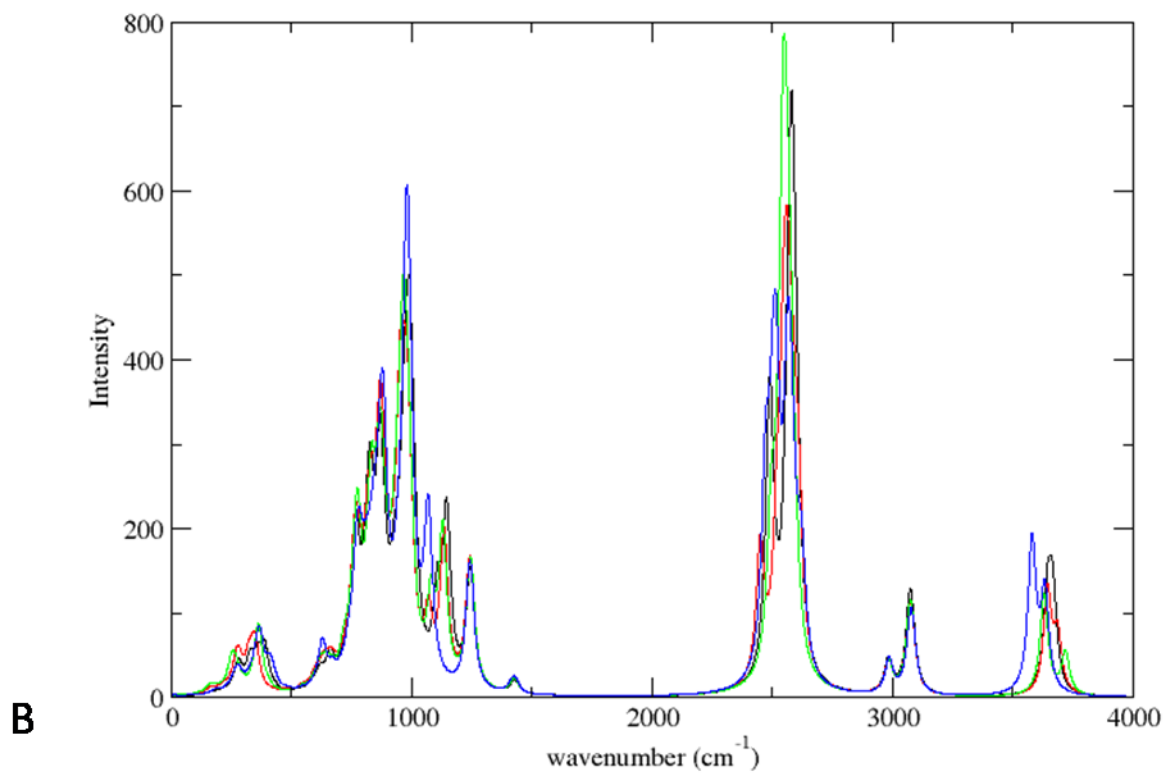
Figure 91. A: -2 charge, damaged cages spectra, B: -1 charge all cage spectra,

When comparing the neutral, -2 and -1 charge spectra, a few trends are clear. The largest change from neutral is in the band at ≈3500 cm⁻¹, which is the –O-H stretch, and in reality is likely to be a broad absorption due to hydrogen bonding with its surrounding environment[140].

For the cage modes, the peak at ≈2500 cm⁻¹ is moved to lower wavenumbers in all the -2 charge examples, which is the B-H breathing term. The peak is also split, as there is now lower symmetry and fewer equivalent B-H breathing modes. A vibrational peak moving to lower wavenumber is indicative of a reduction in bond strength, from Badger's rule[141], which is reflected in the changes in bond lengths, observed in Table 10. For reference, the average bond length in undamaged carborane monomer is 1.194 Å

Table 10. Average B-H bond lengths in optimised damaged monomer structures				
charge	B1	B2	B3	B4
+2	-	1.195	1.245	-
+1	1.191	1.194	1.194	1.193
0	1.197	-	-	-
-1	1.205	1.205	1.206	1.206
-2	1.220	1.220	1.220	1.220

Clearly there is little variation across molecules with the same charge, and that bond lengths are increased by 1.0 and 2.1% in -1 and -2 charge states respectively. This is an indication of a weakening of the B-H bond.

The band at ≈1000 cm⁻¹ is lower in the -1 examples than -2 examples, but both appear to have shifted up in wavenumber, suggesting a stronger bond. This band is representative of concerted B-H bond angle bending, and cage atom movement in relation to other cage atoms, suggesting that removing boron vertices leads to an inflexibility that is reflected in the vibrational spectra.

This could also be expressed as the orbital structure is indicative of strong electrostatic interactions in the damaged examples, as they have a missing node in the wavefunction and an area of localised electron density in one of the highest occupied molecular orbitals. The changes in orbital structure are therefore of interest in this investigation and the high energy occupied orbitals of the relevant species are shown in the following figures.
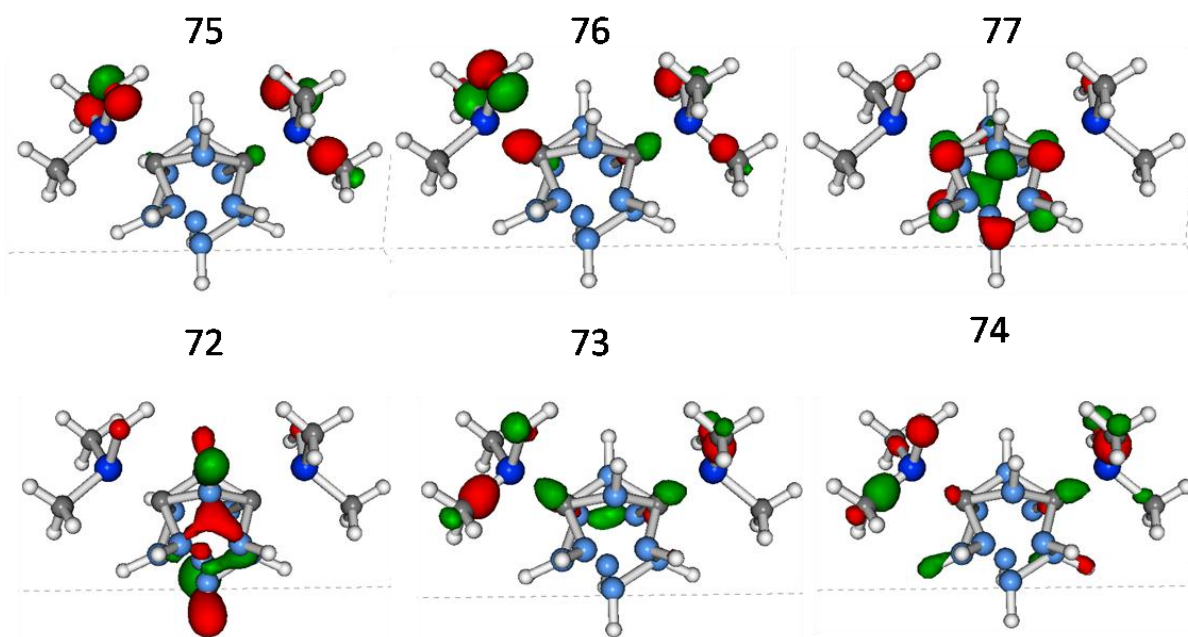
Figure 92. High energy occupied orbitals in undamaged carborane monomer. HOMO=77

-2 charge states
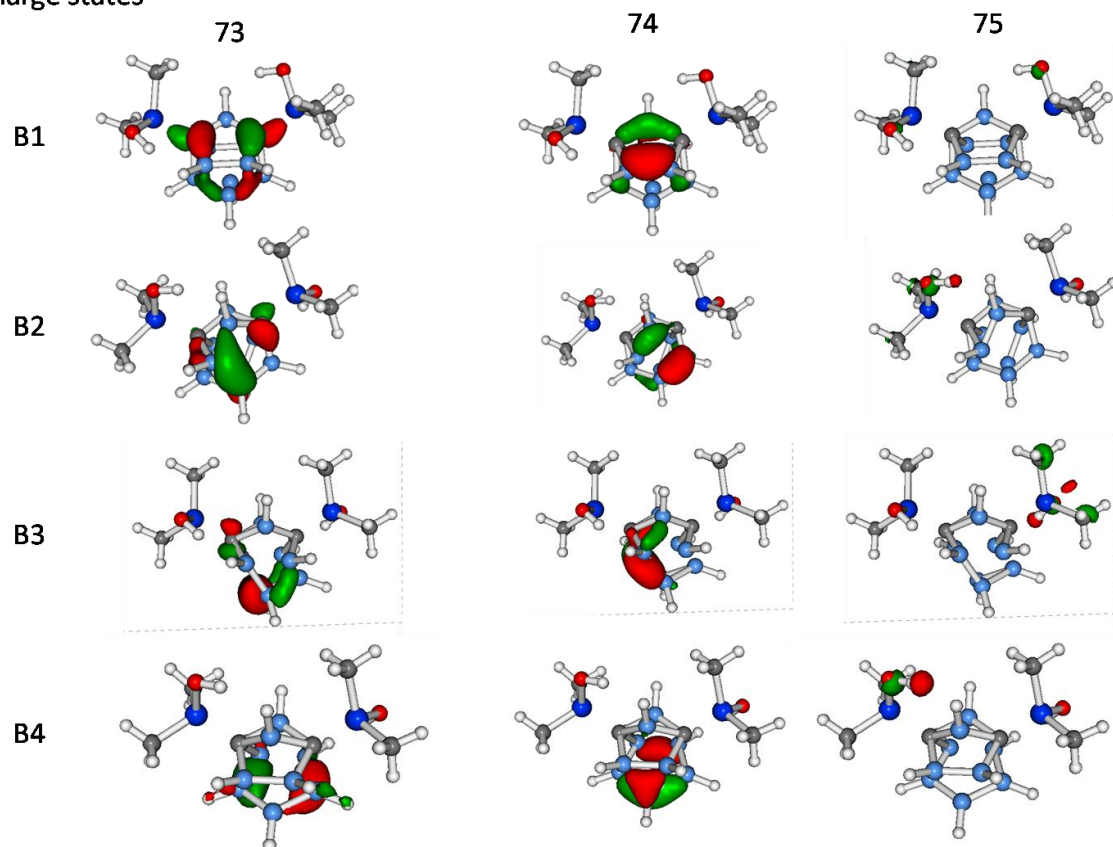
Figure 93. High energy occupied orbitals in damaged monomers, in 2- charge state. HOMO= 74

Analysing the orbital structure, it is clear that in all cases, the HOMO (which is orbital 74) in the -2 charge states is principally composed of the radial p orbitals of vertices closest

to the absent vertex. This is indicative of that specific orbital being destabilised by the radiation damage, in that the boron nuclei would normally be a node of the wavefunction. It shares symmetry with orbital 72 in the undamaged monomer, and the second highest band of orbitals in Figure 2.

Figure 94 shows the equivalent singly occupied orbitals in the -1 cases, where 149 is the SOMO (highest singly occupied molecular orbital), and 150 is the SUMO (lowest singly unoccupied molecular orbital) in all cases.
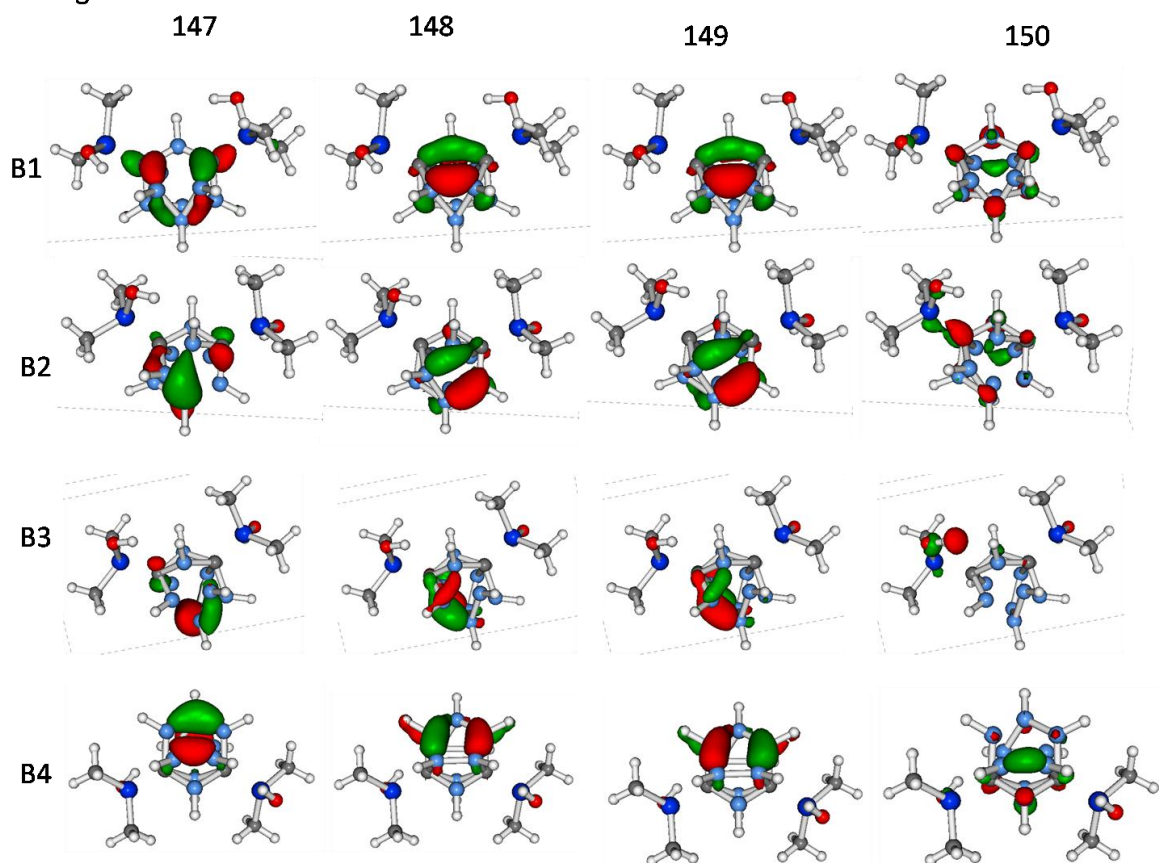
Figure 94. High energy occupied orbitals in damaged monomers, in -1 charge state, SOMO=149, SUMO=150

A more detailed analysis of the B4 −1 case is given in Figure 95. All electrons exist in orbitals with equivalent singly occupied orbitals nearby in energy, except for the 145 case, which is located where the vertex has been removed. Unpaired electron density is consequently found where the damage has occurred, which is responsible for the effect of cage bonding frequencies, in the same manner as the 2- case.

150

151

152

147

148

149

144

145

146

141

142

143

138

139

140

135

136

137
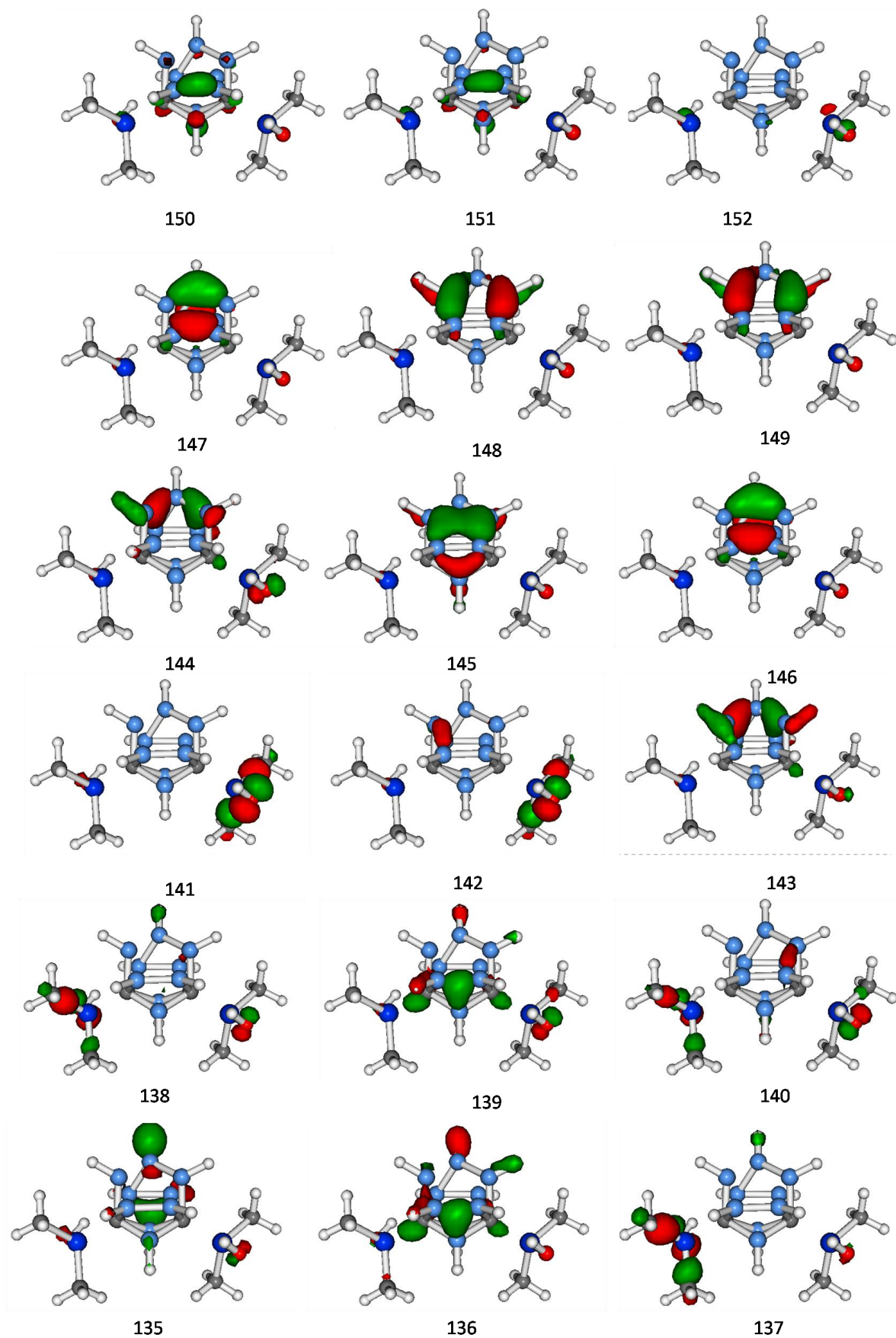
Figure 95. Single electron orbitals in B4 -1 damaged monomer

To conclude, it is expected that the removal of boron vertices from carborane monomers as a consequence of neutron capture events will leave electron density on the cage, providing the cage is not completely destroyed by the accompanying high energy ions. The extent of remaining electron density can be inferred from changes in the IR spectra of the damaged phases, where the B-H breathing mode ($\approx$2500 cm^{-1}) is moved to lower frequency, and the cage distortion peak ($\approx$1100 cm^{-1}) is moved to higher frequency, as a result of changes in orbital structure and bond strength.

5   Boron carbide impact studies

In view of the fact that: (i), the current industry standard material for the adsorption of neutrons is boron carbide embedded resins, and (ii) B-B and B-C terms for boron clusters in the forcefield used in this report were fitted to the experimental properties of boron carbide, it was decided to study this material further.

As alluded to in the introduction, covalent solids based on icosahedral boron units with linear chains composed of other atoms, show a remarkable resistance to radiation, maintaining crystallinity under high dosages of radiative impacts, of energy several orders of magnitude larger than bond dissociation energies[142]. This prompted two theories for healing mechanisms in icosahedral boron solids: (i) impacted atoms are displaced as cations, with electron density remaining on the icosahedron, with "self-healing" occurring as a result of electrostatic interactions between impacted atoms and cage, causing reassembly, and (ii) the inherent disorder in the solids allows impacted atoms to become part of chains, whilst icosahedra are reformed by replacing the impacted atom with a chain atom, without affecting crystallinity. These two theories will be investigated by classical and ab initio methods in the following chapters.

5.1   Methodology

Having derived a forcefield and tested it against various experimental properties, impact studies were performed using the DL_POLY 4 program on a 15 x 15 x 6 supercell containing 60750 atoms of volume 441900 $\mathring{A}^3$ (cell parameters: a=91.64, b=91.63, c=79.00). All simulations were carried out using the NPT ensemble at 298 K, at 1atm pressure, using a 0.001 timestep and 12.0 $\mathring{A}$ cutoff. An elastic impact was simulated by increasing the velocity of a targeted atom in a random direction with an impact energy of between 0.1 - 1.1 keV. 11 simulations were performed, on four atom-types (B1, B3, C1 and C4) creating a library of "damaged" phases.

Some of the damaged systems were further analysed at the *ab initio* (PBEPBE/6-31G**) level of theory, extracting the atom positions of the 45 atom unit cell that includes the impacted atom, as well as 1 unit cell in the positive and negative z direction, and for positive x and y directions (effectively a 2 x 2 x 3 supercell of the impacted atom's unit cell), for a 540 atom cell of volume 5106 $\mathring{A}^3$ from the DL_POLY molecular dynamics runs. This is a compromise between dilution of defect and computational cost. Single point calculations, geometry optimisations, and *ab initio* molecular dynamics were then completed using the CP2K program at the PBE/6-31G* level of theory.

The classical study was then repeated for a larger impact, using 12 keV. This is still a fraction of experimental energies, but results in much larger atom displacements, showing the effect of an impact on the structure at a greater distance from the impacted atom's original lattice position.

5.2   Classical low energy impacts

Initial calculations were performed by simulating impacts on a random selection of bulk atoms, revealing that the direction of impact and selection of impacted atom has an effect on the outcome of an impact simulation, but also that 0.1-1.5 keV is a useful range of impact energies to consider at these conditions (60750 atoms, a timestep of 0.001ps, a cutoff of 12 Å) in that a good number of displacement events were observed, but the energies were not so high so as to render the bulk of the simulations unstable. The changes in cell volume from these impact studies are shown in Figure 96, showing that the initial impact results rapidly in a slight increase in the cell volume, correlated to the impact energy. Over the course of the simulation (8 ps), the volume tends to reduce again for the higher-energy impacts but doesn't return to the original value. However the majority of the simulations were well-behaved in terms of energy conservation and temperature stability. Only those at 1.0 and 1.1 keV failed due to initial instability in the simulation:
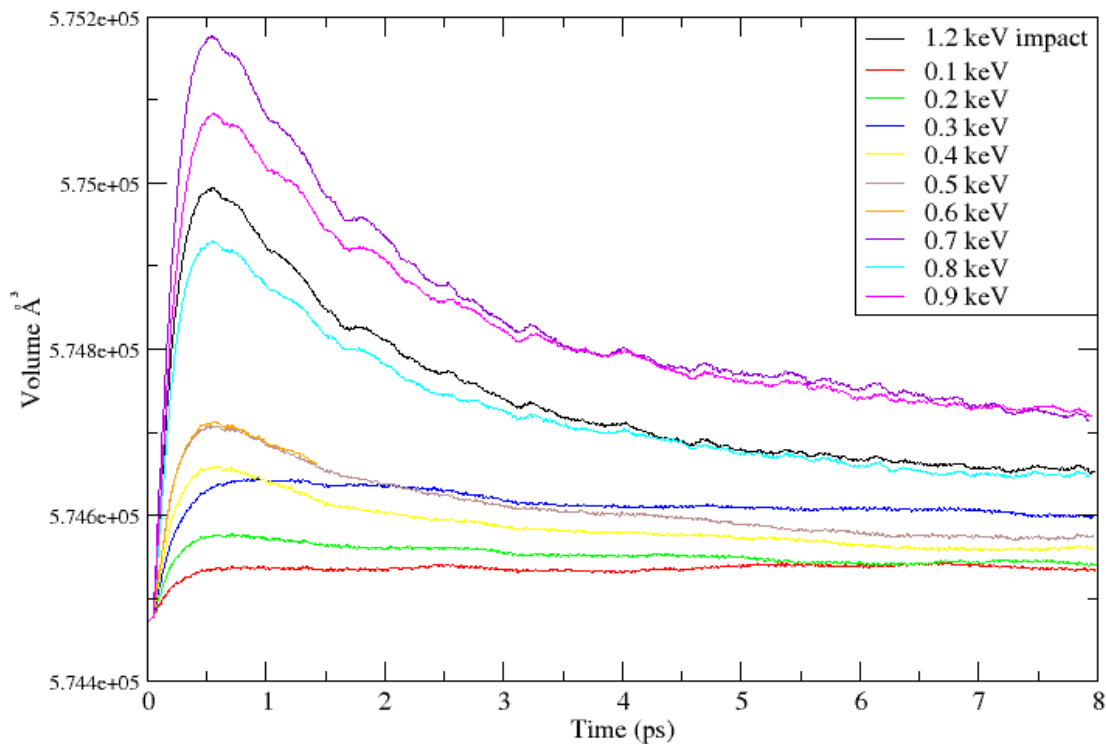
Figure 96. Changes in cell volume as a result of varying impact (classical studies) after 0.1-1.2 keV impact at 0.1ps

Further impact simulations were carried out on the four representative atom types, with the impact energy imparted in a random direction at each of the 11 energies. Displacements of impacted atoms 2.5 ps after impact are given in Table 11 (chosen after testing had shown that atom displacements stabilise after this time with these conditions), give an indication of whether a defect has been generated, while dashes indicate situations where the simulations failed, due to excessive cell volume changes. Similarly, 12 Å being the short-range cut-off, any atom displacements greater than this distance caused DL_POLY to fail. Below a cutoff of ≈0.6Å maximum displacement, the structure is regarded as having retained crystallinity, while above 3.0Å a defect has been generated, with an atom displaced from its lattice position. In the results given in Table 11, it can be seen that there is a clear distinction between these two types of outcome, with no displacement observed between 0.50 and 3.02 Å.

Table 11. Maximum atom displacements at impact energies				
Impact Energy (keV)	Displacement (Å) for atomtype			
	C4	C1	B1	B3
0.1	0.08	0.44	0.08	0.34
0.2	0.16	0.24	0.26	4.05
0.3	0.32	0.38	0.18	0.20
0.4	0.20	0.28	0.09	0.05
0.5	-	0.50	0.07	3.02
0.6	0.30	>12	0.14	0.34
0.7	0.23	-	0.19	3.59
0.8	-	>12	0.16	-
0.9	-	9.38	0.12	>12
1.0	-	0.41	0.08	>12
1.1	-	>12	6.75	>12

Broadly, below impact energies of 0.8 keV, displacements are consistent with crystallographic positions being retained. However there is evidence that some atom types are more easily displaced that others, for instance, B3 at 0.2, 0.5 and 0.7 keV impact, also suggesting that the direction of impact (chosen randomly in our simulations) is important in determining whether an atom will be displaced. At energies higher than 0.8 keV, combined

interstitial/vacancy defects are formed by displacement of the C1, B1 and B3. Stable defect structures were generated for C1 at 0.9 keV and B1 at 1.1 keV, in addition to the B3 cases already mentioned.

The defect energies of these systems were calculated using Equation 5.1, although we note that charge compensation is not modelled in the classical MD simulations.

$$E_{defect} = E_{undamaged} - E_{damaged}$$

Equation 5.1

Where $E_{undamaged}$ is the energy of the system at ambient conditions, before impact, and $E_{damaged}$ is the energy of the same system, having experienced an impact, and had atom positions stabilise at these conditions. The energies against time, for the B1 case are given in Figure 97:
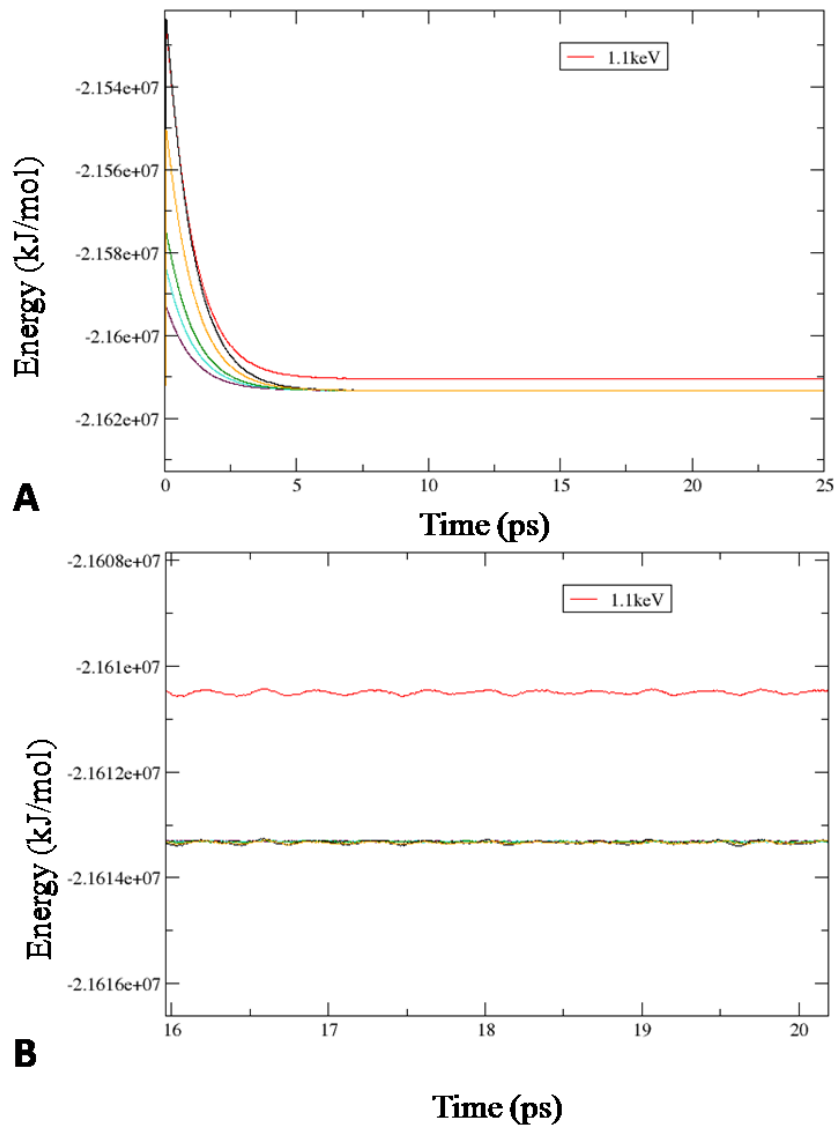
Figure 97. A: showing energy against time for B1 impacts. Energy returns to stable level at ~5ps, apart from defect scenario (1.1kev), as shown in zoomed in graph, B.

159

The effect on local structure for the example of a 1.1keV impact on a B1 atom is shown in Figure 98 which had a defect energy of ~2800 kJ/mol, calculated by comparing the energies of damaged and undamaged structures:
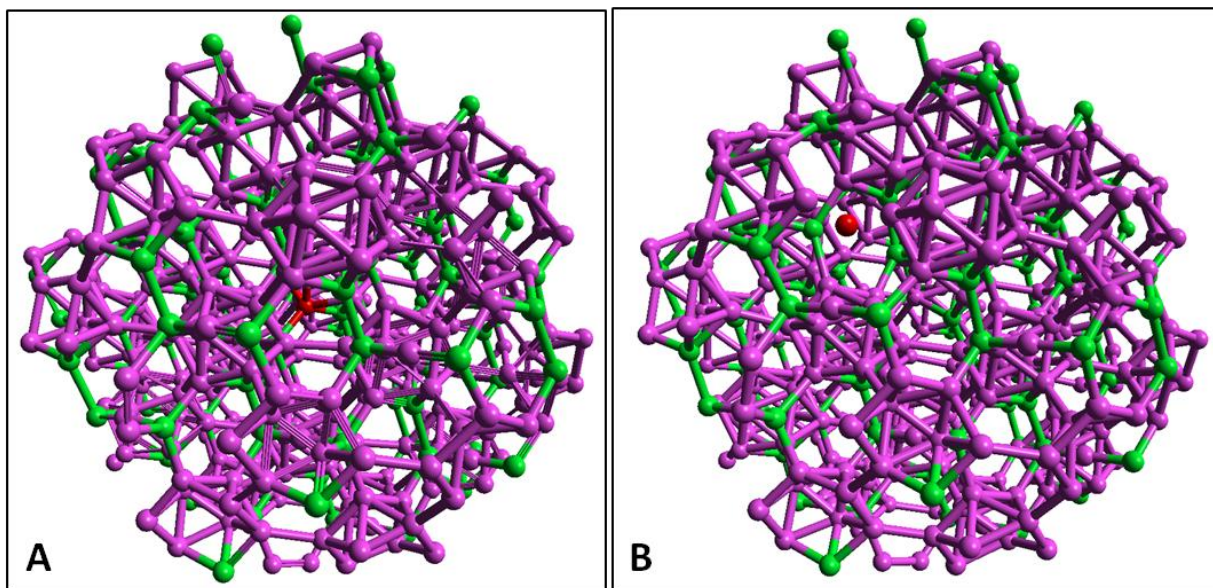
Figure 98. Structure within a 10Å radius of impacted atom in 1.1keV B1 study, A: before, B: 2.5ps after impact. Impacted atom highlighted in red

These results so far do not contradict either of the self-healing hypotheses, in that 6.75 Å is a distance over which Coulombic attraction is significant, and the movement of the impacted atom back to its lattice site could conceivably be achieved within the period of experimental observation (a timescale however that would be unreasonable to model using *ab initio* MD).

Figure 99. Mean square displacement of impacted atom, showing the stability of the impacted atom's new position (classical MD)

Other defect scenarios arising from impact on the B3 atoms are shown in Figure 100, although only the B1 impact of 1.1keV will be the subject of *ab initio* investigations.
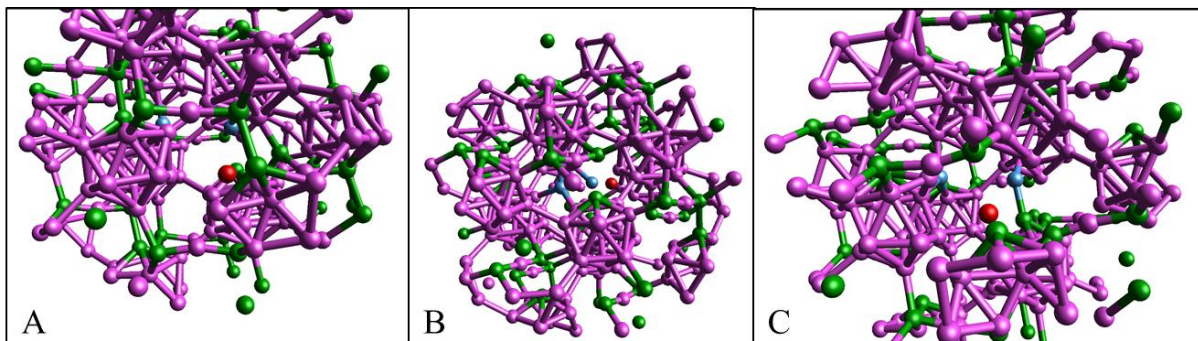
Figure 100. B3 defect scenarios, from classical impact studies. A: 0.7 keV, B: 0.5 keV, C: 0.2keV. impacted atoms are highlighted with red spheres, whilst the chain atoms with which they were initially bonded are highlighted with blue spheres

As can be seen, the chain boron atoms, upon impact, find stable defect positions between layers of icosahedra, in the pocket formed by bonds between three icosahedra in one layer, and one icosahedra in another layer, shown in more detail in Figure 111. In the case of Figure 100B, the impacted atom is still bonded to a chain carbon, where the random impact generated was mainly along the z vector (0.548   0.465   0.894). This was therefore sufficient to break the carbon to boron bond along the negative z vector, but not the positive one.
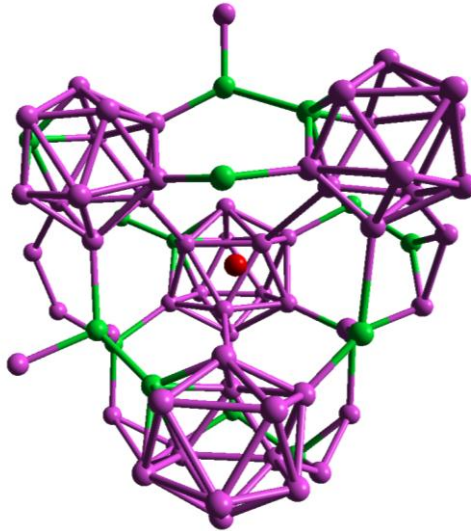
Figure 101. Common structure surrounding the interstitial defect atom (highlighted in red).

5.3   *Ab initio* calculations on damaged phases

In order to further explore this second theory, *ab initio* calculations were carried out on the damaged system: as stated previously, the defects generated by low energy impacts were analysed by selecting the local structure around the defect (1 unit cell in the positive and negative z direction, and for positive x and y directions from the initial impacted atom's lattice site). This supercell includes the impacted atom and its original cage, which are assumed to be distinct and non-interacting. Using the example of the 1.1 keV impact on a B1 atom, the geometry optimisation of the damaged system found a local minimum whereby the impacted atom inserts into a nearby "chain carbon to icosahedral boron atom bond" to become a pseudo 4 atom C-B-C-B chain, with some resultant buckling of the chain, as shown in Figure 102. In this manner, the chain is still a double tetrahedral unit, connecting two hexagonal layers via bonds to three icosahedra in each layer, but one of the C-B_{cage} bonds has changed to C-B_{int}-B_{cage}.

An example of the buckling alluded to earlier is seen in the (previously linear) chain adopting a C-B-C angle of 161.19˚, whilst the previously tetrahedral (114.9˚) bonds from chain to icosahedra adopt an angle of 132.55˚, as seen in Figure 102A. The bond lengths are also changed: the B_{chain}-C_{chain} bond diverges from ≈1.50Å to 1.475 and 1.539Å, and the C_{chain}-B_{cage} bonds are reduced from an average of 1.797 Å to 1.737 Å , whilst the bonded-to icosahedra also have a change in bond lengths: ≈1.89 Å to ≈1.82Å. In this manner, the structure accommodates a change in chain composition.
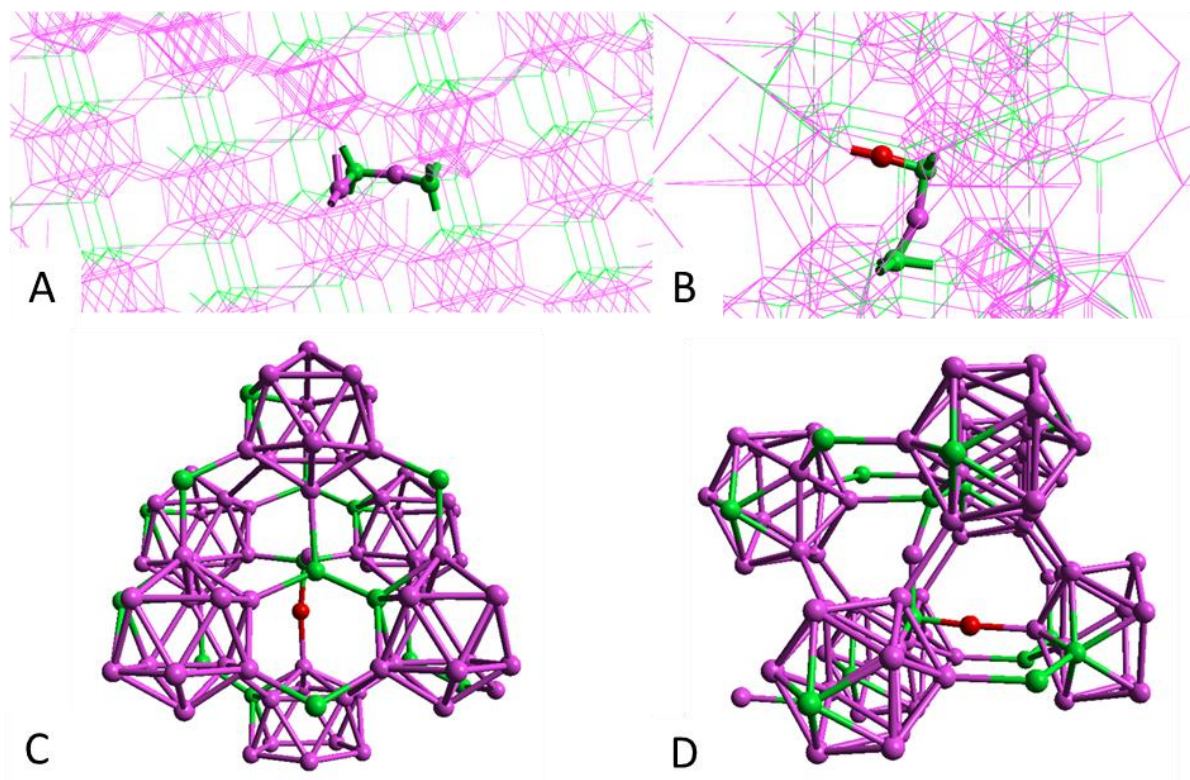
Figure 102. Impacted atom's insertion into chain. A and B: The chain in question is highlighted with spheres, while the surrounding structure is depicted using stick display. The original impacted atom is highlighted in red., C and D: just local surrounding structure of defect shown

The impacted cage assumes a *nido* configuration, as shown in Figure 103. A *nido* boron cluster is stable when it has 2 electrons more than the *closo* equivalent, so it is unsurprising that the atoms involved have a net change (from the pristine example) in charge of -0.79 electrons; while not the full compensating charge, it shows how the electronic structure accommodates the loss of an icosahedral vertex.
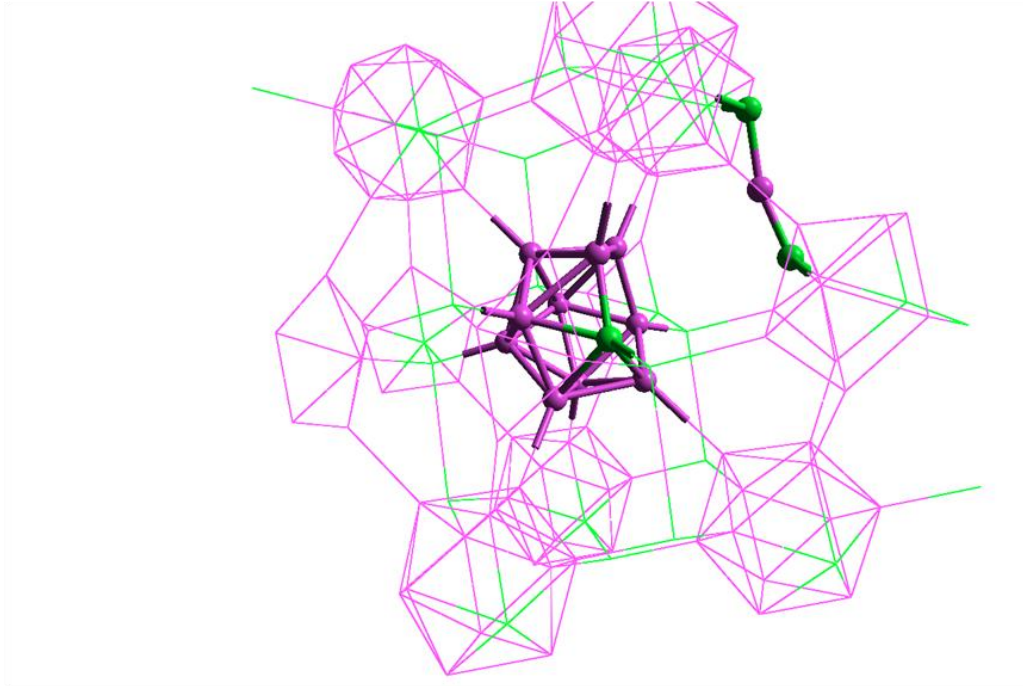
Figure 103. Impacted cage assuming *nido* configuration, highlighted with spheres

This produced a defect energy of 783.51 kJ/mol when the optimised unimpacted structure energy is subtracted, as shown in Equation 5.1. *Ab initio* MD simulations at ambient conditions for 500 fs did not see any extraction of chain atoms into the impacted cage, although this does not approach the period of observation.

However, these results are in support of the second theory, in that the interstitial and defect sites don't recombine, but are quenched locally, by taking advantage of the substitutional disorder of chains.

5.4 Classical high energy impacts

To compare with the low energy displacements, the simulation conditions were altered (cutoff extended to 36 Å, to allow atoms to become significantly separated without causing an error in the software) and, as noted previously a 12 keV impact was simulated.

At this higher impact energy (still fractions of experimental energies ≈160keV[66]), the impacted atom is displaced by 20 Angstroms in 1.0 ps, invalidating the "self-healing" mechanism as proposed by Emin et. al., as columbic interactions between impacted atom and original lattice site are less significant at this range, especially when it is considered that the vacancy and interstitial are shielded by six icosahedral units. The damage to crystal structure is seen in Figure 104.
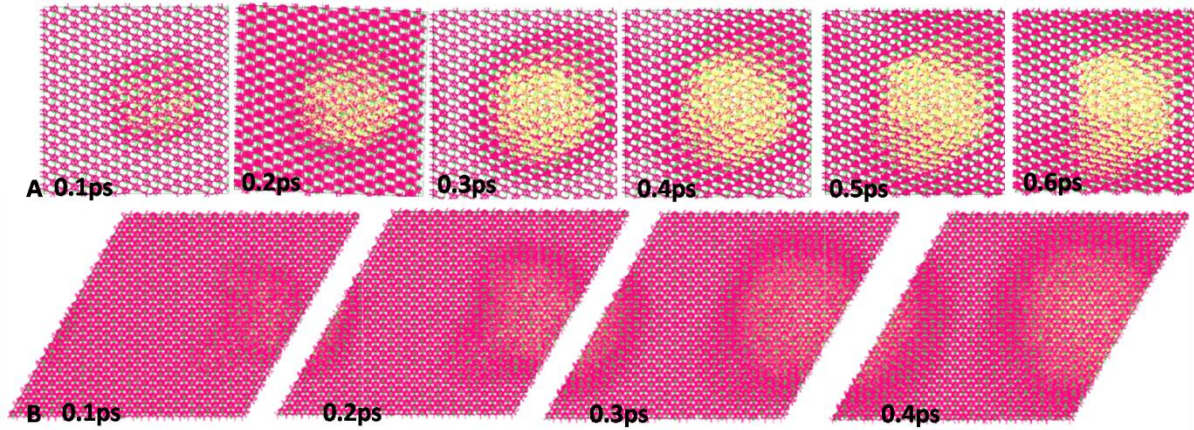
Figure 104. Showing Boron Carbide (60750 atom system), at 0.1 ps intervals following 12 keV neutron impact, viewed along the axis of neutron impact. Atoms that are displaced more than 1.5 angstroms are highlighted in yellow. A: views along the direction of impact, B: views perpendicular to impact direction.

These results would therefore be consistent with the theory that damaged icosahedra subtract a chain atom to complete the cage bonding set, whilst the impacted atom exists as an interstitial, or combines with a nearby chain. This would not affect the crystallinity of the system, since there is an accepted random nature to composition of chains[143], as acknowledged in the introduction.

5.5   Surface calculation

It was decided to extend the bulk boron carbide impact calculations presented here by analysing the effect on a boron carbide surface: the electron/neutron/N^+ impacts will almost certainly be experienced by surface atoms, so this investigation will be experimentally relevant. The investigation was reduced in size, in order to reduce the computational effort.

A surface was therefore created by taking a 4x4x4 supercell of bulk boron carbide and removing those atoms above or below a certain threshold of z position, using a simple python code[1]. This created a surface displayed in Figure 105, representative of a (110) surface, composed of a user defined amount of layers of icosahedra and chains. The dangling bonds created by cleavage of the surface were populated by hydrogen atoms, a process included in the code.
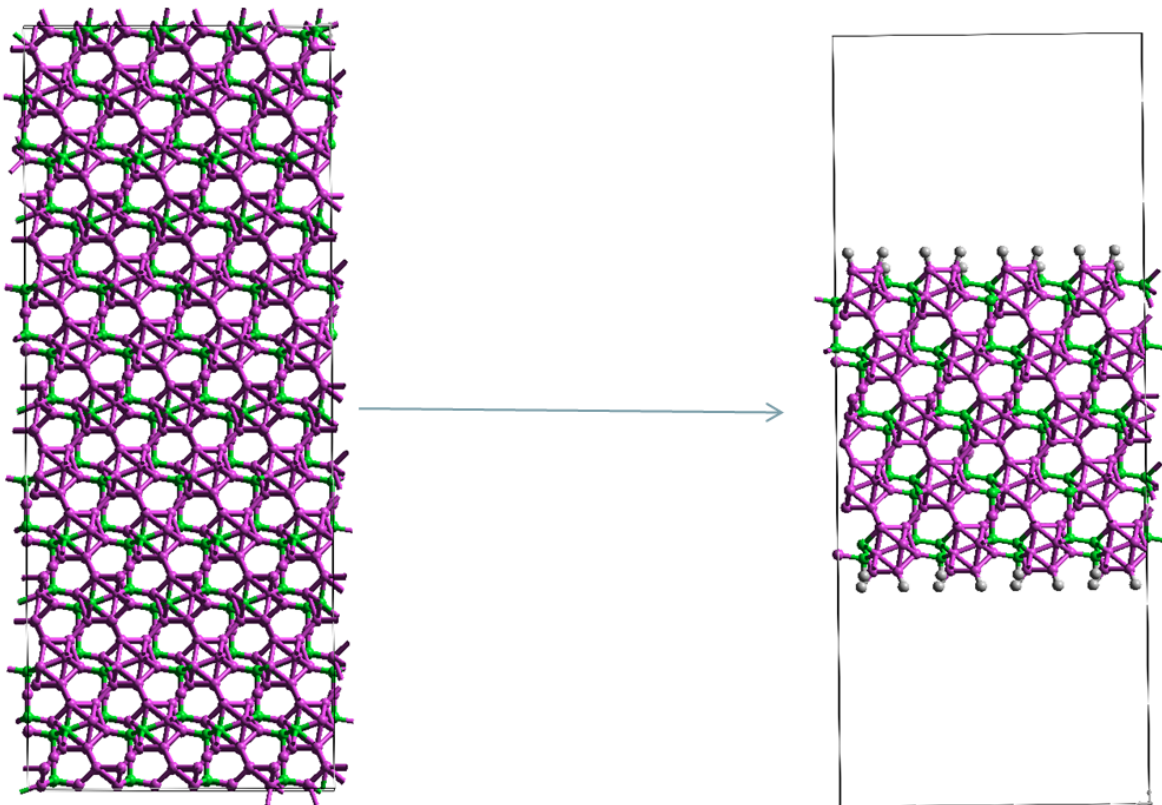
Figure 105. Creation of a boron carbide surface

Hydrogen atoms were chosen to populate the surface, as this   would allow use of B-H forcefield terms already derived in Table 5, whilst C-H bond single bond stretching terms were taken from the pcff forcefield. There is evidence[144] to suggest that a boron carbide

surface is likely to be populated by boron oxide and –OH groups rather than bare hydrogen, but this would have required the fitting of more potentials, and for a simple classical calculation intended to show the change in bulk and surface responses to radiation, this model is considered sufficient. The many examples of boron icosahedral clusters terminated by hydrogen atoms also suggest that this is a valid approximation of the boron carbide surface. It is also noted that this is not the only boron carbide surface available[144] (in terms of lattice planes), but as theoretically the most stable, will be most representative of surface response.

It was decided to use the example of 4 layers, after *ab initio* optimisation of slab thickness had shown that this represented a stable slab, with opposing surfaces distinct and non interacting, and bond distances in the middle two layers equal to those in the bulk.

The cell *c* parameter (controlling the gap thickness due to the surface being (110)) was optimised as shown in Figure 106. Clearly the opposing surfaces are interacting most stably at $c \approx 17$Å, and could be considered distinct and non-interacting at ≈ 25Å; given that the impact calculations would potentially cause some changes in the surface, it was decided to add an arbitrary 20Å to the *c* parameter, for a total of 48.257Å. This allows a buffer zone, and ensures surfaces don't interact through PBC, during the course of these non-equilibrium scenarios.
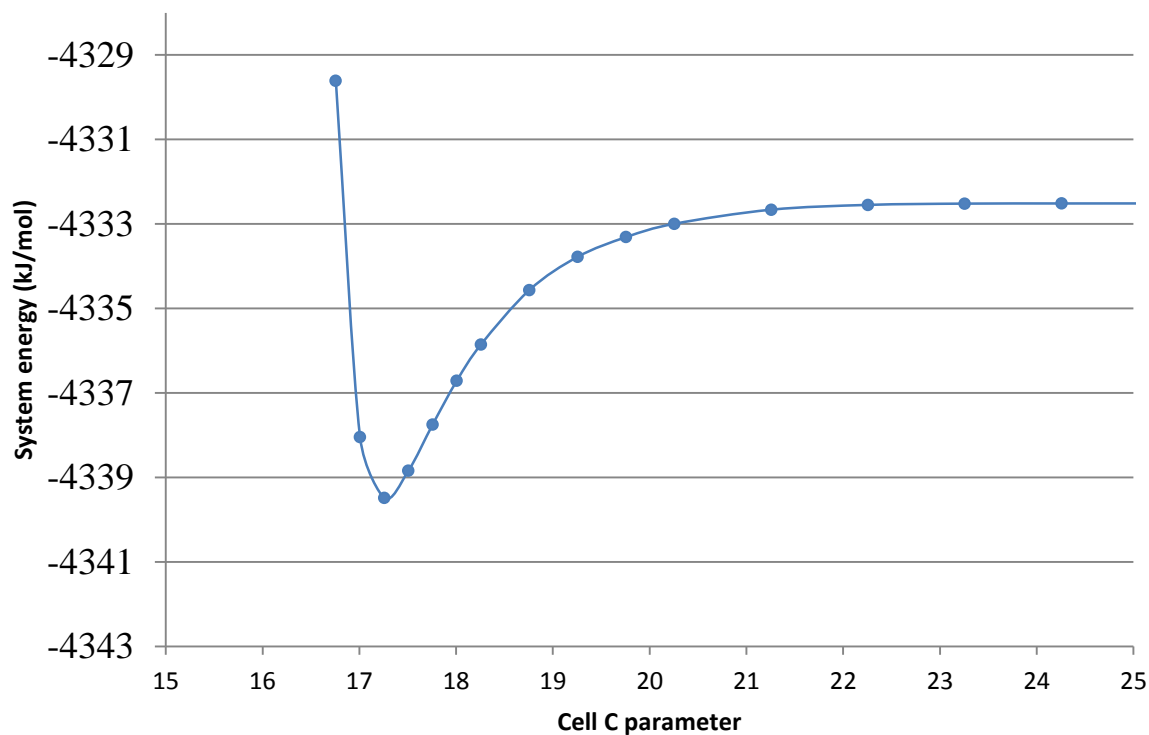
Figure 106. Optimisation of cell *C* parameter in boron carbide 4 layer surface experiment

Having created the surface as described above, the system was optimised using GULP, and then stabilised at ambient conditions using NPT MD. The surface energy was calculated by taking the bulk lattice energy for the large system, dividing by the amount of boron and carbon atoms in the surface example, and subtracting the stable lattice energy in the surface, before dividing by the surface area, giving a surface energy of 6.114775 kJ/mol/Å^2.

10 impacts were simulated in the range 0.1-10 keV, in the [00$\bar{1}$] direction, on a boron atom in the first layer of the surface. The mean squared displacement of the impacted atom over 10ps for the range of impact energies are shown in Figure 107.

Figure 107. MSD graph, showing the effect on position of impacted atom in impact calculations of different impact energies

As can be seen, the impacted atom is stable below impact energies of 0.3 keV, whilst at 0.5keV is displaced from its lattice site. However, upon closer inspection, it was clear that at relatively low impact energies (0.275-0.3keV) the damage generated by the impact was sufficient to throw out a distinct icosahedron into the gap, on the opposite surface to the impacted atom, as shown in Figure 108.
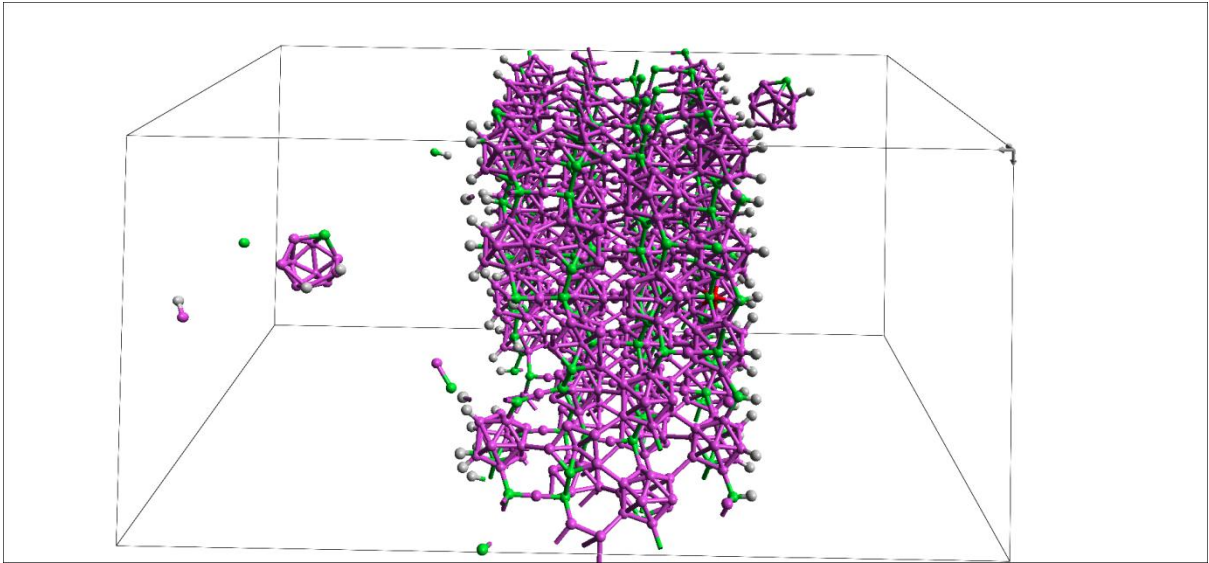
Figure 108. Injury to boron carbide surface following neutron impact. Impacted atom highlighted in red

Obviously, this behaviour is not representative of a surface experiment, since actions on one surface should not be expressed on the opposing surface, and the slab should be representative of the infinite bulk.

As a result it was decided to extend these investigations with a thicker slab, composed of 8 layers of icosahedra. The impact energy range was replicated, producing similar mean squared displacements as seen previously, however a relatively low (0.275keV) energy impact on one surface, again has the effect of displacing an icosahedra on the opposing surface, as seen in Figure 109.
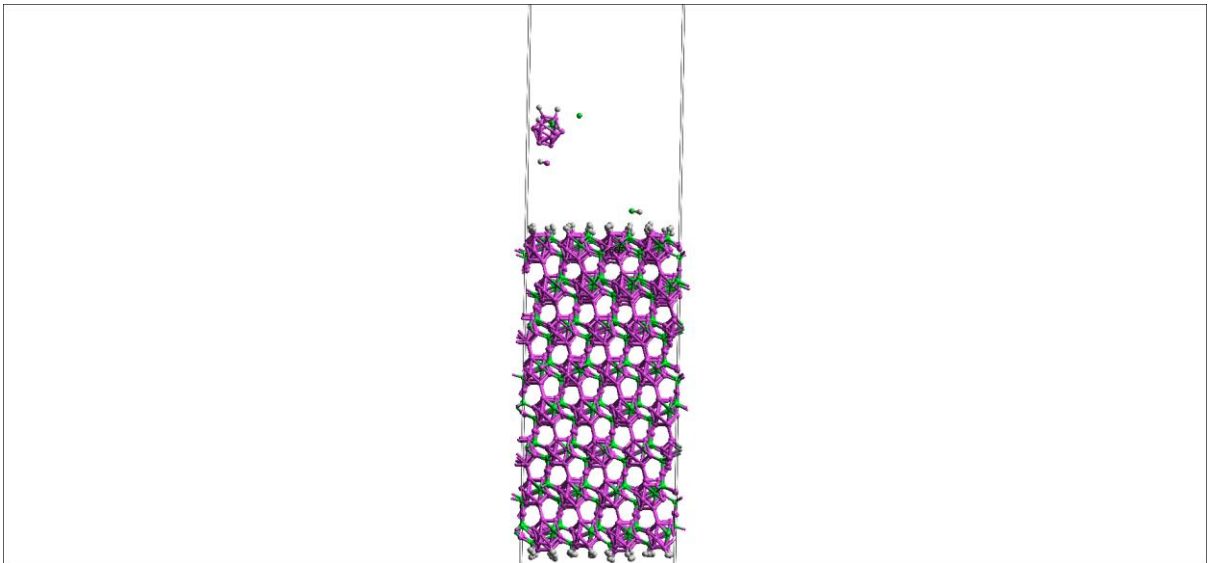
Figure 109. Injury to 8 layer boron carbide surface, impact arrives from the bottom later.

As a result of this, it was decided to conclude surface impact calculations, and rely on bulk calculations to indicate the material's response to radiative impacts. However, these results are indicative of the fragility of boron carbide thin films, which is an emerging technological area[145].

6   Thermal rearrangement of carboranes

This body of work was published as a communication[146].

The three possible isomers of dicarba-closo-dodecacaborane $C_2B_{10}H_{12}$ (commonly referred to as carboranes) exist in a stability series, where thermodynamic stability is determined by carbon atom separation: *meta*-$C_2B_{10}H_{12}$ is more stable than *ortho* but less than *para.* This is borne out by experiment in that *ortho* carborane (1,2-$C_2B_{10}H_{12}$) will irreversibly rearrange to *meta*-carborane at raised temperatures[147], and *meta* (1,7-$C_2B_{10}H_{12}$) rearranges in a dynamic equilibrium to *para* (1,12-$C_2B_{10}H_{12}$)[19]at higher temperatures, as shown in Scheme 8:

$$o - C_2B_{10}H_{12} \overset{(i)}{\rightarrow} \quad m - C_2B_{10}H_{12} \overset{(ii)}{\rightarrow} \quad p - C_2B_{10}H_{12} \qquad \text{Scheme 8}$$
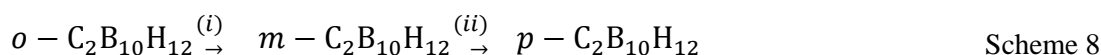
Where (i) is 675 K, and (ii) is 925–975 K. The internal dynamics of carboranes are of interest for a number of reasons: Applications are emerging for carboranes at elevated temperatures in catalytic[148], biological[55,56] and solid state[49] applications. Knowledge of how molecular rearrangement might affect macroscale properties is therefore essential. Complexation of metals by carboranes appears to lower the rearrangement barrier to ambient conditions[149,150], affecting their macroscale properties[6].There have been several theoretical[57] and experimental[58,151] investigations into the mechanisms of rearrangement. No consensus has been achieved, although much useful information has been derived. For instance, isotope labelling of boron positions in the carborane systems has enabled the rates of reaction to be measured, as well as showing a complete scrambling of boron positions, suggesting either boron to boron rearrangement mechanisms exist, or several carbon rearrangement mechanisms, or both.

Finally, within the context of this report, the rearrangement of molecular carboranes appears to have an effect on the macroscale properties of carborane incorporated siloxane polymers. As a result, it was decided to investigate the theoretical reasons for thermal rearrangements, using *ab initio* MD, detailed in the following sections.

6.1   Methodology

The molecules *ortho-* and *meta-* carborane ($C_2B_{10}H_{12}$), borane ($[B_{12}H_{12}]^{2-}$), and the smaller, bicapped- pentagonal pyramid carborane ($C_2B_5H_7$) were all inserted into a large box (cube with 10Å sides). This isolates the molecule, which is fair as the process is almost certainly intramolecular. They were then simulated for ≈ 20 ps at a range of temperatures, principally every 10 K from 3000-3500 K. The smaller carborane was chosen, as it also exhibits rearrangements[152], and would hopefully shed light on some of the processes as it is a

simpler system. Borane was also simulated, as a more symmetrical system could also illuminate the orbital progression.

A rearrangement is judged to have taken place when the connectivity of the vertices is different at the start and finish. Where this is evident, snapshots of rearranging molecules every 1 fs were geometry optimised at the same level of theory, in order to scan for potential intermediates, with transition state searches between products, intermediates and reactants. Where no intermediate was found (i.e. all frames optimised to reactant or product), then the last molecule to optimise to reactant and first to optimise to product were chosen. One optimisation step was performed, principally to clean up hydrogen distances and reduce imaginary frequencies. TS searches were then performed between these "pseudo intermediates" and reactants and products, to establish the TS that typifies that rearrangement mechanism. This method of establishing a reaction coordinate is incomplete because orbital symmetry is ignored, but is still useful, and will be used to show where node inversions take place.

6.2 *Ortho-meta* carborane rearrangement

For the fifty temperatures sampled from 2500-3000 K, there were 14 rearrangements observed, that involved the movement of carbon positions relative to each other. As well as these, there were several rearrangements involving boron vertices (which in itself is interesting, as it confirms that tracking the reaction experimentally, by isotope labelling, is an impossibility since boron positions will be scrambled[58])

Using the scheme detailed above, three independent processes were identified for *ortho-* to *meta-* rearrangements: TFR, non-TFR and nido mechanisms, which were observed 5, 6, and 3 times respectively. These names were chosen in order to compare with mechanisms identified by Brown and McKee.[57], using conventional potential energy surface sampling. The TFR mechanism appears to be similar to the Brown and McKee TFR mechanism, with one TS, however there is more symmetry observed in the example found through our technique. This may be due to differences in computational thoroughness (our results use PBE/6-31G*, Brown uses B3LYP/6-31G++) and requires further investigation. However the non-TFR mechanisms appear identical. The nido mechanism appears to be unique. It has fewer examples than the others, which suggests it might be a non-orbital symmetry allowed process. More detailed analysis of each process is given below.

6.2.1 TFR mechanism

For the TFR mechanism, the PBE level of theory reaction coordinate is given below:
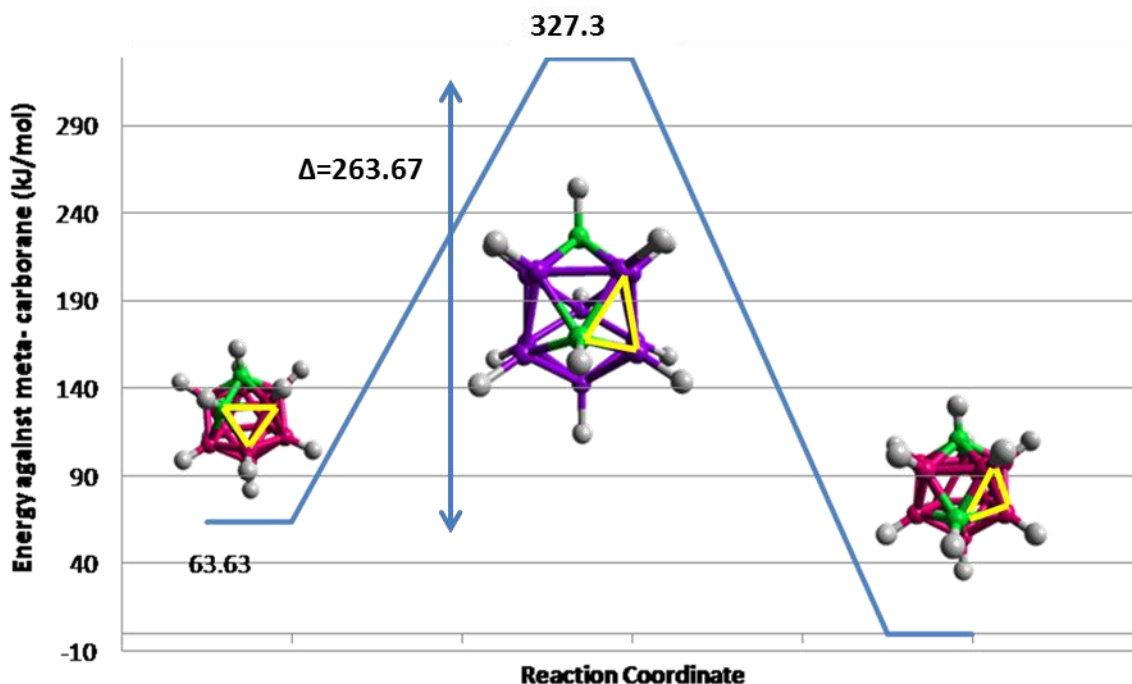
Figure 110. *Ortho* to *meta* carborane rearrangement, TFR mechanism. Rotating triangle indicated by yellow triangle.

It is worth noting that the TFR (triangle face rotation) mechanism refers to a triangular face, which maintains its own connectivity, rotating and changing the connectivity of every vertex in the triangle. While this is true in some cases, several cases saw boron atoms other than those involved in a carbon containing triangle move back into the upper pentagon (as viewed in Figure 110), to remake the icosahedron. Therefore, referring to the mechanism as the Triangle Face Rotation mechanism is a matter of convenience.

This has several consequences. Firstly, it reinforces that trying to follow the rearrangement using isotope labelling is impossible, as boron positions aren't fixed in the process. Secondly the activation energy is much higher in this investigation than in the Brown paper; 264 and 207.6 kJ/mol respectively. This, coupled with the higher symmetry observed in this investigation's transition state, suggests that the processes are non-equivalent. If so, then it is surprising that the Brown TFR mechanism, with lower activation energy, is not observed in the MD calculations, unless it violates orbital symmetry. The higher level computational techniques used in the Brown paper are noted, but it does suggest that further investigation into orbitals as they progress through the mechanism is required.

6.2.2 Non-TFR mechanism

For the mechanism referred to as the Non-TFR mechanism, the reaction coordinate is given below:
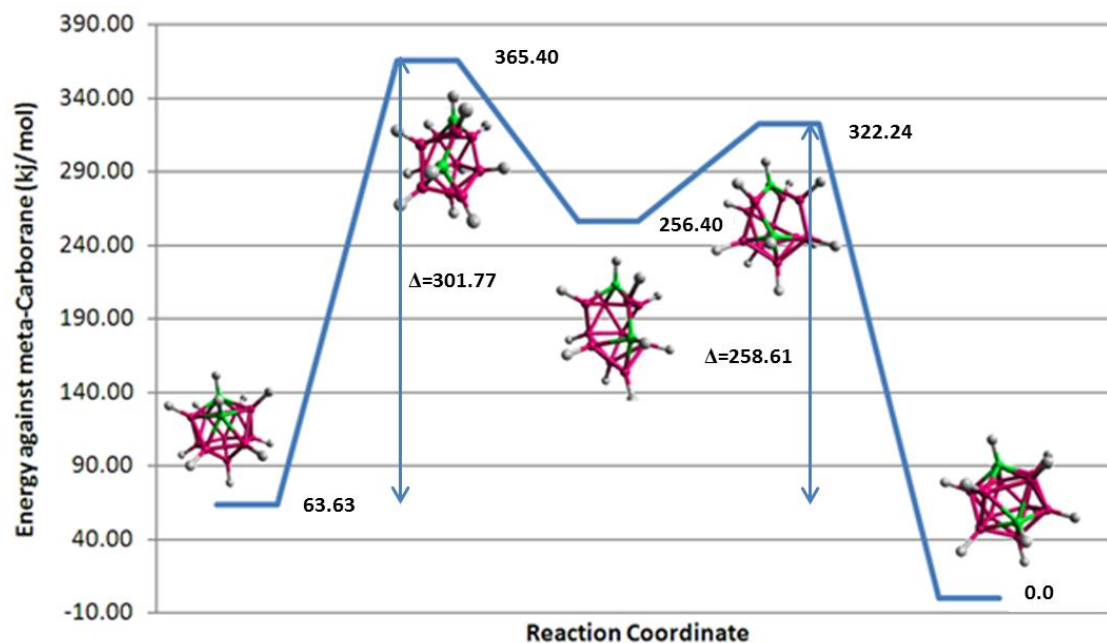
Figure 111. *Ortho* to *meta* carborane rearrangement, Non-TFR mechanism

In this instance, as noted, the similarities are much more striking when compared to the Brown equivalent, which is shown in Figure 112.
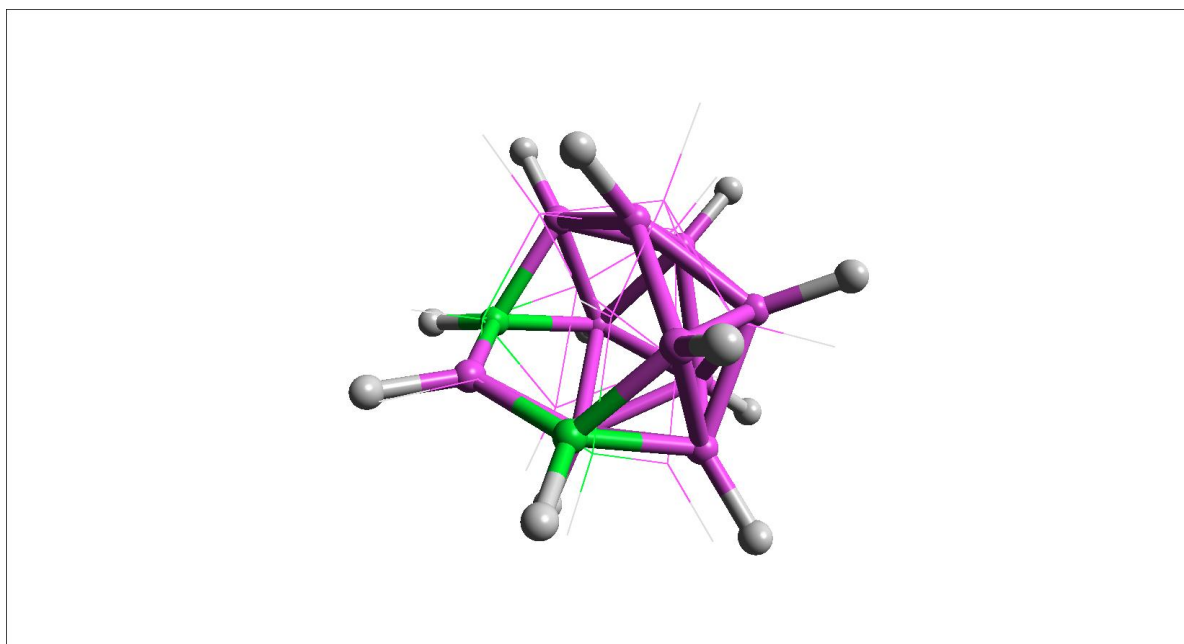
Figure 112. TS1 from this investigation (ball and tube display) and Brown et. al. (stick display)

The activation energies are comparable: 315.9 in Brown and McKee and 302 kJ/mol in this example. More pertinently, the shapes of molecular species are much closer. However, it is still worth noting that there are two boron positions liable to change connectivity, again underlining the difficulty of following the experiment with isotope labelling.

6.2.3 Nido mechanism

The nido mechanism reaction coordinate is given below:
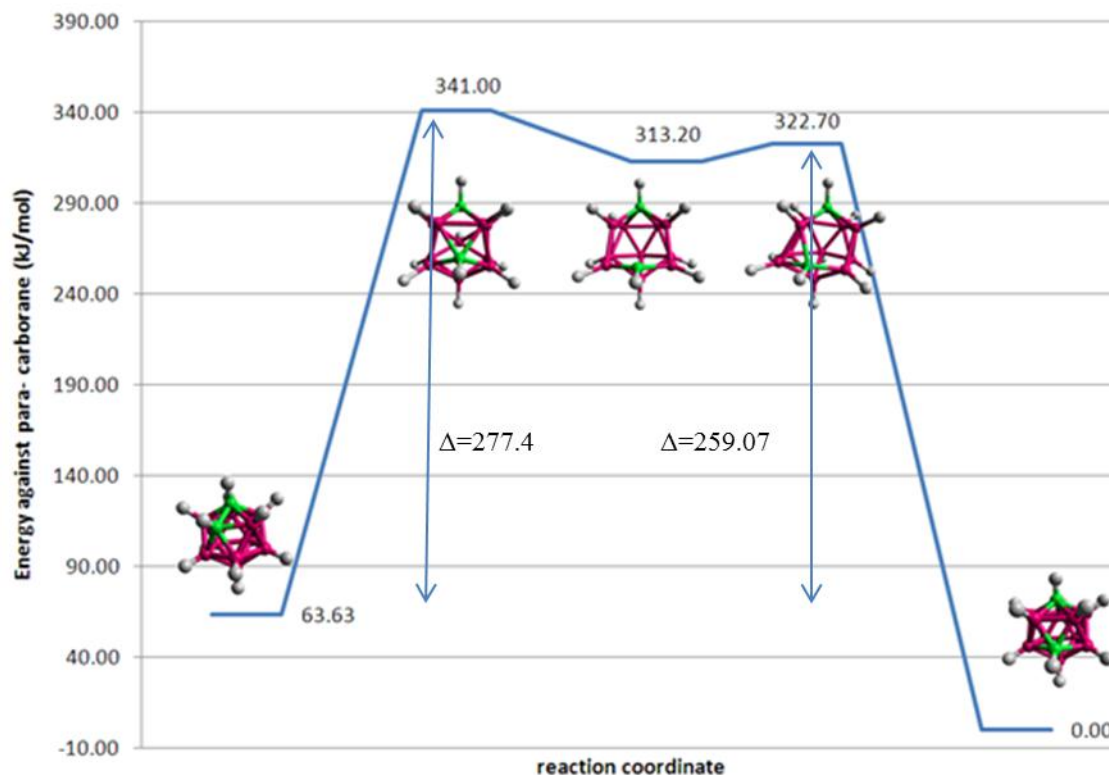
Figure 113. *Ortho* to *meta* carborane rearrangement, *Nido* mechanism

This mechanism was unique as noted in the introduction to this section. It has a lower activation energy than the non-TFR mechanism, but is observed less times (although the small sample size is noted). However, the relatively high energy of the intermediate as compared to the non-TFR example may be notable, as molecules are more likely to get trapped in an energy well in the non-TFR case. Therefore, as well as orbital calculations, it would be useful to record how long species exist in the MD calculations, to support that statement.

This investigation refers to the mechanism as "nido", as it involves the opening of one of the faces, and one can imagine a 13th vertex capping this open face to create a deltahedral shape with 13 vertices. No such molecule exists, but the removal of a vertex from a closed deltahedral shape creates a *nido-* complex.

6.3 *Meta-para* carborane rearrangement

The rearrangement of *meta-* to *para-* carborane happens experimentally at a higher temperature, and also exists in a dynamic equilibrium, so is a more challenging case. It was also necessary to increase the temperature of the calculations (3000-3500 K), as runs at lower temperatures did not produce rearrangements.

The higher temperature runs produced 13 rearrangements, but only 2 of these represent mechanisms that would change *meta*-carborane to *para*-carborane. The rest are boron vertices changing position, finally confirming that isotopes will be scrambled by exposing these molecules to high temperature.

The two runs that produced *para*-carborane progressed through the same mechanism, given below:
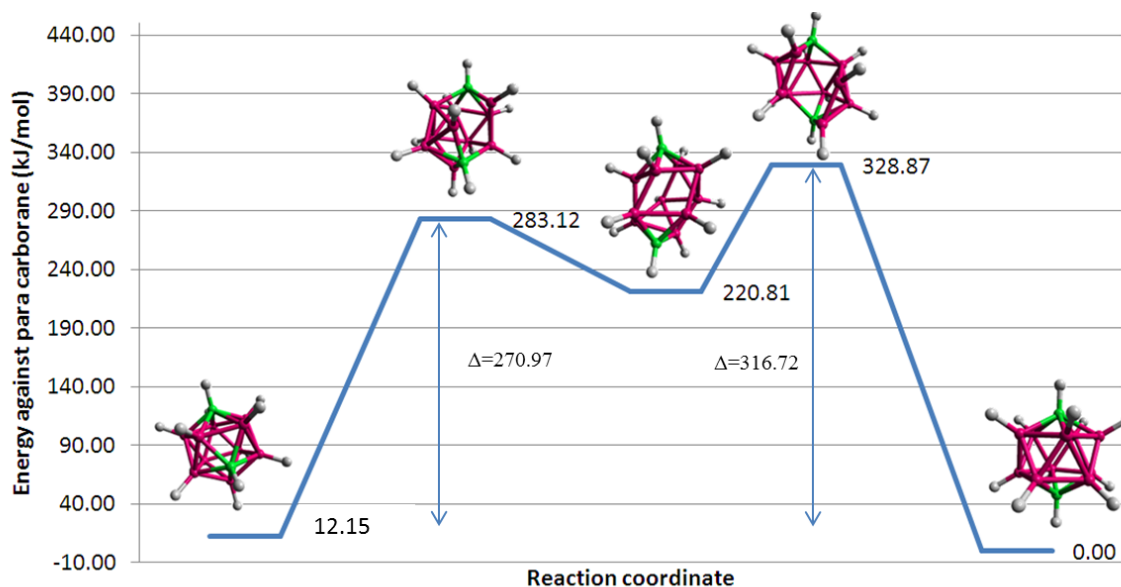
Figure 114. *Meta* to *para* carborane rearrangement, Non-TFR mechanism

This can also be compared to the non-TFR mechanism described in the Brown and McKee paper. It is worth noting that this mechanism involves the molecule essentially rotating in two halves, created by splitting the molecule along the planes indicated below:
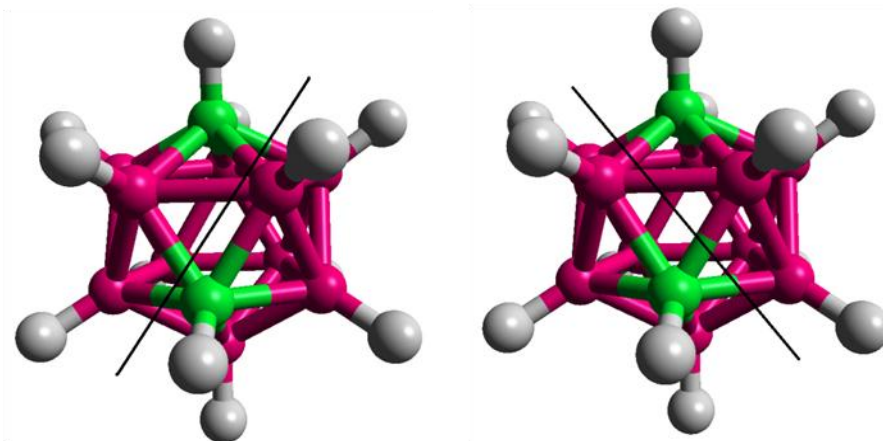
Figure 115. Indicating the 2 planes by which *meta* carborane can be split, with the two halves rotating to form *para-* carborane

Obviously, with two ways for the molecule to rotate, boron positions will be scrambled, before the boron position rearrangements are taken into consideration.

A final note on the *meta-para* rearrangements is that Brown found two mechanisms using potential energy surface sampling. The fact that only one has been observed in these calculations doesn't prove that it is the only possibility, as the sample size is too small.

6.4   Smaller Carborane rearrangement

As mentioned at the start of this section, the *ortho* $C_2B_5H_7$ molecule also rearranges under increased temperature, to its more stable *meta* form. As it is a simpler system, it was decided to perform the same *ab initio* MD calculations on this system, as it would be easier to follow the progress of key orbitals. Several rearrangements were observed, with one unique mechanism:

Thermal rearrangement of carboranes
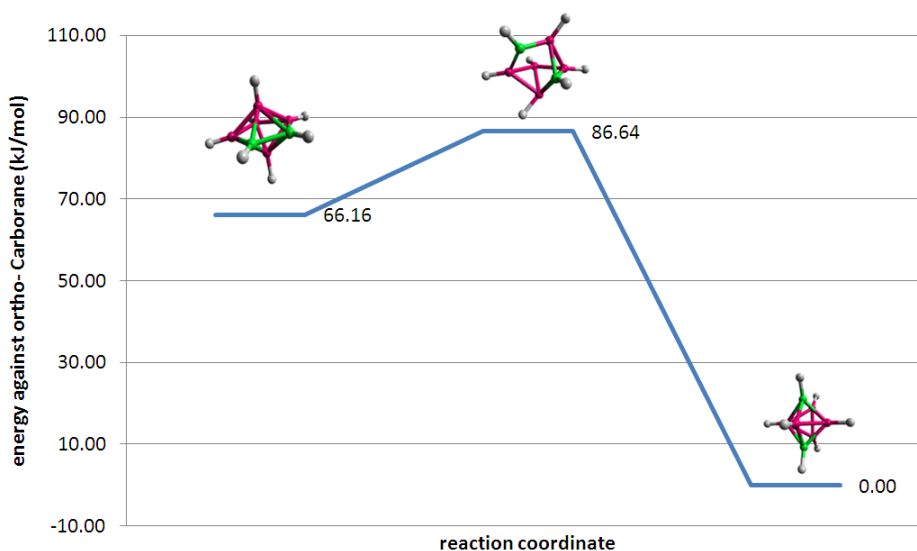
Figure 116. Reaction coordinate of small carborane rearrangement
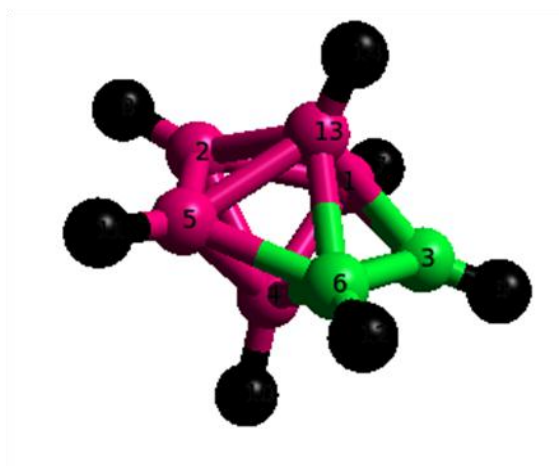
Figure 117. Atom labelling in smaller carborane

The geometries displayed on the reaction coordinate are intentional, as it gives some idea of the mechanism. Following the numbering system given in Figure 117, atoms 4 and 13 begin as capping atoms. The rearrangement mechanism involves the breaking of bonds 6-4, and 6-13. Carbon 6 then rotates around the 5-13 bond, making bonds to 2 and 1, whilst the 3-5 bond is made. In this way, a new pentagon with capping atoms 1 and 5 is made. This rearrangement is unlikely to shed any light on the rearrangements of larger carboranes then, but does answer a question first posed in 1989[152]: how does $C_2B_5H_7$ rearrange?

179

6.5 B$_{12}$H$_{12}$$^{2-}$ rearrangement

Whilst the borane anion did rearrange when considered in isolation, even higher temperatures were required to reveal this (4000-4500 K). When the reaction scheme is produced using the standard technique, the activation energy for rearrangement is 434 kJ/mol, or 0.165 hartrees. This is higher than the B-H bond dissociation energy, so it is expected that borane would disintegrate before rearranging. The bond dissociation calculation is depicted in Figure 118, which unsurprisingly shows that the hydrogen, when lost, will be lost as a proton:

Figure 118. Showing energy changes as hydrogen is removed from equilibrium distance in borane (PBE energy). Black line is with multiplicity 3, red line is multiplicity 1

The reaction coordinate diagram given in Figure 119 shows that the Transition state is actually slightly (3kJ/mol) lower in energy than the intermediate. This is of course unrealistic, and is further confirmation that the borane anion is unlikely to rearrange in a similar way to the carboranes. However, the calculations were retained, as, in terms of vertex connectivity and progress, the rearrangement could be considered to proceed via a TFR mechanism. With a high symmetry system such as this, the progression of orbital symmetry should be easier to view, which is of interest in the carborane work, since orbital symmetry is likely to be a key factor in the mechanisms.

Thermal rearrangement of carboranes

Figure 119. $B_{12}H_{12}^{2-}$ thermal rearrangement reaction coordinate

6.5.1 Analysis of orbital progression

The energies for the rearrangements found in this investigation and by that of Brown and McKee are compared in Table 12:

Mechanism	Energy of TS, or (TS1, INT, TS2) (kJ mol^{-1})	
	This work	Brown *et. al.*
Table 12. Activation energies of proposed rearrangement mechanisms (relative in each case to the lower energy isomer)		
ortho-meta		
TFR	263.67	207.6
Non-TFR	301.77, 192.77, 258.61	315.9, 143.4, 225.6
Nido	277.4, 249.57, 259.07	-
meta-para		
TFR	-	343.4
Non-TFR	270.97, 208.67, 316.72	235.4, 175.9, 279.9

Due to symmetry, in both types of skeletal rearrangement, alternative pathways exist from intermediates and transition states that involve the rearrangement of different but equivalent boron atoms. This makes the experimental tracking of these mechanisms difficult using isotope labelling methods. A further difficulty is that in both series of simulations, rearrangements were also observed which only involved boron atoms, leaving the carbon positions unaltered. This creates a further complication in trying to follow these processes experimentally, as alluded to previously. The experimental[58] rate constants for the *ortho-meta* transition were used to derive the Arrhenius constant and activation energy (E_a): 362217 s^{-1} and 352.1 kJ mol^{-1} respectively, using the explanatory text: "Samples of isotopically normal o-carborane were heated at 400, 420, and 440˚C. The rate of isomerisation of o-carborane to m-carborane for these samples was determined from the relative integrals of the ^{11}B NMR resonances of o-and m-carborane. The rate of isomerisation was (3.73 ± 0.15) x10^{-6} s^{-1}, (1.15 ± 0.05) x10^{5}s^{-1}, and (3.74 ± 0.15) x s^{-1}at 400,420, and 440˚C, respectively. Activation parameters for the isomerisation are $\Delta G^* = 57.3\pm0.4$ kcal mol^{-1}, $\Delta H^* = 54\pm15$ kcal mol^{-1}, and $\Delta S^* = -5\pm11$ kcal mol^{-1}K^{-1}, which are in close agreement with earlier studies". The derivation is shown in Figure 120.

$$y = -10131.8x + 12.80444$$
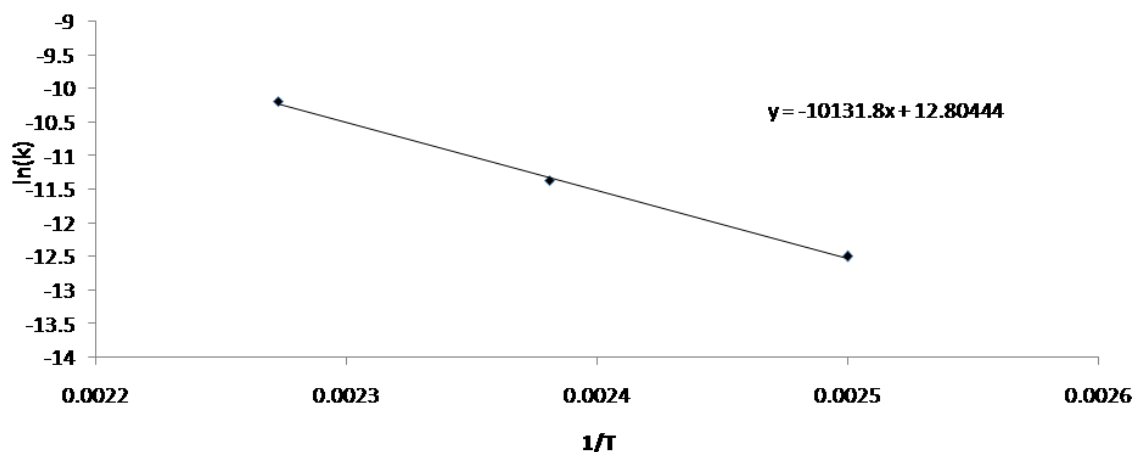
Figure 120. Rate constant derivation for *ortho-meta* carborane rearrangement

The Ea is ~40 kJ/mol higher than the highest theoretically derived energies (315.9 in Brown *et al* and 301.77 in this work), and some 144.5 kJ/mol higher than the lowest theoretically predicted mechanism, using traditional transition state sampling which ignores orbital symmetry. This is observed in Figure 121, which is a collection of all of the other reaction coordinates from previous sections.
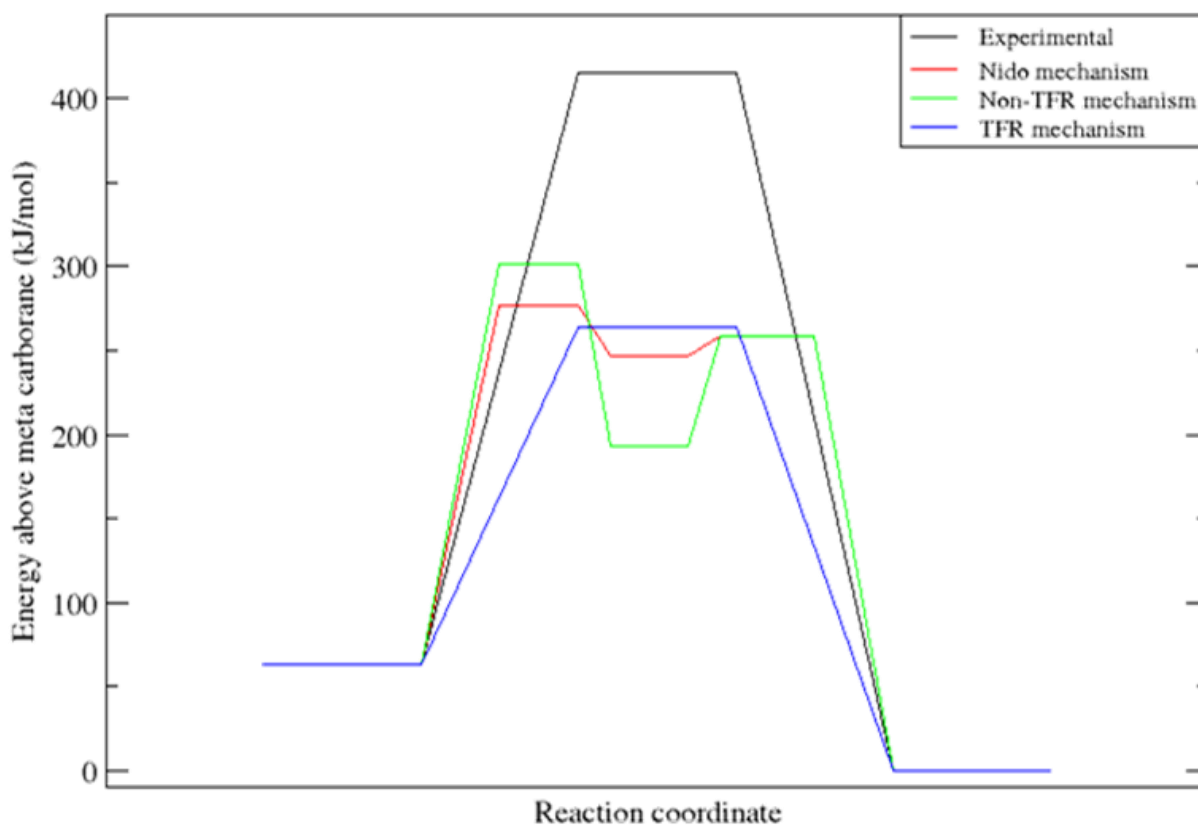
Figure 121. Reaction coordinates for *ortho-meta* rearrangements

Therefore, it is likely that an extra energy penalty must be applied, which we suggest arises from the breaking of phase symmetry. The phase symmetry crossing energy has been estimated to be ≈40 kJ/mol in previous investigations[153] on organic reactions. When incremental linear steps are taken along the reaction paths outlined above, the evolution of orbitals may be followed, and we clearly observe phase inversion in a number of orbitals: the example of the HOMO-2 orbital is given in Figure 122.
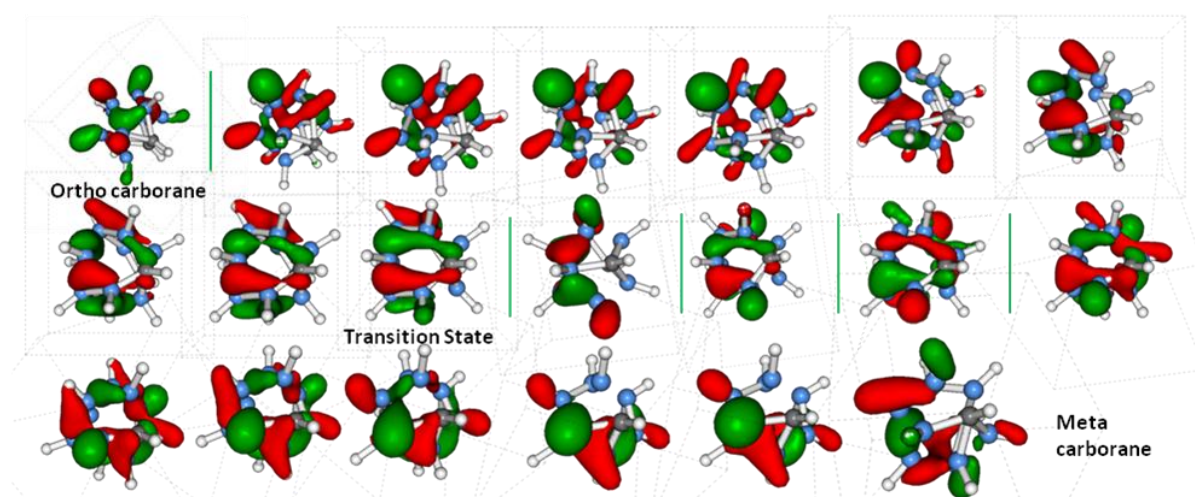
Figure 122. HOMO -2 orbital progression for *ortho - meta* TFR rearrangement process. Green lines indicate node switches. In the example above, there is one node switch from *ortho* carborane to the transition state.

In fact, the HOMO, HOMO-2, HOMO-4, HOMO-5, HOMO-6 and HOMO-7 orbitals in *ortho*-carborane all require node inversions upon rearrangement to *meta*-carborane, which is unsurprisingly reproduced in each of the mechanisms observed, since the ground state products are identical. The critical issue in terms of the activation energy for the mechanisms is whether the inversion occurs between the reactant and transition state, i.e. adding an energy penalty to the activation energy, rather than orbitals reorganising upon reaching a product's "excited state". In the case of the TFR mechanism three orbital crossings occur before the transition state, three for the nido mechanism and two for non-TFR. This suggests that the activation energies of the processes, as calculated without taking orbital phase into consideration, will be underestimated by indeterminate amounts. Adding an "orbital crossing" energy penalty would likely align theory and experiment.

6.5.2 Rearrangements in metal complexes

Another area where phase symmetry is of particular importance is in the technetium-carborane complex which is biologically relevant. Technetium ions, ligated by *nido-ortho* carborane and three carbonyl groups have been suggested as potential imaging agents[56]. Following common practice, initial characterisation experiments were performed using the cheaper and non-radioactive rhenium analogue as a model[154]. The rhenium complex showed good stability. However, in trials with the technetium complex, rearrangements in the carborane ligand were observed. Considering that ionic radii[155] and electronegativities[156] of the two metal ions are almost identical, differing orbital overlap is a possible cause of the different reactivity, since a rearrangement pathway may be available to the technetium complex that maintains orbital phase, whilst the rhenium complex could require orbital phase inversion. By treating the metal atom and carbonyl ligands as non-rearranging vertices, and applying the transformations of the TFR and non-TFR mechanisms, rearrangement pathways for metal carborane complexes can be derived. Using Gaussian03, TS searches were completed, using the structures generated as initial guesses. Transition states were found for both systems, with the structures shown in Figure 123.
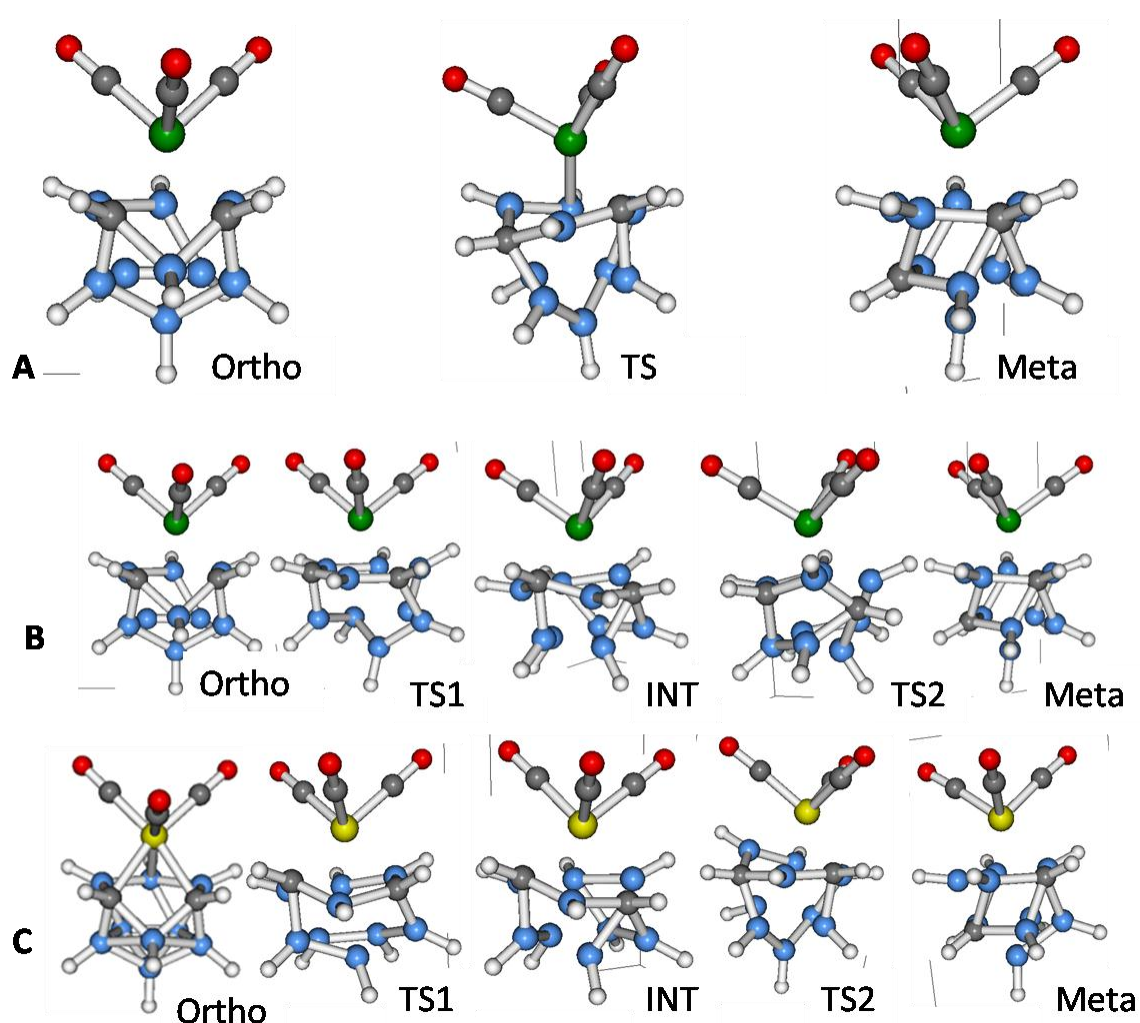
Figure 123. Key structures in metal-carborane complex rearrangements. A: Technetium TFR mechanism B: Technetium Non-TFR mechanism, C: Rhenium Non-TFR mechanism

The energies for the stationary points found through this method are instructive, in that, as predicted in the experimental investigation, the reaction coordinates are almost identical. For the TFR mechanism, activation energies for the two systems were 121.76 and 123.76 kJ/mol for the technetium and rhenium complexes respectively. For the non-TFR mechanism the energies (calculated relative to *ortho*-complex) on the rhenium complex potential energy surface are 105.53, 81.72, 133.72 kJ/mol for the TS, Int, TS2; and for the technetium complex are 105.59, 81.16, 187.86 kJ/mol respectively, as shown in Figure 124.

Figure 124. Reaction coordinates for metal complexes rearranging from *ortho-meta*. Left: Technetium, right: Rhenium complex

Compared to the uncomplexed carboranes, these activation energies are significantly lower, indicating a greater likelihood of room temperature rearrangement, and while most of the orbitals in the *ortho*, TS and *meta* complexes of the two metals are almost identical, a few have opposing signs. For instance, there are node inversions in seven of the twenty highest-lying orbitals progressing from the *ortho* complex to TS for the rhenium complex, and in six for the technetium complex. An example is given in Figure 125.
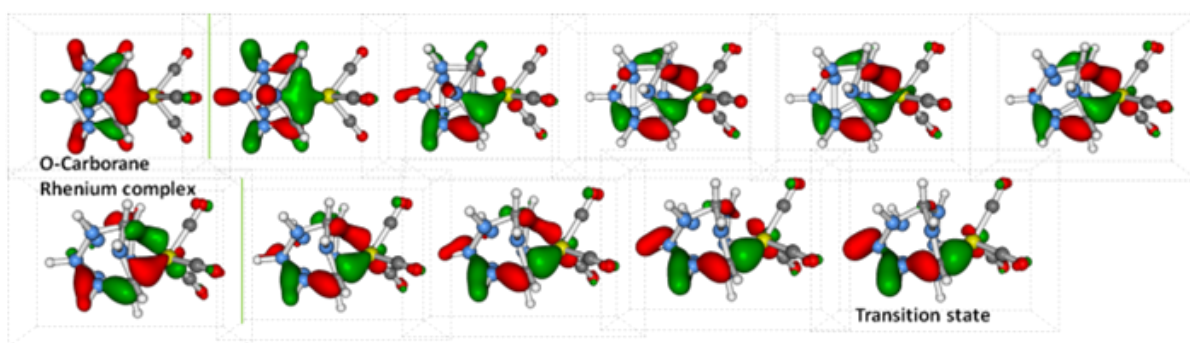
Figure 125. The progression of orbital HOMO-8 from *ortho* to TS rhenium carborane complex

It is proposed that this may be the origin of the differing metal complex activities, although computational methods currently available may not enable a completely accurate assessment of the numbers of node inversions, and associated changes in activation energies.

7   Boron clusters in lithium battery electrolytes

Lithium ion batteries have a theoretically high power density as a result of the small size of lithium ions. However, lithium ion transference and conductivity is affected by ion pairing with its counter anion in the electrolyte[157]. Attempts to avoid this problem include: using a room temperature ionic liquid solvent[158], adding trapping molecules such as crown ethers to isolate the cation[159], and adding molecules to trap the anion[160], indirectly isolating the cation. All approaches have merit, but the use of a less coordinating anion represents a simpler solution.

$B_{12}H_{12}^{2-}$ is considered as a possible alternative anion, on the grounds that its electron density is large and diffuse, reducing the coordinating effect. Ion pairs are observed in the gas phase[161], but the binding energy is notably low, and the lattice energy for the solid $Li_2B_{12}H_{12}$ is also low[162].

Classical molecular dynamics calculations were performed to investigate this system, simulating the experimental conditions of the bulk electrolyte for BF_4^- and $B_{12}H_{12}^{2-}$, and the difference in lithium ion mobility analysed. This is analogous to a seminal study on electrolytic solvent effect[90], although at experimental density and concentration:
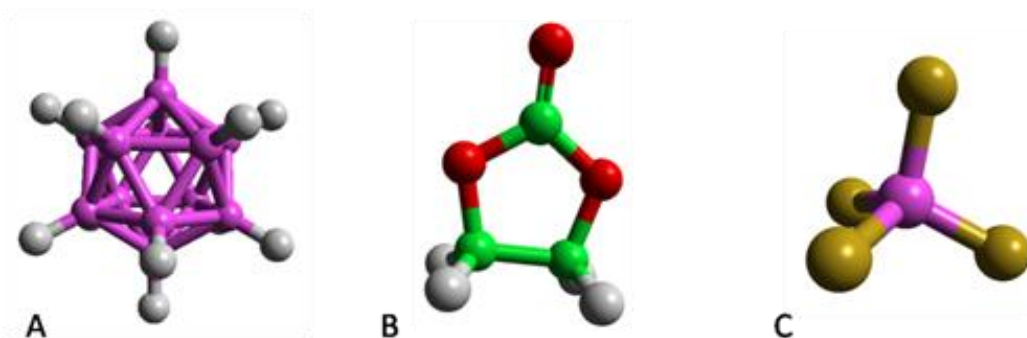
Figure 126. Lithium battery electrolyte components considered, A: $B_{12}H_{12}^{2-}$ B: Ethylene carbonate (EC) C: BF_4^-. Boron, carbon, oxygen, fluorine and hydrogen atoms are purple, green, red, gold, and grey spheres respectively.

Charges for $B_{12}H_{12}$ molecules were derived from the Mulliken potential for *ab initio* calculations at the PBEPBE/6-31G (d,p) level of theory, using the Gaussian03 program. Boron atoms have $q = +0.0464$, and hydrogen $q = -0.2131$, showing that the electron density is located at the hydrogen positions.

The forcefield terms for $B_{12}H_{12}^{2-}$ were taken from Table 5, whilst ethylene carbonate, Li^+ and BF_4^- terms were taken directly from Soetens *et al*.

Liquid eletrolyte phases were created using the program ATEN[108], utilising a process that accepts or rejects insertions of molecules based on their interactions and the given forcefield, at experimental ethylene carbonate (EC) density (1.321 g/cm^3) and solvated concentration (0.5 mol/dm^3)[163]. This was acheived by using 218 ethylene carbonate solvent molecules per 8 lithium ions. Cell volume was then stabilised using constant pressure molecular dynamics at ambient conditions.

Production runs were then performed with an electric field of magnitude $q = 1$ applied in the [100] direction, to simulate a working environment, for 1 ns. Lithium mobility can then be inferred from mean squared deviation data for the species, as shown in Figure 127.
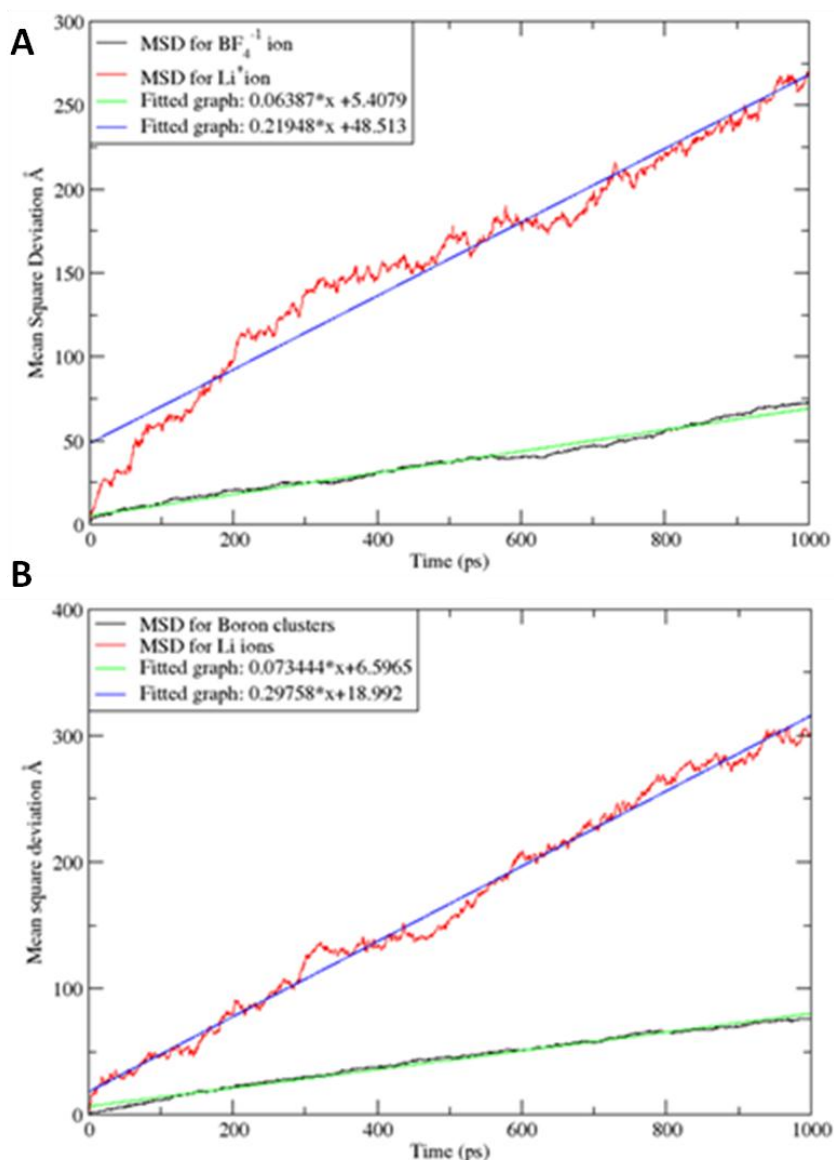
Figure 127. Mean Squared Deviation (MSD) for ions in electrolyte experiments. A: $B_{12}H_{12}^{2-}$ used as counter anion. B: BF_4^- used as counter ion

As can be seen, the average MSD for lithium ions is 278 $Å^2$/ns and 323$Å^2$/ns, for the BF$_4^-$ and B$_{12}$H$_{12}^{2-}$simulations respectively, corresponding to a diffusion coeffecient of 4.63 x 10^{-6} and 5.39x 10^{-6} cm^2/s, (experimentally[164] at these conditions and concentrations, MSD values for BF$_4^-$ is 4.0 x 10^{-6} cm^2/s).

This suggests that the boron cluster simulation sees less complexing between charged species, and a resultant increase in the lithium mobility. This can be further analysed, by looking at Radial distribution data for the simulations, as seen in Figure 128.
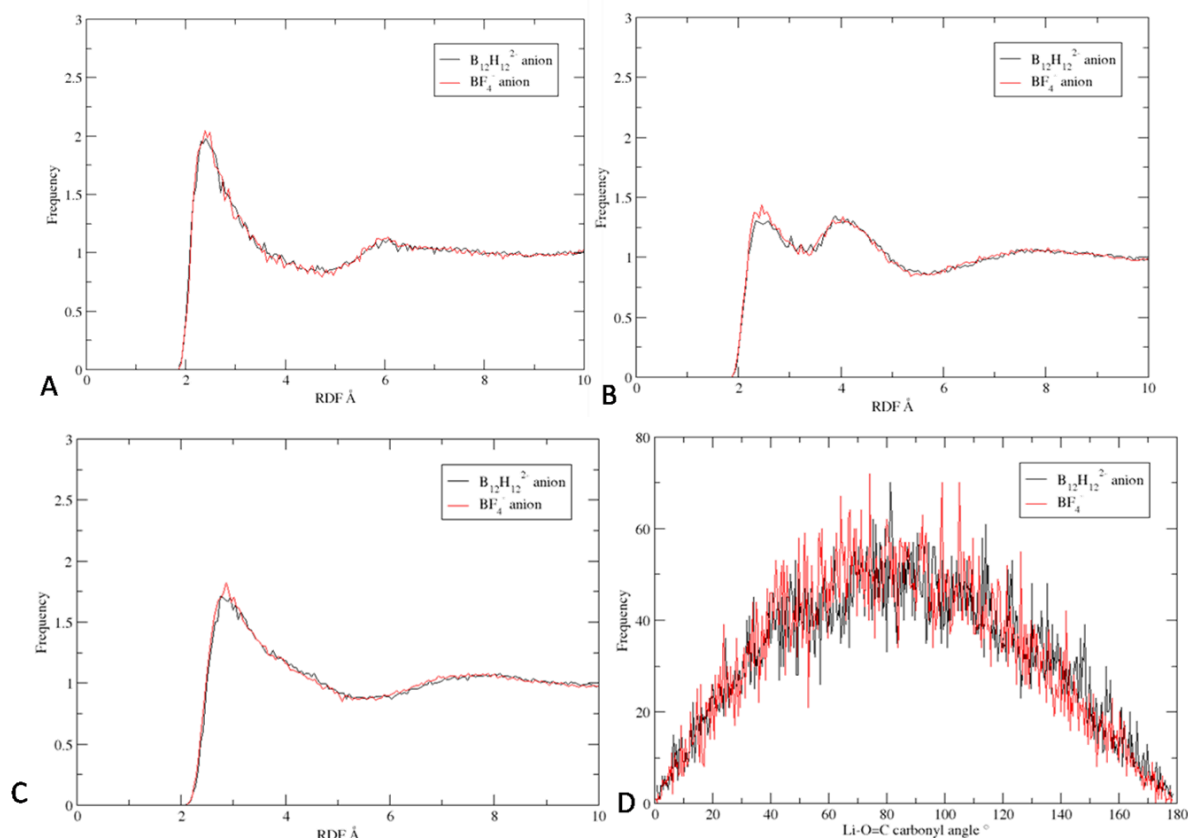
Figure 128. RDF and angle distribution data for electrolyte simulations. A: Li-Carbonyl O RDF, B: Li-ether O, C: Li-C RDF, D: Angle distribution for Li-O=C angle. In all cases, black line is for B$_{12}$H$_{12}^{2-}$ simulation, and red line is for BF$_4^-$ simulations

The interaction between lithium ions and solvent is unexpectedly largely unchanged between the different simulations; the solvation sphere around the lithium appears to include 2 EC molecules, principally bonding at the carbonyl oxygen. However, a small increase in the first peak in the BF$_4^-$ cases is discernable in Figure 128 A,B, and C; potentially an indication of a more order solvation sphere in this example. There is a broad range of Li-O=C angles as seen in Figure 128D, but peaking at ≈ 90˚, suggesting that the EC molecule face is directed towards the ion, providing ether oxygen contacts, backed up by Figure 128B.
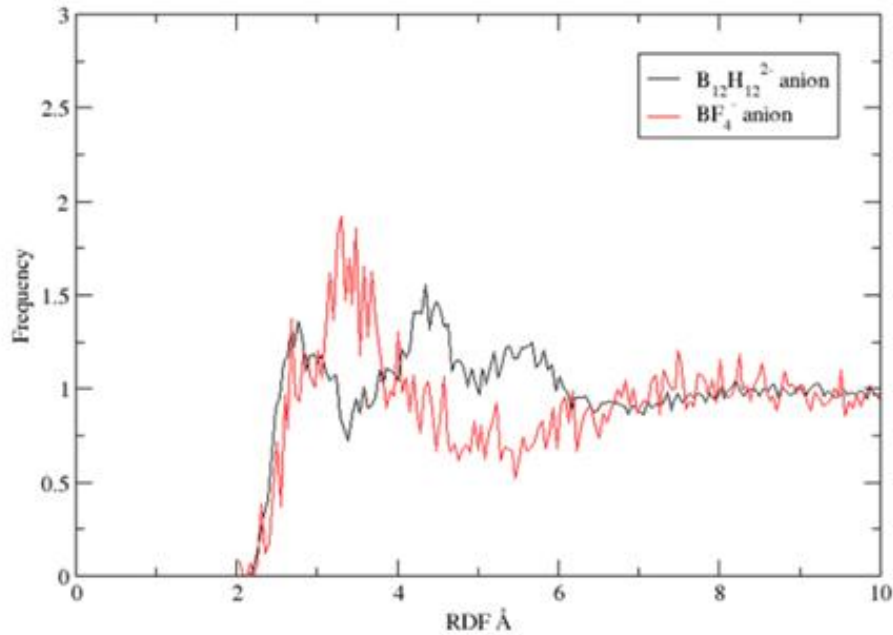
Figure 129. RDF data for lithium ions to borons in anions (Li-B). Black line is for $B_{12}H_{12}^{2-}$, red line is BF_4^- simulations.

Of more interest is the interaction between cation and anion as seen in Figure 129. The Li-B RDF pattern for the $B_{12}H_{12}$ simulations shows three peaks, corresponding to an interaction between the lithium ion and a cage boron for the first peak, and then the boron atoms in *meta* and *para* positions to the first for the remaining peaks. However, these peaks are shallow, and indicative of a loose association.The BF_4^- plot has a large peak at 3.5Å and a shoulder around 3Å, corresponding to lihium ions associating with a face and an edge of the BF_4^- tetrahedron respectively (shown in Figure 130).The large peak in the BF_4^- case suggests that the interaction between ions in the BF_4^- simulation is more ordered. This will affect the mobility of ions in electrolytes with an electric field applied.
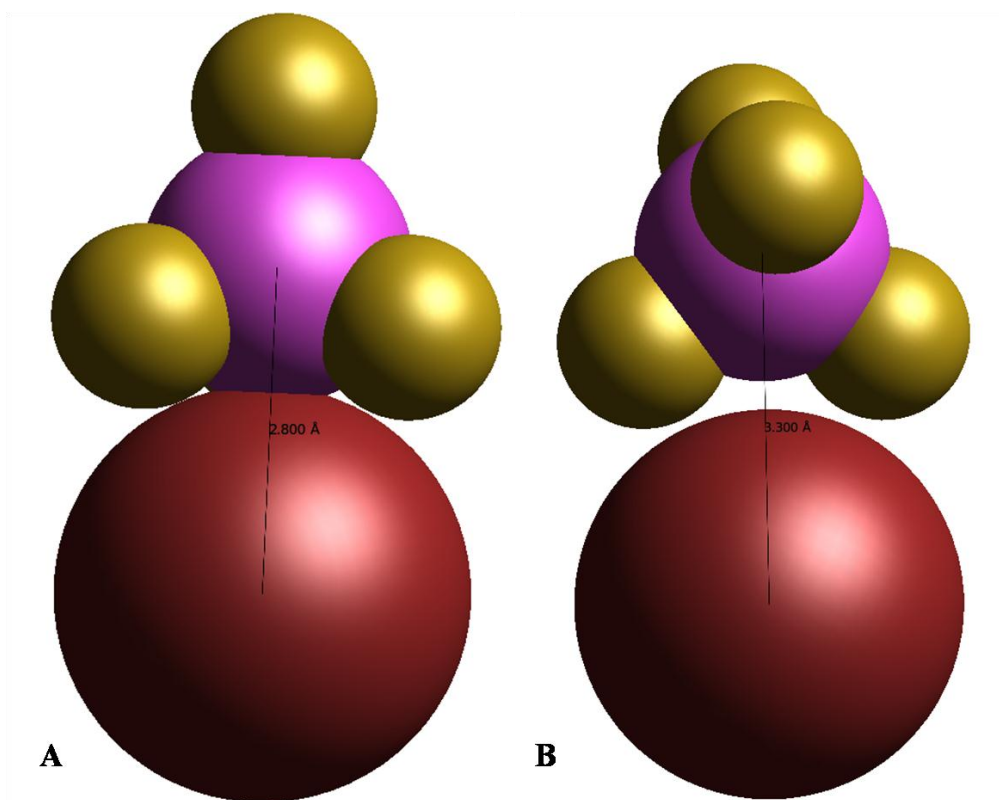
Figure 130. Idealised Li BF_4^- complexes, VdW surfaces scaled by 1.4. A: face interaction, B: edge interaction

Having gathered data relating to the $B_{12}H_{12}^{2-}$ anion, it was decided to investigate other anions that offer low coordination with cations, based on icosahedral boron clusters, namely chlorinated, fluorinated[165] and methylated[166] boron clusters. The electrolyte cell construction and Molecular dynamics equilibration and production runs were repeated to make the simulations equivalent. The partial charges were taken from PBEPBE/6-31G* calculations using CP2K on the gas phases molecules, calculated using the Mulliken method. B-F and B-Cl bonds were treated with constraints to align with previous calculations, whilst B-C bonds used the Morse potentials derived elsewhere, and C-H bonds were treated in the same way as for ethylene carbonate.

The calculated MSD values and diffusion coefficients, as well as partial charges, are given in Table 13, and the collected MSD data are gathered in Figure 131:

Table 13. Details MD runs with different counter anions

Counter anion	BF_4^-	$B_{12}H_{12}^{2-}$	$B_{12}Cl_{12}^{2-}$	$B_{12}F_{12}^{2-}$	$B_{12}(CH_3)_2^{2-}$
B charge (q)	0.9756	0.0464	-0.0095	0.107	0.165
Hetero atom charge (q)	-0.4939	–0.2131	-0.1572	-0.4939	C= -0.523 H= 0.064
MSD ($Å^2$/ns)	278	323	339.3	337.88	323.30
Diffusion coefficient (x 10^{-6} cm^2/s)	4.63	5.39	5.66	5.63	5.39
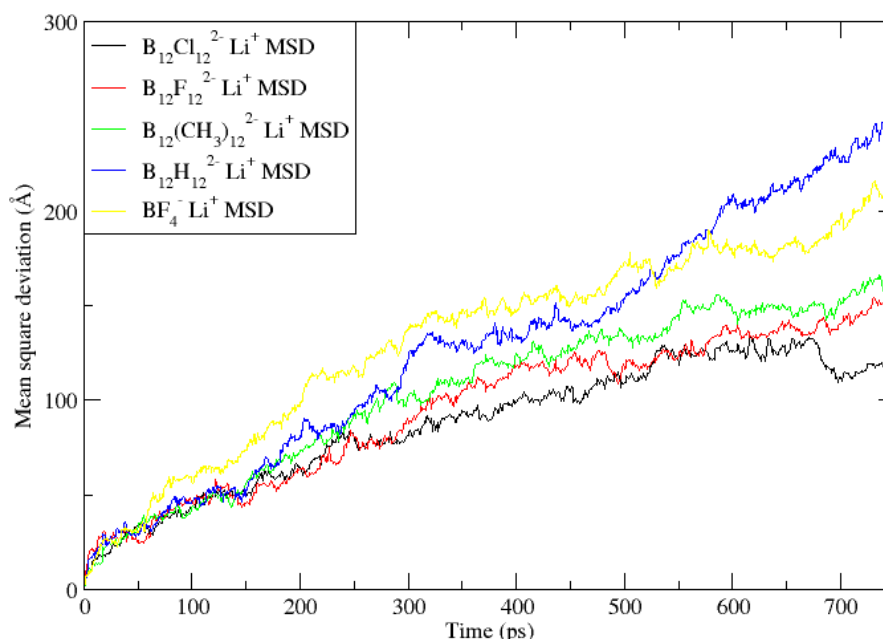
Figure 131. Collected MSD data

In conclusion then, the chlorine derivative appears to allow the corresponding lithium ion the most mobility, which is fairly certain to be as a result of the excess negative charge being more evenly spread in this case, with no optimal site for coordination with lithium ions. However, in all cases an increase in lithium mobility is observed when boron clusters are used, showing the efficacy of using an anion with large diffuse charge in lithium battery electrolytes. The noise of the MSD plots is acknowledged.

Further work would be to analyse the stability of the anion at the cathode, as breakdown of anion at high voltage and cycling speed has also been observed to limit lithium battery life. The more highly stable anions would presumably offer an advantage from this point of view as well, while a redox active boron cluster system is theorised to offer protection to solvent molecules[165], and *ab initio* MD may be a route to examining the stability of anions in a highly polarized environment.

8   Conclusions

The computational design of a siloxane-carborane co-polymer system has been the main area of interest for this work, of which the focus has been on how the ratio of carborane and siloxane monomers affects the bulk physical properties of the material. This required the fitting of a transferable forcefield that describes the interactions in an icosahedral carborane unit; notably bonds and non-bonding parameters. These parameters were derived by fitting them to the experimental crystal structures and vibrational spectra of sodium doceborohydrate and boron carbide, as well as the bulk modulus of boron carbide. All of the experimental data was reproduced satisfactorily, (with some caveats, such as the known breadth of boron carbide composition), suggesting that the parameters are transferable, and allowed for a supplementary investigation into the boron carbide system itself.   In combination with the existing pcff forcefield, this enabled a complete description of the co-polymer system.

A major challenge of the work was in producing manageably sized (in terms of computational resources) polymer phases representing the co-polymer system at different monomer ratios, typically in 10% steps from 0-100%. Three main approaches were taken: "short-strand" phases were produced using the amorphous cell program of Material's studio; "medium-strand" phases were produced by inserting straight-chain, uniform-length polymer strands into an empty box with a random orientation; and "long-strand" phases, which were produced using my own program Ermintrude, which adds monomers sequentially to polymer strands, allowing torsional rotation to occupy available space, and with strand lengths chosen to approximate the Gaussian distribution observed experimentally. Short strand phases were abandoned in order to avoid using approximations of the parameters in the forcefield, and because the phases reproduced crystalline density rather than polymeric, suggesting the phases were too small. The medium and long strand phases were able to give meaningful results in terms of physical properties like density, thermal expansion coefficient and bulk modulus, with the experimental values for siloxane polymer and 50% carborane-siloxane polymer reproduced. However, the long-strand phases give a better representation of experimental conditions, allow the user more control, and are actually quicker to produce relatively, considering the much larger systems considered, because shorter molecular dynamics runs are required to equilibrate cell volume.

It was observed that with increasing carborane content, the material became stiffer and less susceptible to changes in temperature, levelling off above 50 percent carborane content.

Conclusions

This is shown by the thermal expansion coeffecient reducing from $\approx 8.0 \times 10^{-4}$ to $\approx 3.0 \times 10^{-4}$ K^{-1}, and bulk modulus increasing linearly from ≈ 3 to ≈ 5GPa with increasing carborane content. This is as a result of the carborane cages acting as "heat sinks": storing the increased temperature in the form of potential energy in their vibrational modes, and a reduction in the number of extremely flexible Si-O-Si-O torsions respectively.

It is clear then, that introducing carborane cages to siloxane polymer phases has an effect on measurable physical properties, even at low concentrations. The ideal values for these properties depends on context, but if making slight adaptions to the monomer mix would make predictable changes to physical properties, then it would be of great benefit to the design of the material. Therefore, replacing a percent of the monomers with designed monomers was also considered, notably by substituting some *meta-* carborane monomers with *para-*, and dimethyl siloxane monomers with phenyl-methyl- or ethyl-methyl-monomers, at a 50:50 carborane-siloxane ratio, using the program Ermintrude. All substitutions had some effect on physical properties, for instance: *para-* carborane is less polar than *meta-*, so has weaker inter strand interactions, leading to an increase in thermal expansion coefficient. Likewise, introducing rigid phenyl units disrupts the network of strands, leading to a reduction in inter strand interactions and an increase in bulk modulus. As a result, the polymer scientist can make educated guesses at the ideal monomer mix to produce a material with ideal properties.

Finally for the classical simulations on the copolymer system, the effect of aging the material has also been considered; in the materials intended industrial context, it is likely to be subjected to radiation in the form of high energy lithium and helium ions travelling through it, promoting crosslinking. Simulating crosslinking as a result of radiation appears to reduce flexibility, beyond a limit of ≈ 6 crosslinks per 10 polymer strands. This is realised through a slight increase in bulk modulus, and a slight reduction in thermal expansion coefficient for all phases, which is an intuitive result.

The change in vibrational spectra as a result of boron vertices being removed from monomers by radiation has also been considered, at the *ab initio* level, in order to create a diagnostic tool for experimentalists and determine the state of carborane units that have been exposed to neutron radiation. For instance, having removed individual vertices in a model monomer unit, the cage "breathing" vibrational modes (around 1100cm^{-1}) shift upwards in wavenumber, whilst the B-H stretching modes (around 2500cm^{-1}) shift downwards, across all charge states. This is reflective of a change in orbital structure and a weakening of B-H bonds respectively. It is also clear that the only feasible way for carborane cages to survive neutron

radiation is with the retention of electron density; damaged molecules with positive overall charge are unstable.

Alongside these experiments, the current industry standard for neutron capture: boron carbide, has been considered in other radiative environments, with competing theories for the exceptional resistance examined, at classical and *ab initio* levels of theory. This was an extension of the experiments conducted to derive forcefield parameters for boron icosahedral units. A mechanism whereby chain and cage compositional flexibility allows absorption of high impact events has been observed for the first time computationally, contradicting the "self-healing" mechanism initially proposed to explain the resistance of the material and its analogues. This mechanism is supported by the large changes in impacted atom positions even at relatively low impact energies compared to experiment.

This thesis also contains an investigation into the thermal rearrangement reaction of carborane molecules. This is particularly relevant for the copolymer system, where the rearrangement temperature represents the upper working temperature of the material, but is also relevant to biological and catalytic industries, where carboranes are used in environments where rearrangements are possible, and would have an effect on the molecule's funtion. The investigation used high temperature *ab initio* MD to sample the potential energy surface, and used snapshots of rearrangements to find stationary points on the surface using conventional methods. Three mechanisms were observed, as well as many boron to boron rearrangements, agreeing well with the experimental data, which sees a scrambling of boron positions. The underestimation of activation energy when using static calculations on the potential energy surface to follow the reaction path, against the experimental activation energy is revealed as a node–inversion problem: the high energy molecular orbitals comprised of boron p orbitals spread over the surface of the molecule experience a change in sign on going from ground state to transition state. This behaviour isn't revealed by evaluating the wavefunction instantaneously at positions on the potential energy surface, meaning activation energy will be underestimated. This phenomenon also explains the different activity in technetium and rhenium carborane complexes, whose instantaneous reaction coordinates appear identical; a node inversion on going from ground state to transition state is observed in the rhenium complex, that is absent in the technetium complex rearrangement. Therefore, a "node-inversion penalty" needs to be added to the rhenium complex rearrangement reaction path, that is absent in the technetium reaction path, leading to differing activities.

Conclusions

Finally, a boron cluster has been considered as a potential alternative to current anions in lithium battery electrolytes, using classical MD. This is a possible industrial application of icosahedral boron clusters, which exploits the large, diffuse nature of the electron density in boron cluster anions such as $B_{12}H_{12}^{2-}$. This large, diffuse electron density could lead to a remarkably low coordination with cations, and increased cation mobility in solution. A solvent (ethylene carbonate) phase at experimental concentration was created using the program ATEN for the current state of the art $LiBF_4$ system and the proposed $Li_2B_{12}H_{12}$ system, which were both investigated using molecular dynamics at ambient (1 atm, 298K) conditions with an electric field applied to simulate the working conditions in a lithium battery electrolyte. It was observed that there is a ≈20% increase in lithium mobility in the $Li_2B_{12}H_{12}$ system, from root mean square deviation calculations over 1 nanosecond simulations, which would infer a similar increase in power density in the working battery. Altering the boron cluster by replacing hydrogen atoms with fluorine, chlorine and methyl units would also appear to offer a slight increase in power density.

8.1 Future work

Having derived a freeware computational code (Ermintrude) which offers the user the opportunity to use their own forcefield terms and monomers, it would be of interest to extend this investigation by producing a large range of polymer systems. For example phenyl-methyl siloxane is considered in chapter 4.4, simply because the monomer is cheap, and offered a theoretical use by lowering glass transition temperature due to reducing inter-strand interaction. However, there is no reason why more exotic substituents that provide functionality such as organic photochromes[167] that affect the material's colour in different environments, can't be considered. The effect of substituent percentage against common physical properties is trivial to calculate, and will suggest optimal monomer ratios before experiments take place, saving time and money.

A problem encountered in this thesis was in determining the shear modulus of polymer phases. Static calculations are not applicable due to memory issues; second derivative information for each atom is required for shear modulus calculations, and this information is stored in RAM. Even with the smallest polymer phases, the arrays are unworkably large. As a result of this molecular dynamics investigations were implemented, first by applying a shear potential, and evaluating the change in energy after a short time, or by applying a shear wave. Neither method produced satisfactory results: the results from applying a shear field are very sensitive to the choice of relaxation time, whilst shear waves appeared to "tear" or untangle the stable polymer phases. Longer polymer strands may well have sufficient points of contact to allow a shear wave to propagate through the material without untangling strands. This could be a useful area for further work.

A further consideration is that throughout this thesis, the industrial context has been taken into account, with the effect of neutron capture events on a siloxane-carborane copolymer predicted in sections 4.6 and 4.7. It is therefore of great interest for experiments modelling industrial context to take place, in order to compare with theoretical prediction.

Finally, $B_{12}H_{12}^{2-}$ has been considered as a possible counter anion for lithium batteries, and shown to theoretically offer a large improvement in lithium mobility, using classical computational chemistry. A further theoretical advantage of using $B_{12}H_{12}^{2-}$ ions is that they offer increased stability; a current drawback of lithium batteries is that there is degradation of anion and solvent at the cathode at high discharge rates, limiting cyclability[168]. It would therefore be of interest to this report to study the two systems at the cathode at high voltage, using *ab initio* MD.

Conclusions

9 References

(1) www.isaacsugden.moonfruit.com/scripts/.

(2) Patel, M.; Swain, A. C. *Polym Degrad Stabil,* **2004**, *83*, 539.

(3) Salt, C.; Lennox, A. J.; Takagaki, M.; Maguire, J. A.; Hosmane, N. S. *Russian Chemical Bulletin,* **2004**, *53*, 1871.

(4) Lundstedt, C.; Harken, A.; Day, E.; Robertson, B. W.; Adenwalla, S. *Nucl. Instrum. Methods Phys. Res., Sect. A,* **2006**, *562*, 380.

(5) Slatkin, D. N. *Brain,* **1991**, *114*, 1609.

(6) Slatkin, D. N. *J Neuro-Oncol,* **1997**, *33*, 141.

(7) Barth, R. F.; Vicente, M. G. H.; Harling, O. K.; Kiger, W. S.; Riley, K. J.; Binns, P. J.; Wagner, F. M.; Suzuki, M.; Aihara, T.; Kato, I.; Kawabata, S. *Radiation Oncology,* **2012**, *7*.

(8) Patel, H.; Takagaki, M.; Bode, B. P.; Snajdr, I.; Patel, D.; Sharman, C.; Bux, M.; Bux, S.; Kotora, M.; Hosmane, N. S. *Biochem. Biophys. J. Neutron Ther. Cancer Treat*, *1*, 15.

(9) Share, G. H.; Murphy, R. J.; Tylka, A. J.; Kozlovsky, B.; Ryan, J. M.; Gwon, C. *J Geophys Res-Space,* **2011**, *116*.

(10) Simms, P. *J Appl Crystallogr,* **1981**, *14*, 58.

(11) Sezgi, N. A.; Ersoy, A.; Dogu, T.; Ozbelge, H. O. *Chem Eng Process,* **2001**, *40*, 525.

(12) Jemmis, E. D.; Balakrishnarajan, M. M.; Pancharatna, P. D. *J. Am. Chem. Soc.,* **2001**, *123*, 4313.

(13) Mingos, D. M. P. *J Chem Soc Chem Comm,* **1983**, 706.

(14) Sweet, W. H.; Soloway, A. H.; Wright, R. L. *J. Pharmacol. Exp. Ther.,* **1962**, *137*, 263.

(15) Soloway, A. H.; Wright, R. L.; Messer, J. R. *J. Pharmacol. Exp. Ther.,* **1961**, *134*, 117.

(16) In *Aldrich Chemical Co. Inc. MSDS for o carborane* 2006.

(17) In *Strem Chemicals Inc. MSDS for caesium chloride* 1989.

(18) Lenga, R. E.; Sigma-Aldrich Corporation. *The Sigma-Aldrich library of chemical safety data*; Ed. 1 ed.; Sigma-Aldrich Corp: Milwaukee, WI, USA (P.O. Box 355, Milwaukee 53201), 1985.

(19) Heying, T. L.; Ager, J. W.; Clark, S. L.; Papetti, S.; Alexander, R. P.; Reid, J. A.; Trotz, S. I. *Inorg. Chem.,* **1963**, *2*, 1097.

(20) Kipping, F. S. *J. Chem. Soc.,* **1905**, *87*, 628.

(21) Carfax Publishing: Abingdon, 1989, p v.

(22) McNaught, A. D.; Wilkinson, A.; International Union of Pure and Applied Chemistry. *Compendium of chemical terminology : IUPAC recommendations*; 2nd ed.; Blackwell Science: Oxford England ; Malden, MA, USA, 1997.

(23) Thomas, N. R. *Silicon,* **2010**, *2*, 187.

(24) Osaki, K. *Rheol Acta,* **1993**, *32*, 429.

(25) Kanner, B.; Reid, W. G.; Petersen, I. H. *Ind Eng Chem Prod Rd,* **1967**, *6*, 88.

(26) Daudt, W. H.; Hyde, J. F. *J Am Chem Soc,* **1952**, *74*, 386.

(27) Lauter, U.; Kantor, S. W.; Schmidt-Rohr, K.; MacKnight, W. J. *Macromolecules,* **1999**, *32*, 3426.

(28) Kresse, H.; Wiegeleben, A.; Krucke, B. *Acta Polym,* **1988**, *39*, 583.

(29) Rochow, E. G. *Unnatural products; new and useful materials from silicon*; Pennsylvania State University: University Park,, 1960.

(30)   Mera, G.; Ionescu, E. In *Encyclopedia of Polymer Science and Technology*; John Wiley & Sons, Inc.: 2002.

(31)   Stark, F. O.; Falender, J. R.; Wright, A. P. In *Comprehensive Organometallic Chemistry*; Editors-in-Chief: Geoffrey, W., Stone, F. G. A., Abel, E. W., Eds.; Pergamon: Oxford, 1982, p 305.

(32)   Yin, Y.; Li, J.; Liu, Y.; Li, Z. *J. Appl. Polym. Sci.,* **2005**, *96*, 1394.

(33)   Mays, R. L.; Dickey, M. D.; Genzer, J. *Lab Chip,* **2013**.

(34)   Abd-El-Aziz, A. S.; Carraher, C. E.; Pittman, C. U.; Zeldin, M. *Macromolecules Containing Metal and Metal-Like Elements, Boron-Containing Particles*; Wiley, 2007.

(35)   Shimomura, H.; Muramatsu, H. In *Abstracts of Papers. Symposium on Radiochemistry* 1999; Vol. 43, p 188.

(36)   Mark, J. E. *Polymer data handbook*; 2nd ed.; Oxford University Press: Oxford, 2009.

(37)   Beltzung, M.; Picot, C.; Herz, J. *Macromolecules,* **1984**, *17*, 663.

(38)   Shih, H.; Flory, P. J. *Macromolecules,* **1972**, *5*, 758.

(39)   Smith, D.; Babb, D. *Macromolecules,* **1996**, *29*, 852.

(40)   Jarvis, N. L. *J. Phys. Chem.,* **1966**, *70*, 3027.

(41)   Krea, M.; Roizard, D.; Moulai-Mostefa, N. *Polym. Int.,* **2013**, *62*, 1413.

(42)   Cabanelas, J. C.; Prolongo, S. G.; Serrano, B.; Bravo, J.; Baselga, J. *J. Mater. Process. Technol.,* **2003**, *143–144*, 311.

(43)   Bose, A.; Gilpin, R. K.; Jaroniec, M. *J. Colloid Interface Sci.,* **2000**, *226*, 131.

(44)   Kosfeld, R.; Heß, M.; Uhlenbroich, T. In *Integration of Fundamental Polymer Science and Technology*; Springer: 1986, p 331.

(45)   Wang, B. Y.; Krause, S. *Macromolecules,* **1987**, *20*, 2201.

(46)   Clarson, S. J.; Dodgson, K.; Semlyen, J. A. *Polymer,* **1985**, *26*, 930.

(47)   Lotters, J. C.; Olthuis, W.; Veltink, P. H.; Bergveld, P. *J. Micromech. Microeng.,* **1997**, *7*, 145.

(48)   Peters, E. N.; Kawakami, J. H.; Kwiatkowski, G. T.; Hedaya, E.; Joesten, B. L.; Mcneil, D. W.; Owens, D. A. *J Polym Sci Pol Phys,* **1977**, *15*, 723.

(49)   Patel, M.; Swain, A. C.; Cunningham, J. L.; Maxwell, R. S.; Chinn, S. C. *Polym Degrad Stabil,* **2006**, *91*, 548.

(50)   Hedaya, E.; Kawakami, J. H.; Kopf, P. W.; Kwiatkowski, G. T.; Mcneil, D. W.; Owen, D. A.; Peters, E. N.; Tulis, R. W. *J Polym Sci Pol Chem,* **1977**, *15*, 2229.

(51)   Zhang, X. C.; Kong, L. H.; Dai, L. N.; Zhang, X. Z.; Wang, Q.; Tan, Y. X.; Zhang, Z. J. *Polymer,* **2011**, *52*, 4777.

(52)   Peters, E. N., 1980, *Method for producing carborane-siloxane polymers directly from carborane*, **1980**

(53)   Patel, M.; Swain, A. C.; Skinner, A. R.; Mallinson, L. G.; Hayes, G. F. *Macromol Symp,* **2003**, *202*, 47.

(54)   Kalousti.Mk; Wiersema, R. J.; Hawthorn.Mf *J. Am. Chem. Soc.,* **1972**, *94*, 6679.

(55)   Bregadze, V. I. *Chem. Rev.,* **1992**, *92*, 209.

(56)   Armstrong, A. F.; Valliant, J. F. *Dalton Trans.,* **2010**, *39*, 8128.

(57)   Brown, C. A.; Mckee, M. L. *J. Mol. Model.,* **2006**, *12*, 653.

(58)   Edvenson, G. M.; Gaines, D. F. *Inorg. Chem.,* **1990**, *29*, 1210.

(59)   Juhasz, M.; Hoffmann, S.; Stoyanov, E.; Kim, K. C.; Reed, C. A. *Angew. Chem. Int. Ed.,* **2004**, *43*, 5352.

(60)   Gimarc, B. M.; Warren, D. S.; Ott, J. J.; Brown, C. *Inorg. Chem.,* **1991**, *30*, 1598.

(61)   Gimarc, B. M.; Zhao, M. *Inorg. Chem.,* **1996**, *35*, 825.

(62)   Johnson, B. F. G.; Roberts, Y. V.; Parisini, E. *Inorg. Chim. Acta,* **1993**, *211*, 17.

(63)   Johnson, B. F. G. *J. Chem. Soc., Chem. Commun.,* **1986**, 27.

(64)   Wales, D. J. *J. Am. Chem. Soc.,* **1993**, *115*, 1557.

(65)   Dunks, G. B.; Wiersema, R. J.; Hawthorn.Mf *J. Am. Chem. Soc.,* **1973**, *95*, 3174.

(66)   Emin, D. *J. Solid State Chem.,* **2006**, *179*, 2791.

(67)   Mingos, D. M. P. *Acc. Chem. Res.,* **1984**, *17*, 311.

(68)   Bouchacourt, M.; Thevenot, F. *J. Less. Common. Met.,* **1979**, *67*, 327.

(69)   Beauvy, M. *J. Less. Common. Met.,* **1983**, *90*, 169.

(70)   Morosin, B.; Kwei, G. H.; Lawson, A. C.; Aselage, T. L.; Emin, D. *J Alloy Compd,* **1995**, *226*, 121.

(71)   Aydin, S.; Simsek, M. *Phys. Status. Solidi. B,* **2009**, *246*, 62.

(72)   Domnich, V.; Reynaud, S.; Haber, R. A.; Chhowalla, M. *J. Am. Ceram. Soc.,* **2011**, *94*, 3605.

(73)   Ogitsu, T.; Gygi, F.; Reed, J.; Motome, Y.; Schwegler, E.; Galli, G. *J. Am. Chem. Soc.,* **2009**, *131*, 1903.

(74)   Liu, Z. L.; Kawamura, J.; Nagasono, M.; Maeda, K.; Kawai, J. *J. Electron. Spectrosc. Relat. Phenom.,* **2004**, *135*, 73.

(75)   Ownby, P. D. *J. Am. Ceram. Soc.,* **1975**, *58*, 359.

(76)   Kobayashi, M.; Higashi, I.; Brodhag, C.; Thevenot, F. *J. Mater. Sci.,* **1993**, *28*, 2129.

(77)   Inoue, T.; Onchi, T.; Koyama, H.; Suzuki, H. *J. Nucl. Mater.,* **1978**, *74*, 114.

(78)   Jimbou, R.; Kodama, K.; Saidoh, M.; Suzuki, Y.; Nakagawa, M.; Morita, K.; Tsuchiya, B. *J. Nucl. Mater.,* **1997**, *241*, 1175.

(79)   Schmirgeld, L.; Zuppiroli, L.; Brunel, M.; Delafon, J.; Templier, C. *Aip. Conf. Proc.,* **1991**, *231*, 630.

(80)   Tarasikov, V. P. *At. Energ.,* **2009**, *106*, 220.

(81)   Shcherbak, V. I.; Tarasikov, V. P.; Bykov, V. N.; Rudenko, V. A. *Sov. Atom. Energy,* **1986**, *60*, 227.

(82)   Kushita, K. N.; Hojou, K.; Furuno, S. *Microsc. Microanal. M.,* **1995**, *6*, 149.

(83)   Inui, H.; Mori, H.; Fujita, H. *Scr. Metall.,* **1988**, *22*, 249.

(84)   Simeone, D.; Mallet, C.; Dubuisson, P.; Baldinozzi, G.; Gervais, C.; Maquet, J. *J. Nucl. Mater.,* **2000**, *277*, 1.

(85)   Xin, F.; Jun, J.; Chao, L.; Jun, Y. *Nanotechnology,* **2009**, *20*.

(86)   Schwetz, K. A.; Sigl, L. S.; Greim, J.; Knoch, H. *Wear,* **1995**, *181*, 148.

(87)   Chen, M. W.; McCauley, J. W.; Hemker, K. J. *Science,* **2003**, *299*, 1563.

(88)   Bao, R. Q.; Chrisey, D. B. *J. Mater. Sci.,* **2011**, *46*, 3952.

(89)   Dymon, J.; Wibby, R.; Kleingardner, J.; Tanski, J. M.; Guzei, I. A.; Holbrey, J. D.; Larsen, A. S. *Dalton Trans.,* **2008**, 2999.

(90)   Soetens, J. C.; Millot, C.; Maigret, B. *J. Phys. Chem. A,* **1998**, *102*, 1055.

(91)   Rappe, A. K.; Casewit, C. J.; Colwell, K. S.; Goddard, W. A.; Skiff, W. M. *J. Am. Chem. Soc.,* **1992**, *114*, 10024.

(92)   Sun, H. *Macromolecules,* **1995**, *28*, 701.

(93)   Kohn, W.; Sham, L. J. *Phys. Rev.,* **1965**, *140*, 1133.

(94)   Perdew, J. P.; Burke, K.; Ernzerhof, M. *Phys Rev Lett,* **1996**, *77*, 3865.

(95)   Slater, J. C. *Phys. Rev.,* **1930**, *36*, 0057.

(96)   Guseinov, I. I. *Int. J. Quantum Chem.,* **2002**, *90*, 114.

References

(97) Atkins, P. W.; Friedman, R. S. *Molecular quantum mechanics*; Oxford university press Oxford, 1997; Vol. 3.

(98) Lippert, G.; Hutter, J.; Parrinello, M. *Mol. Phys.,* **1997**, *92*, 477.

(99) Barnett, R. N.; Landman, U. *Phys. Rev. B.,* **1993**, *48*, 2081.

(100) Gale, J. D.; Rohl, A. L. *Mol Simulat,* **2003**, *29*, 291.

(101) Smith, W.; Todorov, I. T. *Mol. Simul.,* **2006**, *32*, 935.

(102) M. J. Frisch, G. W. T., H. B. Schlegel, G. E. Scuseria, M. A. Robb, J. R. Cheeseman, G. Scalmani, V. Barone, B. Mennucci, G. A. Petersson, H. Nakatsuji, M. Caricato, X. Li, H. P. Hratchian, A. F. Izmaylov, J. Bloino, G. Zheng, J. L. Sonnenberg, M. Hada, M. Ehara, K. Toyota, R. Fukuda, J. Hasegawa, M. Ishida, T. Nakajima, Y. Honda, O. Kitao, H. Nakai, T. Vreven, J. A. Montgomery, Jr., J. E. Peralta, F. Ogliaro, M. Bearpark, J. J. Heyd, E. Brothers, K. N. Kudin, V. N. Staroverov, R. Kobayashi, J. Normand, K. Raghavachari, A. Rendell, J. C. Burant, S. S. Iyengar, J. Tomasi, M. Cossi, N. Rega, J. M. Millam, M. Klene, J. E. Knox, J. B. Cross, V. Bakken, C. Adamo, J. Jaramillo, R. Gomperts, R. E. Stratmann, O. Yazyev, A. J. Austin, R. Cammi, C. Pomelli, J. W. Ochterski, R. L. Martin, K. Morokuma, V. G. Zakrzewski, G. A. Voth, P. Salvador, J. J. Dannenberg, S. Dapprich, A. D. Daniels, Ö. Farkas, J. B. Foresman, J. V. Ortiz, J. Cioslowski, and D. J. Fox *Gaussian, Inc., Wallingford CT,,* **2009**.

(103) Laino, T.; Mohamed, F.; Laio, A.; Parrinello, M. *J. Chem. Theory Comput.,* **2006**, *2*, 1370.

(104) Delley, B. *J. Chem. Phys.,* **2000**, *113*, 7756.

(105) Boyd, R. H.; Gee, R. H.; Han, J.; Jin, Y. *Abstr. Pap. Am. Chem. S,* **1994**, *207*, 24.

(106) Mullerplathe, F. *Acta Polym.,* **1994**, *45*, 259.

(107) Kong, Y.; Manke, C. W.; Madden, W. G.; Schlijper, A. G. *Int. J. Thermophys.,* **1994**, *15*, 1093.

(108) Youngs, T. G. A. *J. Comput. Chem.,* **2010**, *31*, 639.

(109) Accelrys *Materials Studio Release Notes, Release 4.1, Accelrys Software, Inc.: San Diego.,* **2006**.

(110) Sun, H.; Mumby, S. J.; Maple, J. R.; Hagler, A. T. *J. Am. Chem. Soc.,* **1994**, *116*, 2978.

(111) Jorgensen, W. L.; Tiradorives, J. *J. Am. Chem. Soc.,* **1988**, *110*, 1657.

(112) Dodd, S. P.; Saunders, G. A.; James, B. *J. Mater. Sci.,* **2002**, *37*, 2731.

(113) Werheit, H.; Kuhlmann, U.; Rotter, H. W.; Shalamberidze, S. O. *J. Phys.: Condens. Matter,* **2010**, *22*.

(114) Kwei, G. H.; Morosin, B. *J. Phys. Chem.,* **1996**, *100*, 8031.

(115) Sologub, O.; Michiue, Y.; Mori, T. *Acta Crystallographica Section E,* **2012**, *68*, i67.

(116) Her, J. H.; Zhou, W.; Stavila, V.; Brown, C. M.; Udovic, T. J. *J. Phys. Chem. C,* **2009**, *113*, 11187.

(117) Geis, V.; Guttsche, K.; Knapp, C.; Scherer, H.; Uzun, R. *Dalton Trans.,* **2009**, 2687.

(118) Peters, E. N. *Ind Eng Chem Prod Rd,* **1984**, *23*, 28.

(119) Lewis, D. W.; Willock, D. J.; Catlow, C. R. A.; Thomas, J. M.; Hutchings, G. J. *Nature,* **1996**, *382*, 604.

(120) Ardo, H. http://code.google.com/p/shedskin/ 2013.

(121) Wohlfarth, C. *CRC handbook of enthalpy data of polymer-solvent systems*; CRC/Taylor & Francis: Boca Raton, Fla. ; London, 2006.

(122) Voronkov, M. G.; Mileshkevich, V. P.; Yuzhelevskii, Y. A. *The siloxane bond : physical properties and chemical transformations*; Consultants Bureau: New York, 1978.

References

(123)   Andriot, M.; Chao, S.; Colas, A.; Cray, S.; deBuyl, F.; DeGroot, J.; Dupont, A.; Easton, T.; Garaud, J.; Gerlach, E.; Nova Science Publishers, New York: 2009; Vol. 84.

(124)   Carey, V. P. *Statistical thermodynamics and microscale thermophysics*; Cambridge University Press: Cambridge, 1999.

(125)   Darrigo, J. S. *Am. J. Physiol,,* **1978**, *235*, C109.

(126)   Hirschfelder, J. O.; Bird, R. B.; Curtiss, C. F. *Molecular theory of gases and liquids*; Corrected printing with notes added ed.; Wiley: New York, 1964.

(127)   Cohen, E. R.; Royal Society of Chemistry (Great Britain); International Union of Pure and Applied Chemistry. Physical and Biophysical Chemistry Division. *Quantities, units and symbols in physical chemistry*; 3rd ed.; Royal Society of Chemistry: Cambridge, 2007.

(128)   http://en.wikipedia.org/wiki/shear_modulus.

(129)   Landsberg, P. T. *Thermodynamics and statistical mechanics*; Dover: New York, 1990.

(130)   Todorov, I. T.; Smith, W.; Trachenko, K.; Dove, M. T. *J. Mater. Chem.,* **2006**, *16*, 1911.

(131)   Lendlein, A.; Kelch, S. *Angew. Chem. Int. Ed.,* **2002**, *41*, 2034.

(132)   Gratton, S. E. A.; Parrott, M. C.; Adronov, A. *J Inorg Organomet P,* **2005**, *15*, 469.

(133)   Lee, S. H.; Lee, W. G.; Chung, B. G.; Park, J. H.; Khademhosseini, A. *Macromol. Rapid Commun.,* **2009**, *30*, 1382.

(134)   Tillet, G.; Boutevin, B.; Ameduri, B. *Prog. Polym. Sci.,* **2011**, *36*, 191.

(135)   Szycher, M.; Valdez, R. *J. Clin. Eng.,* **1983**, *8*, 234.

(136)   Bueche, A. *Rubber Chem. Technol.,* **1955**, *28*, 865.

(137)   Buwalda, S. J.; Perez, L. B.; Teixeira, S.; Calucci, L.; Forte, C.; Feijen, J.; Dijkstra, P. J. *Biomacromolecules,* **2011**, *12*, 2746.

(138)   Nishide, S.; Shimizu, H. *J. Polym. Sci., Part A: Polym. Chem,* **1979**, *17*, 1821.

(139)   Makuuchi, K.; Cheng, S. *Radiation processing of polymer materials and its industrial applications*; John Wiley & Sons, 2012.

(140)   Clayden, J.; Greeves, N.; Warren, S. G. *Organic chemistry*; 2nd ed.; Oxford University Press: Oxford, 2012.

(141)   Cioslowski, J.; Liu, G. H.; Castro, R. A. M. *Chem. Phys. Lett.,* **2000**, *331*, 497.

(142)   Carrard, M.; Emin, D.; Zuppiroli, L. *Phys. Rev. B.,* **1995**, *51*, 11270.

(143)   Aselage, T. L.; Tallant, D. R. *Phys. Rev. B.,* **1998**, *57*, 2675.

(144)   Li, X. G.; Jiang, D. L.; Zhang, J. X.; Lin, Q. L.; Chen, Z. M.; Huang, Z. G. *J. Eur. Ceram. Soc.,* **2013**, *33*, 1655.

(145)   Echeverría, E.; Pasquale, F. L.; Colón Santana, J. A.; Zhang, L.; James, R.; Sokolov, A.; Kelber, J. A.; Dowben, P. *Mater. Lett.,* **2013**.

(146)   Sugden, I. J.; Plant, D. F.; Bell, R. G. *Chem. Commun.,* **2013**, *49*, 975.

(147)   Grafstein, D.; Dvorak, J. *Inorg. Chem.,* **1963**, *2*, 1128.

(148)   Kaloustian, M. K.; Wiersema, R. J.; Hawthorne, M. F. *J. Am. Chem. Soc.,* **1972**, *94*, 6679.

(149)   McIntosh, R. D.; Ellis, D.; Giles, B. T.; Macgregor, S. A.; Rosair, G. M.; Welch, A. J. *Inorg. Chim. Acta,* **2006**, *359*, 3745.

(150)   Ellis, D.; Garrioch, R. M.; Rosair, G. M.; Welch, A. J. *Polyhedron,* **2006**, *25*, 915.

(151)   Dunn, S.; Rosair, G. M.; Thomas, R. L.; Weller, A. S.; Welch, A. J. *Angew. Chem., Int. Ed..* **1997**, *36*, 645.

(152)   Ott, J. J.; Brown, C. A.; Gimarc, B. M. *Inorg. Chem.,* **1989**, *28*, 4269.

(153)   Leach, A. G.; Catak, S.; Houk, K. N. *Chem. Eur. J,* **2002**, *8*, 1290.

(154)   Wust, F.; Skaddan, M. B.; Leibnitz, P.; Spies, H.; Katzenellenbogen, J. A.; Johannsen, B. *Bioorg. Med. Chem.,* **1999**, *7*, 1827.

(155)   Shannon, R. D. *Acta Crystallogr., Sect. A,* **1976**, *32*, 751.

(156)   Petersen, C. *D-Lib Magazine,* **2005**, *11*, 1.

(157)   McBreen, J.; Lee, H. S.; Yang, X. Q.; Sun, X. *Elec. Soc. S,* **2000**, *99*, 494.

(158)   Best, A. S.; Bhatt, A. I.; Hollenkamp, A. F. *J. Electrochem. Soc.,* **2010**, *157*, A903.

(159)   Xu, W.; Xiao, J.; Wang, D. Y.; Zhang, J.; Zhang, J. G. *Electrochem. Solid-State Lett.,* **2010**, *13*, A48.

(160)   Sun, X.; Lee, H. S.; Yang, X. Q.; McBreen, J. *Electrochem. Solid-State Lett.,* **2002**, *5*, A248.

(161)   Davalos, J. Z.; Gonzalez, J.; Guerrero, A.; Hnyk, D.; Holub, J.; Oliva, J. M. *J. Phys. Chem. C,* **2013**, *117*, 1495.

(162)   Ohba, N.; Miwa, K.; Aoki, M.; Noritake, T.; Towata, S.; Nakamori, Y.; Orimo, S.; Zuttel, A. *Phys. Rev. B.,* **2006**, *74*.

(163)   Chen, H. P.; Fergus, J. W.; Jang, B. Z. *J. Electrochem. Soc.,* **2000**, *147*, 399.

(164)   Chausse, A.; Berhil, M.; Messina, R. *Electrochim. Acta,* **1999**, *44*, 2365.

(165)   Ionica-Bousquet, C. M.; Casteel Jr, W. J.; Pearlstein, R. M.; GirishKumar, G.; Pez, G. P.; Gómez-Romero, P.; Palacín, M. R.; Muñoz-Rojas, D. *Electrochem. Commun.,* **2010**, *12*, 636.

(166)   Peymann, T.; Knobler, C. B.; Hawthorne, M. F. *J. Am. Chem. Soc.,* **1999**, *121*, 5601.

(167)   Nakao, R.; Ueda, N.; Abe, Y. S.; Horii, T.; Inoue, H. *Polym Advan Technol,* **1996**, *7*, 863.

(168)   Zhang, S.; Xu, K.; Jow, T. *Electrochem. Solid-State Lett.,* **2002**, *5*, A206.